Inner-Core Vacillation Cycles during the Rapid Intensification of Hurricane Katrina

by

Nguyen Chi Mai

Main supervisor: Prof. Dr. Michael J. Reeder

Associate Supervisor: Dr. Noel E. Davidson

PhD Thesis

SCHOOL OF MATHEMATICAL SCIENCES

MONASH UNIVERSITY

Date of submission: 10 FEBRUARY 2010

Contents

List of Figures

List of Tables

Abstract.

Tropical cyclone intensity change by internal processes is studied using the Australian Bureau of Meteorology operational model, TCLAPS. An ensemble of high-resolution simulations of Hurricane Katrina (2005) reveal a robust feature, in which the majority of modelled vortices go through cycles of structure change, vacillating between a more symmetric and a more asymmetric phase during rapid intensification.

- During the ***Symmetric*** phase the eye-wall has a high level of symmetry, consisting of relatively uniform elongated convective bands. Low-level vorticity and equivalent potential temperature exhibit a ring-like structure. The largest intensification rates occur near the radius of maximum tangential wind (RMW).

- The ***Asymmetric*** phase is characterised by a highly asymmetric eyewall, having a polygonal form with vortical hot towers (VHTs) located at the vertices. Low level vorticity and equivalent potential temperature have a monopole structure with the maximum near the center. The largest intensification rates occur inside the RMW.

Detailed analyses suggest the following transition mechanisms:

- ***Symmetric to Asymmetric*** transitions are associated with the outbreak of VHTs in the eyewall, which result from a cooperative combination of barotropic and convective instability. These VHTs actively mix air between the eye and eyewall, thus, creating the monopole structure.

- ***Asymmetric to Symmetric*** transitions occur as the VHTs weaken due to exhausted convective instability. They become horizontally strained convective bands that move radially outward as vortex rossby waves (VRWs). High intensification rates resume near the RMW as result of a) increased horizontal vorticity fluxes associated with redevelopment of convection in the reduced rapid filamentation zone outside of the weakened VHTs; and b) VRW-mean flow interactions.

We hypothesise that these cycles are an alternative mode of hurricane intensification during rapid intensification of less mature storms as opposed to Eyewall Replacement Cycles that are observed primarily in strong hurricanes with a mature structure.

Declarations

Inner-Core Vacillation Cycles during the Rapid Intensification of Hurricane Katrina

I declare that this thesis is my own work and has not been submitted in any form for another degree or diploma at any university or other institute of tertiary education. Information derived from the published and unpublished work of others has been acknowledged in the text and a list of references is given.

[redacted]

Nguyen Chi Mai
Melbourne, February 10, 2010

Notice 1

Notice 2

I certify that I have made all reasonable efforts to secure copyright permissions for third-party content included in this thesis and have not knowingly added copyright content to my work without the owner's permission.

Acknowledgments.

I am deeply grateful to my supervisors, Prof. Michael J. Reeder (Monash Univeristy) and Dr. Noel E. Davidson (Bureau of Meteorology) for their insighful scientific knowledge, experience and thoughtful guidance throughout the years of my PhD study. They are especially patient and supportive during the last few months of my writing-up period. I honestly appreciate their enourmous efforts in correcting my writing and posing difficult questions, which help to improve this manuscript substiantially. Overall, their passion and enthusiasms towards science inspire me to try to become truly interested in the research I am working on. After these 4 years of PhD study, I realise that my supervisors indeed help me to grow (not only older with more grey hair ;)) more confident as a true scientist.

I am indebted to Professors Roger K. Smith (University of Munich, Germany) and Michael T. Montgomery (Naval Postgraduate School, USA) for their insightful inputs and constructive comments to my research. They have spent several hours working on a manuscript of a paper that we are planning to publish. I appreciate their great patience towards my imperfect English while I try to express complex scientific ideas.

I am also greatly benefited from scientific discussions with scientists from Bureau of Meteorology Drs. Kevin Tory, Jeff Kepert, Gary Dietachmayer, Lawrie Rikus; with visiting scientists Drs. Johny Chan, Craig Bishop, Chris Snyder, Jun-Ichi Yano; and scientists from overseas Drs. John Knaff and James Kossin (by email correspondence). Their expertise and experience in slightly different areas of meteorology are helpful for me to broaden my knowledge.

I am thankful to Dr. Lawrie Rikus (Bureau of Meteorology) for calculating synthetic cloud brightness temperature from my simulations so that I can compare with satellite data for validation. Digital satellite data of hurricane Katrina used for validation are from the (CIRA; Cooperative Institute for Research in the Atmosphere)/(RAMMB; Regional and Mesoscale Meteorology Branch) tropical cyclone polar image archive. The data and the code to read it are kindly provided by Drs. John Knaff and Ray Zehr and NESDIS (National Environmental Satellite, Data, and Information Service).

The data, model, and computing facility of this research are fully supported by Bureau of Meteorology. Dr. Noel Davidson had helped me in getting data and setting up scripts to run the simulations. I am also thankful to Les Logan and Robin Owen (Bureau of Meteorology) for their helps in computing matters.

This work is funded fully by an AusAID scholarship, without it my study in Australia would not be possible. During the course of study, I have also received travel supports from Monash University for attending national and international conferences, and for visiting University of Munich, Germany in 2008. These trips are very helpful for me to get in touch with new ideas, to discuss with top scientists in the field from overseas, and to present my work for a broader audience.

Last but not least, I have received great moral and emotional supports from my housemates while in Australia, and my close friends both in Australia and overseas, whose names are not mentioned here but they know that I am thinking of them right now. Their cares and supports keep me feel 'alive' and connected to the world from this PhD 'tunnel'. I am thankful to the father of my children who agreed for the children to accompany me to Australia while I am doing PhD. Otherwise I would not have been able to concentrate to work. I am blessed to have love from my brothers, Nghia, Hieu and Zdung, and theirs wives, who assure me that I always can count on them if worst times were arrived.

During the last month of this writting, my children and housemate, Hoang Anh, have assisted me greatly to do house chores so that I could concentrate to write. I would like to thank God for arranging everything so magically so that I can write this line now with the peace in mind that I will be able to submit this thesis on time.

This work is dedicated to my parents Nguyen Doan Trung and Tran Thi Thoa, and my children Mai Linh and Hoang Linh. I wish my parents could see this small accomplishment which shows my maturity and ability to live with confidence. I hope this token of love will encourage my children to have confidence to fulfil their dreams.

Chapter 1

TROPICAL CYCLONE INTENSIFICATION

Tropical Cyclones (TCs) are one of the natural phenomena that have attracted man's attention since the earliest times of our civilization (Emanuel, 2005). The great interest in understanding TCs arose from their power to cause catastrophic loss of property and human lives. Thus, our ultimate goal is to be able to accurately predict their movement and development so that steps can be taken to minimize their adverse impacts.

Our understanding of TCs has advanced greatly along with progress in science and technology. In olden times, TCs were perceived as divine natural 'creatures' because of their sudden appearance with deadly strong wind, torrential rain, and destructive storm surge. Nowadays, TCs do not take us by surprise since their formation, movement and development are closely monitored using the global satellite and observational network.

Moreover, the skill in forecasting TC tracks has also improved significantly during the last few decades. Currently, the average forecast errors for TC tracks over the North Atlantic and Northeast Pacific basins are of the order of 100 km, 180 km and 280 km for 24 h, 48 h and 72 h, respectively (NHC, 2008). Figure 1.1a shows the annual average errors in track forecasts from the National Huricane Center (NHC) for TCs in the Atlantic basin. On average, the current skill of five-day track forecasts is about the same as the two-day forecast skill twenty years ago. This enormous improvement in predicting TC tracks is due largely to the improvement of numerical models in forecasting large-scale dynamical features as well as the use of ensemble forecasts. The improvement in TC track forecasts arising from better predictions of large-scale flows is a reflection of the fact that TCs are generally smaller than large-scale features (such as mid-latitude trough and ridge systems). Consequently, to a first approximation, TCs can be considered as point-vortices embedded in and steered by the large-scale systems.

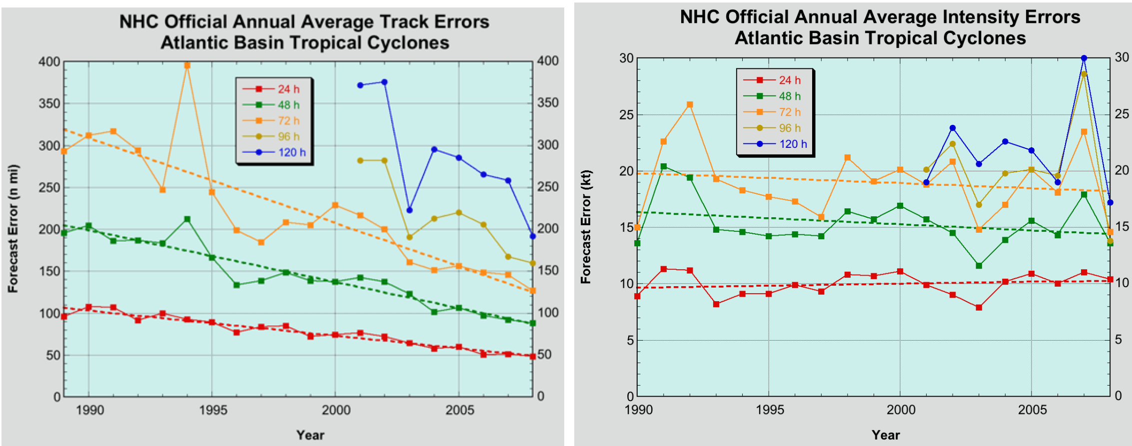

(a) Forecast track errors

(b) Forecast intensity errors

Figure 1.1: Annual average forecast errors for Atlantic basin tropical storms and hurricanes for the period 1970-2008, with least-squares trend lines superimposed. Data source from NHC (2008).

In contrast, our skill in predicting TC intensity is not improving at a comparable rate. For example, the average intensity errors of NHC, shown in Figure 1.1b, does not exhibit any detectable decreasing trends since 1990. This lack of improvement, despite the improvements in large-scale prediction, indicates that finer features of TC structure, which are not well represented by large-scale fields, are important in the intensification. Our current deficiencies in representing TC structure, and thus, deficiencies in intensity forecasts, are due to several reasons, including: a) a paucity of observations necessary to define the intense inner-core structure of TCs; b) a lack of sufficient horizontal and vertical resolution in numerical systems to represent the key dynamical and thermodynamical processes; and c) an incomplete understanding of the physical processes that affect TC intensity. Therefore, it is still a challenge and great research interest to study and understand better intensification mechanisms of TCs.

In this chapter, a review of the current state of understanding in TC intensification will be presented. The main characteristics of the structure of TCs and a brief discussion of the different intensification mechanisms are presented in Section 1. As this study is focused on internal intensification mechanisms, inner-core processes will be discussed in detail in Section 2. Finally, an outline of the thesis and its motivation are given in Section 3.

1.1 Tropical Cyclone Structure and Mechanisms for Intensification

1.1.1 Structure of Tropical Cyclones

The structure of TCs has been studied intensively since the early 70s. These studies have been based mainly on rawindsonde observations (see e.g. Frank, 1977a,b), flight data (Shea and Gray, 1973, Gray and Shea, 1973), and satellite imagery (Dvorak, 1975). Nowadays, the characteristic structure of TCs is well-known. Figure 1.2 shows the structure of the composite TC, constructed by Frank (1977a) using rawinsonde data at a coarse resolution. The main features of the composite TC are described below.

- ***Tangential wind.*** As shown in Figure 1.2a, the structure of a typical TC is characterised by a cyclonic rotating wind system with a maximum in the lower troposphere, just above the boundary layer, and decreasing with height thereafter. At upper levels, the tangential flow becomes anticyclonic, reaching a maximum near 150 hPa. The horizontal size of the cyclonic circulation (defined as the region with tangential wind speeds greater than 5 m s^{-1}) is around of 10 degrees, whereas the anticyclonic circulation at upper levels occupies a much larger area with the maximum located near 14 degrees. This tangential circulation in TCs is termed as primary circulation.

- ***Radial wind.*** Figure 1.2b shows the vertical profiles of the azimuthally-mean radial wind. The radial wind structure of TCs consists of: 1) an inflow layer in the lower part of the troposphere, up to about 700 hPa ; 2) a middle layer between 700 and 400 hPa where the radial wind is relatively weak; and 3) an outflow layer at upper levels having a maximum near 150 hPa, which coincides with the anticyclone aloft.

- ***Vertical motion.*** The vertical motion field, as shown in Figure 1.2c, has a strong upward branch at inner radii (inside of 2 degrees), which occupies nearly the whole depth of the troposphere. At outer radii there is mean compensating downward motion, with weak upward motion embedded in narrow bands.

  The combination of radial and vertical motions in TCs including: a) an inflow layer near the surface, b) a strong upward branch near the core, c) an outflow

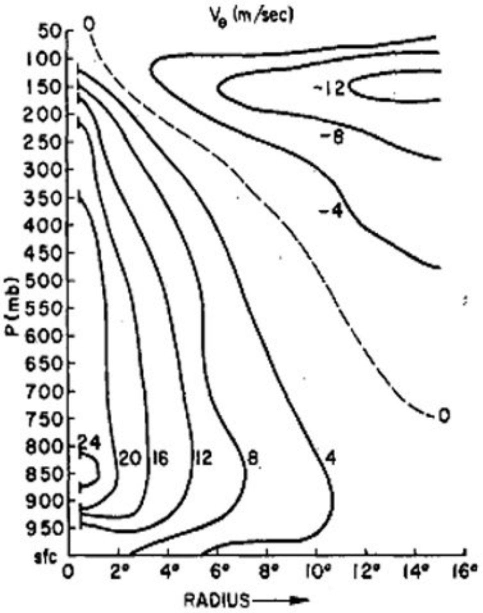

(a) Tangential wind $\bar{V}$t (m s^{-1})

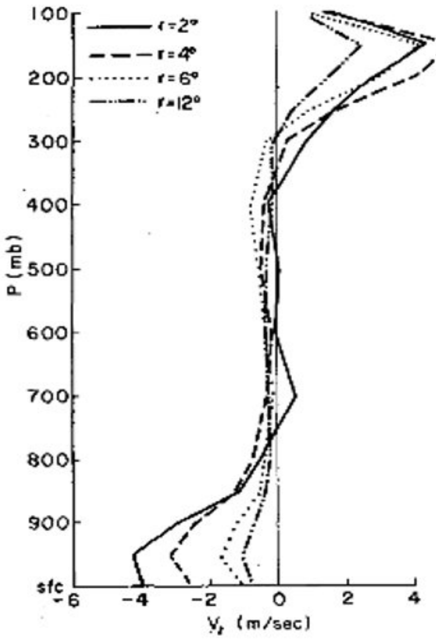

(b) Radial wind $\bar{V}$r (m s^{-1})

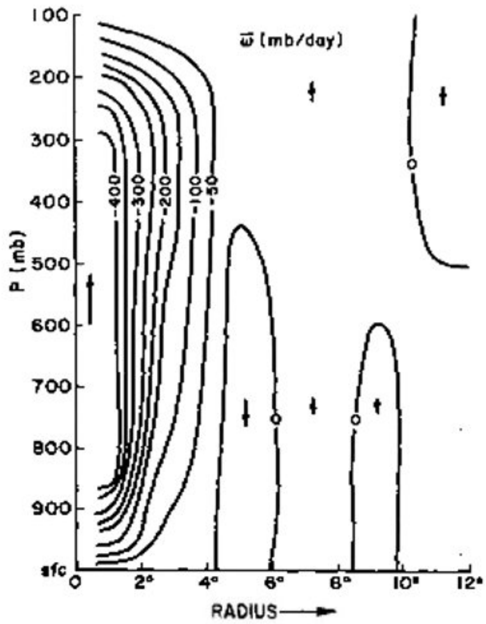

(c) Vertical motion $\bar{\omega}$ (mb day^{-1})

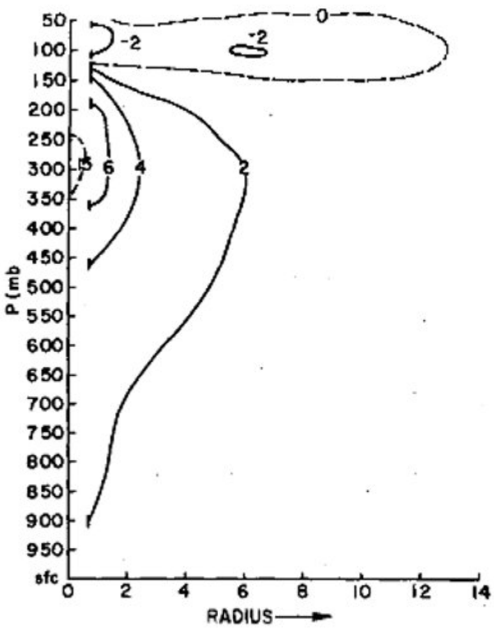

(d) Temperature anomaly $\bar{T} - \bar{T}_{14^o}$ (^{o}C)

Figure 1.2: Mean azimuthal structure of the composite TC from (Frank, 1977a).

layer at upper level, and d) a slow descending motion in a large area at outer radii is termed the secondary circulation.

- ***Temperature.*** The temperature structure of TCs is characterised by a distinctive warm core at upper levels. As can be seen in Figure 1.2d, the maximum of the warm core is located near 300 hPa and is warmer than the far field temperature by more than 6°C. This warm core structure in TCs is consistent with the decrease of the mean tangential wind with height through the thermal wind relationship[1].

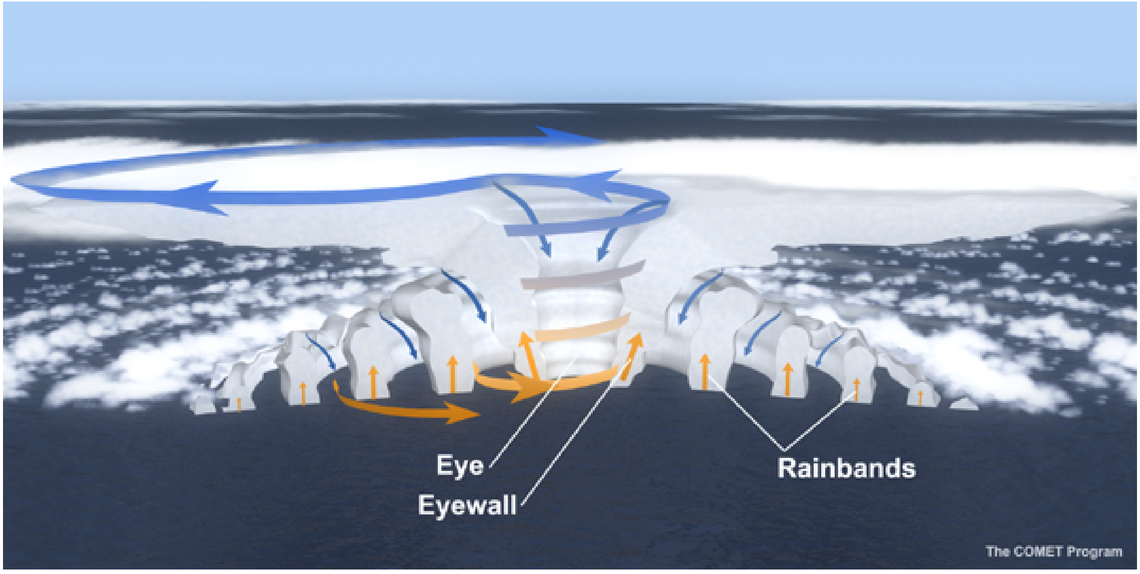

Figure 1.3: Schematic structure of a mature tropical cyclone. This image is available from COMET program http://www.comet.ucar.edu/.

Figure 1.3 shows schematically a vertical cross-section through the center of a typical mature tropical cyclone. The mean air streams in the core region are indicated by arrows and can be described as follows. At low levels, air spirals cyclonically inward towards the vortex center, increasing its moist entropy through surface fluxes from the warm ocean surface. When close to the vortex center, the air is forced upward (due to the continuity of the converging flow near the surface) in the convective clouds of the eyewall and in rainbands. In this upward branch, water vapour condenses as the air cools adiabatically, thus, releasing aloft the latent heat extracted from the surface. Finally, air spirals anticyclonically outwards at upper levels while cooling radiatively.

With the structure described above, tropical cyclones may be regarded as a natural heat engine, as suggested by Emanuel (1986), Bister and Emanuel (1998), Emanuel (2003, 2005). The hurricane-engine acquires moist entropy from the ocean

[1]The thermal wind relationship in TCs has the form $(2v/r + f)\partial v/\partial lnp = -R\partial T/\partial r$ (Elsberry et al., 1987). Thus, this relationship requires a warm core structure, i.e. a decrease of temperature with increasing radius ($\partial T/\partial r < 0$), to match with a decrease of the tangential wind with height ($\partial v/\partial lnp > 0$).

surface, ascends, and ultimately gives off heat at the much lower temperature of the lower stratosphere or upper troposphere. Then, for this engine-like system to maintain or increase its intensity, favourable conditions need to be present in some or all of the three branches, including:

- The ***inflow branch*** at low levels that determines the moist entropy intake of the system;
- The effectiveness of the ***outflow branch*** in removing the heat at the upper levels; and
- The favourable configuration of the ***upward branch***, where the energy conversion occurs. Since energy conversion processes of this hurricane-engine occur in deep upright convective clouds, it is crucial for hurricanes to have a vertically stacked structure.

1.1.2 Intensification mechanisms

The mechanisms by which TCs intensify can be grouped into three main classes: 1) intensification by surface processes, 2) intensification by large-scale dynamical processes, and 3) intensification by internal processes. Our current understanding of these mechanism is summarised below.

Intensification by surface processes

The condition of the underlying surface affects TC intensity by regulating the fluxes of latent and sensible heat from the warm ocean surface that fuel the storm and the momentum fluxes lost due to the friction. It is well-known that TCs dissipate quickly after making landfall because of the increased friction over land surfaces, and the removal of their main energy supply, latent heat fluxes from the warm ocean surface. Similarly, TCs tends to weaken as they cross colder water due to decreased surface heat fluxes. In contrast, TCs may intensify rapidly upon encountering warm surface areas such as warm core eddies in the cases of hurricanes *Opal* in 1995 (as suggested by Shay et al., 2000) and hurricane *Katrina* in 2005 (see for example McTaggart-Cowan et al., 2007).

Among the most intensively studied, the wind-induced surface heat exchange (WISHE) mechanism has attracted great research interest and application. WISHE has been proposed by Emanuel (1986), Rotunno and Emanuel (1987) as a mechanism for the intensification and maintenance of TCs. Emanuel suggests that TCs may intensify through a positive feedback between the wind speed near the surface and the evaporation of water from the underlying ocean, which depends on the wind speed. Then, the mechanism is one of self-induced heat transfer from the ocean, which is possible even without conditional instability. While this mechanism has achieved broad acceptance in current literature (e.g. Holton, 2004, Lighthill, 1998, Montgomery et al., 2006), Montgomery et al. (2009) have shown recently that TCs can intensify by pathways different from WISHE. Nevertheless, these authors do conclude that WISHE plays a role in accelerating the intensification process.

Although the concept that boundary layer processes control surface heat fluxes, and thus, the intensity of TCs is intuitively easy to understand, the actual physical processes in real TCs are not well observed, and probably not well represented in numerical models. For instance, it is a complicated task to calculate accurately the surface fluxes in very high wind conditions in the TC inner core regions (Moon et al., 2007).

Furthermore, TCs are not only influenced by the conditions of the ocean surface, the latter is also influenced by the former to some extent. For example, the portion of the ocean surface in the wake of a TC is observed to have a lower temperature than the surrounding areas. This cooling of the ocean surface is due partly to the evaporative cooling by precipitation from the TC system, and partly due to the curl of wind stress which generates divergence in the upper layer of the ocean, producing regions of upwelling. Upwelling cools the ocean surface by transporting and mixing colder water from deeper levels upwards. This effect is more pronounced for slow moving storms and in ocean regions with a shallow surface mixed layer (Lin et al., 2008, 2009).

Consequently, it is thought now that knowledge of the ocean heat content (OHC) of the upper layer, instead of just sea surface temperature, is important in determining the effects of the ocean surface on TC intensity (see e.g. Mainelli et al., 2008). Furthermore, to account for these complicated air-sea interactions, atmosphere-ocean coupled hurricane models are developed and used increasingly in hurricane modeling nowadays (Bender et al., 1993, Bender and Ginis, 2000, Bender et al., 2007, Yablonsky and Ginis, 2009).

Intensification by large-scale dynamical processes

Unlike TC track forecasting problems, in which TCs can be approximated as point-size objects embedded in and advected by large-scale circulations, for forecasting TC intensity, the structure of TCs must be adequately represented and the resulting intensity change is subject to the effects of the large-scale systems on the TC structure. Therefore, to understand the influence of large-scale systems on TC intensity, it is necessary to know how TCs respond to changing conditions in the surrounding environment.

From a kinematic point of view, the strong cyclonic circulation in the core of a TC resists the horizontal movements towards or away from the vortex center, including those originating from external regions. This resistance is represented by inertial frequency, which has the following form in an axisymmetric vortex in the gradient wind balance (Elsberry et al., 1987):

$$I^2 = (f_0 + \zeta)\left(f_0 + \frac{2V}{r}\right), \qquad (1.1)$$

where f_0 is the Coriolis parameter at the vortex center, and all others symbols are standard as explained in Table A.1. If I^2 is non-zero, any horizontal movement will produce a gradient wind imbalance and radial accelerations. For $I^2 < 0$, the acceleration will be in the direction of displacement, which will result in an unstable, growing circulation. For $I^2 > 0$, the acceleration will oppose the initial displacement and induce a stable oscillation with frequency I. According to Equation 1.1, the upper levels of TCs are the regions where responses of the TC vortex to the external forcing may penetrate close to the vortex center since I^2 may become negative with strong anticyclone (i.e. large negative value of ζ). Thus, the conditions at upper levels are commonly regarded as important for this intensification mechanism.

Some of the ways suggested by which large-scale processes can change the intensity of TCs are summarised as follow:

- ***Upper level outflow.*** TCs may intensify rapidly upon entering a region where the large-scale circulation at upper levels encourages strong outflows from the TC circulation. Such conditions are reported by Sadler (1978) to occur in certain regions below the Tropical Upper Tropospheric Trough (TUTT). Periods of rapid intensification in Typhoons *Rita, Physllis and Tess* in 1972 are thought to be associated with multi-directional outflow channels of the large-scale system at upper levels. Similarly, the enhanced divergence near the jet-entrance region at upper levels has been identified by Bosart et al. (2000) as a possible reason (among others) for the unpredicted rapid intensification of hurricane *Opal* in 1995.

- ***Vertical wind shear.*** It is well established that strong environmental vertical wind shear is detrimental to the genesis and intensification of TCs (Gray, 1968, McBride and Zehr, 1981, Merrill, 1988). Zehr (1992) found empirically a threshold value for vertical shear of 12.5 m s^{-1} above which TCs could not form in western North Pacific. Strong vertical shear is commonly found under mid-latitude troughs and the TUTT.

  An early explanation of the effect of vertical shear is the so-called "ventilation" effect (Gray, 1968), in which the warm core is advected away by the flow in the upper levels relative to the low-level TC circulation. Frank and Ritchie (2001) offer an alternative explanation, in which strong vertical shear induces wavenumber 1 asymmetries with convection concentrated on the left side of the shear vector in the downshear quadrant (for TCs in the northern hemisphere). Then, asymmetries at upper levels act to mix air of high potential vorticity and high equivalent potential temperature out of the core, thereby ventilating the core and weakening the vortex from top down.

- ***Additional momentum/vorticity sources.*** Troughs at upper levels may intensify TCs by providing fluxes of cyclonic angular momentum (Challa and Pfeffer, 1980, Molinari and Vollaro, 1990). This mechanism has been proposed by Molinari and Vollaro (1989, 1990) as an explanation for the rapid intensification of hurricane *Elena* of 1985. These authors suggested that as hurricane *Elena* approached a baroclinic wave, the region with localised flux convergence of cyclonic angular momentum shifted to progressively smaller radii, exciting an internal instability of the TC system. The latter is manifested as an enhancement of the local secondary circulation with increasing surface fluxes and associated convection supporting the formation of a contracting secondary eyewall.

  On the other hand, Molinari et al. (1995) re-examined the interaction of hurricane *Elena* using a potential vorticity (PV) viewpoint and showed that this hurricane intensified rapidly as a narrow upper-level positive PV anomaly become nearly superposed over the low-level center. The intensification appeared to be the response to an evaporation-wind feedback activated by constructive interference of the PV anomalies. The same mechanism is shown by Molinari et al. (1998) to occur also in tropical storm *Danny* of 1985.

It is recognised that the resulting intensity change in TCs upon interacting with large-scale dynamical systems depends largely on the structure of TCs and their response to the external forcing. For example, Molinari et al. (1998) find that whether or not a hurricane intensifies from the interaction with environmental PV filament depends on the relative strength of the positive and negative PV anomalies. The capacity of hurricane vortices to resist vertical wind shear has been studied by several authors (e.g. Jones, 1995, Frank and Ritchie, 2001, Reasor et al., 2004, Mallen et al., 2005, Braun et al., 2006, Davis et al., 2008). Thus, the interactions between the large-scale environment and TCs are not well understood and are still a fruitful area for further research. Better representations of hurricane vortices in numerical models and their behaviour during the interaction are of great importance.

Intensification by internal processes.

The intensification by internal processes refers to all those physical mechanisms which change the intensity of the TC directly by changing the structure of the TC inner core. Note that external processes such as changes of the ocean surface and large-scale processes may also change TC structure, and thus, the intensity. Nevertheless, internal processes stand out as an independent class as they can occur independently of the external forcing. As these mechanisms are the focus of this study, they will be presented separately in detail in the next section.

1.2 Intensification by inner core processes

Intensification mechanisms by internal processes can be grouped into two broad classes: symmetric mechanisms, in which the intensification occurs as a result of changes in the axisymmetric structure of the TC vortex, and asymmetric mechanisms, in which intensity changes are associated with asymmetries in the TC structure.

The pioneering studies of Yamasaki (1968c,a,b), Ooyama (1969) and others recognised that TC vortices can intensify by symmetric mechanisms. Two main symmetric processes that are currently well-known for influencing TC intensity are:

- The ***symmetric contraction*** of the primary circulation, i.e. the contraction of the radius of maximum wind (RMW) and the eyewall ring (Ooyama, 1969, 1982, Shapiro and Willoughby, 1982);

- ***Eyewall Replacement Cycles*** (ERC), which are reported comprehensively by Willoughby et al. (1982).

During the last two decades, intensification by internal mechanisms has received renewed research interest with the discovery of several processes associated with asymmetric features. They include:

- ***Vortex Rossby Waves*** (VRWs, Guin and Schubert (1993), Montgomery and Kallenbach (1997);
- ***Barotropic instability*** and **eyewall mesovortices** (Schubert et al., 1999); and
- ***Vortical Hot Towers*** (VHTs) as described by Hendricks et al. (2004), Montgomery et al. (2006), and Nguyen et al. (2008).

Although occurring in the same small area of the tropical cyclone inner core, these processes were mostly studied separately and in different contexts. Consequently, it is of interest to explore the interactions and relationships between these processes in order to better understand the intensification of TCs. These processes are discussed in detail below.

1.2.1 Symmetric contraction of the primary circulation

Using in situ aircraft observations from Atlantic hurricanes and tropical storms, Willoughby (1990) confirms that the usual mechanism of tropical cyclone intensification involves contracting maxima of the axisymmetric tangential wind. The contraction of the eyewall and the RMW is also simulated well by axisymmetric models (e.g. Ooyama, 1969, Willoughby et al., 1984, Nguyen et al., 2002, Hausman et al., 2006), and in azimuthally-averaged fields of three-dimensional models (such as Zhu et al., 2001, Braun et al., 2006, Nguyen et al., 2008).

The mechanisms that may contribute to the inward movement of the convective rings have been discussed by Shea and Gray (1973), Shapiro and Willoughby (1982), Willoughby et al. (1982), Willoughby (1990). Shea and Gray (1973) proposed the generation of supergradient winds just inside of the RMW as follows. Outside of the RMW, the inflowing air maintains a subgradient balance between frictional dissipation of angular momentum and inward advection by the mean circulation. Just inside of the RMW, there is angular momentum convergence that is not balanced by dissipation and the winds become supergradient. The inward flowing air then decelerates, turns upwards and outwards into the eyewall. Gray and Shea (1973) suggested that if the generation of supergradient wind is not balanced by upward advection the resulting azimuthal wind accelerations will cause the belt of maximum winds and convective ring to contract inward. However, this explanation with supergradient wind is not complete since it neglects the feedback from diabatic heating in the eyewall convection.

Shapiro and Willoughby (1982) use the diagnostic technique of Eliassen (1951) to investigate the response of a balanced hurricane-like vortex to point sources of heating (representing the diabatic heating in the eyewall). Their solutions show also that the tangential wind increases most rapidly just inside of the RMW, thereby contracting the wind maximum as the vortex intensifies. With the imposition of the heat source just inside of the RMW, which represents the convective heating in the eyewall, compensating subsidence is induced in its surrounding area with more concentrated subsidence in the inner side (due to the inertial stability gradient). Then, adiabatic warming associated with this concentrated subsidence increases pressure gradient just inside the convective band, which causes, via gradient wind equation, a marked local azimuthal wind acceleration.

The contraction and strengthening of the tangential wind, i.e. the primary circulation, can be explained by changes in the secondary circulation, i.e. movement of air in the radial-vertical plane while conserving absolute angular momentum. Figure 1.4 illustrates schematically the conceptual association between the primary and secondary circulation via conservation of absolute angular momentum. The absolute angular momentum is defined by:

$$M = rV + \frac{r^2 f}{2} = constant$$

where M is the absolute angular momentum, r is radius, V is the tangential wind and f is Coriolis parameter. As the air moves inwards to smaller radii, in the absence of frictional dissipation, the tangential wind V has to increase to compensate for the decrease in r while conserving absolute angular momentum.

Note that the inflow induced by the friction in the BL does not intensify the TC. It is because under effects of friction alone, the inflow in the BL induces upward motion out of the BL, which, in turn, induces outflow at the top of the BL due to continuity. Then, the induced outflow by friction above the BL spins down the vortex as the air conserves angular momentum. Thus, it is widely assumed in previous studies (Ooyama, 1969, 1982, Willoughby, 1988, 1995, Raymond et al., 1998, Smith, 2000) that the convergence above the boundary layer is necessary for intensification and this convergence must be large enough to offset the frictionally induced divergence outflow above the boundary layer. The convergence above the BL can occur by latent heat realease by convective cloud within the eyewall. Modelling studies such as Zhu et al. (2001) and Nguyen et al. (2002) show that the modelled TC start to intensify rapidly after saturation, and thus, latent heat release occurs in the eyewall.

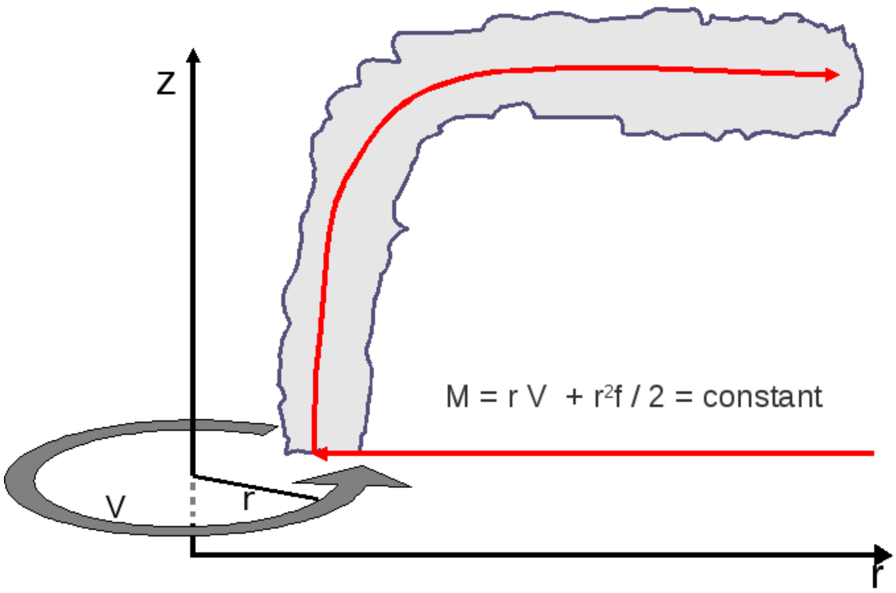

Figure 1.4: Schematic of the conceptual association between the primary and secondary circulations in TCs. Red lines with arrows show the mean radial-vertical movement (i.e. the secondary circulation). Thick grey arrow represents the mean tangential wind (i.e. the primary circulation). In the absence of friction, the inflowing air rotates faster while reaching smaller radii as the absolute angular momentum is conserved.

Recently, Smith et al. (2009) revisit the symmetric spin-up problem. They show that the convergence of absolute angular momentum above the boundary layer (BL) spins up the outer circulation, increasing the vortex size but does little to the intensity of the core. Instead, the inner core intensifies by the radial convergence within the BL. "Although absolute angular momentum is not materially conserved in the BL, large wind speeds can be achieved if the radial inflow is sufficiently large to bring the air parcels to small radii with minimal loss of angular momentum". This process is accompanied by the development of supergradient winds in the BL, the return flow upwards and outwards towards the RMW as first identified by Gray and

Shea (1973).

1.2.2 Eyewall replacement cycles

Eyewall replacement cycles (ERCs) are observed primarily in strong hurricanes. Although TCs with double eyewall structures have been reported since very early times (e.g. Fortner, 1958, Jorndan, 1966, Hoose and Colon, 1970, Holliday, 1977), Willoughby et al. (1982) were the first to study this process in detail. During an ERC, with the appearance of the outer eyewall, the inner eyewall weakens while the intensification rate slows, sometimes becoming negative. An eyewall replacement cycle is complete when the inner eyewall totally disappears and the outer eyewall starts to contract, resuming the intensification.

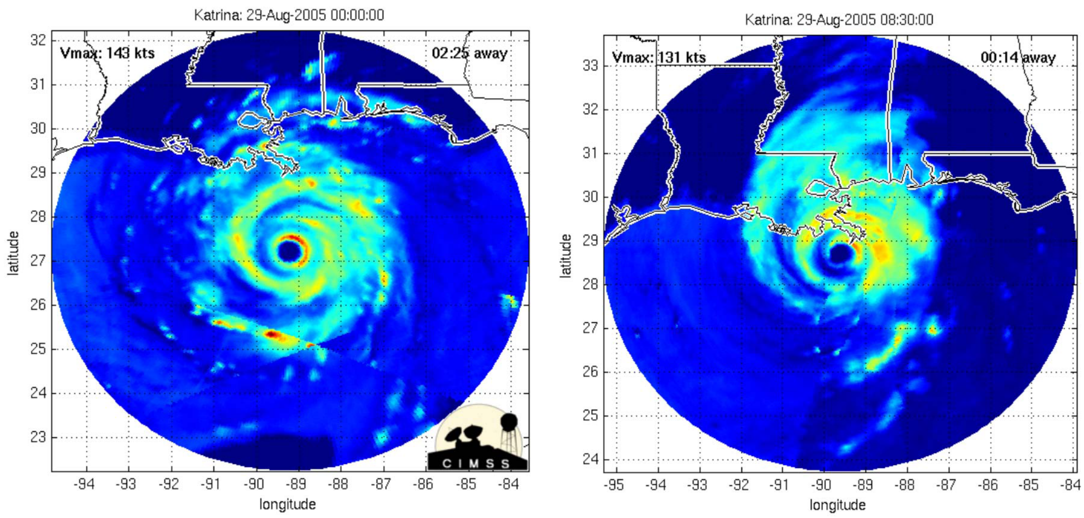

Figure 1.5: Example of the double eyewall structure in hurricane *Katrina* at (left) 00Z 29 August 2005, and (right) 08Z 29 August 2005. These images are microwave satellite images produced by the Morphed Integrated Microwave Imagery at CIMSS program (MIMIC), which can be retrieved from http://cimss.ssec.wisc.edu/tropic/real-time/marti/marti.html.

Figure 1.5 shows an example of the double eyewall structure of hurricane *Katrina* before it made landfall in Louisiana on 29 August 2005. At 00Z 29 August, the outer eyewall has developed outside of the main inner eyewall, which is still strong (see left panel in Fig. 1.5). At 08/30Z 29 August, the inner eyewall has almost disappeared whereas the outer eyewall has become much stronger (right panel). Thus, hurricane *Katrina* went through an ERC during this period. During the ERC, its intensity decreased even though the inner core system has not made landfall. Note that even though the eyewall does not always cover a full circle, an ERC is essentially an axisymmetric process.

Although the occurrence and behaviour of eyewall replacement cycles are well documented and analysed in observations (Willoughby, 1990, Kodama and Yamada, 2005), the formation mechanism for secondary eyewalls is still debated with widely diverse explanations by different authors (Willoughby et al., 1982, Hawkins, 1983, Willoughby et al., 1984, Molinari and Vollaro, 1989, Montgomery and Kallenbach, 1997, Nong and Emanuel, 2003, Kuo et al., 2004, Rozoff et al., 2006, Terwey and Montgomery, 2008). Terwey and Montgomery (2008) provide a comprehensive review of these mechanisms. Recently, the topic has attracted much attention due to the increased potential for a large storm surge associated with the broadening of the outer wind profile with the development of the secondary eyewall as happened in hurricane *Katrina* (2005). Attempts are now made to predict the probability of secondary eyewall formation operationally (Kossin and Sitkowski, 2009).

1.2.3 Vortex Rossby Waves

As the core rotates rapidly, the typical vorticity distribution in a TC has high vorticity near the center and lower values in the outer region. This configuration provides an environmental radial vorticity gradient, on which vorticity perturbations may propagate, similar to planetary Rossby waves. The term Vortex Rossby Wave (VRW) was first proposed by McDonald (1968) in relating the movement of spiral bands in hurricanes. VRWs have been proposed as an asymmetric mode of intensification (Guin and Schubert, 1993, Montgomery and Kallenbach, 1997, Möller and Montgomery, 1999, 2000) and are described in terms of potential vorticity (PV) asymmetries.

The dispersion relationship of the VRWs was derived by Montgomery and Kallenbach (1997), and modified by Möller and Montgomery (2000) to include the vertical structure. For a barotropic basic state vortex with a constant static stability, the local dispersion relation is:

$$\omega = n\overline{\Omega} + \frac{n}{R}\frac{\overline{\xi}}{\overline{q}}\frac{\overline{q'}_{(R)}}{\left[k^2 + n^2/R^2 + (\overline{\eta}\overline{\xi}m^2)/N^2\right]}, \tag{1.2}$$

where n,k,m are azimuthal, radial and vertical wavenumbers, respectively; R is the reference radius; $\Omega = \overline{V}_R/R$ is the angular velocity; $\overline{V}_R$ is the azimuthally-mean tangential wind speed at radius R; η is the absolute vorticity; $\xi = f + 2\overline{V}_R/R$ is the inertial parameter; N^2 is the static stability; q, q' are potential vorticity and its radial gradient at radius R; $\overline{(\ )}$ is the averaging operator in the azimuthal direction. Möller and Montgomery (2000) suggest the use of a time-dependent radial wavenumber in the form $k = k_0 - nt\overline{\Omega'}(R)$, where $\overline{\Omega'}(R)$ is the radial gradient of $\overline{\Omega}(R)$. However, we found that this formula produce unrealistically rapid decrease of radial propagation speed. Thus, a constant k is used in our calculations in Chapter 6.

From Equation 1.2 the azimuthal phase speed is

$$C_{p\lambda} = \frac{\omega}{(n/R)} = \overline{V}_R + \frac{\overline{\xi}}{\overline{q}} \frac{\overline{q'}_{(R)}}{\left[k^2 + n^2/R^2 + (\overline{\eta}\overline{\xi}m^2)/N^2\right]} \tag{1.3}$$

and the azimuthal component of the group velocity is

$$C_{g\lambda} = \frac{\partial \omega}{\partial (n/R)} = \overline{V_R} + \frac{\overline{\xi}\overline{q'}_{(R)}}{\overline{q}} \frac{\left[k^2 + (\overline{\eta}\overline{\xi}m^2)/N^2 - n^2/R^2\right]}{\left[k^2 + n^2/R^2 + (\overline{\eta}\overline{\xi}m^2)/N^2\right]^2}. \tag{1.4}$$

Likewise, the radial phase speed is

$$C_{pr} = \frac{\omega}{k} = \frac{n}{kR}\left(\overline{V}_R + \frac{\overline{\xi}}{\overline{q}} \frac{\overline{q'}_{(R)}}{\left[k^2 + n^2/R^2 + (\overline{\eta}\overline{\xi}m^2)/N^2\right]}\right) = \frac{n}{kR} C_{p\lambda}, \tag{1.5}$$

the radial component of the group velocity is

$$C_{gr} = \frac{\partial \omega}{\partial k} = -\frac{n}{R} \frac{\overline{\xi}\overline{q'}_{(R)}}{\overline{q}} \frac{2k}{\left[k^2 + n^2/R^2 + (\overline{\eta}\overline{\xi}m^2)/N^2\right]^2}, \tag{1.6}$$

the vertical phase speed is

$$C_{pz} = \frac{\omega}{m} = \frac{n}{mR}\left(\overline{V}_R + \frac{\overline{\xi}}{\overline{q}} \frac{\overline{q'}_{(R)}}{\left[k^2 + n^2/R^2 + (\overline{\eta}\overline{\xi}m^2)/N^2\right]}\right), \tag{1.7}$$

and the vertical component of the group velocity is

$$C_{gz} = \frac{\partial \omega}{\partial m} = -\frac{n}{R} \frac{\overline{\eta}}{N^2} \frac{\overline{\xi}^2 \overline{q'}_{(R)}}{\overline{q}} \frac{2m}{\left[k^2 + n^2/R^2 + (\overline{\eta}\overline{\xi}m^2)/N^2\right]^2} \tag{1.8}$$

Equation 1.3 for the azimuthal phase speed implies that VRWs in an environment with a positive radial vorticity gradient (i.e. an environment in which the vorticity increases with radius) propagate in the azimuthal direction faster than the mean tangential wind. In contrast, VRWs propagate slower than the mean tangential wind in the environment with a negative radial vorticity gradient. Equation 1.6 for the radial component of the group velocity of VRWs shows that a VRW wave-packet, and hence the wave energy, propagates outward in a negative gradient environment and inward in a positive gradient environment.

These PV asymmetries are thought to be created by convection and are commonly associated with inner spiral rain bands. In an environment with a mean negative radial gradient of PV, the asymmetries tend to propagate radially outwards and cyclonically in the azimuthal direction, while retrogressing relative to the mean tangential wind. As they move outwards, these disturbances are strongly strained and sheared by the differential rotation of the mean tangential flow, becoming thinner as their radial wavenumber increases. Consequently, according to Equation 1.6, their radially-outward group velocity decreases and there may exist a critical radius at which the group velocity becomes zero. At this radius the disturbance transfers its energy to the mean flow (Montgomery and Kallenbach, 1997, Möller and Montgomery, 1999, 2000), at least according to inviscid theory.

The early theoretical treatment of VRWs (Montgomery and Kallenbach, 1997) and the subsequent numerical simulations (Montgomery and Enagonio, 1998, Möller and Montgomery, 1999, 2000) were formulated mainly in terms of barotropic dynamics. Later studies using primitive equation models with full physics in both idealised configurations (Wang, 2002a,b) and simulated hurricanes (Chen and Yau, 2001, Chen et al., 2003) found evidence that VRWs act to axially symmetrise the storm. Observational evidence for the existence of VRWs is presented by Corbosiero et al. (2006), who used radar reflectivity data for their detection in Hurricane *Elena* (1985). In summary, VRWs are believed to axisymmetrise asymmetric disturbances bringing the vortex into a more symmetric state while strengthening it by wave-mean flow interactions.

1.2.4 Barotropic instability and eyewall mesovortices

In contrast to the axisymmetrising effects of VRWs, a symmetric vortex may breakdown into small vortices through barotropic instability. The concept of barotropic instability dates back to the 19^{th} Century and the work of Rayleigh (1880), who showed that a strip of enhanced vorticity may become unstable. In the context of TC vortices, it was shown by Schubert et al. (1999) that barotropic instability in symmetric vortices with a thin ring of enhanced vorticity may act to fracture the ring into asymmetric features like mesovortices. Schubert et al. (1999) explain the barotropic instability of the PV ring structure in TC vortices as follows. In terms of Rossby wave theory (see Equation 1.5), a PV wave on the inner edge of the annular ring (at which the mean PV radial gradient is positive) will propagate faster than the mean tangential flow in their vicinity, while a PV wave on the outer edge will propagate slower than the surrounding flow there. Thus, it is possible for these two counter-propagating (relative to the tangential flow in their vicinity) PV waves to have the same angular velocity relative to the earth. In this case, the waves are said to be phase locked. If the locked phase is favorable, each PV wave will make each other grow, and exponential instability will result.

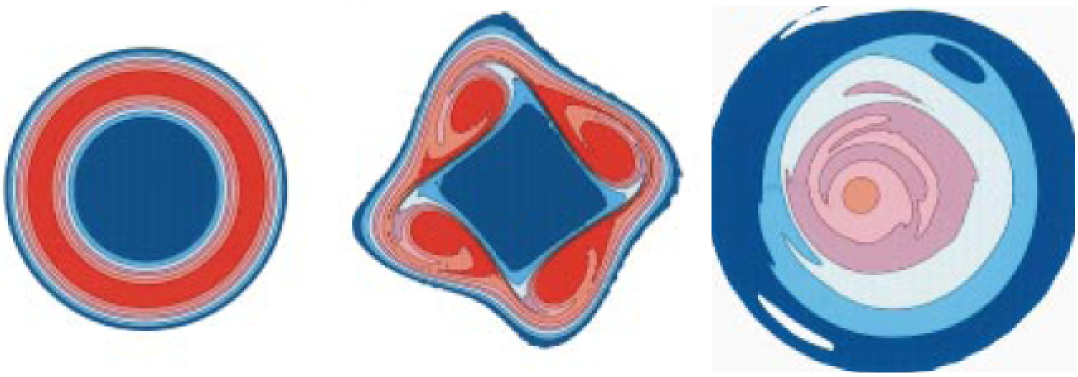

(a) 0 h (b) 6 h (c) 42 h

Figure 1.6: Results from simulations of Schubert et al. (1999). Panel a,b and c show the vorticity fields at 0, 6, and 42 h of integration, respectively. These figures are copied from Figures 3a and 3c in Schubert et al. (1999).

Figure 1.6 shows the vorticity fields simulated by Schubert et al. (1999). At the initial time (panel a), the vorticity has a ring structure with the maximum vorticity located at some radius from the center. After 6 h of integration (panel b), the vortex consists of four small vortices evenly spaced around the vortex center. Later in the integration, the vorticity field has the form of a monopole structure with the maximum located at the center (panel c). Schubert et al. (1999) explain that the ring of high vorticity at the initial time is barotropically unstable, which enables the growth of disturbances into mesovortices. Vigorous mixing by the mesovortices eventually brings the vortex to a monopole structure with a PV maximum at the centre.

This process has been confirmed and extended by several other works. Using a two-dimensional barotropic model, Kossin et al. (2000) found that the mesovortices merge with their neighbours and may evolve in two different ways: 1) they can relax to a monopole, or 2) form an asymmetric quasi-steady state, comprising a lattice vortices rotating nearly as a solid body. In the latter case, the flow around the mesovortices has the configuration of straight line segments in the form of polygonal shapes. This configuration has been observed in a number of hurricanes such as Hurricane *Erin, Nari,Podul* (2001), *Isabel* (2003). Figure 1.7 shows the pattern of six mesovortices inside the eye of hurricane *Isabel* (2003).

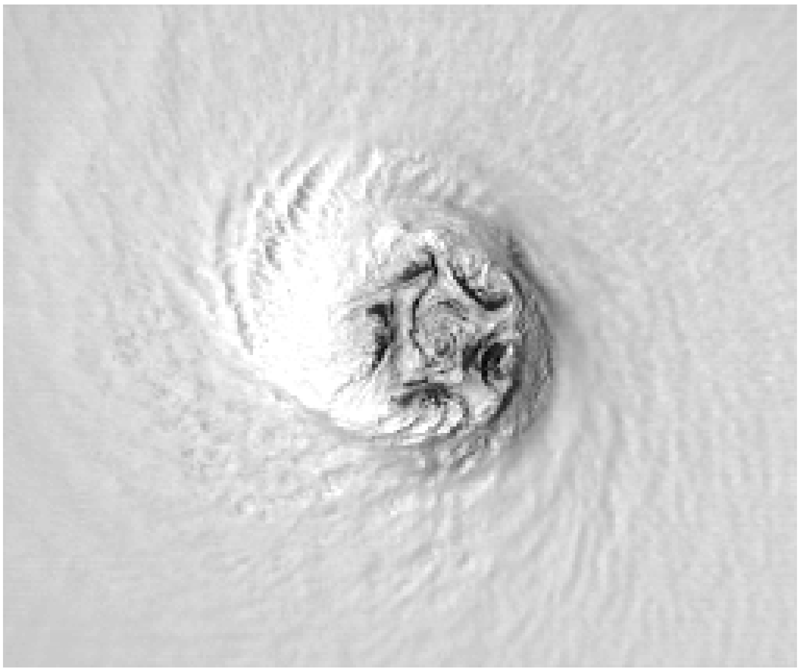

Figure 1.7: Defense meteorological Satellite Program (DMSP) image of Hurricane Isabele at 1315 UTC 12 Sep 2003. The pattern in the eye is caused by the presence of six mesovortices. This figure is reproduced from Figure 1 of Kossin and Schubert (2004)

Using flight level data collected over a 20 year period (1977-96), Kossin and Eastin (2001) demonstrated that there exist two distinct regimes in the kinematic and thermodynamic structure of hurricanes. In the first regime, which often accompanies intensification, the profiles of vorticity and equivalent potential temperature exhibit a ring structure with elevated values near the eyewall and smaller values in the eye. In contrast, a monopole structure with the maximum at the centre is observed for both vorticity and θ_e in the second regime. The transition from regime 1 to regime 2 is observed to occur in less than a few hours. Kossin and Eastin (2001) explained this transition by barotropic instability and horizontal mixing theory suggested by Schubert et al. (1999). Investigating the dynamics of these two states and the transition from one to the other is the central theme of this thesis.

Rozoff et al. (2009) used a two-dimensional barotropic model to study the sensitivity of vorticity ring geometry to spatially and temporarily varying forcing. They have found that the mixing of vorticity by mesovortices acts as an internal brake on the intensification process resulting from vorticity generation in the hurricane eyewall. The life cycles of hurricane-like vorticity rings have been systematically investigated by Hendricks et al. (2009) using a non-divergent barotropic model. Experimenting on 170 simulations with variable parameters of the hollowness of the vortex and the thickness of the ring, they found that the most likely end state of an unstable ring is a monopole. Very hollow and thin rings tend to breakdown to multiple long-lived mesovortices which persist (on the order of 15 h) before mixing to a monopole, whereas thick, filled rings take longer to relax to the monopole state. For some thick and moderately filled rings, the end state was a polygonal eyewall of the same character as the initial instability.

In summary, the inner core processes of hurricane-like vortices, in which vorticity rings break due to barotropic instability to form mesovortices, and which subsequently mix vorticity to form a monopole structure, have been studied in detail in the barotropic framework. Several characteristics of these processes are observed in real hurricanes including mesovortices, polygonal eyewall and structures having the ring and monopole configurations. As the eyewall in real tropical cyclones is dominated by diabatic heating due to convection, it is of great interest to investigate how convective instabilities modify these essentially barotropic processes.

1.2.5 Vortical Hot Towers

The term Hot Tower dates back to the pioneering work by Riehl and Malkus (1958) who emphasised that these "horizontally small but intense cumulonumbus convection cores that reach the tropopause via nearly undiluted ascent" play roles in the vertical flux of heat and mass in the tropical overturning circulation (Hadley cell). Recently, these deep convective entities have received renewed interest because of their role in producing local vortical flows. Thus, the term vortical hot towers (VTHs) was coined by Hendricks et al. (2004) to describe these coherent rotating structures.

VHTs are thought to be an important ingredient of tropical cyclone genesis and intensification (Hendricks et al., 2004, Montgomery et al., 2006, Nguyen et al., 2008, Shin and Smith, 2008). For example, Montgomery et al. (2006) demonstrated that once embedded in the cyclonic, vorticity-rich environment of a mesoscale convective vortex (MCV), the embryo VHTs can produce large vertical vorticity by tilting horizontal vorticity from the MCV and stretching the vertical vorticity of the MCV and that generated by other VHTs. Furthermore, VHTs may overcome the adverse effects of downdrafts by consuming local available convective potential energy and merging with neighboring VHTs. Collectively, the VHTs are shown to converge cyclonic vorticity on the system scale and increase mean tangential near-surface wind speed, and thereby acting as an upscale process to intensify the system (Montgomery et al., 2006).

Note that although eyewall mesovortices and VHTs are both mesoscale systems that occur in the inner core of TCs and have cyclonic vorticity, they are essentially different entities. As shown in Figure 1.7, eyewall mesovortices consist of low level cloud structure that are located at the inner periphery of the eyewall. On the other hand, VHTs are deep convective entities, thus, associated with deep convective clouds with cold cloud tops. We will show later in Chapter 6 that they may well be related.

In summary, the inner-core processes described above may be organised schematically as shown in Figure 1.8. The eyewall contraction and eyewall replacement cycles are essentially symmetric processes, whereas vortical hot towers are asymmetric. Barotropic instability provides a mechanism for a symmetric vortex to become asymmetric. In contrast, VRWs play a role in axisymmetrising the vortex to the symmetric mode.

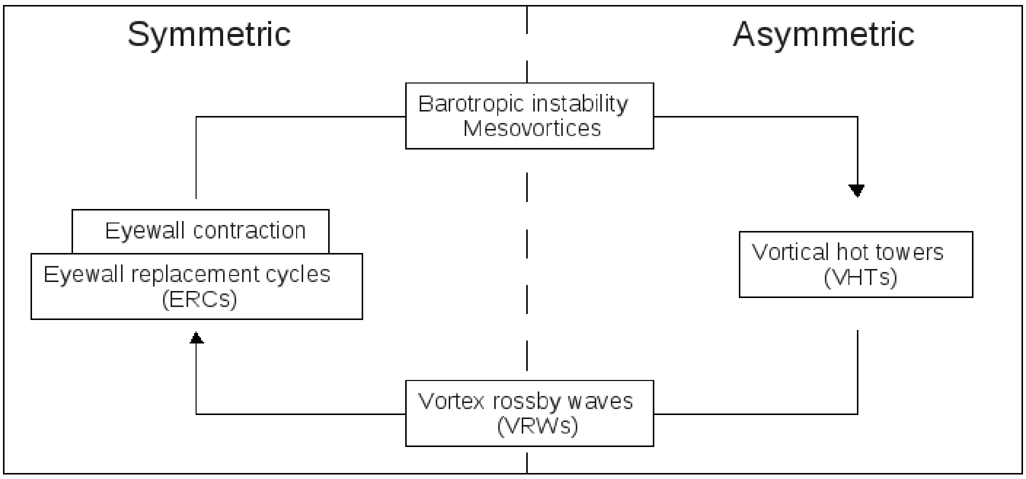

Figure 1.8: Schematic for the relationships between different inner core processes in the context of symmetric and asymmetric modes of intensification.

1.3 Research objectives and thesis plan

Research obvectives

Previous studies have provided great insights into different processes that occur in the inner core of tropical cyclones. These processes hav been shown to play roles in changing TC intensity associated with changes in TC structure. However, these processes have been studied and reported in different frameworks and contexts, making it difficult to understand the relationships among them. Therefore, it is of great interest to understand how these processes are linked with each other and whether they are all important in changing the intensity of a TC.

In the present study, we examine how these different mechanisms work together in changing TC intensity and whether there are relationships and interactions between them. In other words, how do the symmetric and asymmetric processes evolve during intensity change?

Hurricane Katrina

For this purpose, a high resolution version of the Australian Bureau of Meteorology's operational model for tropical-cyclone prediction (TCLAPS) is used to simulate Hurricane *Katrina* (2005). Hurricane *Katrina* is reported in Knabb et al. (2006) to have gone through two ERCs: 1) during 27 August 2005 and 2) just before it made landfall in Louisiana on 29 August. Our simulations are chosen to run from the base time at 00Z 27 August, the aim of which is to simulate the first reported event of ERC during 27 August 2005. As can be seen in Figure 1.9, hurricane *Katrina* was located in the eastern part of the Gulf of Mexico while there is a trough situated over the west coast of the Gulf. This trough is almost stationary (compare its positions in panels a and b), thus, steers hurricane *Katrina* to the north-west and eventually to the north.

One interesting aspect of hurricane Katrina is its rapid increase in size during 27 August. Beven et al. (2008) reported that hurricane *Katrina* nearly doubled its size on the 27^{th} August. By the end of this day, the tropical storm-force winds extended up to about 140 n mi from the centre. While the reason for the size increase is not addressed specifically for hurricane *Katrina*, Hill and Lackmann (2009) suggest that the increase of the environmental humidity is a favourable factor for the expansion of TC circulations. This thesis is focused on inner core processes and will not study this phenomenon.

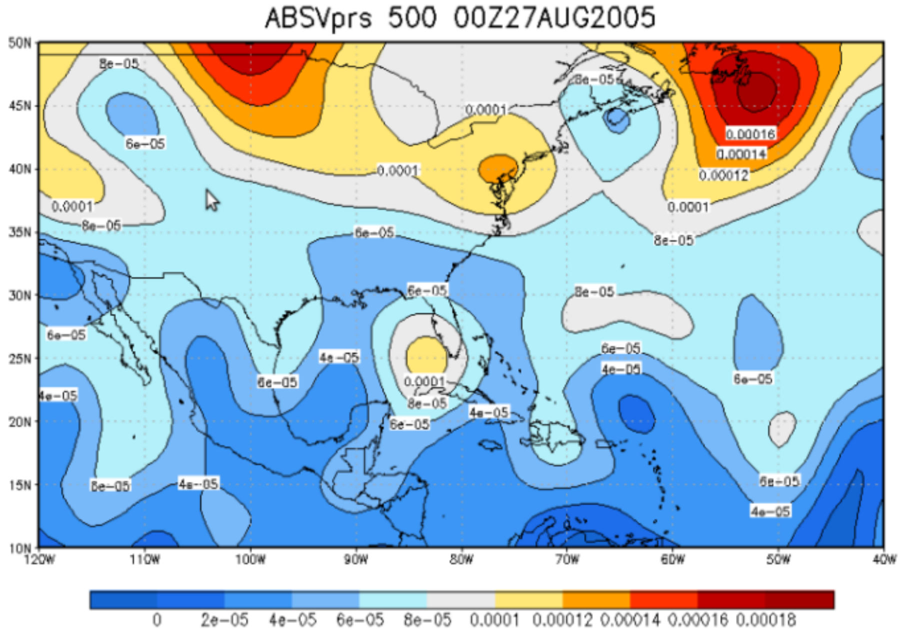

a

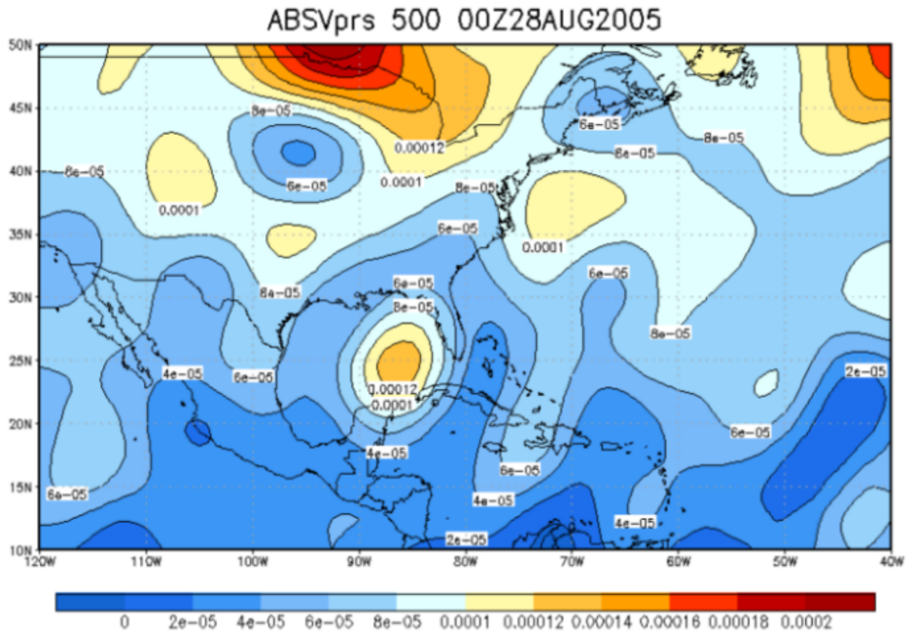

b

Figure 1.9: Absolute vorticity at 500 hPa valid at a) 00Z 27 and b) 00Z 28 August 2005. These plots are produced using data from National Climate Environment Prediction (NCEP) reanalysis available from http://nomad1.ncep.noaa.gov/ncep_data/index.html.

An ensemble of simulations was carried out to identify robust features of the structure change processes. It is found that the majority of simulated ensemble members tend to go through cycles of structure change between a more symmetric phase and a more asymmetric phase. Consequently, detailed analysis is performed to investigate the characteristics of the vortex structure during each phase, and to understand mechanisms responsible for the transition between them.

Thesis plan

The thesis is organised as follows. The description of the numerical model and the setting of experiments are presented in Chapter 2. Results from the ensemble runs are included in Chapter 3. Detailed analysis of the vortex structure during the two different phases is examined in Chapter 4. Consequently, the evolution of different averaged fields are studied and presented in Chapter 5. Chapter 6 identifies the physical mechanisms occuring during the transitions between the two phases and to relate them to the inner core processes described above. Finally, discussions and conclusion are given in Chapter 7.

Chapter 2

THE MODEL

2.1 Governing equations

The numerical model used in this study is a high-resolution (5 km horizontal grid, 29 vertical levels) version of the Tropical Cyclone Limited Area Prediction System (TCLAPS). TCLAPS is a hydrostatic, limited-area Numerical Weather Prediction model, which includes a TC bogus scheme and assimilation technique specially designed for predicting TCs (Davidson and Weber, 2000). The prognostic equations on which TCLAPS is based are similar to those described in McDonald (1986), which use a semi-Lagrangian and semi-implicit two time-level integration scheme. The equations in spherical coordinates (λ, ϕ) with σ (normalised pressure) as the vertical coordinates, can be written as follows:

The momentum equations:

$$\frac{d_H u}{dt} + \dot{\sigma}\frac{\partial u}{\partial \sigma} + \frac{1}{acos\phi}\frac{\partial \Phi}{\partial \lambda} + \frac{RT}{acos\phi}\frac{\partial lnp_s}{\partial \lambda} - \left[f + \frac{utan\phi}{a}\right]v = F_u + D_u \quad (2.1)$$

$$\frac{d_H v}{dt} + \dot{\sigma}\frac{\partial v}{\partial \sigma} + \frac{1}{a}\frac{\partial \Phi}{\partial \phi} + \frac{RT}{a}\frac{\partial lnp_s}{\partial \phi} + \left[f + \frac{utan\phi}{a}\right]u = F_v + D_v \quad (2.2)$$

The equations for temperature and mixing ratio:

$$\frac{d_H T}{dt} + \dot{\sigma}\frac{\partial T}{\partial \sigma} - \frac{RT}{c_p}\left[\frac{dlnp_s}{dt} + \frac{\dot{\sigma}}{\sigma}\right] = \frac{1}{C_p}(H + F_T + D_T) \quad (2.3)$$

$$\frac{d_H q}{dt} + \dot{\sigma}\frac{\partial q}{\partial \sigma} = Q + F_q + D_q \quad (2.4)$$

The continuity equation:

$$\frac{d_H lnp_s T}{dt} + D + \frac{\partial \dot{\sigma}}{\partial \sigma} = 0 \quad (2.5)$$

The hydrostatic equation:

$$\frac{\partial\Phi}{\partial ln\sigma} = -RT \tag{2.6}$$

where

$$\frac{d_H}{dt} = \frac{\partial}{\partial t} + \frac{u}{acos\phi}\frac{\partial}{\partial\lambda} + \frac{v}{a}\frac{\partial}{\partial\phi} \tag{2.7}$$

and

$$D = \frac{1}{acos\phi}\left[\frac{\partial u}{\partial\lambda} + \frac{\partial vcos\phi}{\partial\phi}\right] \tag{2.8}$$

In the above equations, the symbols used are conventional and are listed in Table A.1. The terms F_u and F_v include surface frictional forces and momentum transfer in the free atmosphere, F_T and F_q include sensible heat and evaporation from the surface and vertical turbulent exchange in the free atmosphere, H is the diabatic heating arising from cumulus convection, large-scale condensation and radiation. The symbols D_u, D_v, D_T, and D_q denote horizontal diffusion terms. These terms are discussed in more detail in the next section on the representation of physical processes.

A horizontal resolution of 5 km is probably near the limit of validity of hydrostatic balance, particularly in regions of deep convection (see e.g. Thunis and Bornstein, 1996). However, despite utilizing hydrostatic approximation, TCLAPS is still used in this study for the following reasons.

- Firstly, this model shows good performance for real-time TC prediction (Davidson and Weber, 2000). Using forecasts from 17 base date-times for 13 TCs with a broad spectrum of characteristics such as size, intensity change and movement patterns, Davidson and Weber (2000) have demonstrated that TCLAPS has significant track prediction skills. For instance, the average track errors for these 17 cases of TCLAPS are 115 and 259 km for 24 and 48 h forecasts, respectively. These errors are significantly smaller than those of the CLImate PERsistent (CLIPER) method, which are 191 and 428 km, for these two forecast lead times, respectively. Furthermore, TCLAPS also shows encouraging skill in predicting TC intensity as reported by Davidson and Weber (2000). The mean error of minimum pressure forecasts of TCLAPS is near zero, indicating that there is no bias in the predictions to overintensify or weaken the circulations. For the reported cases, the root mean square errors of TCLAPS for central pressure show a skill level comparable to CLIPER out to 24 h and small improvement over persistence beyond that time.

- Secondly, as will be described in the next section, TCLAPS has an assimilation and initialisation scheme specifically suitable for TC prediction, which includes a TC bogus scheme (Davidson et al., 1993) and a diabatic dynamical nudging scheme (Davidson and Puri, 1992). These features have led to improved model performance in predicting severe weather events, such as TC tracks, monsoon circulation and heavy rainfall events in the Australian tropics (see Davidson and Puri, 1992).

Therefore, it is anticipated that 5-km resolution simulations with TCLAPS are useful in investigating the inner core processes which are largely influenced by dynamical aspects of the tropical cyclone circulation.

2.2 Physical processes

The physical parameterizations used in TCLAPS are similar to those of the Limited-Area Prediction System (LAPS) as described in Puri et al. (1998). Note that effects of physical parameterizations are represented as terms on the right hand side in Equations 2.2-2.4. They include:

2.2.1 Radiation

The radiation scheme is a combination of the Lacis and Hansen (1974) parametrisation for solar wave lengths and the Fels and Schwarzkopf (1975) method for terrestrial wavelengths, and includes diurnal variation.

In Lacis and Hansen (1974), the solar radiation is absorbed at the earth's surface and in the atmosphere as a function of altitude. The absorption of the short-wave radiation depends on the amount and type of the cloud, the humidity, the zenith angle of the sun and the albedo fo the earth's surface, and the vertical distribution of ozone in the stratosphere.

For the long-wave radiation scheme of Fels and Schwarzkopf (1975), the heating rate has the general form:

$$q \approx q^e - q^e_{CTS} + q_{CTS} \tag{2.9}$$

where q is the heating rate, q^e is an emissivity heating rate calculated using the strong-line approximation and neglecting the variation of line intensity with temperature, q^e_{CTS} is the heating rate calculated using the cool-to-space approximation and the emissivity assumption, and q_{CTS} is the heating rate calculated by the cool-to-space approximation.

2.2.2 Bulk explicit microphysics (BEM)

This scheme is described in Dare (2004), which is similar to the Lin et al. (1983) scheme. There are 6 classes of water species: water vapor, cloud water, rain water, cloud ice, snow and graupel. Each class is represented by a mixing ratio alone, with no prognostic estimation of number concentration or size distribution. Number concentration and size distribution of hydrometeor species are predefined. The microphysical processes represented in this scheme are:

1. Condensation of water vapour to form cloud water and rain water.
2. Evaporation of cloud water, rain water, melting snow and melting graupels.
3. Autoconversion of cloud water to rain water, cloud ice to snow and snow to graupel.
4. Water vapour deposition onto cloud ice, snow flakes and graupel pellets.
5. Bergeron-driven growth of snow to form cloud water.
6. Initiation of cloud ice.
7. Multiplication of ice particles.
8. Sublimation of cloud ice, snow and graupel to water vapour.
9. Fragmentation of snow crystals to form cloud ice.
10. Heterogeneous freezing of cloud droplets to form cloud ice.
11. Melting of snow flakes and graupel pellets to form rain drops.
12. Homogeneous freezing (melting) of cloud water (cloud ice) to form cloud ice (cloud water).
13. Accretion of cloud water to form rain water, by snow flakes to form graupel pellets and rain drops, and by graupel pellets.
14. Accretion of rain drops by cloud ice to form snow flakes and graupel pellets, by snow flakes, and by graupel pellets.
15. Accretion of cloud ice by snow flakes, by graupel pellets, by rain drops to form snow flakes and graupel pellets.
16. Accretion of snow flakes by cloud droplets to form graupel pellets, by rain drops to form graupel pellets, and by graupel pellets.

2.2.3 Convective parameterization

Apart from the microphysics scheme BEM, there is an option to include the convective parameterization scheme developed by Tiedtke (1989). The inclusion of convective parameterization is crucial for models of coarser resolutions. For a resolution of 5 km, however, the validity of the approximations assumed in the convective parameterization scheme and its effects on the model simulations are not clear. This scheme can be switched on and off.

The convective parameterization scheme of Tiedtke (1989) is a mass flux scheme, which considers a population of clouds where the cloud ensemble is described by a one-dimensional bulk model. Different types of convective clouds are represented including: penetrative convection, midlevel convection and shallow convection. The bulk cloud mass fluxes of the first two convective types are assumed to be maintained by large-scale moisture convergence. On the other hand, the shallow convection is supplied by the moisture from surface evaporation. This scheme includes also cumulus scale downdrafts. Full description of the scheme can be found in Tiedtke (1989).

2.2.4 Boundary layer scheme

The boundary layer parameterisation scheme of TCLAPS is based on the scheme of ECMWF's model and is described in the work of Beljaars and Betts (1992).

Surface fluxes

The surface fluxes of momentum, heat and moisture are parametrised using the Monin-Obhukov formulation and follow Louis (1979) in specifying the flux profile relationships in terms of numerically fitted functions of the bulk Richardson number.

The surface stress τ_*, sensible heat flux H_*, and latent heat flux E_* have the form

$$\vec{\tau_*} = \rho_1 C_D |\vec{V_1}|\vec{V_1} \tag{2.10}$$

$$H_* = \delta\rho_1 C_P C_H |\vec{V_1}|(\theta_s - \theta(\sigma_1)) \tag{2.11}$$

$$E_* = \rho_1 C_W C_E L |\vec{V_1}|(q_s(T_s) - q_1) \tag{2.12}$$

where the subscript 's' denotes the surface, subscript '1' the first model level, ρ the density and θ the potential temperature. The factor $\delta = (p_s/p_0)^{R/Cp}$, where p_0= 1000 hPa, arises from the formulation of sensible heat flux in terms of potential temperature. The transfer coefficients C_D, C_H and C_E are stability dependent and functions of the bulk Richardson number and the roughness length z_0. The roughness length is assigned a fixed value of 0.17 m over land and 0.001 m over sea-ice. Over ocean the roughness length is calculated by formula $z_0 = 0.032|\vec{\tau}_*|/\rho_g$. A soil wetness factor C_W is used in the parametrisation of the evapotranspiration. Over oceans, sea-ice or snow, C_W is set to unity while a simple 'bucket' method is used over land.

Surface and subsurface temperature

Over ocean, sea-surface temperature analyses are interpolated to the model grid. Over land and sea-ice, the surface temperature is diagnosed from a surface heat balance at each time step. The heat balance at the surface is given by

$$H_* + E_* + C + \epsilon\sigma T_s^4 - Q_s - Q_L = 0 \tag{2.13}$$

where Q_s and Q_L are the net downward short and long wave radiation at the surface, ϵ is the surface emissivity for black-body radiation at the surface temperature T_s, σ is the Stefan-Boltzmann constant and C represents conduction of heat to the subsurface soil or ocean. On land the heat flux into the soil is specified as being proportional to the vertical temperature gradient in the ground, that is,

$$C = \rho_a C_g K_g \frac{\partial T_g}{\partial z}$$

where ρ_g is the density of soil, C_g is the specific heat, K_g is the thermal diffusivity and T_g is the ground temperature. There are three subsurface levels at depths of 0.05, 0.5 and 5 m. The 5 m level is held at a constant temperature of 280 K; initial values of the first and second subsurface temperatures are found by interpolation and these temperatures are updated using an explicit finite difference form of the diffusion equation.

$$\frac{\partial T_g}{\partial t} = K_g \frac{\partial}{\partial z}\left(\frac{\partial T_g}{\partial z}\right) \tag{2.14}$$

The heat balance equation (Equation 2.13) is solved for T_s by using Newton-Raphson iteration scheme.

Vertical diffusion

In the boundary layer, subgrid-scale vertical transports of heat, moisture and momentum by dry processes are parametrised as diffusive fluxes in a similar manner to turbulent transfer processes. The tendencies of $\vec{V}$, potential temperature θ and water vapour mixing ratio can be written as

$$\frac{\partial V}{\partial t} = \frac{1}{\rho}\frac{\partial}{\partial z}\left(K_V \frac{\partial V}{\partial z}\right) \tag{2.15}$$

$$\frac{\partial \theta}{\partial t} = \frac{1}{\rho}\frac{\partial}{\partial z}\left(K_H \frac{\partial \theta}{\partial z}\right) \tag{2.16}$$

$$\frac{\partial q}{\partial t} = \frac{1}{\rho}\frac{\partial}{\partial z}\left(K_H \frac{\partial q}{\partial z}\right) \tag{2.17}$$

Vertical diffusion coefficients K_V, K_H are defined in terms of a mixing length l and the magnitude of the wind shear:

$$K_V = K_H = l^2 |\frac{\partial V}{\partial z}|$$

where the mixing length l is set at 30 m for $\sigma \geq 0.5$ and zero for $\sigma < 0.5$, with a separate dry adiabatic adjustment to remove any spurious dry superadiabatic lapse rages.

2.2.5 Horizontal diffusion

For all model variables (u, v, T and q), the diffusion equation is solved for given viscosity coefficients using a forward-time-differencing. Spatial derivatives are approximated using the second-order Laplacian operator. The equation of horizontal diffusion for a variable A has the following general form:

$$\left(\frac{\partial A}{\partial t}\right)_{hdiff} = k_{hd}\nabla^2 A \tag{2.18}$$

where the horizontal diffusion coefficient k_{df} is set to 4000.0 with the time step for horizontal diffusion of 120 s.

In addition, divergence diffusion is applied to the horizontal wind components u and v as follow:

$$u = u + k_{hd}\Delta t \frac{\partial D}{\partial x} \tag{2.19}$$

$$v = v + k_{hd}\Delta t \frac{\partial D}{\partial y} \tag{2.20}$$

2.3 Model Configuration and Initialization Procedures

Simulations of Hurricane *Katrina* (2005) were carried out from 00 UTC 27 August 2005 base time, with assimilation cycles starting from 00 UTC 26 August 2005. Initial and boundary conditions are provided by the global model GASP (Davidson and Weber, 2000) with the horizontal resolution of 0.7°. The large-scale environment of the storm is obtained from a 4-dimensional data assimilation cycle using a

6-h forecast, and a generalised statistical interpolation method to do the objective analysis (Seaman et al., 1995). A synthetic vortex is constructed based on TC advisories, which define the location, size and past motion of the storm (Davidson and Weber, 2000). Synthetic observations from this method are extracted at a resolution sufficient[1] to define the maximum wind at the radius of maximum wind. The statistical interpolation method is used to objectively analyse the synthetic observations, which are merged with the standard observational data. The first guess is obtained from the coarser-resolution data assimilation, and background error covariances and observational errors were tuned for the high-resolution analysis.

The vortex specification and high-resolution analysis are performed every 6 h from 24 h prior to the base time of the simulation. To initialize the synthetic vortex, which does not have an imposed boundary layer structure or secondary circulation, and may not be in mass-wind balance, a nudging technique is used. For this technique, additional forcing terms are introduced into the momentum equation of the model:

$$\frac{\partial u}{\partial t} = \cdots + G_1\frac{\partial}{\partial y}(\zeta_a - \zeta_p) - G_2\frac{\partial}{\partial x}(D_a - D_p) \tag{2.21}$$

$$\frac{\partial v}{\partial t} = \cdots + G_1\frac{\partial}{\partial y}(\zeta_a - \zeta_p) - G_2\frac{\partial}{\partial x}(D_a - D_p) \tag{2.22}$$

where subscripts 'a' and 'p' refer to 'analysed' and 'predicted', respectively. These extra terms will appear as additional terms in the equations of vorticity and divergence as follow:

$$\frac{\partial \zeta}{\partial t} = \cdots - G_1\nabla^2(\zeta_a - \zeta_p) \tag{2.23}$$

$$\frac{\partial D}{\partial t} = \cdots - G_2\nabla^2(D_a - D_p). \tag{2.24}$$

Then, by setting G_2 to zero, the prediction model can be nudged or "diffused" toward the analyzed vorticity while allowing the model to develope its own divergence. G_1 is set to a value of 1.0×10^7 m^2 s^{-1}.

For surface pressure and temperature, the the nudging equation has the following form:

$$\frac{\partial A}{\partial t} = \cdots - \eta(A_a - A_p) \tag{2.25}$$

where $\eta = 1.0 \times 10^{-4}$ s^{-1} for surface pressure and $\eta = 0.4.0 \times 10^{-4}$ s^{-1} for tempera-

[1]For these simulations, the synthetic vortex is extracted from a cylindrical grid having 25 circles extending out to 500 km. There are 12 points on each circle.

ture.

From 24 h prior to the base time of the simulation, the forecast model is initiated and nudged towards the 6-hourly analyses which contains the synthetic vortex. During the 24 h of nudging initialization, the model develops the storm's boundary-layer structure, the vertical motion field and secondary circulation, and forms the mass-wind balance based on its (the model's) dynamics. There are options to nudge the mass field (surface pressure and temperature), or wind field (vorticity), or both towards analyses.

In the case where infrared satellite cloud data are available to define the cloud distribution, their effects may be incorporated by the imposition of cloud heating profiles for deep convection. Insertion of heating profiles where observed deep convection is occurring causes the model to generate upward motion (adiabatic cooling) over these regions. In this way the vertical motion field is re-defined and convective asymmetries inserted at the initial time of the simulation to be consistent with the satellite imagery (Davidson and Weber, 2000). After initialization, the synthetic vortex (a) is embedded in a large-scale environment obtained from advanced data analysis procedures, (b) has a primary circulation defined by estimated vortex parameters, (c) has a secondary circulation and boundary layer structure defined from the model dynamics and physics, (d) contains a vertical motion field consistent with the observed distribution of deep convection and (e) is in mass-wind balance defined by the model's dynamics and physics.

Chapter 3

ENSEMBLE EXPERIMENTS

The main goal of this study is to understand the relationship between different the intensification mechanisms occuring by inner core processes, including those between symmetric and asymmetric mechanisms. Therefore, the evolution of asymmetries in the modeled vortex is among the first characteristics to be examined together with the conventional characteristics such as TC track and intensity. It was found from a pilot run that the simulated inner-core vacillates between states of relatively high and relatively low levels of asymmetry. Furthermore, the state of high asymmetries tends to be accompanied by low intensification rates and vice versa. As asymmetries are generally associated with factors of a somewhat random nature such as convection, numerical truncation errors and dynamic instability (see e.g. Anthes, 1972, Zhu et al., 2001, Nguyen et al., 2008), the model does not necessarily simulate the asymmetries in detail. Nonetheless, if the evolution pattern of asymmetries and its association with the intensification rates represent realistic processes, then it is expected that this pattern be present in other simulations of the model as well. Thus, we perform an ensemble of different simulations to examine the robustness of the above mentioned features.

In this chapter, the characteristics of the ensemble experiments are presented in Section 3.1, followed by Section 3.2, which describes the main characteristics of the ensemble simulations including the tracks and the minimum surface pressure of the simulated vortices. This information is used to determine the sensitivity of the model to perturbations to the boundary and initial conditions and parameter settings. The evolution of the asymmetries of the simulated vortices are examined in Section 3.3.

3.1 Experiments

For this study, the experimental design is a three-step approach consisting of: (1) a control run with the TCLAPS's standard settings for preliminary identification of possible interesting features; (2) a set of ensemble runs from different realisations, to test the sensitivity of the model simulations and the robustness of the features in question, and (3) a detailed analysis of an ensemble member, based on its simulation outcomes and model configuration, to study the underlying physical mechanisms. The details of these three steps are as follows.

(1) The control run, denoted C0, uses most of the standard features of TCLAPS. Specifically, the run uses:

- forecasts from GASP, initialised 12 h prior to the forecast base time to provide the lateral boundary conditions;
- SST taken from the weekly analysis for the previous week;
- no convective parameterisation, only a bulk explicit microphysics scheme (Dare, 2004) for moist processes;
- a synthetic vortex, with estimated vortex parameters taken from TC advisories, and used at 6 h intervals during the 24 h initialisation period prior to the forecast base time.

The model is integrated forward for 48 h, with a domain of 301×301 grid points, having the southwest corner at (17.5N, 267.5E). Nudging was not implemented in this run so as to not interfere with the evolution of the modelled vortex.

(2) Ensemble simulations fall into five main groups designed to test the sensitivities of the model to different factors.

Group I: Observation perturbations. For the four members in this group (C1 to C4), the observations, including those from the synthetic vortex, are perturbed randomly with a standard deviation similar to that of observation errors.

Group II: Nudging methods. There are three members in this group (A0, B0, and D0). They differ from the control run only in the nudging method. There are three options for nudging the model towards the analysis: one can nudge the mass fields (surface pressure and temperature), the wind field (vorticity) or both of these.

Group III: Boundary conditions. In this group, the boundary conditions are taken from the runs of GASP, initialised 4, 3, 2, and 1 day(s) prior to the base time (corresponding to E1, E2, E3, and E4, respectively). In addition, the run E5 uses analyses as boundary conditions. As the forcing from the model boundaries would naturally propagate into the domain, this sensitivity test is a simple way to estimate the effects of the large-scale environment on the simulation of the vortex.

Group IV: Physics and vortex characteristics. In this group:

- Run STC uses SSTs from the analysis of the current week (which of course is not available in real-time for operational forecasting);
- Run CB uses a convective parameterisation scheme (Tiedtke, 1989) in conjunction with the explicit microphysics scheme BEM.
- Runs AS1 and AS2 are implemented to examine the effects of the vortex size. In these runs, the Radius of the Outermost Closed Isobar (ROCI) decreased and increased by 50%, respectively.
- Runs E5C and E5CS are designed to have the best settings, including the boundary conditions from analysis and the SSTs from the same week analysis. These two runs are different from each other only by the use of cloud nudging in E5CS.

Group V: Runs with constant SST. In this group, the SST is set to a constant value of 28^{o}C. With a constant SST, intensity changes of the simulated vortex are influenced by factors other than the surface processes. Experiments with different boundary conditions (EF1 to EF5) and different vortex sizes (ASF1 and ASF2) are carried out to compare with their counter parts with variable SSTs and vortex sizes, i.e. (E1 to E5) and (AS1 and AS2), respectively.

(3) The track and intensity simulations of all ensemble runs were verified against the observations. It was found, not surprisingly, that the use of analyses as boundary conditions and the analysed SST of the same week provide the best hindcast of *Katrina*. The run E5C is obtained with the application of both of these settings, which indeed gives the closest match to the observed track and

intensity. Moreover, E5C exhibits very strong vacillation cycles and, therefore, is used for further detailed analysis.

Table 3.1: Characteristics of ensemble simulations. 'ss' stands for Standard Setting, which means that the current characteristic is similar to that of the control run C0.

	Run ID	I.C	B.C.	SST	Nudging	ROCI (km)	CON
I	C0	not perturbed	12Z 26/08/05	W1	not used	450	not used
	C1-C4	perturbed	ss	ss	ss	ss	ss
II	A0	ss	ss	ss	P and ζ	ss	ss
	B0	ss	ss	ss	ζ	ss	ss
	D0	ss	ss	ss	P	ss	ss
III	E1	ss	00Z23/08/05	ss	ss	ss	ss
	E2	ss	00Z 24/08/05	ss	ss	ss	ss
	E3	ss	00Z 25/08/05	ss	ss	ss	ss
	E4	ss	00Z 26/08/05	ss	ss	ss	ss
	E5	ss	analysis	ss	ss	ss	ss
IV	STC	ss	ss	W0	ss	ss	ss
	CB	ss	ss	ss	ss	ss	Tiedtke
	AS1	ss	ss	ss	ss	300	ss
	AS2	ss	ss	ss	ss	600	ss
	E5C	ss	analysis	W0	ss	ss	ss
	E5CS	ss	analysis	W0	Cloud	ss	ss
VI	STF	ss	ss	28^oC	ss	ss	ss
	EF1	ss	00Z 23/08/05	28^oC	ss	ss	ss
	EF2	ss	00Z 24/08/05	28^oC	ss	ss	ss
	EF3	ss	00Z 25/08/05	28^oC	ss	ss	ss
	EF4	ss	00Z 26/08/05	28^oC	ss	ss	ss
	EF5	ss	analysis	28^oC	ss	ss	ss
	ASF1	ss	ss	28^oC	ss	300	ss
	ASF2	ss	ss	28^oC	ss	600	ss

The important characteristics of each simulation are summarised in Table 3.1. In this table, "I.C." (initial condition) can be either not-perturbed, or perturbed by adding random errors to the observations. "B.C." column shows the base time of the GASP forecasts which are used for boundary conditions. Nudging variables can be either pressure (P) or vorticity (ζ), or both. The cloud nudging method is described by Davidson and Puri (1992). "ROCI" is the value of ROCI assumed for the bogus vortex. CON is the convective parameterisation scheme used in the simulation.

The SSTs are taken from the weekly analysis of the previous week (W1) or the same week (W0) of the base time (00Z 27 August 2005). The SST of W1 and the difference (W1-W0) are shown in Figure 3.1. As can be seen from panel b, the SSTs in the current week of the storm are lower than those of the previous week by about 0.5 to 1^oC in the central part of the Gulf of Mexico. For the whole domain, the mean SST of W1 and W0 are 303.02 K and 302.87 K, respectively. The standard deviation of the SSTs for the corresponding fields are 3.14 K and 4.92 K, respectively. Thus, although the SST is lower in W0 than in W1, its variation is larger in W0. This characteristic of the SST during week W0 can be partly explained by the cooling and mixing effects by the circulation of hurricane *Katrina* itself.

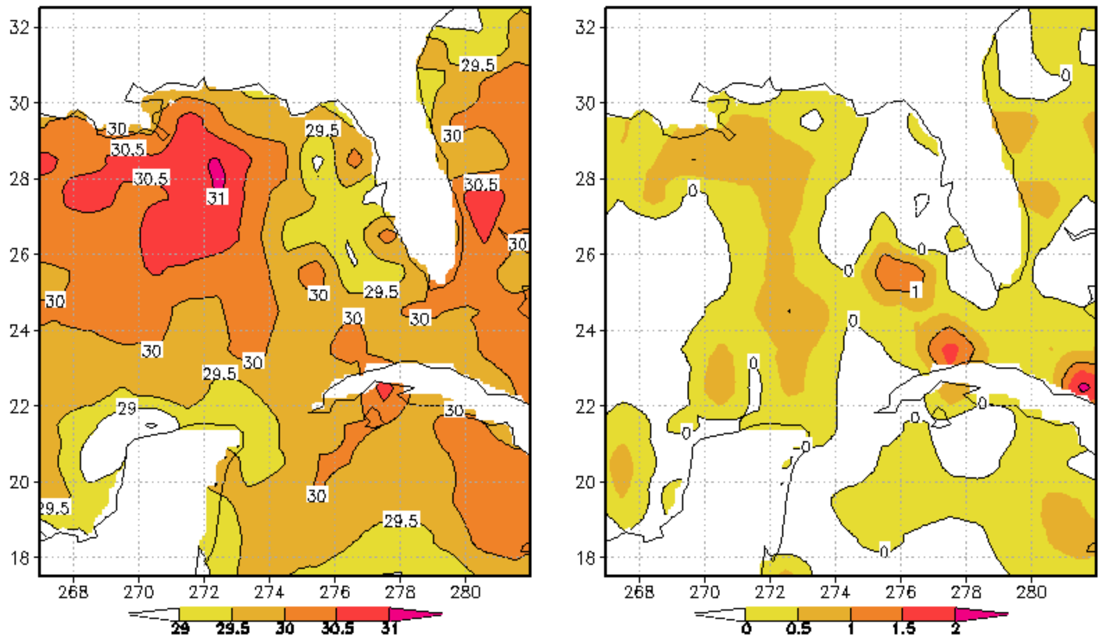

(a) SST of W1

(b) SST difference (W1 - W0)

Figure 3.1: Sea Surface Temperature [deg. C] of the analysis from the previous week (W1) and its difference from the analysis of same week of the storm (W1-W0).

3.2 Track and intensity forecasts of ensemble members

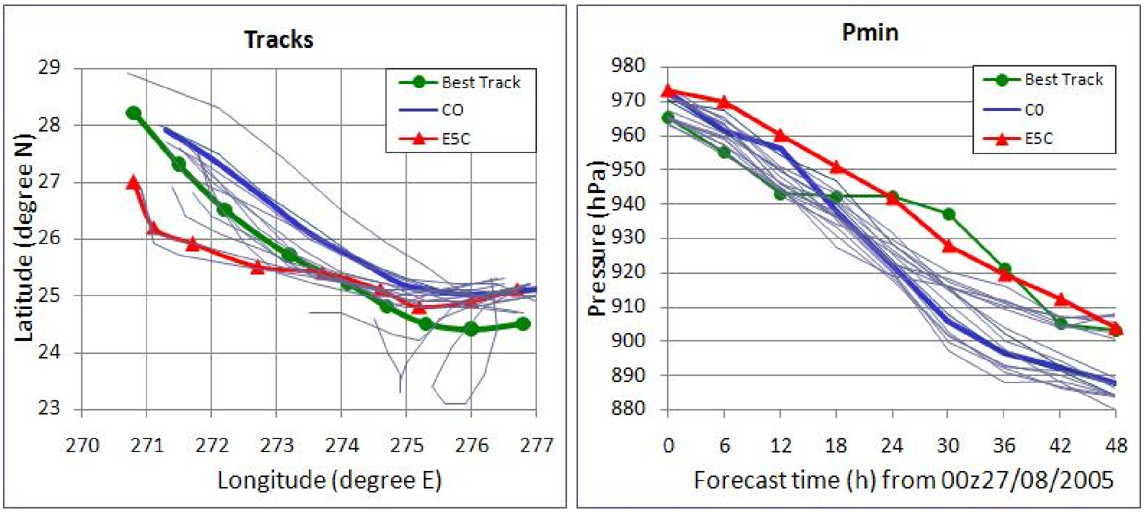

(a) Track (b) Minimum surface pressure

Figure 3.2: Ensemble simulations of hurricane *Katrina* with high-resolution (5 km) version of TCLAPS. The base-time of simulations is 00Z on 27 August 2005. Green lines with circles represent the official best track provided by National Hurricane Centre. Red lines with triangles show the run E5C.

The simulated tracks and the minimum central surface pressure (P_{min}) of all ensemble runs are shown in Figure 3.2. On the whole, the forecasts of ensemble members are similar to each other and are in good agreement with the observations (green lines with circles). Nonetheless, there are three members with erratic tracks (see panel a) different from other runs and the observed track of hurricane *Katrina*. As will be explained in Subsection 3.2.1, the cause of this behaviour is the inaccurate boundary conditions used in these runs. On the other hand, the evolution of P_{min} (panel b) shows two groups of forecasts: one, which consists of the majority of the ensemble members, has P_{min} lower than the observed values by about 10 hPa; and the other achieves P_{min} similar to the observations. The cause for the former group to over-predict the intensity is attributed largely to the use of the sea surface temperature (SST) of the previous week, which is higher than the actual SST experienced by the vortex (see Figure 3.1). The dependence of the intensity on SST will be addressed later in Subsection 3.2.2 .

Among the ensemble members, the run E5C, which is marked with red lines in Figure 3.2, is chosen for detailed analysis with the aims of exposing the physical processes controlling the development of the asymmetries and discovering the connection to rapid cyclogenesis. This choice is based on the model configuration and the initial and boundary conditions, which represent the most accurate information available. Accordingly, the evolution of the track and intensity in this run is close to that observed, suggesting that this run has captured the essential physical processes that shaped hurricane *Katrina*.

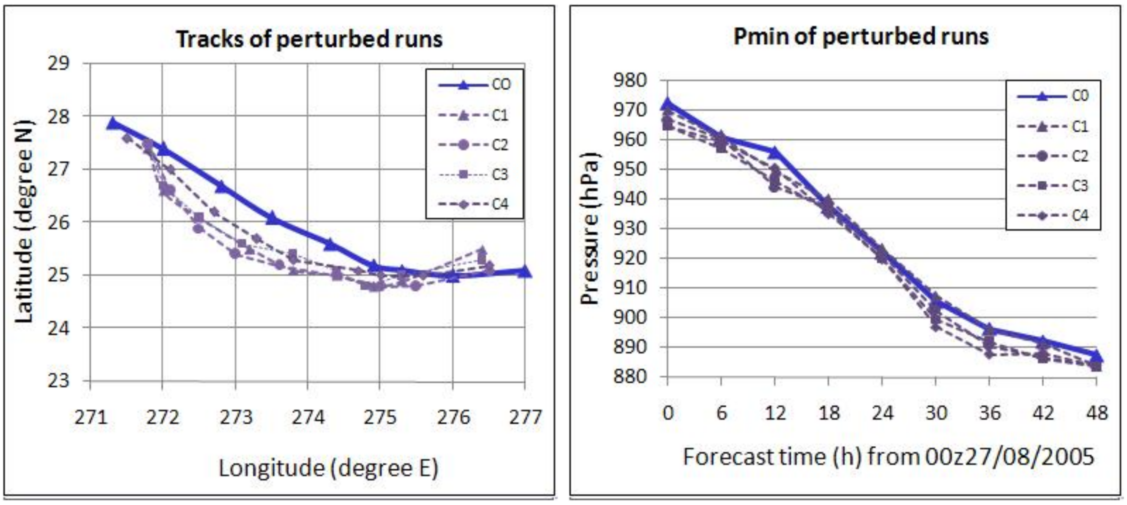

(a) Track (b) Minimum surface pressure

Figure 3.3: Simulations of Group I: perturbed observations.

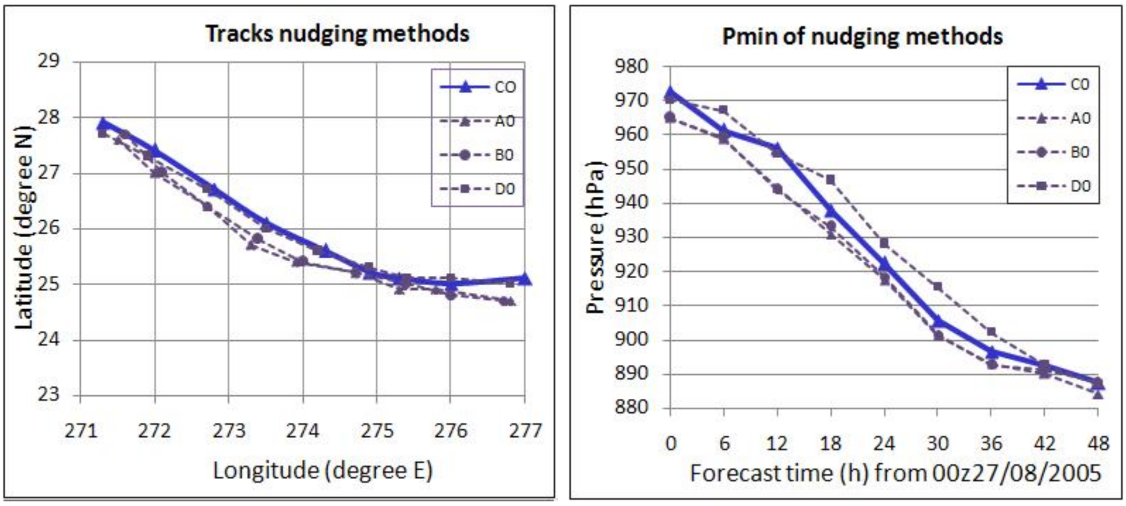

(a) Track (b) Minimum surface pressure

Figure 3.4: Simulations of Group II: different nudging methods.

3.2.1 Model sensitivity

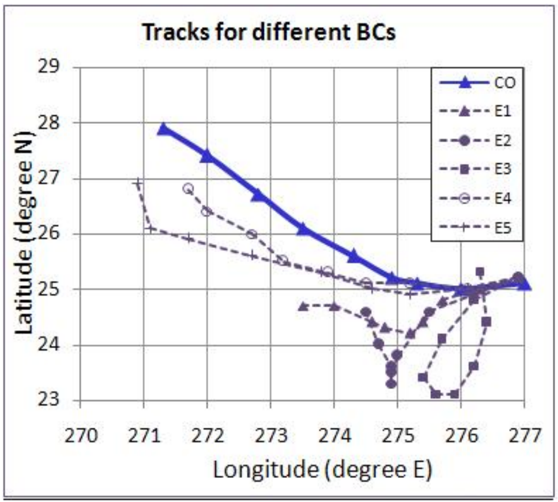

(a) Track

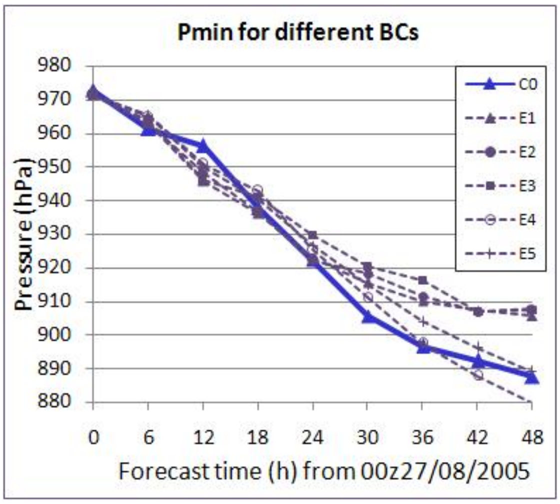

(b) Minimum surface pressure

Figure 3.5: Simulations of Group III: different boundary conditions.

Figures 3.3 and 3.4 show the simulated tracks and minimum surface pressure of the runs from Group I with perturbed observations, and Group II with different nudging methods. For Group I, the introduction of perturbations to the observations, including the synthetic observations for the bogus vortex, leads to more noticeable changes in tracks than in the intensity. The difference in minimum pressure between each member from the control run, and amongst different members are typically less than 5 hPa at any given time (Fig. 3.3b), whereas their differences in location are greater than 0.5^0 (Fig. 3.3a). In contrast, the track variations of the members in Group II are relatively small (generally less than 0.3^0), whereas the induced variation of minimum surface pressure is in order of 15 hPa, thus, significantly larger than that in Group I (see Figs. 3.4a and b, respectively). Nevertheless, both of these two groups exhibit relatively small variations in the simulated track and intensity.

In contrast, changes in the boundary conditions (Group III), which imply different large-scale dynamical configurations, lead to more pronounced variations in the track and intensity of the simulated vortices (Figure 3.5). The simulated TCs using the earlier base times of GASP as the boundary conditions (runs E1, E2 and E3) have erratic paths: E1 first deflects the vortex southwards and then slowly westward; E2 moves the vortex to the south-west, and then makes a loop before turning to the north-west direction; and E3 turns the vortex anticlockwise nearly a full circle, and ultimately comes back to the original position after 48 h. Thus, the distance of these simulated vortices to the corresponding control run after 48 h is very large, exceeding 500 km. This behaviour is different from other members in the ensemble, and clearly different from the observed track of hurricane *Katrina*. The reason for these forecast failures is that these particular forecasts from GASP with long lead times (96 h, 72 h, and 48 h for E1, E2, and E3, respectively) predict an upper level trough too far to the east, which steers the simulated TC in the above-mentioned manner.

Although not central to the theme of this dissertation, this strong influence by the boundary conditions on the simulated tracks suggests an important practical implication on the use of limited area model for predicting tropical cyclones. As seen in the three runs presented above, although a bogus vortex is implemented to represent the vortex realistically at the initial time of the integration, the boundary conditions take control after just 6 hours and affect the future track of the modelled vortex.

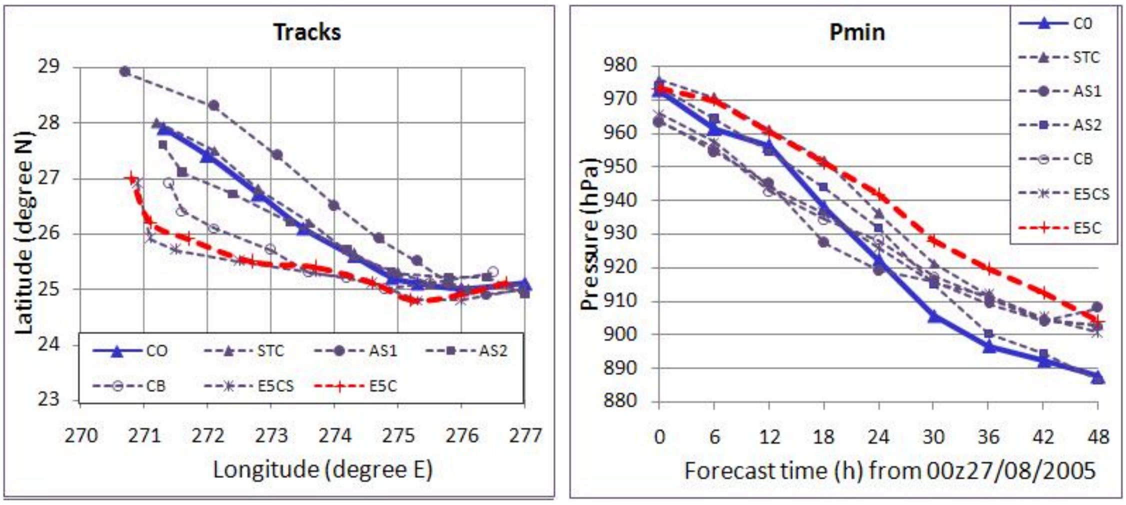

(a) Track (b) Minimum surface pressure

Figure 3.6: Simulations of Group IV: Model and vortex configuration.

Figure 3.6 shows the simulations in Group IV, which has different model configuration and vortex characteristics. The variation of the track and intensity of this group is large compared with other groups. The runs STC, E5C and E5CS using the SST analysis of the corresponding current week produce a minimum surface pressure of 10 hPa higher than the control run C0 (Figure 3.6b), which uses the higher SST from the analyses of the previous week. On the other hand, the track of STC is very close to that of the control run C0 (see Figure 3.6a), suggesting that changes in the SST do not affect the track directly. This is consistent with the commonly accepted knowledge that TC movement is largely influenced by environmental steering and a beta effect(see e.g. Holland, 1983), which in turn, depend on the vertical and horizontal dimensions of the TC vortex. Then, changes in the SST may indirectly affect the movement of TC by modifying the convective structure, and thus, the size of the TC vortex.

Changes in the vortex size, which is measured by the ROCI, lead to noticeable variations in the track and intensity of the simulated vortices. For example, the track of the run AS1 with a smaller initial vortex (ROCI decreased by 50% from the control run C0) is deflected about 1^o northwards of C0, whereas the larger vortex AS2 (with ROCI increased by 50%) deflects slightly southwards. With regards to intensity, the larger vortex AS2 intensifies at a later time than the smaller vortex AS1 but eventually achieves a lower minimum pressure after 48 h (see Figure 3.6b). Although it would be interesting to understand the effects of the vortex size on the track and intensity of the modelled vortex, it is not the main goal of this research and will be investigated in future work.

With the use of the convective parameterisation scheme (Tiedtke, 1989) in conjunction with the explicit microphysics scheme, the simulated vortex in CB achieves a P_{min} of 10 hPa higher than that of the control run at 48 h. This lower intensity is comparable with that achieved by the simulations with lower SST (STC, E5C, E5CS), a smaller initial vortex (AS1), and the values observed in hurricane *Katrina* (see e.g. Figures 3.6b and 3.2).

3.2.2 The relative importance of sea surface temperature

As shown earlier in Figure 3.2b, there are two distinct groups of simulations with noticeably different minimum surface pressure of the order 10 to 15 hPa. The group with higher intensities include C0, C1-C4, E4 and E5, and use the SSTs from the analysis of the previous week (W1). It is shown in Appendix C that the mean SSTs along the tracks of these runs are significantly higher than those in STC, E5C and E5CS that use the SST analysis of the same week (W0). This result is not surprising since the current configuration of TCLAPS is not coupled with the ocean. With the use of the SST analysis from the current week (W0), some effects of the hurricane in reducing the SSTs by upwelling and mixing of the upper layers of the ocean are likely to be included, giving a more realistic evolution of the simulated vortex.

The work described in Section 1.1.2 suggests that SST (i.e. surface processes) may affect TC intensity strongly. As variations of track and intensity of the simulated vortices tend to occur together, the intensity change of a TC may be associated with the particular track followed by the TC. This connection is substantiated by the fact that the uneven distribution of SST provides TCs, going along different paths, with different strength surface fluxes. For this reason, this section assesses the effects of surface processes by first estimating the correlation between TC intensity and the SST at the location of the TC, and secondly, running experiments with a constant SST while varying other conditions.

Correlation between the simulated intensity and SST

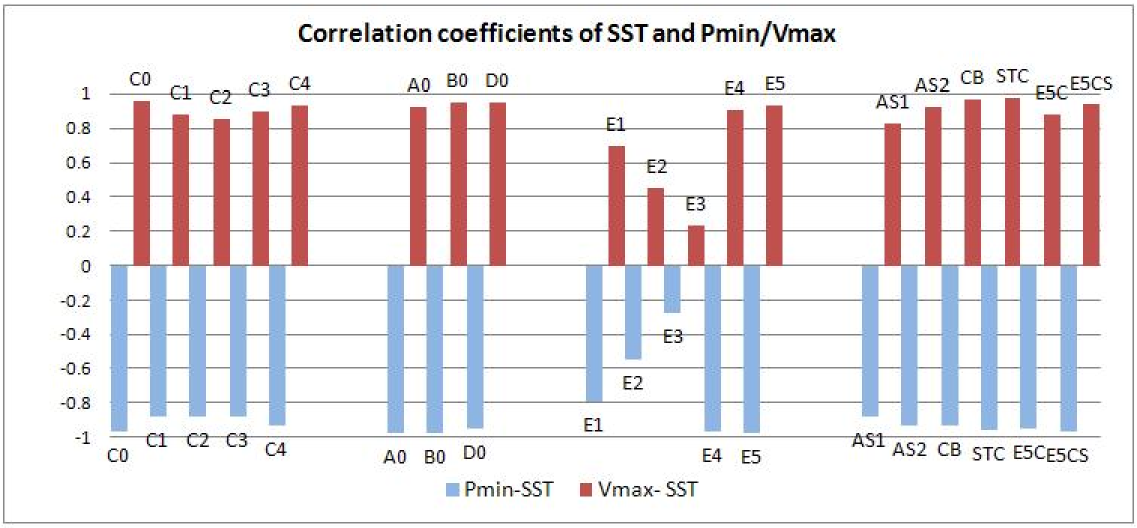

Figure 3.7: Correlation coefficients between SST and P_{min} (blue columns) and V_{max} (red columns) of the ensemble runs. SSTs are averaged over the 1×1 degree box at the locations of the vortex center.

Figure 3.7 shows the correlation between the simulated P_{min} (and V_{max}) and the SST immediately beneath and following the vortex center. For each ensemble member, the correlation coefficient is calculated from a set of corresponding values of the SST, which is averaged over the regions inside of 100 km radius from the vortex center, and the P_{min} and V_{max} at each hour. In general, the correlation is high, indicating that more than 80% of the variation in the intensity can be explained by the variation in SST.

However, there are two exceptions with the runs E3 and E2, which have low correlation coefficients. Recall that these runs have the curving and looping tracks (Figure 3.5a) as being affected strongly by the erroneous position of a large scale trough which is provided by the boundary conditions. The variation of SST along the tracks of these runs is small (see Table C.1 of Appendix C) and, thus, changes in the intensities of these vortices are likely to be influenced by factors other than SSTs. For E2 and E3 runs, it is most likely that the large-scale trough mentioned above influences the intensity of the simulated vortices strongly.

Experiments with constant SST

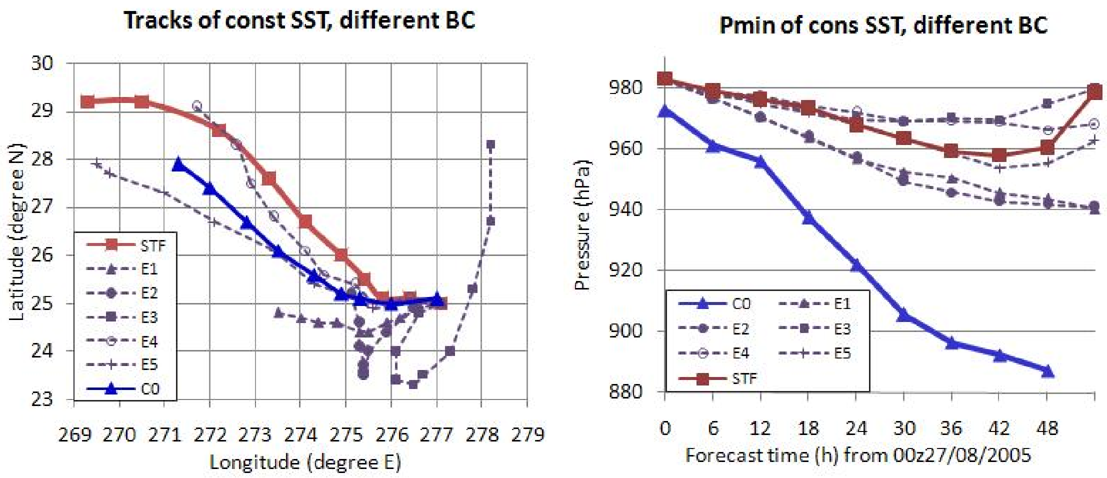

(a) Track (b) Minimum surface pressure

Figure 3.8: Simulations of Group V: Constant SST (28^{o}C) and different boundary conditions.

Figures 3.8 shows the tracks and the evolution of P_{min} simulated by the ensemble runs with a constant sea surface temperature of 28^{o}C and different boundary conditions. The tracks of the simulated TCs are similar to the tracks of Group III with variable boundary conditions (Figure 3.5a). In contrast, the intensity of all runs with constant SST are significantly lower than the control run C0 (see Figure 3.8b), which can be explained by the colder sea surface. Thus, the sea surface temperature appears to much more strongly influence intensity than tracks of the simulated TCs.

Nonetheless, changes in the SST may also affect the TC track to some extent. The run STF, which differs from the control run C0 by using a lower but constant

SST, has the track deflected to the poleward of the control track. This deflection pattern is similar to the effect of decreasing vortex size as in the run AS1 (see Figure 3.6a). Thus, it is likely that the lower SST used in STF is unfavourable for convection. Hence the vortex is unable to develop its full convective cloud system resulting in a small size[1], which is similar to the vortex in the AS1 run.

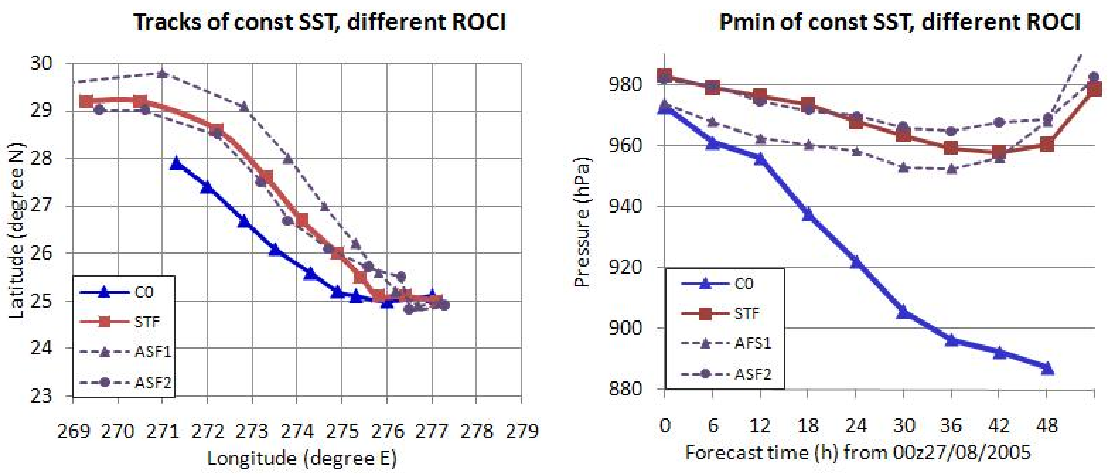

(a) Track (b) Minimum surface pressure

Figure 3.9: Simulations of Group V: Constant SST (28^{o}C) and different ROCI.

Figure 3.9 shows tracks and intensity of the simulations (ASF1 and ASF2) with the constant SST (of 28^{o}C) and the modified initial vortex size similar to those in AS1 and AS2. Here again, the effects of the lower SST can be seen more clearly in intensity rather than the tracks of the simulated vortices. In addition, the smaller vortex (ASF1) deviates to the poleward side of STF track, in a manner similar to the case when realistic SSTs are used, i.e. the poleward deflection of the small vortex AS1 relative to the control run C0.

In summary, the ensemble experiments show that the simulated tracks are strongly affected by large scale dynamics, whereas the intensities are influenced more prominently by the conditions of the sea surface, the configuration of the model and the vortex structure. Strong dependence of the vortex intensity on the SST may occur if other factors (such as large scale dynamics and vortex structure) are favourable for development.

[1]Radius-time plots of the azimuthally-averaged tangential wind of the ensemble runs are examined but not shown here for brevity. They indicate that the area occupied by the 40 (m s^{-1}) mean tangential wind of the run STF extends to a radius comparable to that in the run AS1.

3.3 Evolution of asymmetries

As discussed in Section 1.2, the intensity of tropical cyclones may be changed by asymmetric mechanisms, which are the main focus of this study. Therefore, the evolution of the asymmetries and the associated intensification of the simulated vortices is examined next.

3.3.1 Azimuthal analysis and representation of asymmetries

The method used to determine azimuthal asymmetry is outlined and comprises 3 steps.

1. **Locating the vortex center.** The center of the simulated TC is determined by searching model output using the down-hill method, similar to that used in Davidson and Weber (2000). At each level, the TC center is defined as the local minimum in the mean sea level pressure for the surface and geopotential for other pressure levels. The use of a local minimum in the mass field instead of a local maximum in vorticity is intended to avoid mislocation of TC centres due to (a) possible occurrence of mesovortices having relatively high vorticity in the eyewall region, and (b) high vorticity associated with cyclonic shear not at the system's centre.

2. **Calculation of azimuthal means.** The region near the vortex center (up to 400 km radius) is divided into 80 concentric annuli, centered at the TC center, having the thickness equivalent to the horizontal resolution of the model (i.e. 5 km in this case). The azimuthal mean of a variable X at a radius R is defined as the average value of that variable from all grid points located inside the annulus having radius R as follow:

$$\overline{X}_R = \frac{1}{n}\sum_{1}^{n} X(d_i), (R - \frac{\Delta r}{2}) \leq d_i < (R + \frac{\Delta r}{2}), \tag{3.1}$$

where $X(d_i)$ is the value of X at point i, which has the distance d_i to the TC center, Δr is the thickness of the annulus (which is set to 5 km in these simulations), and n is the number of grid points located inside that annulus.

3. **Representation of asymmetry.** The asymmetry of the potential vorticity (PV)[2] on pressure surfaces in the azimuthal direction is characterised by two quantities: the PV spectral amplitudes calculated using a Fast Fourier Transform (FFT), and the maximum standard deviation of potential vorticity (SDPVmax).

The FFT analysis uses PV values along circles of constant radii (25 km, 50 km, 75 km and 100 km), which are obtained by bilinear interpolation from surrounding grid points. The amplitudes of different wave numbers decomposed by the FFT are then used as measure of the asymmetry at each radius. Thus, this method provides the full asymmetric structure at particular radii.

A second measure of the asymmetry is also used. The asymmetry at each radius is characterised by the standard deviation of PV (hereafter SDPV) within the annulus having radius R. The SDPV is calculated by

$$SDPV_R = \sqrt{\frac{1}{n-1}\sum_{1}^{n}\left(PV(d_i) - \overline{PV}_R\right)^2}, (R - \frac{\Delta r}{2}) \leq d_i < (R + \frac{\Delta r}{2}), \quad (3.2)$$

where $X(d_i), d_i$, n, and Δr are the same as those in Eq. 3.1. Then, SDPVmax is the maximum value of SDPV at all radii inside of 300 km. Thus, with the use of SDPVmax, the information of the maximum asymmetry is condensed into a single value, which is convenient for fast examination of different runs.

3.3.2 Characteristics of the asymmetries in the ensemble simulations

Figures 3.10 to 3.13 show the evolution of SDPVmax and the tendencies of the maximum tangential wind ($\partial \overline{V}_{max}/\partial t$, where $\overline{V}_{max}$ is the maximum of the azimuthally-averaged tangential wind at radii inside of 300 km) at 850 hPa for ensemble members. Examination of the radial profiles of standard deviation of PV (not shown here for brevity) indicates that SDPVmax occurs near the maximum of the azimuthally-averaged vertical motion, i.e. the eyewall. Thus, SDPVmax and $\partial \overline{V}_{max}/\partial t$ are located close to each other, the former typically occurs at about 10 km inside of the

[2]The potential vorticity on pressure surfaces is calculated using Equation 13 in Hoskins et al. (1985) and has the form: $PV = -g(f\overrightarrow{k} + \nabla_p \times \overrightarrow{V}) \cdot \nabla_p \theta$ [PVU], where PVU=$10^6\times$ m^{-2} K kg^{-1}, symbols are conventional as described in Table A.1. Asymmetries are more evident in the potential vorticity field than in the tangential wind field.

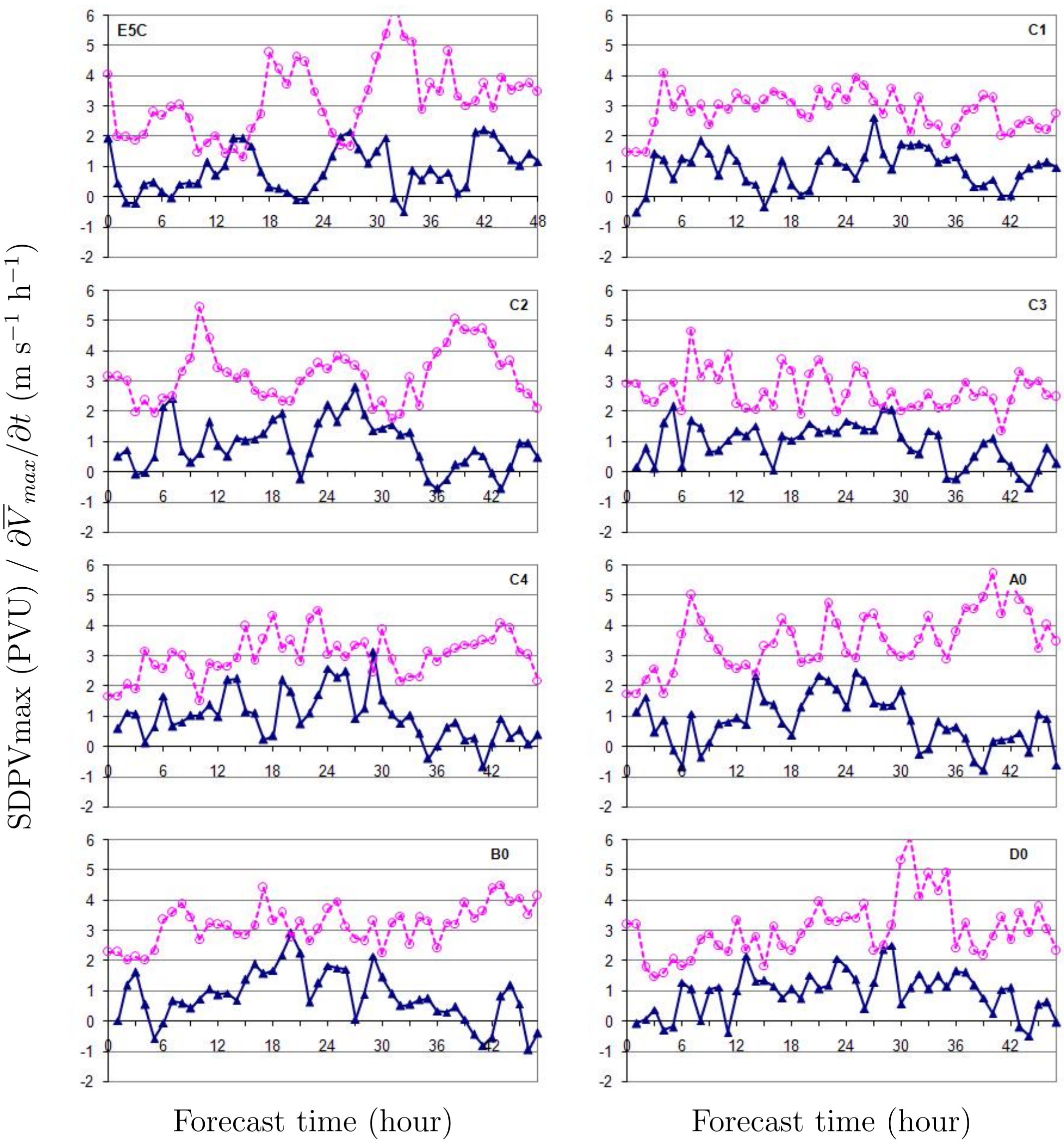

Figure 3.10: The evolution of asymmetries (SDPVmax) at 850 hPa for the runs E5C, C1-C4, A0, B0 and D0. The horizontal axis shows the elapsed time [hours] from 00Z 27 August 2005. Dashed pink lines with open circles represent SDPVmax [PVU]. Tendencies of the maximum (azimuthally-mean) tangential wind $\partial\overline{V}_{max}/\partial t$ [m s^{-1} h^{-1}] are shown by solid blue lines with filled triangles.

latter (which is the RMW).

The maximum PV asymmetry changes in a periodic manner, vacillating between a more symmetric and a more asymmetric phase. Note that the vortex never achieves a completely symmetric state (i.e. zero asymmetry), which is consistent with the finding by Nguyen et al. (2008) using their idealized high resolution ensemble runs with the MM5 model. Rather, the level of asymmetry changes between relatively high and low values, which are referred to as asymmetric and symmetric phases in this work.

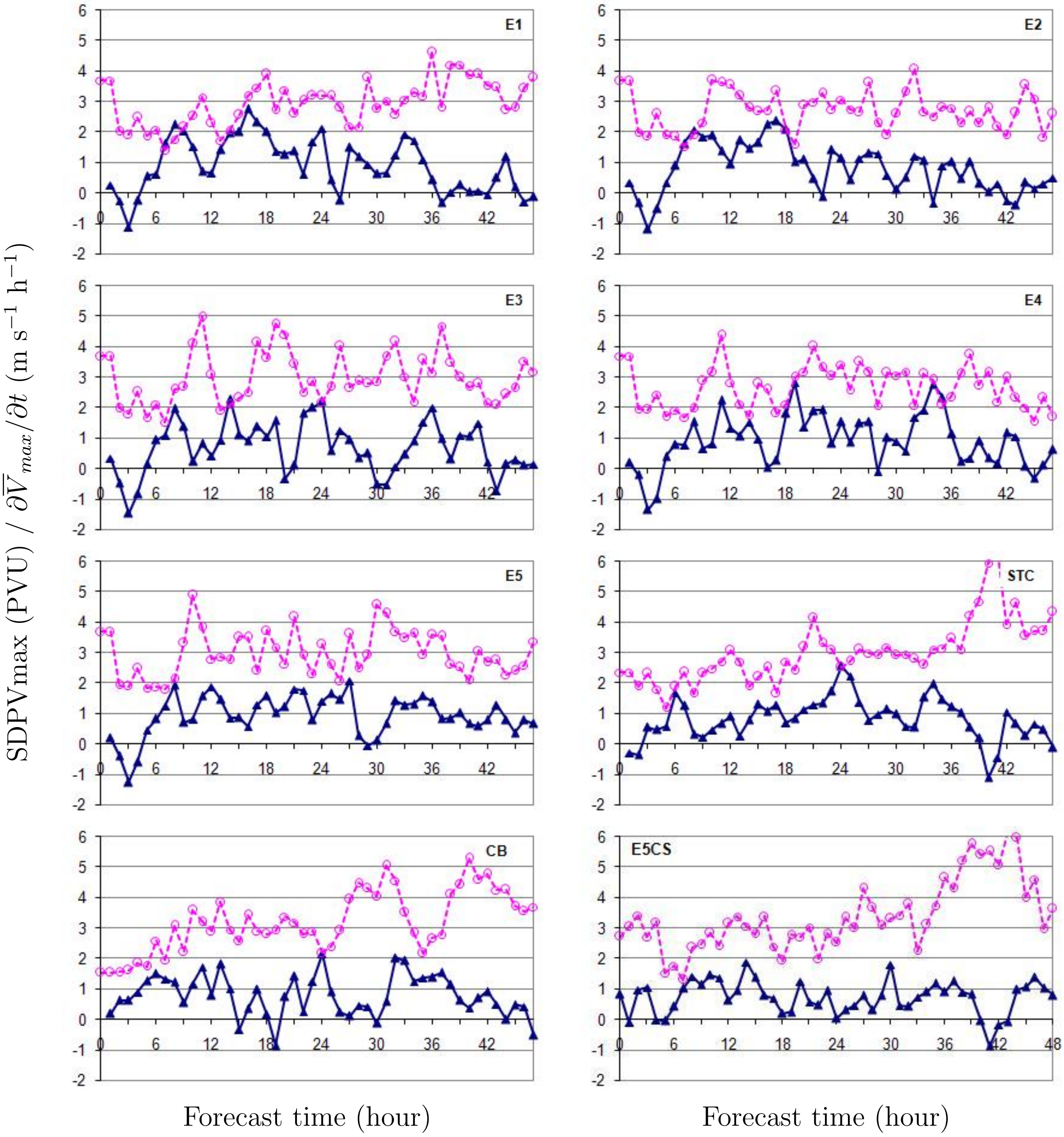

Figure 3.11: As for Figure 3.10 but for the runs E1-E4, CB and E5CS.

Based on the evolution of all ensemble runs, we define the transition between the symmetric phase and the asymmetric phase as the periods with the following characteristics:

1. Change in SDPVmax is not less than 2 PVU,
2. The phase of higher asymmetry has SDPVmax is not less than 4 PVU,
3. The length of the Symmetric to Asymmetric (S-A) transition period is calculated as hours elapsed from time of lowest asymmetry until the SDPVmax becomes greater than 4 PVU

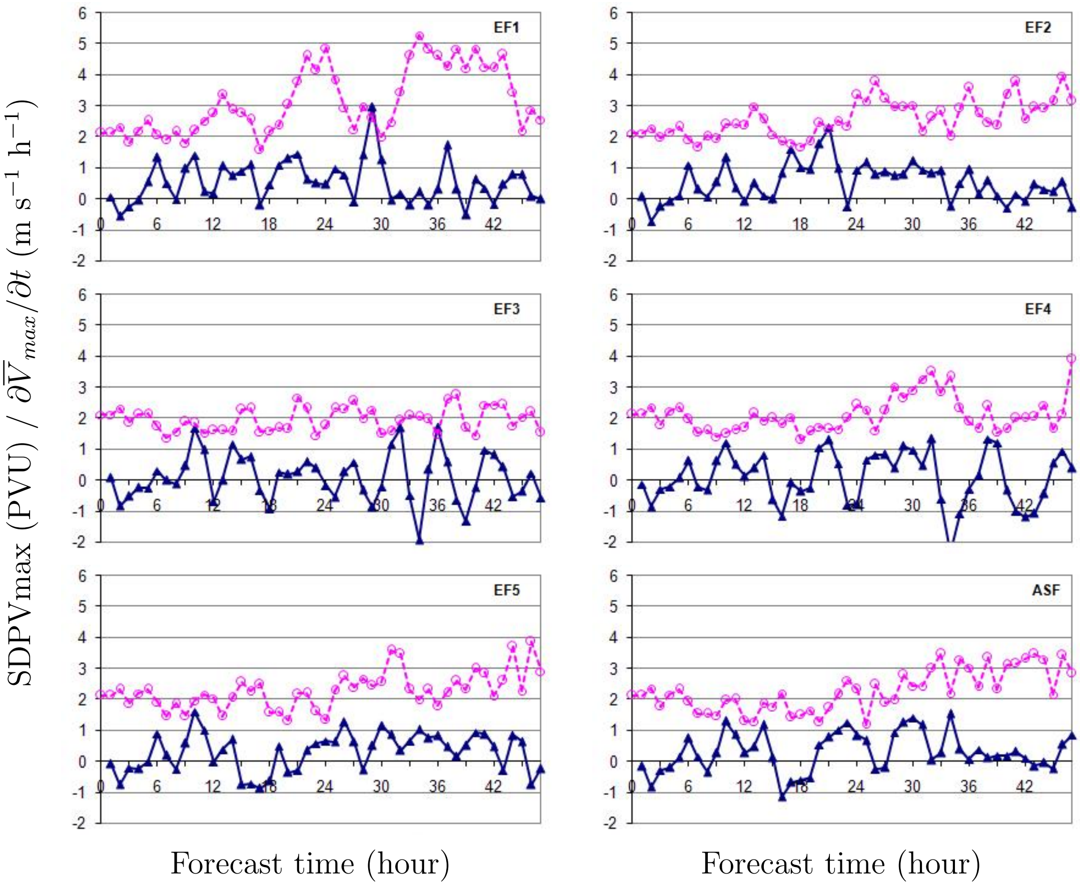

Figure 3.12: As in Figure 3.10 but for the runs with constant SST: EF1 - EF5, and STF.

4. The length of the Asymmetric to Symmetric (A-S) transition period is calculated as hours elapsed from the time the SDPVmax becomes greater or equal 4 PVU until the SDPVmax reaches the next local minimum.

Using the above classification, the evolution of the asymmetries in the ensemble runs can be identified with the number of vacillation cycles, amplitudes and the length of transition periods, details of which are presented in Appendix C. The basic statistical properties of the vacillation cycles are summarised in Table 3.2. The majority of simulations (22 out of 27) exhibits a vacillation pattern with an average of 2 cycles during the 48 h forecasting period. The 95% confidence intervals are from 9 to 11 h for the mean period of one cycle, and from 2.5 to 2.9 PVU for the mean vacillation amplitude. Furthermore, it can be concluded, by a paired one-sided t-test[3] with a p-value of 3.5×10^{-6}, that the A-S transition tends to occur during a longer period than that of the S-A transition.

[3]Descriptions of the t-test method can be found in most textbooks on basic statistics such as Rosenkrantz (1997).

Table 3.2: Statistical properties of vacillations cycles in the ensemble members. Columns S-A, A-S and S-A-S show the duration (in hour) of the transition periods S-A, A-S and the whole cycle from the Symmetric to Asymmetric and to Symmetric phase. A-$\mathbf{I_{corr}}$ is the correlation coefficient between SDPVmax and $\partial \overline{V}_{max}/\partial t$, thus, representing relation ship between the Asymmetries and Intensification rates.

	Cycles	**S-A** (h)	**A-S** (h)	**S-A-S** (h)	**Amplitude** (PVU)	**A-I$_{corr}$**
Average	2.0	3.8	6.4	10.1	2.7	-0.2
Standard deviation	1.0	2.0	2.9	3.6	0.7	0.4
Standard error	0.3	0.6	0.8	1.0	0.2	0.1
Confidence interval 95%	1.7 2.3	3.3 4.4	5.5 7.2	9.0 11.1	2.5 2.9	-0.3 -0.1
T-test	$P_{(S-A)\geq(A-S)}$ =3.45782×10^{-06}					
Runs with vacillation	22 out of 27					

It can be seen also from Figures 3.10 to 3.11 that the asymmetric phase tends to be associated with a smaller acceleration of $\overline{V}_{max}$ and the symmetric phase with higher acceleration rates. This behaviour appears as the apparent anti-correlation between the red and blue lines (see e.g. C0, C2, A0, D0, E1, E2, STC, CB, E5C, E5CS and EF1 runs). The correlation coefficients between SDPVmax and $\partial \overline{V}_{max}/\partial t$, here after A-$\mathbf{I_{corr}}$, are calculated for each identified cycle and are presented in Appendix C. The mean A-$\mathbf{I_{corr}}$ for all ensemble runs is -0.2 with the 95% confidence interval ranging between -0.3 and -0.1, indicating a negative association. Among all ensemble members, the run E5C shows the clearest anti-correlation pattern (Figure 3.10) and a high correlation coefficient of 0.94 (Table C.3). Note that as correlation coefficients reflect the strength of the linear association, their magnitudes may be small for strong but non-linear associations. The simulations which exhibit the apparent anti-correlation pattern mentioned above may have correlation magnitudes as small as 0.25 (see tables in Appendix C).

The influence of SST and vortex size on the vacillation cycles.

As discussed in the previous section, SSTs are shown to have a strong link with the intensity of the simulated vortices. Higher SSTs tend to be associated with more intense vortices. We determine now the relationship between the SST and vacillation cycles.

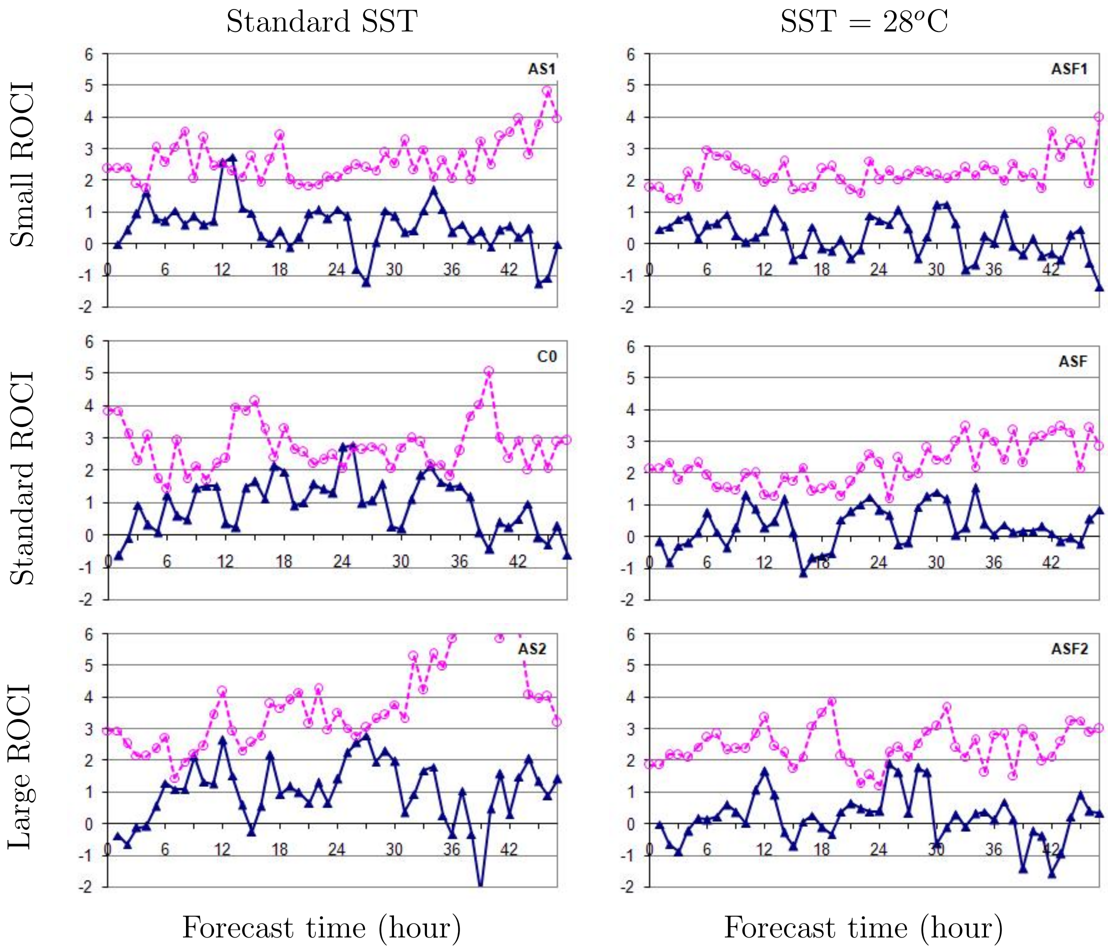

Figure 3.13: As in Figure 3.10 but for the runs AS1, STF1, C0, STF, AS2 and ASF2. Left panels are the runs with standard SST as described in Table 3.1, whereas right panels show the corresponding runs with a constant SST of 28^{o}C.

Table 3.3 shows characteristics of the SSTs along the tracks of the simulated vortices with regard to vacillation cycles. Based on their largest negative values of A-$I_{\mathbf{corr}}$, simulations are grouped into two classes: strong or weak vacillation cycles. A simulation is defined as having strong vacillation cycles if there is at least one cycle having the A-$I_{\mathbf{corr}}$ less than -0.5.

One-sided t-tests[4] with unequal variances are performed to determine whether there are differences between the two groups in terms of the mean and standard deviation of the SSTs following the tracks of the simulated vortices. With the p-values of 9.412×10^{-7} and 0.0046 for the mean and standard deviation of SSTs, respectively, one can conclude, at the 99% confidence level, that vortices with strong vacillation cycles tend to pass over the sea surface of lower but more variable SSTs along their

[4]Note that the t-test on the mean SSTs uses all hourly data for each simulation, whereas the test for standard deviation of the along-track SSTs uses only one value for each simulation.

paths, compared with the vortices having weaker cycles.

Furthermore, it is found that the correlation of the largest negative A-$I_{\mathbf{corr}}$ with the mean along-track SST is positive (0.24), and with the standard deviation of the along-track SST is negative (-0.33), thus, supporting the hypothesis that stronger cycles (with large negative A-$I_{\mathbf{corr}}$) tend to occur at lower but more variable SSTs. However, the magnitudes of these associations are relatively small, indicating that SST plays a relatively small role in regulating these vacillation cycles.

Figure 3.12 (EF1-EF5, and STF runs) shows the evolution of asymmetries in the simulations with a constant SST of 28^{o}C. Among these 6 runs, only two exhibit vacillation cycles (EF1 and EF2), whereas their corresponding runs that use realistic SST (E1 to E5) all exhibit at least one vacillation cycle. It is probable that the cause of the lack of the vacillation in the runs with constant SST is the less active convective environment associated with the homogeneously low SST.

The characteristics above suggest that vacillation cycles are likely to be associated with pulsing of convection. This is because the larger changes in the SST along the tracks of the simulations having strong cycles imply that convective instability is more variable for these vortices. On the other hand, the lack of these cycles in the runs with constant SST of 28^{o}C may be explained by the lack of or low convective instability due to the relatively cool sea surface. However, it is unclear why there is an association between cooler sea surface and strong cycles.

It is seen from Figure 3.13 that there are connections between the vortex size and the evolution of asymmetry as well. For example, vortices in the runs AS1, C0 and AS2, which are ordered with increasing values of ROCI, appear to have increasingly stronger vacillation cycles (see panels a, c and e). These runs indeed have the correlation A-$I_{\mathbf{corr}}$ of increasing magnitudes (-0.525, -0.728 and -0.731, respectively). Likewise, the corresponding runs (ASF1, STF and ASF2) using a constant SST also exhibit an increasing vacillation pattern (see panels b, d and f), in which the larger vortex tends to vacillate more. ASF1 and ASF are classified as non-vacillating, whereas ASF2 has two identified cycles with the largest A-$I_{\mathbf{corr}}$ having a value of -0.347 (see Table C.3 in Appendix C). The explanation for this apparent association will be discussed in Chapter 7.

3.4 Summary of Chapter 3

An ensemble of high-resolution simulations for hurricane *Katrina* has been constructed. Analysis of the ensemble simulations shows the following features:

- **Simulation consistency:** In general, the simulated tracks and intensity of the ensemble runs are similar to each other and consistent with the observations of hurricane *Katrina*.

- **Model sensitivity:**

  a) Perturbations to the observations and the use of different nudging methods during the assimilation period do not create large variations in the simulated track and intensity. The typical variation of track and intensity of these two group is of the order of 0.5^o and 5hPa, respectively.

  b) Changes in boundary condition, and hence, large scale dynamics, induce significant changes in the simulated tracks, which may be lead to a difference in the location as large as more than 500 km by 48 h. In addition, the boundary conditions tend to affect the simulated track soon after the integration. Thus, this finding implies that inaccurate boundary conditions may quickly degrade the simulated tracks even if the vortex is initialised at the correct locations at the beginning of the integration.

  c) Changes in the vortex structure and model configuration may lead to noticeable changes in the simulated tracks and intensity of the order of 1^o and 10 hPa, respectively.

  d) The magnitude of the sea surface temperature affects the intensity more than the tracks. The variations of SST account for more than 80% of variations in the simulated intensity in the majority of ensemble members. However, under strong influence of large scale dynamics such as westerly troughs, this correlation between SST and TC intensity may become small.

- **Evolution of asymmetries:** The majority of the simulated vortices (22 out of 27) undergo cycles of structure change, vacillating between phases of relatively higher and lower asymmetry. The main characteristics of these cycles can be summarised as follows.

  a) There is a connection with intensification rates of the mean vortex: the highly asymmetric phase coinsides with a lower intensification rate and the highly symmetric phase with a higher rate.

b) The simulated vortices that exhibit strong correlation between asymmetries and intensification rates (A-$I_{\mathbf{corr}}$) encounter SSTs that are lower but more variable along their tracks.

c) Most of the simulations with a constant SST of 28^{o}C, which is about 2^{o}C lower than the control run, do not show vacillation cycles.

d) Vacillation cycles with stronger A-$I_{\mathbf{corr}}$ occur in the larger vortex.

Thus, although these cycles appear to have different periods, amplitudes and timing, the vacillating behaviour and the association pattern between the asymmetry and intensification rates are a common feature of the simulated vortices. In addition, the above characteristics indicate that convection play an important role in these vacillation cycles.

The consistency of the ensemble simulations and the robustness of the vacillation cycles suggest that the features found in our simulations may well be present in real tropical cyclones. In the next chapters we will analyse one specific simulation in detail to study the underlying mechanisms leading to the evolution of the vortex structure and the associated intensity changes. Observational evidence of the vacillations will also be presented.

Table 3.3: Relationship between SST and vacillation cycles. The mean μ and standard deviation σ of the SST following TC tracks as in Table C.1. The third column shows values of the largest negative A-I$_{corr}$ amongst the vacillation cycles in each run as listed in Tables C.2 and C.3 .

	Run ID	**Minimum** A-I$_{\mathbf{corr}}$	**SST** μ	**SST** σ
Weak cycles	C1	0.735	302.894	0.412
	C3	0.342	302.89	0.428
	C4	-0.277	302.874	0.440
	B0	-0.120	302.856	0.460
	E1	-0.431	303.016	0.163
	E2	-0.031	302.947	0.093
	E3	-0.440	302.82	0.233
	E4	-0.141	303.281	0.370
	E5	-0.276	303.3	0.365
	E5CS	-0.442	302.889	0.491
	Average	**-0.1081**	**302.977**	**0.346**
Strong cycles	C0	-0.728	302.815	0.506
	C2	-0.598	302.87	0.397
	A0	-0.626	302.875	0.439
	D0	-0.501	302.824	0.5207
	CB	-0.741	302.913	0.467
	AS1	-0.525	302.688	0.505
	AS2	-0.731	302.835	0.538
	STC	-0.862	302.797	0.513
	E5C	-0.945	302.898	0.509
	Average	**-0.695**	**302.835**	**0.488**

t-test	
$\mathbf{P}(\mu_{\mathbf{strong}} \geq \mu_{\mathbf{weak}})$	$\mathbf{9.412 \times 10^{-7}}$
$\mathbf{P}(\sigma_{\mathbf{strong}} \leq \sigma_{\mathbf{weak}})$	**0.0046**

Chapter 4

SYMMETRIC AND ASYMMETRIC PHASES IN E5C

In this chapter, the run E5C is analyzed in detail. This run is chosen because the track and intensity of the simulated vortex fits best with the observations of hurricane *Katrina* (see e.g. Figure 3.2). Moreover, as will be shown, E5C is particularly interesting because it exhibits a clear pattern of vacillation between symmetric and asymmetric states, in which asymmetries and rates of intensification are strongly correlated. This run uses the boundary conditions from analysis and the SST from the week of the storm, which may, to some extent, include the cooling effects of the TC on the ocean surface.

First, the evolution of asymmetries is examined and the symmetric and the symmetric phases are identified. Second, the vortex structure is examined in detail and the key characteristics of each phase is documented. Third, obvservational evidence for the presence of these two phases during the evolution of hurricane *Katrina* is presented.

4.1 Identification of the two phases in vortex structure

Figure 4.1a shows the same features as those in Figures 3.10, 3.11, but for the E5C run only. Note that from this point foreward, forecast hours are counted as the time elapsed from the start of assimilation, which is 24 h prior to the forecast base time. Thus, 0 h corresponds to 00 UTC 26 August 2008, instead of 00 UTC 27 August 2008 as in the previous chapter.

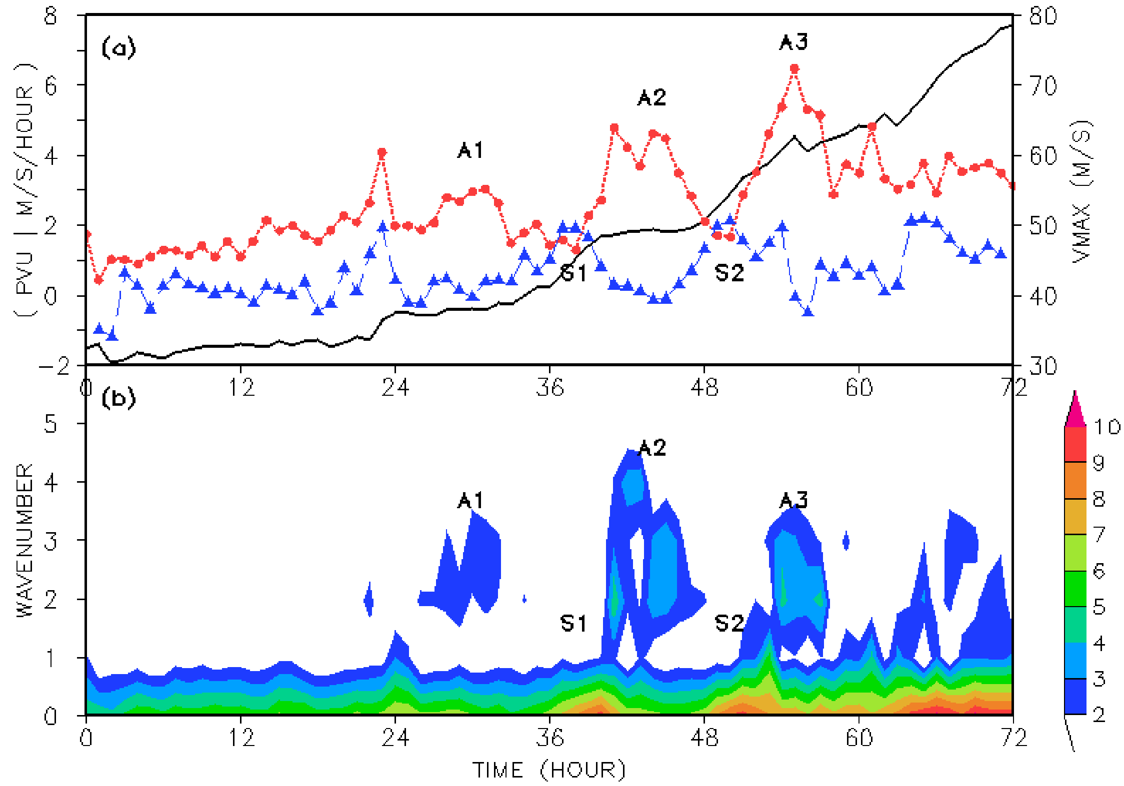

Figure 4.1: Evolution of PV asymmetries at 850 hPa. (a) SDPVmax (dotted pink line with circles, unit = $[PVU]$), maximum mean tangential wind (black solid line, $[ms^{-1}]$), and the tendency of the mean tangential wind (dashed blue line with triangles, $[ms^{-1}hour^{-1}]$). (b) Amplitudes of azimuthal wavenumbers from 0 to 6 of PV (unit [PVU]) at the 50 km radius. Note that 0 h corresponds to 00UTC 26 August 2008, which is 24 h prior to the base time.

During the period from about 26 h to 60 h, the PV vacillates between highly symmetric and highly asymmetric states. The asymmetric and symmetric phases are defined by the times at which the vortex attains its local maximum or local minimum, respectively, as measured by SDPVmax (see the red line with filled circles in Figure 4.1a). Note that in Chapter 3, a value of 4 PVU for the SDPVmax is defined as the threshhold, above which the vortex is considered to be in an asymmetric phase. Accordingly, E5C has two vacillation cycles from 39 to 51 h and 51 to 59 h (i.e. from 15 to 27, and 27 to 35 h as in Table C.3 and Appendix C). However, spectral analysis of PV (shown below) reveals that there is an early episode with increased asymmetries of wavenumber 2 and 3 at 31 h while the SDPVmax is less than 4 PVU. This episode is, therefore, identified here as an asymmetric phase. Thus, in this simulation, the asymmetric phases occur at 31 h, 44 h and 54 h from the start of the integration, and persist for three to four hours. These phases are subsequently referred to as A1, A2 and A3, respectively. The symmetric phases attain their maxima at 39 h and 50 h and are shorter, lasting one to two hours. These phases are referred to as S1 and S2, respectively.

In Figure 4.1a, the asymmetry (dotted pink line with circles) appears to be associated with the rate of intensification of maximum tangential wind (the blue line with triangles). During the period from 31 h to 54 h (or during two cycles from A1 to A3) when the vacillation is clearly evident, the correlation coefficients between SDPVmax and the acceleration of the maximum tangential wind is relatively high (-0.7). During shorter time periods the correlation is even larger, reaching -0.94 from 39 h to 50 h (or one cycle from S1 to S2); and -0.92 from 44 h to 54 h (one cycle from A2 to A3).

The vacillation between symmetric and asymmetric states is reflected in the amplitudes of different azimuthal wavenumbers defined by a Fourier decomposition of PV at 850 hPa. As depicted in Figure 4.1b, the asymmetric phases (A2 and A3) are associated with an increase in the amplitudes of wavenumbers 2 to 4. This increase occurs shortly after the peaks in the amplitude of the symmetric component (wavenumber 0) at 39 h (S1) and 50 h (S2).

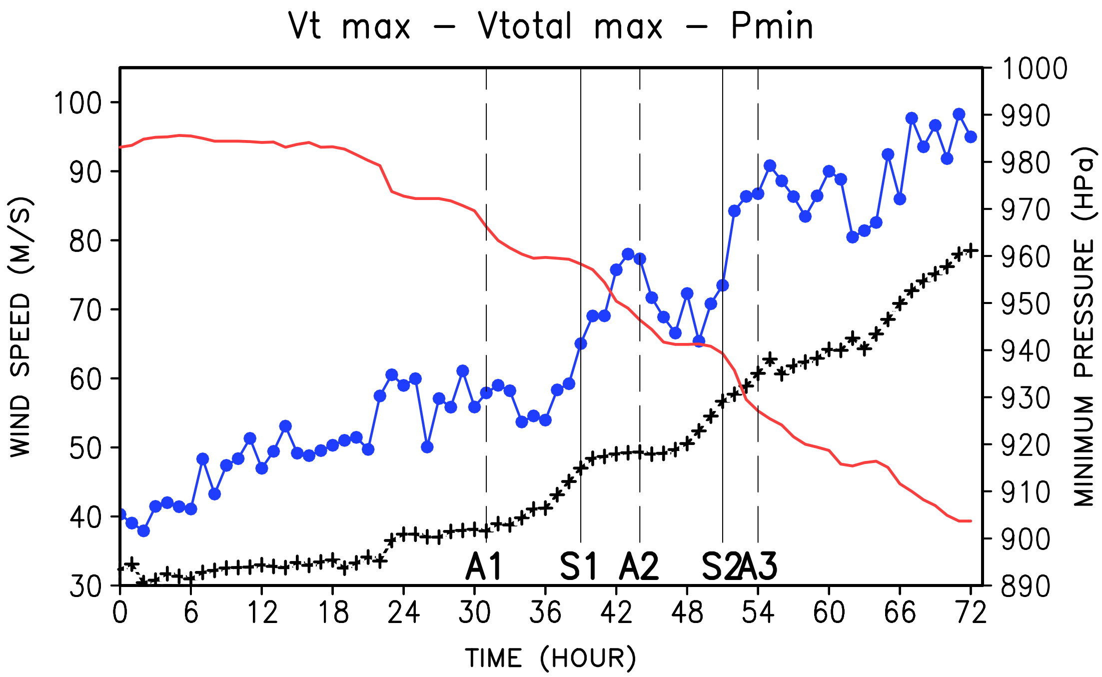

Figure 4.2: Evolution of maximum mean tangential wind at 850 hPa (black line with crosses), maximum total wind (blue line with circles) and minimum surface pressure (red line).

Figure 4.2 shows the evolution of maximum mean tangential wind at 850 hPa (as in Figure 4.1), the maximum total wind speed in the whole three-dimension domain, and the minimum surface pressure. During the symmetric phase, both maximum mean tangential wind and maximum total wind speed increase rapidly, reaching a local maximum during the asymmetric phase. During the latter, the intensification rates of maximum mean tangential wind and maximum total wind are nearly zero[1]. Therefore, the symmetric phase can be considered as the intensifying phase, and the asymmetric phase as non-intensifying, with respect to maximum wind. In contrast, the evolution of the minimum surface pressure indicates that minimum surface pressure decreases at a faster rate during the asymmetric phase and stays almost unchanged during the symmetric phase. Therefore, from the perspective of minimum pressure, one may also identify the asymmetric phase as the intensifying phase and the symmetric phase as non-intensifying. Nevertheless, since maximum wind is a direct measure of TC's distructive power, we choose to use maximum wind to identify a phase as either intensifying or non-intensifying.

The idealized studies by Zhu et al. (2001) and Nguyen et al. (2002) classified the intensification into three stages: the gestation stage, the rapid intensification stage, and the mature stage. A similar classification is used here. During the gestation stage, the vortex spins down slowly due to friction, but surface fluxes moisten the boundary layer and the moisture is carried inwards by the frictionally-induced inflow. The rapid intensification stage begins when deep convective structures are initiated in the inner-core region. Finally, the mature stage is achieved once the vortex developes a well-defined eye which is enclosed almost completely by eyewall cloud. Based on the evolution of the maximum mean tangential wind (the solid black line in Figure 4.1a), and the vortex structure, we define these three stages of the E5C simulation approximately as the periods 0-22 h, 22-60 h and 60-72 h, respectively. Note that the symmetric-asymmetric cycles described above are evident only during the rapid intensification stage, not during the mature stage. The next section is focused on the two phases during the rapid intensification stage.

Numerically simulated tropical cyclones typically go through a gestation stage during which the vortex slowly spins down before it intensifies. This raises the question as to whether the evolution of the simulated vortex during rapid intensification

[1] The maximum total wind speed decreases after the asymmetric phase, reaching a local minimum prior to the following symmetric phase, whereas the maximum mean tangential wind maintains the same value during this period. The occurence of maximum total wind speed during the asymmetric phase and decrease afterwards is associated with strong convective elements, namely VHTs, which will be shown in the next sections to occur during this phase.

is an artifact of the way in which the numerical model is initialized. TCLAPS has demonstrated significant skill in predicting the intensity of tropical cyclones under different conditions (Davidson and Weber, 2000) as well as in the ensemble members of hurricane *Katrina*'s simulation as shown in Chapter 3. Moreover, as shown by statistics from the Atlantic basin (DeMaria and Kaplan, 1994), in the real world rapid intensification tends to occur in weak storms, which are similar to the stage of the simulated vortex being analysed. For these reasons, it is likely that the internal dynamics simulated by TCLAPS, including the vacillation, have parallels in real TCs and Hurricane *Katrina* in particular.

Role of vertical wind shear

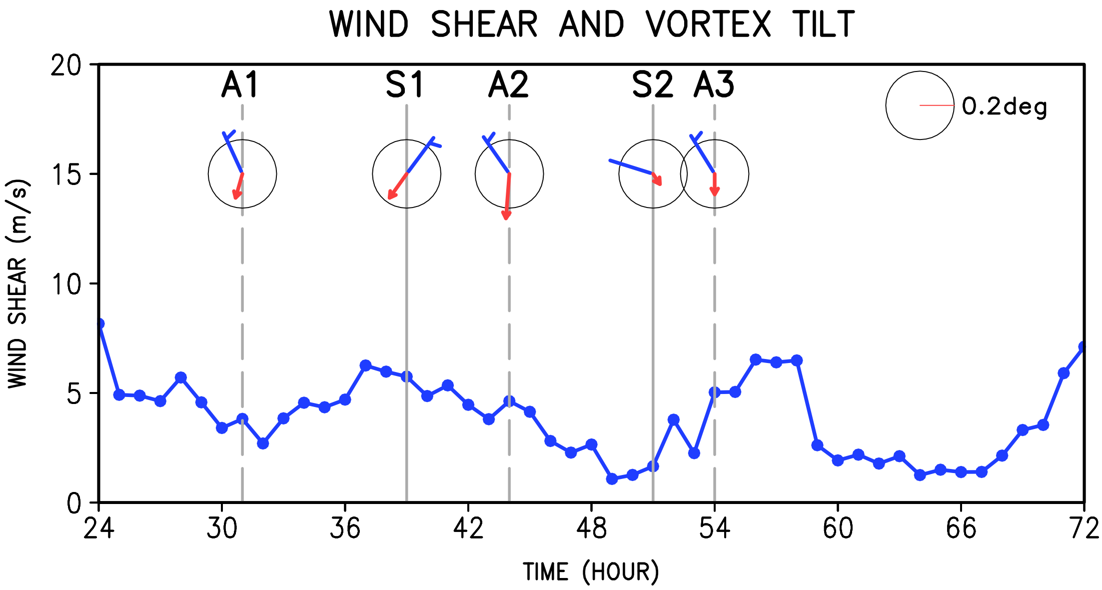

Figure 4.3: Evolution of environmental wind shear ($\vec{V}_{shear} = \vec{V}_{200} - \vec{V}_{850}$) and the vertical tilt of the vortex. Windshear vectors and their magnitude are shown by blue wind barbs and the solid blue line with circles, respectively. Red vectors represent the vertical tilt of the vortex: the base is the position of TC center at the surface; the point is the TC center at the 500 hPa level. Circles indicate a scale of 0.2 degree for tilt vectors.

As suggested by several studies, asymmetries may arise from vertical shear of the horizontal environmental wind, which tilts the vortex and provides favourable conditions for convective development in the downtilt-right side of the eyewall (see e.g. Black et al., 2002, Rogers et al., 2003, Zhu et al., 2004, Braun et al., 2006). Therefore, we investigate next the evolution of the environmental wind shear and the vertical tilt of the vortex center to see if the observed vacillation pattern in PV asymmetries is associated with changes in the environmental shear.

Figure 4.3 shows the evolution of the environmental windshear calculated as the difference between 200 hPa and 850 hPa. The environmental winds are defined here as the average over a 200 km radius from TC center. As can be seen from Figure 4.3, throughout the period of interest the environmental vertical windshear is relatively small (less than 7 m s^{-1}) and is not associated with the defined symmetric-asymmetric phases. Accordingly, the vertical tilt of the vortex center is small with the distance between the centers at the surface and 500 hPa not greater than 0.2 degrees. On the other hand, as shown by Black et al. (2002), Rogers et al. (2003), Braun et al. (2006), the asymmetries induced by environmental windshear project onto wavenumber 1, which is not large in our simulation (see Figure 4.1b). Therefore, the evidence suggests that the vacillation pattern of PV asymmetries in the simulation is not associated with changes in the environmental vertical wind shear.

4.2 Vortex structure during the two phases

This section documents the structure of the tropical cyclones during the two phases of the rapid intensification stage.

4.2.1 Dynamical fields

Velocity

Sections of the vertical velocity at 850 hPa at the times of maximum symmetry S1 and S2, and maximum asymmetry A2 and A3 are shown in Figures 4.4. These times are representative of the symmetric and asymmetric phases. During the symmetric phases (panels a and c), the eyewall has a ring-like form consisting of elongated bands of moderately strong updrafts, although there are still noticeable asymmetries. In contrast, during the asymmetric phases (panels b and d), the eyewall has a triangular shape with three intense updrafts at the vertices. These updrafts have enhanced rotation and are essentially VHTs, which are described earlier in Section 1.2.5. As will be shown later in Figure 6.5, these strong updrafts are associated with positive PV anomalies, and thus can be considered as VHTs.

The contours of low-level horizontal wind speed (thin grey contours in Figure 4.5) do not exhibit significant differences between the two phases apart from an intensifying trend of the main vortex. However, the structure of local extrema of

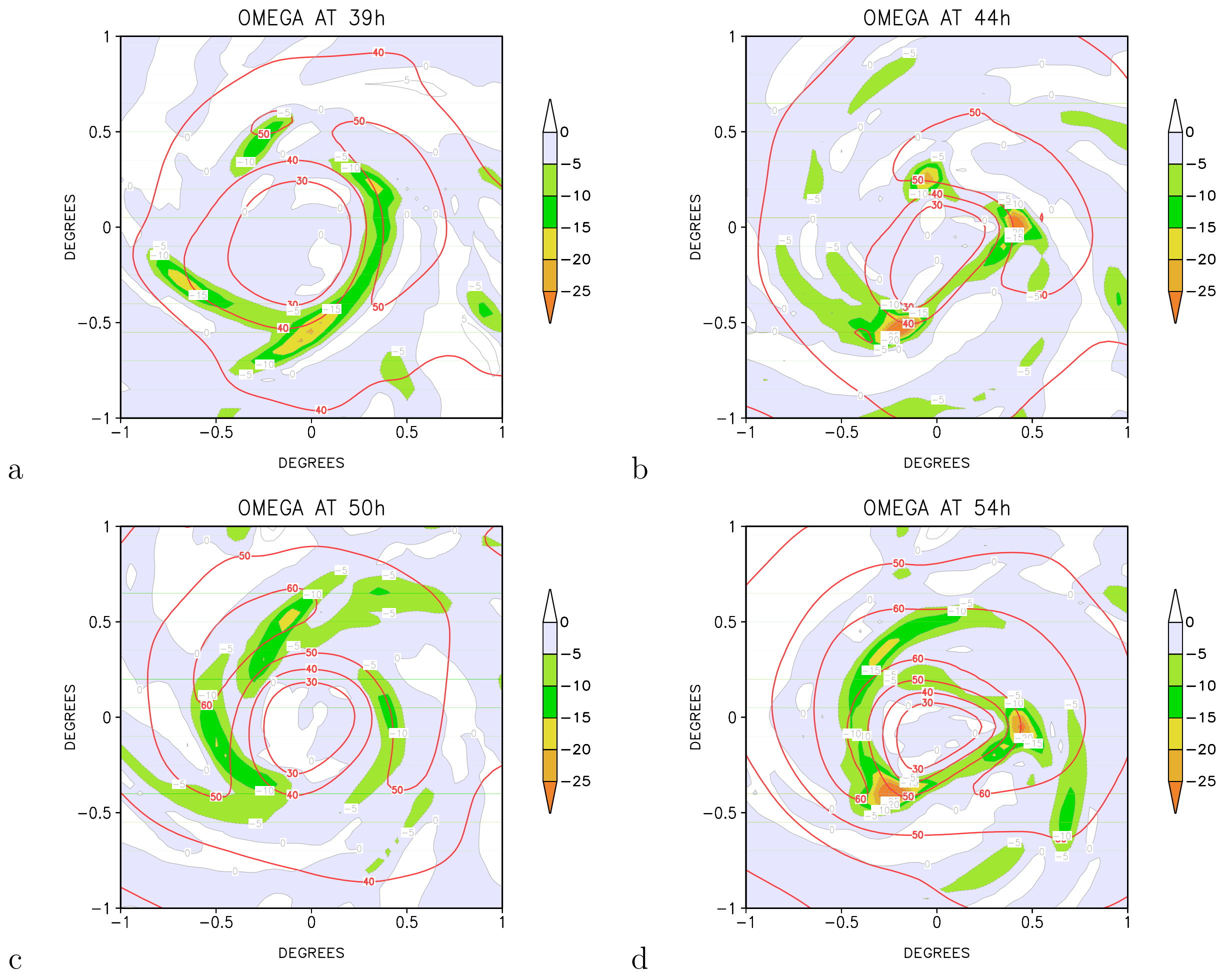

Symmetric phase **Asymmetric phase**

Figure 4.4: Vertical velocity (areas with upward motion are shaded, unit [Pa s^{-1}]) overlayed with the horizontal wind speed (red thick solid contours, unit [m s^{-1}]) at the 850 hPa level. Left panels (a,c) show S1 and S2, respectively. Right panels (b,d) show A2 and A3, respectively.

horizontal wind speed shown by its Laplacian $(-\nabla^2 V_{mag})^2$ indicates remarkable differences during the symmetric and asymmetric phases (shaded in Figure 4.5). It can be seen from this figure that local maxima in horizontal wind speed occur near the vertical velocity maxima during asymmetric phases (b and d). Accordingly, the structure of surface latent heat fluxes, shown in Figure 4.6, and the θ_e at the model lowest level (shown later in Figure 4.12) have high values near the locations of VHTs.

During the asymmetric phase, the local maxima of vertical velocity within the eyewall (i.e. VHTs) are accompanied by local maxima of horizontal wind speed, surface latent heat fluxes and the θ_e at the model lowest level. The colocation of these thermodynamical characteristics near the VHTs is not coincidental, but

[2]See Appendix B for the justification for the use of Laplacian.

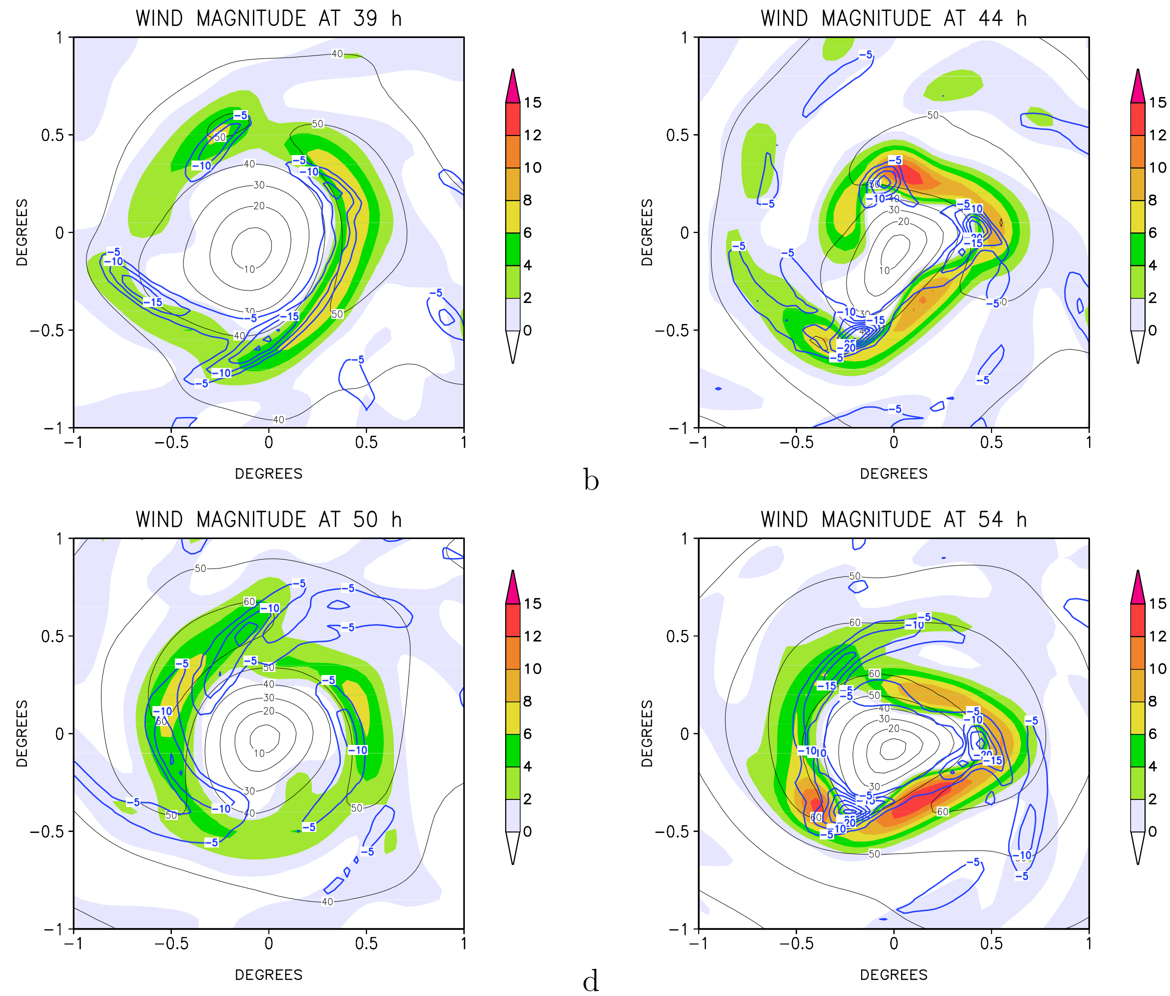

Symmetric phase **Asymmetric phase**

Figure 4.5: Horizontal wind magnitude (thin contours, unit $[ms^{-1}]$). Local anomalies of wind magnitude as represented by $-\nabla^2 V_{mag}$ (shaded, unit $[10^{-8}\times$ m s $^{-1}]$). Vertical velocity (blue solid contours, [unit Pa s^{-1}]) at the 850 hPa level. Left panels (a,c) show S1 and S2, respectively. Right panels (b,d) show A2 and A3, respectively.

rather, an indication of a positive feedback interaction between surface fluxes and convective circulations. That is, bursts of enhanced vertical motion increase the surface wind speed in the vicinity as air is drawn in, replacing the uplifted mass. In turn, increased wind speeds near the surface enhance the surface latent heat fluxes, increasing θ_e at low levels. As a result, the atmosphere becomes more conditionally unstable, and thus, induce stronger convection, i.e. enhanced updraft.

The above process resembles the WISHE mechanism (which is introduced earlier in Section 1.1.2) that occurs at the convective scale. Note that the duration of this positive feedback process may be small as the cooling downdraft associated with the convective precipitation decreases the θ_e at low levels, and thus, may interupt the

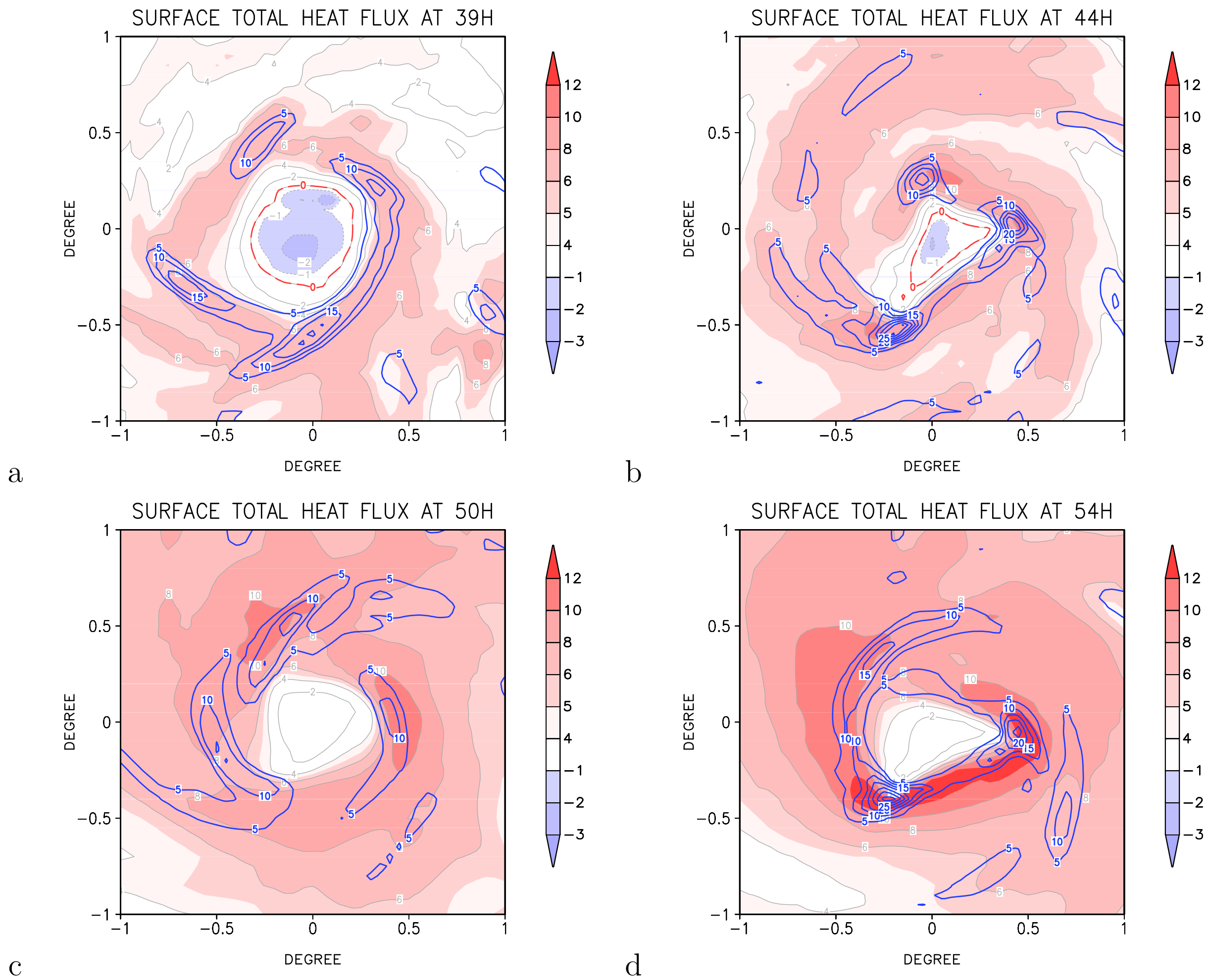

Symmetric phase **Asymmetric phase**

Figure 4.6: Total surface heat flux [$10^2 \times$W m^{-2}] during phases a) S1, b) A2, c) S2, d) A3. Blue contours are vertical motion at 850 hPa.

whole process. This counter effect of the cooling downdraft by precipitation is likely to present in ordinary oceanic thunderstorms as well as in TCs. However, the manifestation of the local WISHE as seen in this simulation of Hurricane *Katrina* suggests that the strong cyclonic circulation of TCs may have a special dynamical mechanism that supports and maintains the local maxima of the dynamical properties. It will be shown later in Chapter 6 that barotropic instability is a possible explanation.

Potential Vorticity

The potential vorticity at 850 hPa is shown in Figure 4.7. There are prominent differences in the structure of the potential vorticity between the two phases which include: a ring structure with a maximum at some radius from the center during the symmetric phase (a and c), and a monopole structure with the maximum located

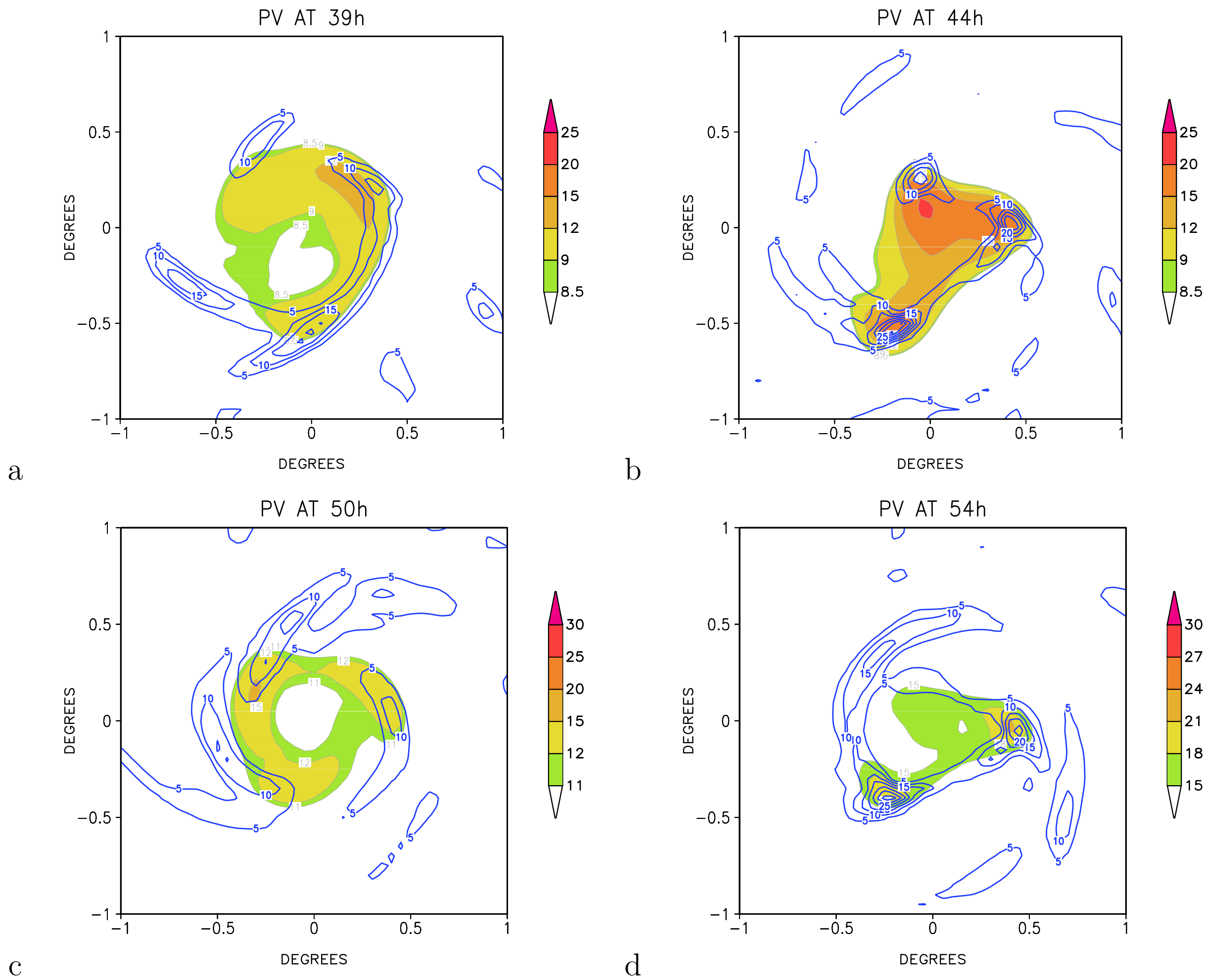

Symmetric phase **Asymmetric phase**

Figure 4.7: As for Figure 4.5 but for potential vorticity (high values are shaded, unit [PVU=10^{-6} m^{-2} s^{-1} K kg^{-1} Pa s^{-1}]).

near the vortex center during asymmetric phases (b and d). This configuration is similar to the two regimes identified in Kossin and Eastin (2001), with the symmetric phase corresponding to their Regime 1 and the asymmetric phase to their Regime 2.

These two distinct structures can be seen also in the mean azimuthal profiles of PV. Figures 4.8a and b show radial profiles of azimuthal mean PV and their corresponding radial gradients at the times of maximum symmetry during S1 and S2, and the times of maximum asymmetry during A1 and A2, respectively. Not only do these mean profiles have different shapes during the two phases, they also exhibit significant differences in their magnitude near the vortex center. Specifically, the vorticity near the center increases significantly during the asymmetric phases and decreases in the subsequent symmetric phases. It will be shown in Chapter 5 (Figure

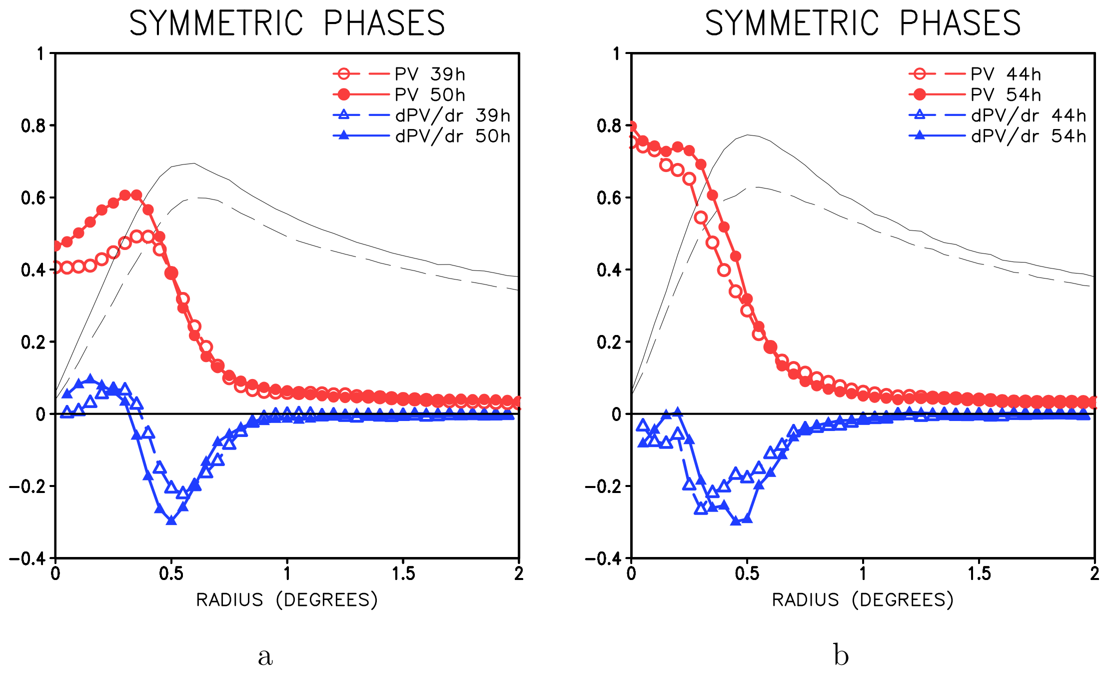

Figure 4.8: Mean PV (red lines with circles) and its radial gradient ($\frac{\partial PV}{\partial r}$) (blue lines with triangles) at times (a) S1, S2 and (b) A2 and A3 at 850 hPa. Grey thin solid lines show mean tangential wind. All variables are normalized to their maximum values achieved during the whole integration time, where: PV_{ref}= 20.7 PVU; $\left[\frac{\partial PV}{\partial r}\right]_{ref}$ =6.9 $\times$ 10^{-4} PVU m^{-1}; V_{ref} = 78.45 m s^{-1}. Here, the subscript *ref* indicates the maximum value achieved. The PV gradient is further reduced by a half to improve graphical presentation.

5.14) that the increase of the vorticity near the vortex center during the asymmetric phase is associated with the horizontal mixing effects of VHTs.

The ring structure of low level potential vorticity during symmetric phases indicates barotropic instability since the radial gradient of PV changes sign at some radius near the eyewall (see e.g. blue lines with triangles in Figure 4.8a). This barotropic instability is suggested by Kossin and Eastin (2001) as the cause for the breakdown of the eyewall during the transition from their Regime 1 to Regime 2. We will address this process in Chapter 6.

Shearing strain and strain dominated zones

Another property of the wind field is the difference between the strain rate and enstrophy (sometimes called the Okuba-Weiss parameter)D $=$ $S^2 - \zeta^2$, where ζ is the vertical component of relative vorticity, and S^2 is the square of total horizontal

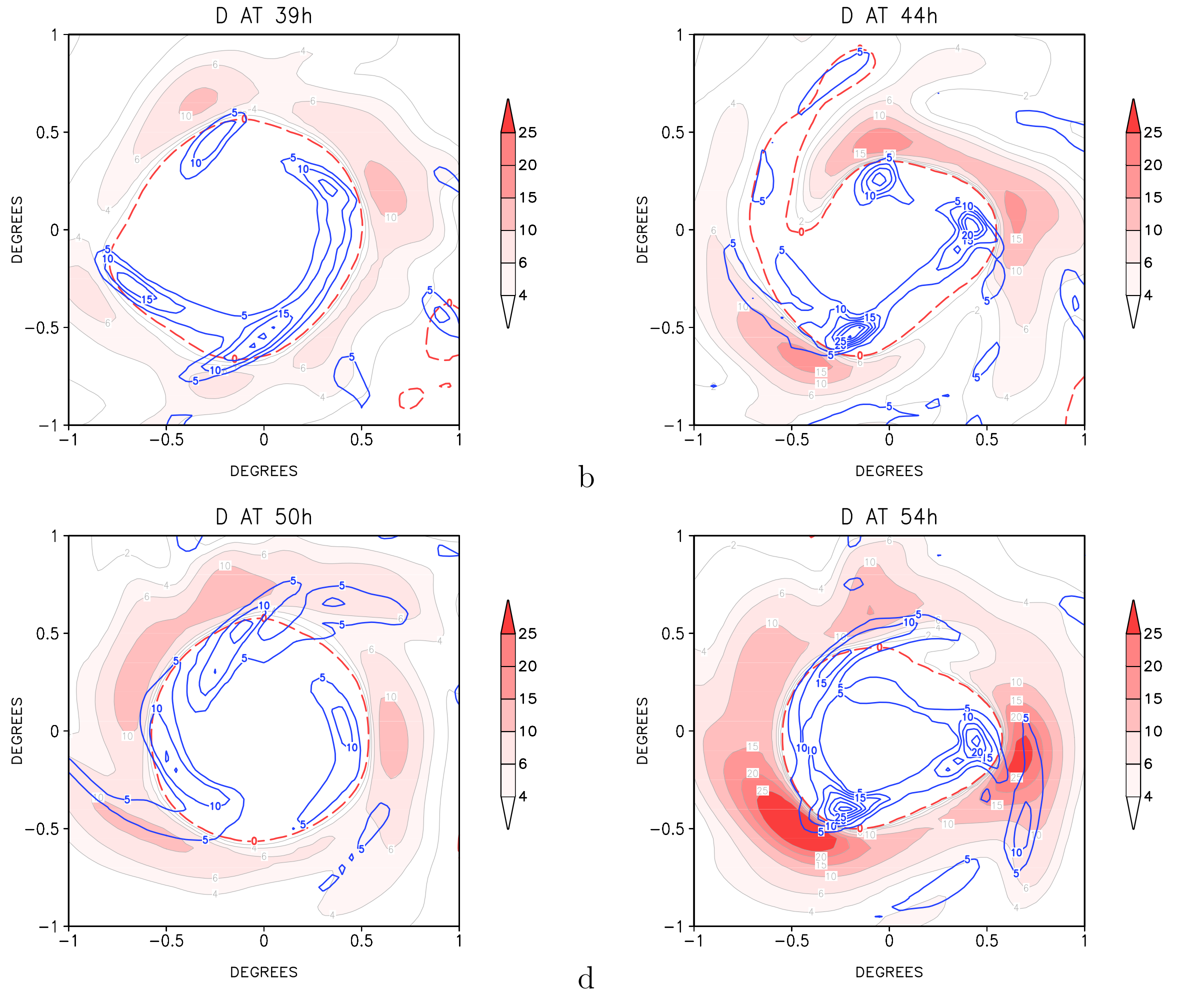

a b c d

Symmetric phase **Asymmetric phase**

Figure 4.9: As for Figure 4.7 but for the difference D between the strain rate and enstrophy at 850 hPa. Red shades show positive values (unit $[10^{-7}\times \text{ s}^{-2}]$), i.e. the strain dominated region where strain is greater than rotation. Dashed red contours are lines of zero D value, i.e. the boundary between the rotation dominated (inside the contours) and filamentation dominated (outside the contours) regions.

strain rates defined by:

$$S^2 = (E^2 + F^2) \;= \left(\frac{\partial U}{\partial x} - \frac{\partial V}{\partial y}\right)^2 \;+ \left(\frac{\partial V}{\partial x} + \frac{\partial U}{\partial y}\right)^2 \qquad (4.1)$$

As discussed by Rozoff et al. (2006), D is inversely proportional to the filamentation rate. These authors suggested that in the regions where the filamentation time scale ($\tau_{fil} = 2D^{-1/2}$, where $D > 0$) is less than the convective time scale (e.g. 30 minutes as in Rozoff et al. (2006)), the strong strain may mix growing convective elements before they reach maturity. In this so-called rapid filamentation zone, convective features and their induced cyclonic vorticity are likely to be quickly elongated, becoming thinner and eventually disappearing due to lateral diffusion. Rapid filamentation was thought first to be important in the formation of the moat areas in hurricances (Rozoff et al., 2006). However, later studies including those of Rozoff et al. (2008) and Wang (2008a) suggested that the rapid filamentation zone is less relevant in explaining the lack of convection within the moat. While Rozoff et al. (2008) indicates that the moat is governed by enhanced static instability associated with a strengthening outer eyewall, Wang (2008a) suggests the moat is associated with the overturning flow from eyewall convection and downdrafts from the anvil stratiform precipitation outside of the eyewall. Nevertheless, the suppressing effect of rapid filamentation on convection is still commmonly accepted (see e.g. Terwey and Montgomery, 2008).

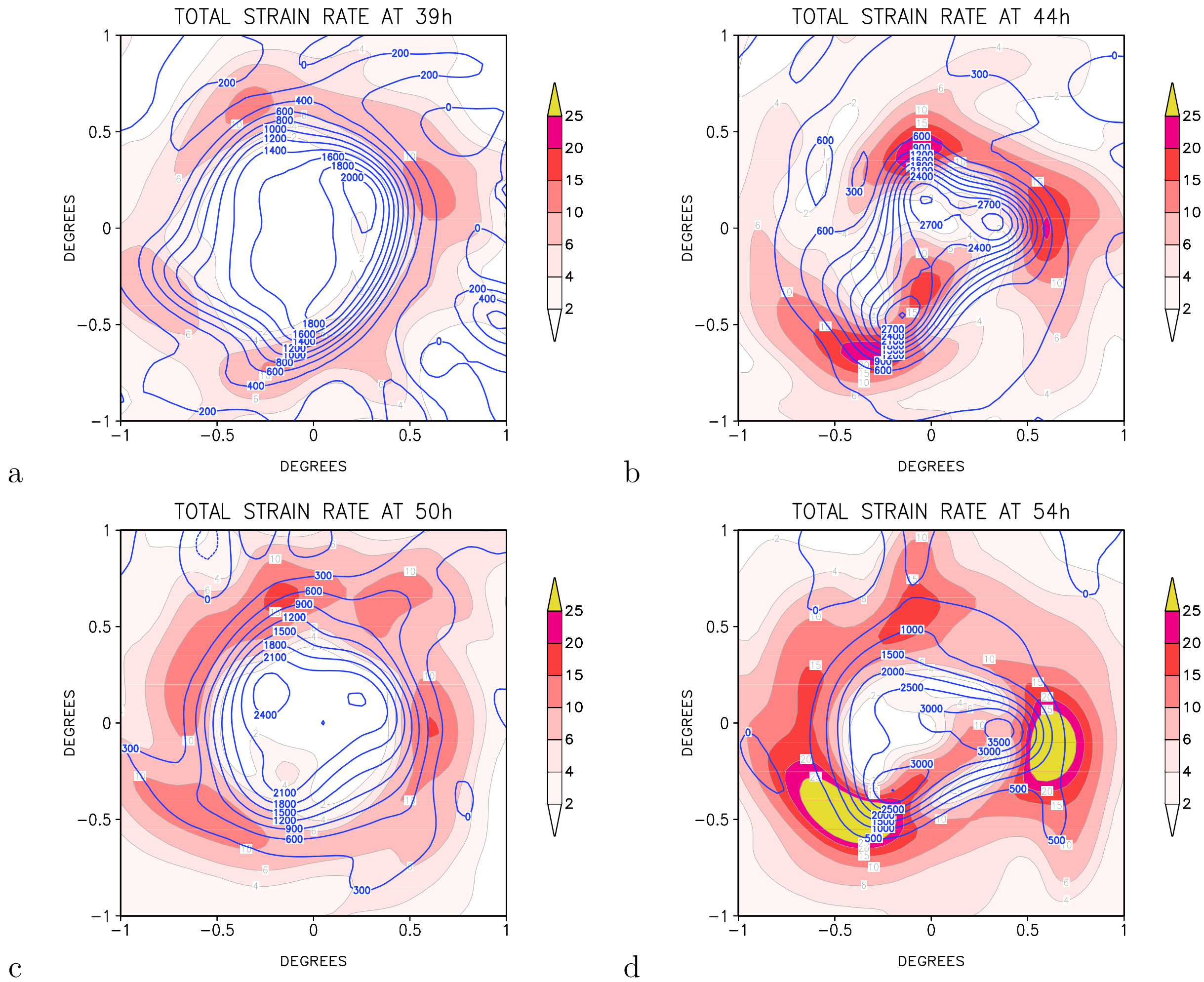

Symmetric phase **Asymmetric phase**

Figure 4.10: As for Figure 4.7 but for total strain rates (S^2=E^2+F^2, unit [$10^{-7}\times$ s^{-2}]). Blue contours are relative vorticity (ζ, unit [$10^{6}\times$ s^{-1}])

Rapid filamentation has been shown to damp asymmetries in wavenumbers greater than four (Wang, 2008a), whereas Terwey and Montgomery (2008) suggest that the development of convection outside of the main eyewall, and thus, the formation of the secondary eyewall requires (in conjunction with other conditions) the level of filamentation to be at most moderate, corresponding to the τ_{fil} greater than 30 minutes.

Figure 4.9 shows that values of D in the strain-dominated region outside the RMW is much stronger during asymmetric phases (panels b and d) than during symmetric phases (panels a and c). During the period from 39 to 54 h, despite the typical increasing trend of strain associated with the strengthening main vortex, the regions immediately outside of the VHTs at the asymmetric phase A2 at 44 h (Fig. 4.9b) have larger values of D than during the subsequent symmetric phase S2 at 50 h. Larger strain rates imply stronger stirring and consequently less favourable conditions for convection to develop.

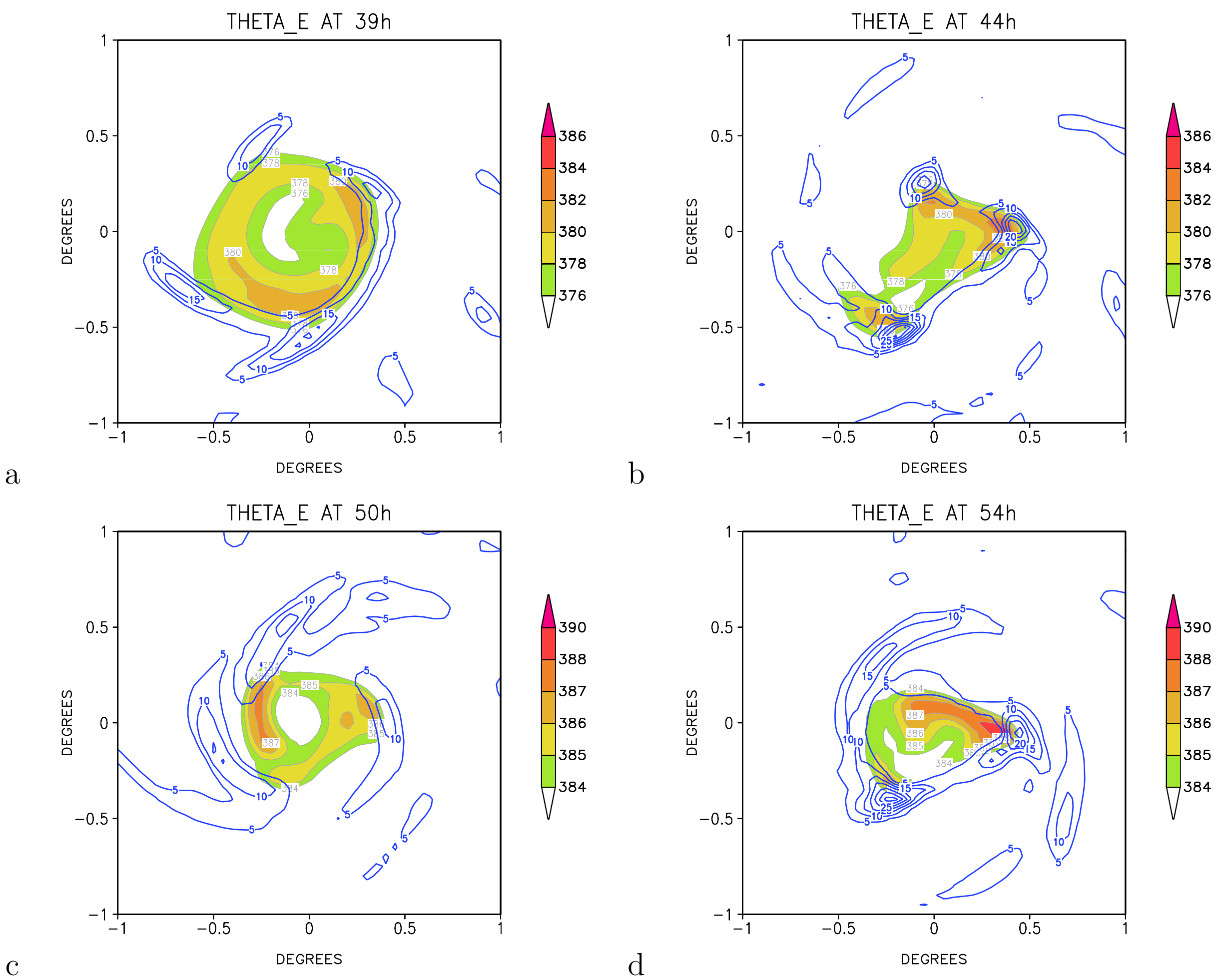

Symmetric phase **Asymmetric phase**

Figure 4.11: As for Figure 4.7 but for equivalent potential temperature θ_e [K] (high values are shaded) at 850 hPa.

The fields of total strain rates, shown in Figure 4.10, are noticeably different in the two phases. During the symmetric phases, the region inside of the eyewall has low strain rates (panels a and c). Conversely, during the asymmetric phases A2 and A3 (panels b and d), the region inside of the eyewall are strongly stirred (shaded areas inside of the eyewall). During this time, large strain (shaded areas in Figures 4.10b and d) in the core region is collocated with strong rotation (contour of relative vorticity in Figures 4.10b and d). Thus, the vorticity is mixed effectively in the region between the eye and the eyewall. Note that the term 'mixing' used throughout this thesis is not the small scale mixing due to horizontal diffusion. Rather, 'mixing' is used to indicate the horizontal advection and deformation occuring in resolved entities, such as mesoscale vortices inside of the eyewall in this case. The term 'stirring' is sometimes used to describe such small scale transport (Haynes, 1999)

4.2.2 Thermodynamical fields

Equivalent Potential Temperature

Figure 4.11 shows the equivalent potential temperature θ_e at 850 hPa. Once again, the two phases exhibit distinctive patterns: the ring structure is evident during symmetric phases and the monopole structure during the asymmetric phases. Thus, θ_e structure is consistent with the two regimes described in Kossin and Eastin (2001).

Figure 4.12 shows the equivalent potential temperature θ_e at the lowest model level. In contrast to 850 hPa, θ_e has the monopole structure throughout the whole simulation at the lowest model level. Nonetheless, there are clear differences between the two phases. During symmetric phases (a, c) the core of high θ_e has a relatively more circular shape which covers a larger area and higher maximum values at the center. This can be seen by comparing the areas having values of θ_e, say arbitrarily, greater than 400 K in Figure 4.12. In contrast, during asymmetric phases the core of high θ_e near the center is deformed into a polygonal form with decreased values near the vortex center. VHTs are located at the vertices of the high θ_e core, and thus, still have access to the air with high moist entropy.

Figure 4.13 shows the tendencies of the θ_e at the lowest model level due to horizontal advection $[-(u\partial\theta_e/\partial x + v\partial\theta_e/\partial y)]$. The decrease in the θ_e near the vortex center during the asymmetric phase is associated with horizontal advection, which is connected with mesoscale circulations of the VHTs near the vortex center (note the negative tendencies due horizontal advection). This can be seen as stronger negative tendencies occuring in the core region during the asymmetric phases (panels b and

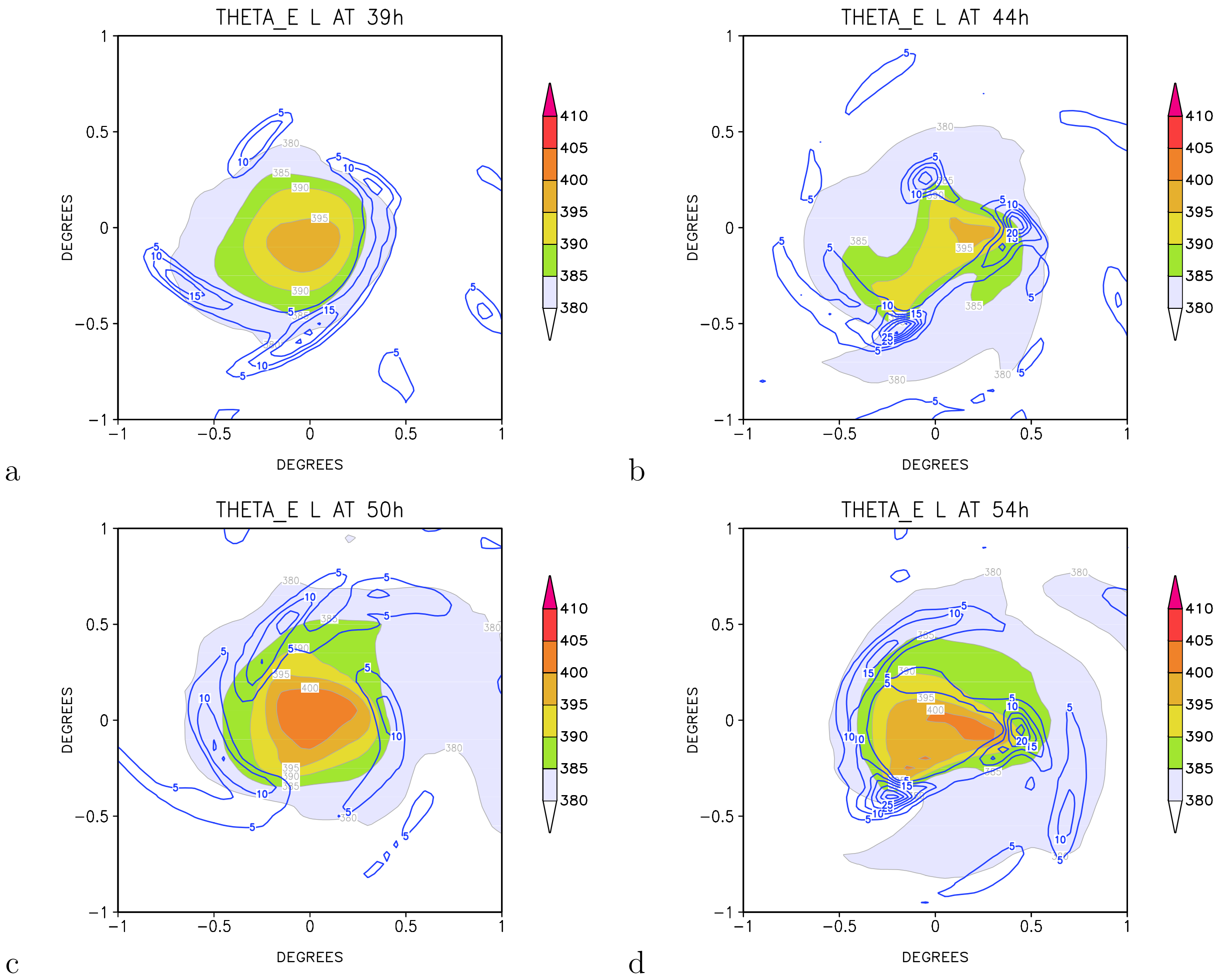

Symmetric phase **Asymmetric phase**

Figure 4.12: As for Figure 4.7 but for equivalent potential temperature θ_e [K] (high values are shaded) at the lowest model level.

d) compared with the symmetric phases (panels a and c).

On the other hand, the core restores its high values of θ_e during the symmetric phase due to two reasons: 1) the core is continuously fed by surface heat fluxes, and 2) less dilution by lateral mixing with the air of lower θ_e from outside since the mesovortices associated with the VHTs are weakened.

Convective Available Potential Energy

The behaviour of convection is known to be influenced by the Convective Available Potential Energy (CAPE). Since the convective VHTs play important roles during the asymmetric phase, it is instructive to examine the distribution of CAPE during

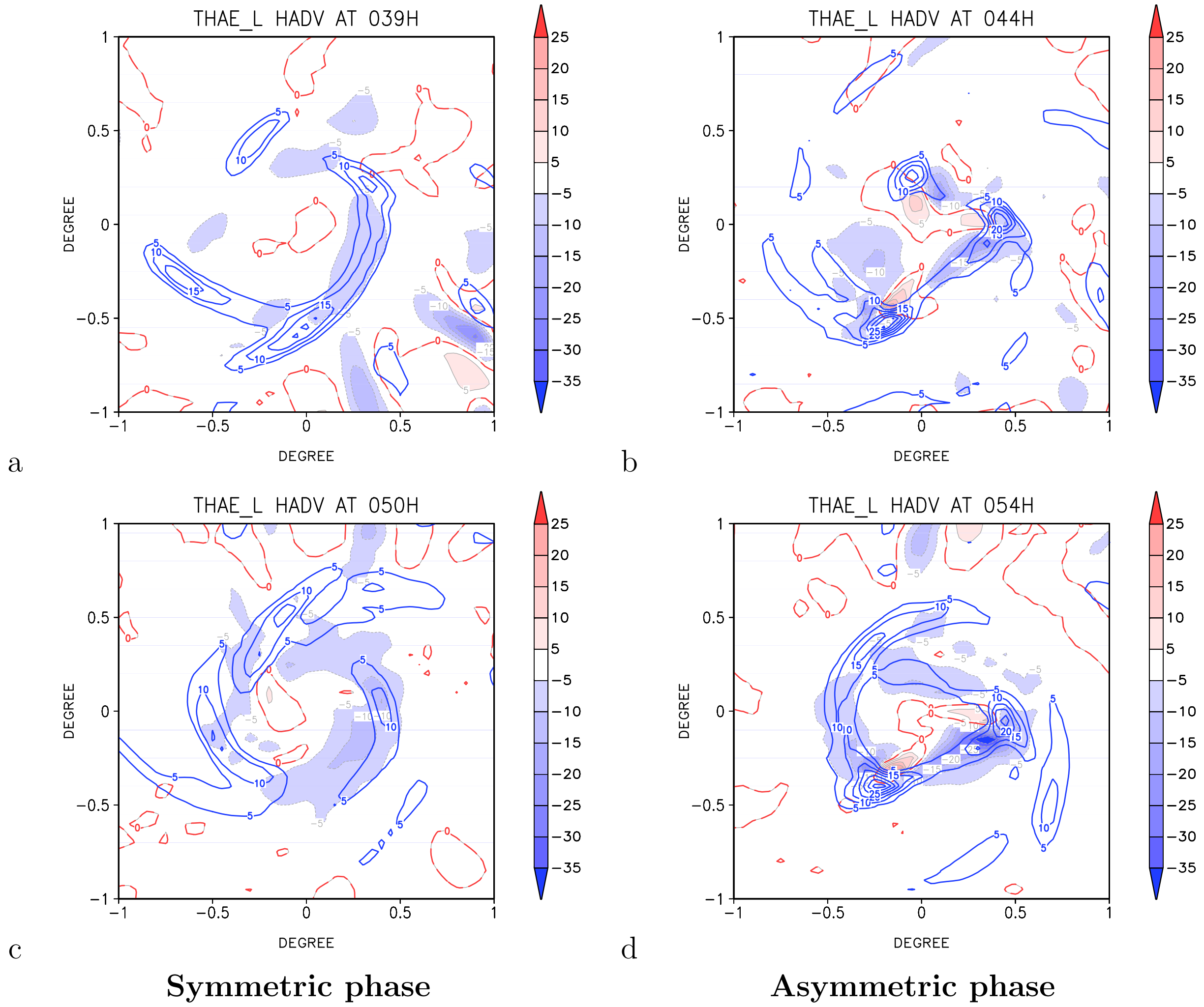

Figure 4.13: Tendencies of the θ_e [$10^{-3}\times$ K s^{-1}] at the lowest model level due to horizontal advection [$-(u\partial\theta_e/\partial x + v\partial\theta_e/\partial y)$] at times a) S1 at 39 h, b) A2 at 44 h, c) S2 at 50 h, and d) A3 at 54 h. Dashed red contours mark the zero isoline of the tendencies. Blue contours show vertical motion at 850 hPa.

the two phases. Figure 4.14 shows the distribution of CAPE[3] during symmetric and asymmetric phases. Although the distribution of CAPE reflects the main features of low-level θ_e fields, including a core with high values corresponding to a high entropy core as described above, we highlight here the regions with low CAPE (shaded in Fig. 4.14) as there have a lower potential for convection.

The areas of relatively low CAPE are associated with regions of active convection are displaced slightly towards the outer part of the convective cores. These relatively low CAPE areas reflect the stabilization of the atmosphere as the VHTs

[3] CAPE is calculated using a modified version of 'plotskew.gs', a script to plot SkewT-LogP diagrams. This script is kindly provided by Bob Hart, from Pennsylvania State University, and is shared with the Grid Analysis and Display System (GrADS) users community.

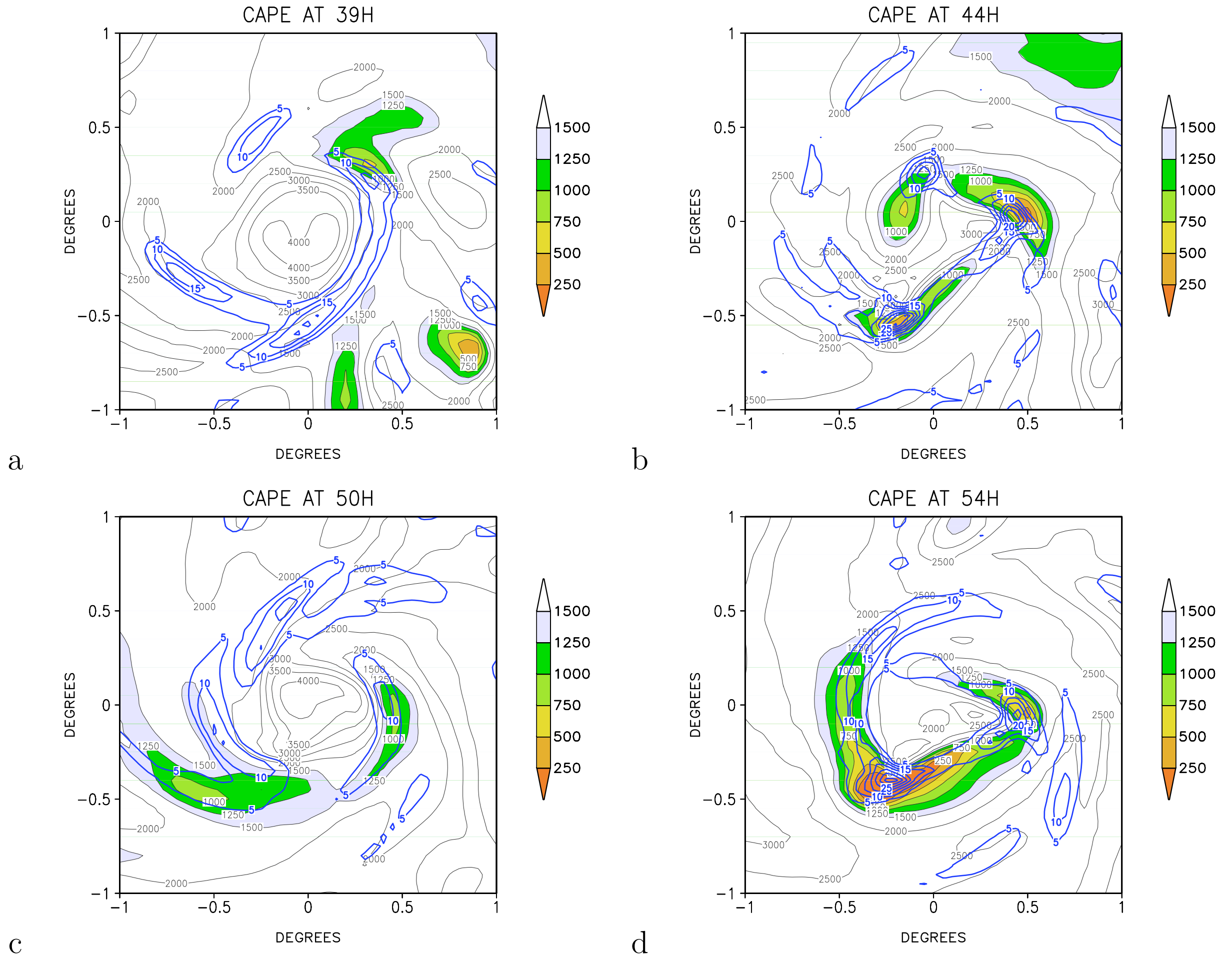

Symmetric phase **Asymmetric phase**

Figure 4.14: As in Figure 4.7 but for Convective Available Potential Energy (CAPE). Values lower than 1500 J kg^{-1} are shaded.

rapidly use the available energy. Thus, much lower values of CAPE are found near the VHTs during the asymmetric phases (Figs. 4.14b and d d) than those associated with the convective bands during the symmetric phases (e.g. Fig. 4.14 a and c). During the asymmetric phases the outer side of the VHTs has relatively low CAPE whereas the inner side is connected with the polygonally-shaped high CAPE core. Thus, the VHTs are supported by sources of convective instability. It will be shown in Section 4.3 that, in contrast, during the mature stage, the eyewall is embedded wholly inside the regions of low CAPE.

Not only is the eyewall exhausted of CAPE by vigourous convection in VHTs, the eye of the TC experiences also a noticeable CAPE decrease during the asymmetric phase (see contour values in the core regions of Figure 4.14). Specifically, point values of CAPE at the vortex center are 3830 and 4163 Jkg^{-1} during the symmetric phases S1 and S2, compared with their counter part of 2400 and 1864 Jkg^{-1} during the asymmetric phases A2 and A3, respectively (see values in Figures 4.16).

While the decrease of CAPE near the vortex center during the asymmetric phase is consistent with the decrease of low level θ_e as described above, the CAPE is proportional to the vertical integral of the parcel buoyancy and consequently its value is affected by changes above the surface also. As will be shown in the next section, a stronger warm core aloft (say above the 500 hPa level, see Figure 4.15 later) and the temperature increase in the 500-700hPa layer (refer to Figure 4.16) also contribute to a more stable stratification, and hence lower CAPE, during the asymmetric phases.

4.2.3 Vertical structure of the mean fields

In this section, the azimuthally-averaged structure of the vortex during the two phases identified in the 850 hPa fields is examined.

Mean vertical velocity and pertubation temperature

Figure 4.15 shows the vertical structure of the mean vertical velocity and the perturbation temperature during the symmetric and asymmetric phases. The perturbation temperature is defined as the difference between the core temperature and the mean temperature at the 300 km radius, $T_{warmcore} = T - T_{300km}$. As the vortex intensifies, ascent in the eyewall strengthens and a pronounced warm core in the middle troposphere (maximum is in the 300-400 hPa layer) develops. However, noticeable differences are present during the two phases.

During the symmetric phase (Figure 4.15a and c), the eyewall tends to be more tilted outward with the strongest updrafts below 400 hPa. In contrast, the eyewall during the asymmetric phase (Figure 4.15b and d) is more upright, and more intense with the maxima located at higher levels (near 200 hPa at 44 h, and in the 300-400 hPa layer at 54 h). The mean downward motion near the vortex center is slightly more intense during the asymmetric phase. Similarily, the region with downward motion just outside of the eyewall occupies a larger area and is located closer to the center during the asymmetric phase. Thus, this stronger downward motion during the asymmetric phase is consistent with the more intense upward motion in the eyewall, which would induce stronger compensating downward motion.

The structure of the warm core (as marked by the shaded areas in Figure 4.15) during the two phases is consistent with the mean vertical velocity described above.

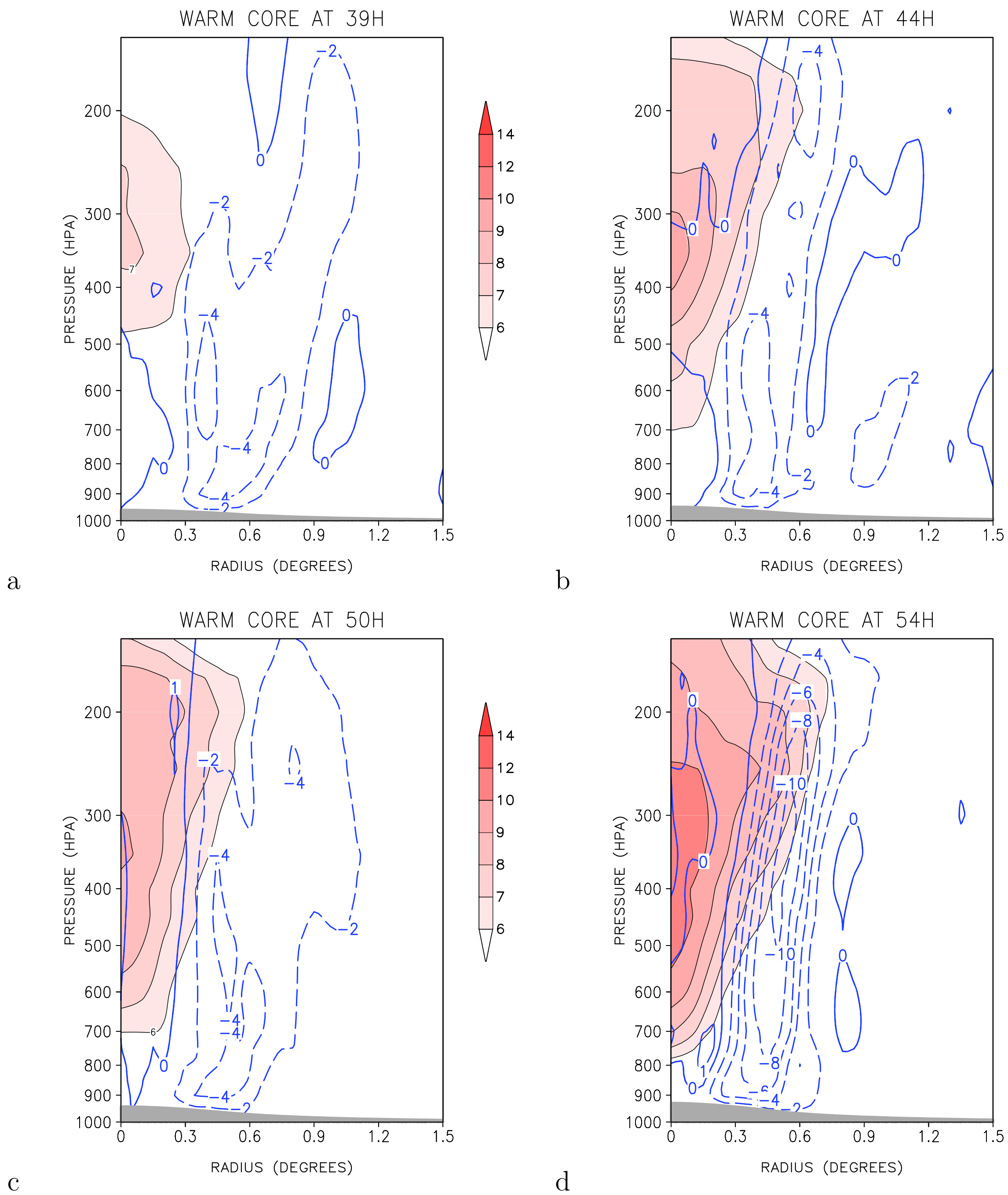

Symmetric phase **Asymmetric phase**

Figure 4.15: Temperature perturbation (shaded), defined by the difference between azimuthal mean of temperature and the temperature of the same pressure surface at the 300 km radius [K]. Mean vertical motion [Pa s^{-1}] is shown by blue contours. Dashed lines represent negative values and hence upward motion. Left panels (a,c) are the symmetric phases (S1 and S2). Right panels (b,d) are the asymmetric phases (A2 and A3).

During the symmetric phase, the warm core extends to smaller radii, but is distributed relatively evenly in a deep layer. In contrast, during the asymmetric phase

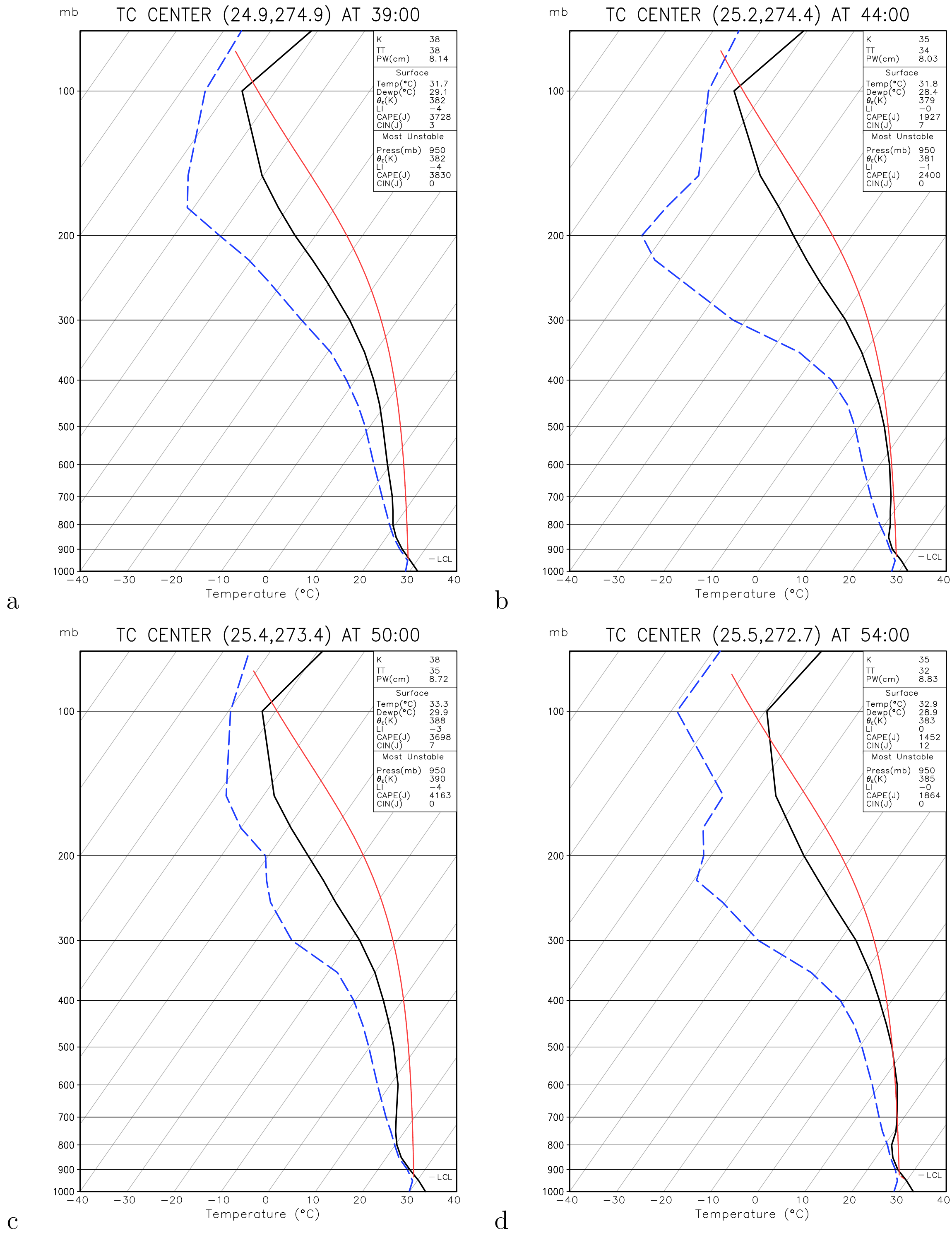

Symmetric phase **Asymmetric phase**

Figure 4.16: SkewT-LogP diagrams of the temperature and dewpoint temperature profiles at the vortex center during symmetric phases S1 and S2 (a and c, respectively) and the asymmetric phases A2 and A3 (b and d).

(b and d), the warm core is more intense and extends to a larger radius, which is consistent with the stronger compensating downward motion in response to larger upward motion in the eyewall.

Figure 4.16 shows vertical profiles of the temperature and dewpoint at the vortex center during the two phases. During the asymmetric phase (b and d), the stronger downward motion near the center of the vortex produces a large dew point depression (as shown by large distance between temperature and dewpoint temperature lines) in the upper part of troposphere, as well as higher temperatures compared with the symmetric phase (a and c). At lower levels, the temperature in the 500-700 hPa layer is significantly higher during the asymmetric phase. As will be shown in Appendix E, the mid-tropospheric temperature increases near the center during asymmetric phase are associated primarily with horizontal advection by eyewall mesovortices which are explicitely resolved by model dynamics. Thus, decrease of θ_e at the lowest model level in conjunction with the temperature increase above explains the decrease of CAPE near the vortex center during the asymmetric phase.

Potential Vorticity

Vertical cross sections of the azimuthally averaged PV fields (Figure 4.17) reveal that during both phases, the middle levels (say between 700 hPa and 500 hPa) have a monopole structure, in which the PV has its maximum value at the center, decaying monotonically with radius. In contrast, upper levels (above 500 hPa) and lower levels (below 700 hPa) vacillate between the monopole structure and the ring structure[4]. In addition, during each phase, the PV structure at lower levels is in the opposite phase of that at upper levels. For example, while the ring structure is evident at 850 hPa with the maximum occuring at the 35 km radius, during symmetric phases S1 and S2 (Figure 4.17a and c), the upper levels have a monopole structure. Conversely, during asymmetric phases A2 and A3 (Figure 4.17b and d), the lower levels have the monopole structure while upper levels show a ring structure with the maximum values at radii between 20 and 40 km.

In the vertical cross-section, the ring structure at upper levels during the asymmetric phase (Figure 4.17b and d) is seen as a bowl-shaped hollow structure. This bowl-shaped hollow structure is found also in high-resolution simulations of idealised vortices (Chen and Yau, 2001, 2003, Chen et al., 2003) as well as in real hurricanes such as hurricane Andrew (1992) (Yau et al., 2004) and hurricane Bonnie (1998) (see Figure 12a in Braun et al., 2006). An analysis of the vorticity budget in Ap-

[4]Recall that the ring structure is the one having the maximum value at some distance from the center (see e.g. Figures 4.7a, c and 4.8a), whereas the monopole structure has the maximum at the vortex center (see Figures 4.7b, d and 4.8b).

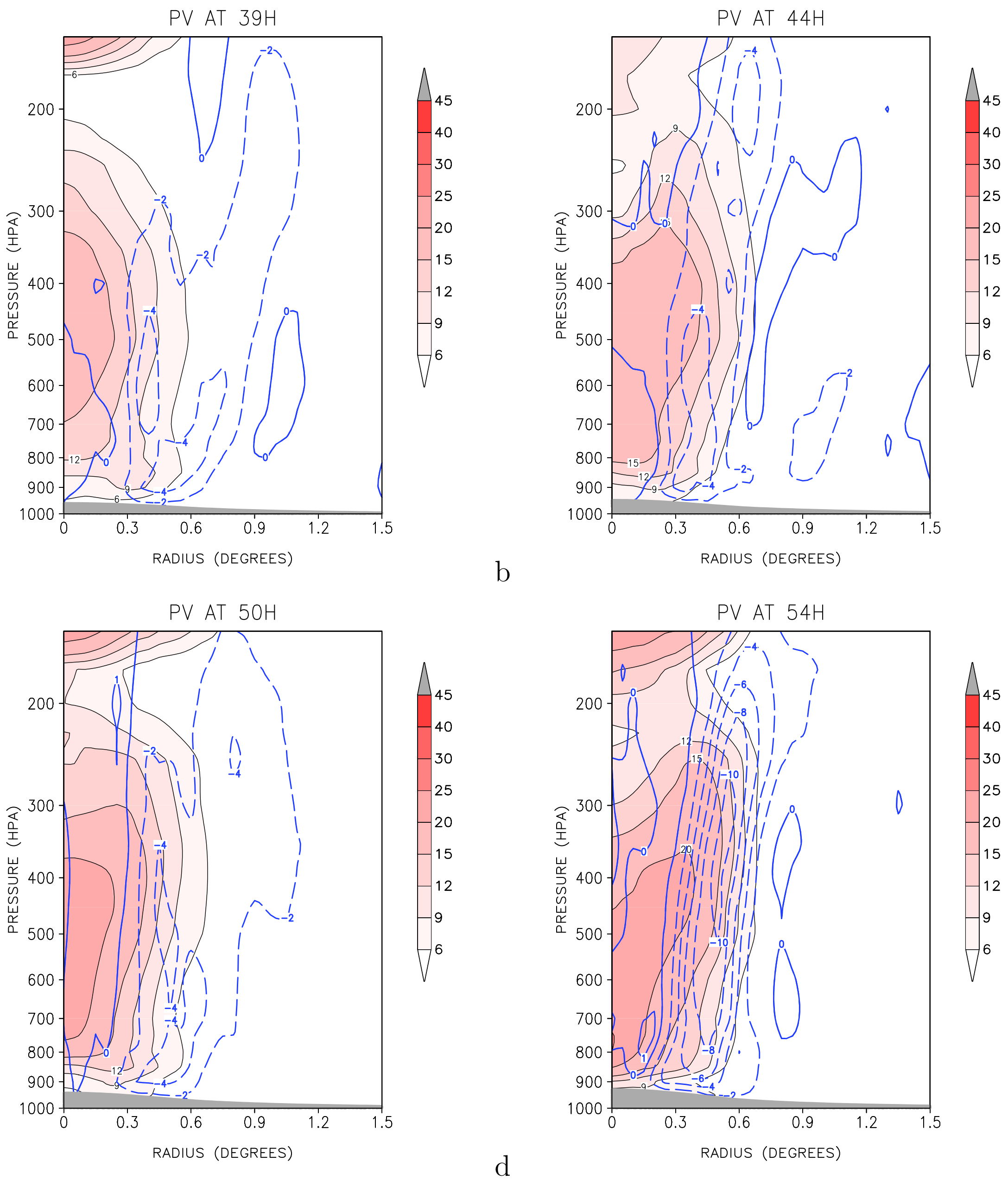

a b c d

Symmetric phase **Asymmetric phase**

Figure 4.17: PV (shaded) [PVU]. Mean vertical motion [Pa s^{-1}] is shown by blue contours. Dashed lines represent negative values and hence upward motion. Left panels (a,c) are the symmetric phases (S1 and S2). Right panels (b,d) are the asymmetric phases (A2 and A3)

pendix E shows that the ring structure at these levels is a result of the tilting and stretching of the vorticity by the convection in the eyewall region. This large and continuous generation of PV by the eyewall convection is suggested by Chen and Yau (2001, 2003) as the cause for the persistence of the ring structure even though it is barotropically unstable (the barotropic instability of the vorticity ring structure is discussed in Section 1.2.4)

Although present in simulations of real hurricanes (Yau et al., 2004, Braun et al., 2006), the ring structure at lower levels (say below 700 hPa) has not attracted much attention perhaps because the ring is so shallow. However, as demonstrated in the previous section, this low-level ring structure is associated with the symmetric phase in our simulation. Moreover, as will be shown in Chapter 6, the wavenumber 4 asymmetries may be explained by barotropic instability of the low-level ring structure. Thus, this ring structure, albeit shallow, may play a role in the initiating the transition between symmetric and asymmetric states.

Equivalent Potential Temperature

Figure 4.18 shows the vertical structure of mean equivalent potential temperature θ_e during the symmetric and asymmetric phases during rapid intensification. The development of the θ_e structure in the core region is essentially a bottom-up process, in which the region of high θ_e in the vortex core develops to upper levels from below as the vortex intensifies. This can be seen from the moist isentropes (e.g. $\theta_e = 370K$ in panels from a to d), which gradually displace to upper levels as time progresses.

Apart from the upward transport of high θ_e, the development of the high θ_e structure occurs in a stepwise fashion. During the symmetric phase, the high θ_e air is transported upwards in the eyewall convection, which is seen as the increase of θ_e at some radius just inside of the RMW (see Figures 4.18a and c). In contrast, during the asymmetric phase, θ_e increases substantially near the center, as seen by comparing the 365 K moist isentropes in panels a and b; and the 370 K moist isentropes in c and d. Budget analysis, which is included in Appendix E, shows that the increase of θ_e in the eyewall during the symmetric phase is dominated by the contributionfrom upward vertical advection. In contrast, the increase of θ_e near the center during the asymmetric phase is associated primarily with the enhanced horizontal advection, which is accompanied by the VHTs in the core region.

In summary, the vertical structure of the simulated vortex reflects the vacillation cycles during rapid intensification. Distinct ring and monopole structures in the PV and θ_e develop in a relatively shallow layer (below 700hPa) during the symmetric and asymmetric phases, respectively.

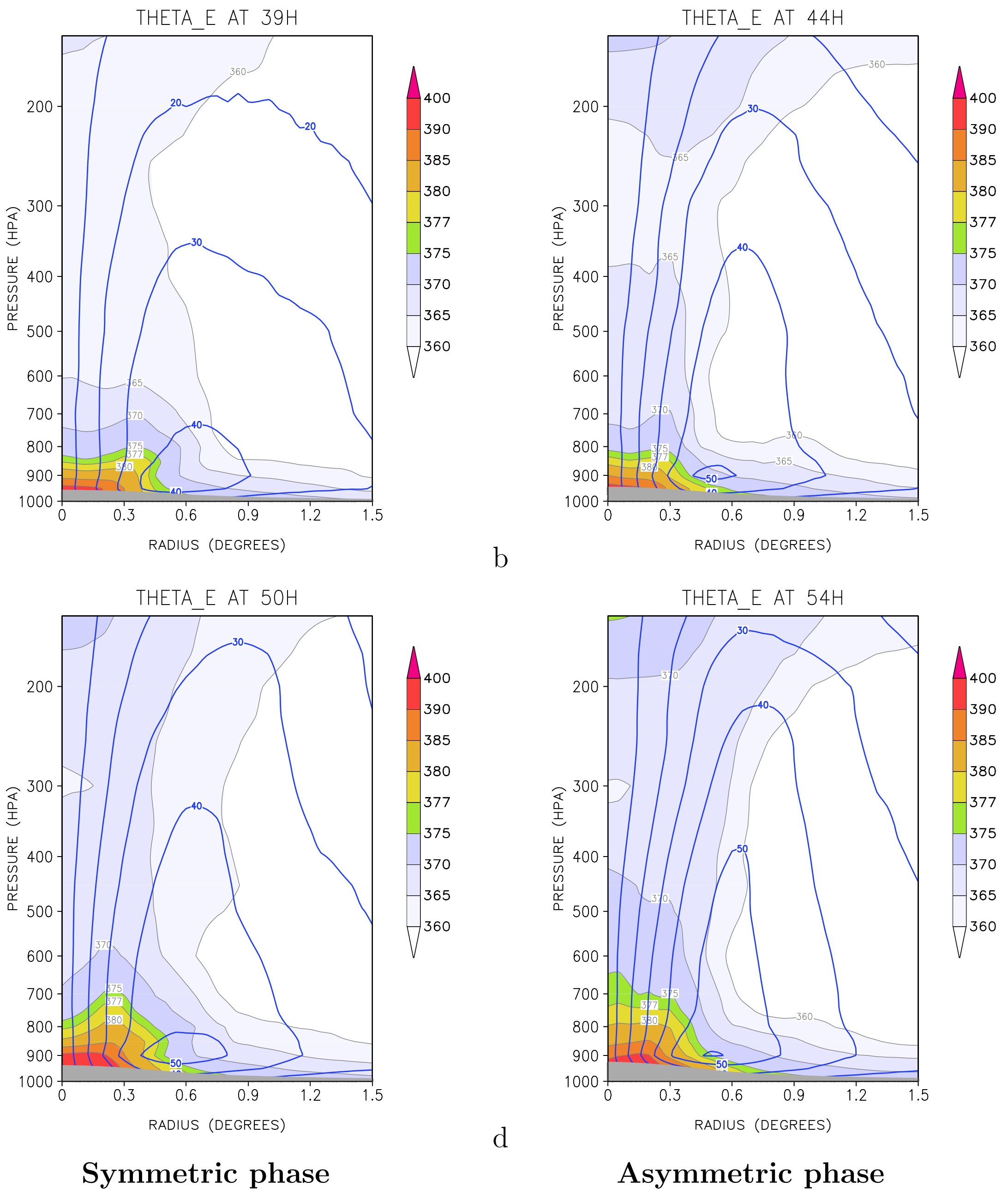

Figure 4.18: Similar to Figure 4.15 but for equivalent potential temperature θ_e [K] (shaded). Solid blue lines show mean tangential wind [m s^{-1}].

4.3 Vortex structure during the mature stage

Once the simulated vortex reaches its mature stage[5], it ceases to vascillate. Although our study focuses on the vacillation between the two phases during the period of rapid intensification, it is still important to document the vortex structure during the mature stage in order to understand the reasons leading to the cessation of these vacillation cycles.

[5]The mature stage is defined in Section 4.1 as from 60 to 72 h.

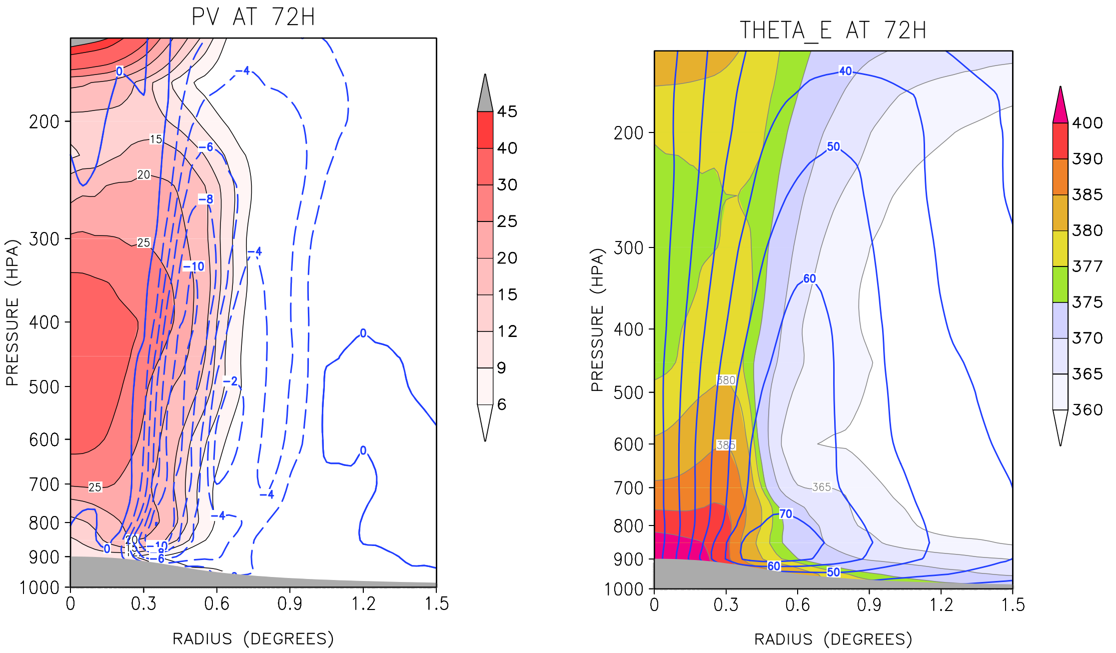

a) **Potential vorticity** b) **Equivalent potential temperature**

Figure 4.19: Vertical structure of (a) mean PV and (b) θ_e during the mature stage at 72 h. Dashed blue contours in (a) is vertical velocity [Pa s^{-1}]. Solid blue lines in (b) are isotachs of the mean tangential wind [m s^{-1}].

Figure 4.19a shows the vertical structure of the azimuthal mean PV during its mature stage at 72 h. The mature stage possesses characteristics of both phases, namely a ring structure at both lower and upper levels. This implies that the mean flow may become barotropically unstable, especially at low levels as the ring structure is narrower there. For example, Hendricks et al. (2009) suggest that very hollow and thin rings may break into mesovortices, which may last for more than 15 hours before merging to form the monopole structure. The vertical velocity structure during the mature stage (contours in Figure 4.19a) exhibits similar characteristics to that of the symmetric phase, having a well-defined tilted eyewall with the maximum at the lower part of the troposphere.

In the θ_e field shown in Figure 4.19b, the mean vortex has a monopole structure below 780 hPa, and a ring structure with the maximum located near the eyewall between 700 and 200 hPa. The high θ_e region near the eyewall extends vertically upward from low levels and connects to the region of high θ_e from the top of the troposphere. Note that the θ_e in the eyewall does not reach the homogeneous structure, in which moist neutral ascent occurs as hypothesized in steady state hurricanes at their Maximum Potential Intensity (Emanuel, 1986). Thus, the mature stage defined

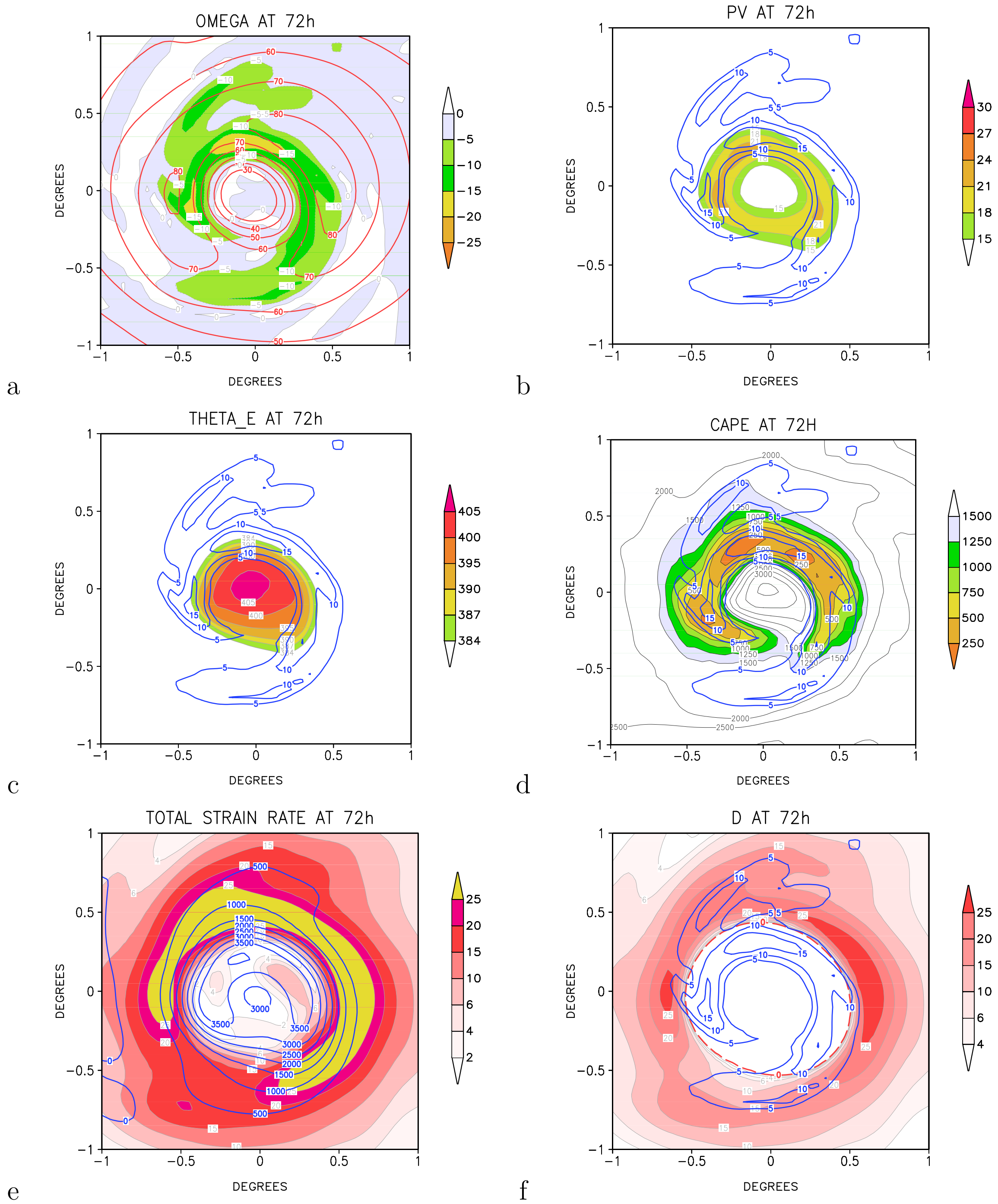

Figure 4.20: Structure of the vortex during the mature stage at 72 h. Shaded values show: (a) vertical motion; (b) PV; (c) θ_e; (d) CAPE; (e) difference D between strain rates and enstrophy; and (f) total strain rates S^2. All fields, except CAPE (d), are at 850 hPa. Contours in (a) are isotachs [m s^{-1}], in (b,c,d,f) are isolines of vertical motion [Pa s^{-1}], and in (e) are isolines of relative vorticity [$10^6\times$ s^{-1}].

in our simulation, although steady in a dynamical sense (i.e. without the vacillation cycles), is not mature with regards to the thermodynamical steady state defined by Emanuel (1986).

The horizontal structure of several dynamical and thermodynamical characteristics during the mature stage (72 h) at 850 hPa are shown in Figure 4.20. The eyewall is marked by a thick band of upward motion located just inside of the RMW (Fig. 4.20a) almost completely encircling the eye. The PV field has a ring structure collocated with the eyewall, but with the maximum values at a radius slightly smaller than that of the vertical motion (Fig. 4.20b). Thus, this configuration is similar to that of the symmetric phase during rapid intensification. On the other hand, the θ_e structure has a monopole shape with the maximum located in the center (Fig. 4.20c) which is a feature of the θ_e structure at the asymmetric phase (e.g. Figs. 4.11b,d).

The distribution of CAPE during the mature stage is of special interest. As shown in Fig. 4.20d, the eyewall is embedded almost completely in the low CAPE area. This configuration can be explained by the persistent precence of deep convecion in this area, which consumes the convective instability. Relatively low CAPE means that the eyewall has less convective energy available to convert to kinetic energy. Thus, the relatively low CAPE is consistent which the lack of strong isolated convection or VHTs (see in Fig. 4.20a). Satellite images discussed in the next section shows that VHTs were absent in the mature stage of hurricane *Katrina*.

The total strain rates S^2 and the difference between the total strain rate and enstrophy $D = S^2 - \zeta^2$ are shown in Figures 4.20e and f, respectively. During the mature stage, a thick annulus of large strain occupies the outer periphery of the eyewall, extending from 45 km to 90 km. The strain dominated region (large positive D values) outside of the RMW is strong and completely encloses the inner core completely. This structure indicates that the flow is strongly strained just outside of the RMW, thus, not favourable for the development of convection (see e.g. Rozoff et al., 2006).

4.4 Observational evidence for the two phases

While verifying the simulated track and intensity is a relatively straightforward task, verifying the vortex structure is more difficult because of the paucity of data. One immediate question would be whether or not hurricane *Katrina* vacillated similarly during the period of rapid intensification. To address this question, infrared satel-

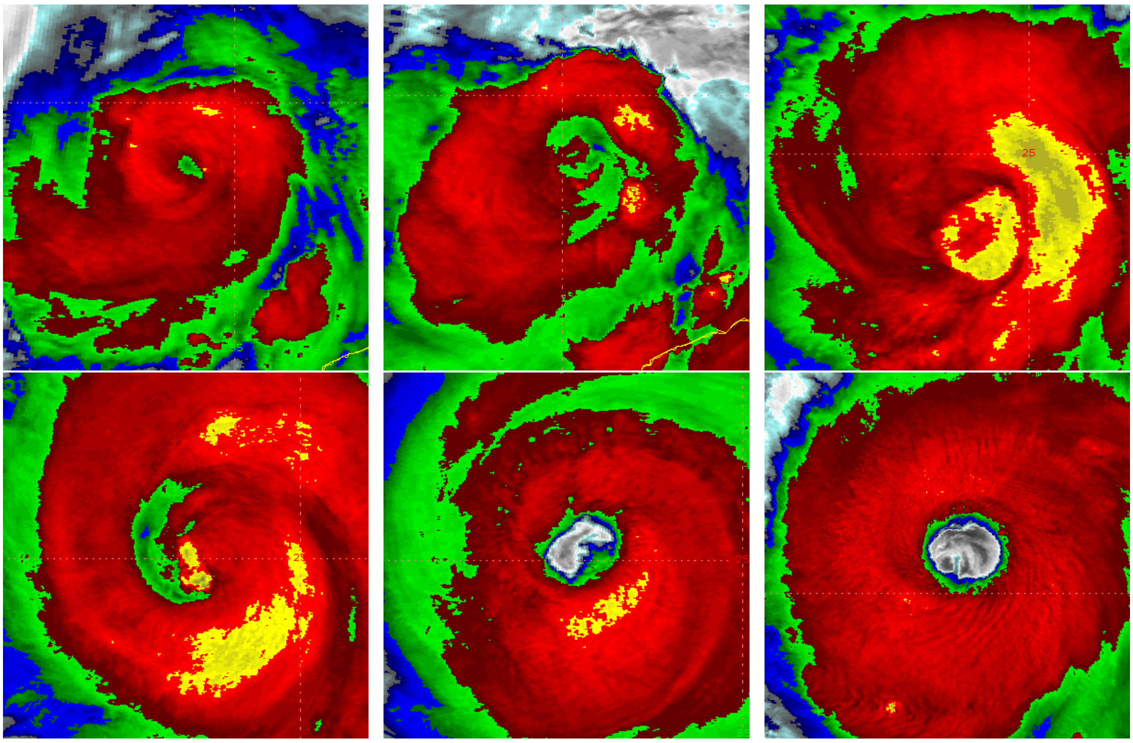

a	b	c
d	e	f

Figure 4.21: Infrared satellite images at 1 km-resolution for hurricane *Katrina* at a)1106Z, b)1537Z, c)2004Z, d) 2357Z on 27 August, e)0433Z and f)0730Z 28 August 2005. Data are available from GOES Algorithm Working Group, Corporative Institute for Research in the Atmosphere, CIRA.

lite images from the tropical cyclone polar image archive[6] are compared with the brightness temperatures of the synthetic clouds produced from model output using a method similar to that described in Rikus (1997) and Sun and Rikus (2004).

Figure 4.21 shows a sequence of IR satellite images from 1106Z 27 August to 0730Z 28 August 2005. (Note that these images are irregular in time due to availability of data from polar-orbitting satellites). During this period, hurricane *Katrina* changes from a relatively symmetric ring structure (panel a), to a highly asymmetric structure with a seemingly broken eyewall, having more than one strong overshooting embedded convective region (marked by the yellow color in panels b and c). Subsequent figures (d and e) show some weakening of the convection near the core while the vortex becomes more symmetric. The large area of cold cloud tops (yellow color) to the south-east of the TC center in (d) and (e) mark cirrus clouds, which

[6]The IR data at 1 km horizontal resolution from various satellites and the code for reading brightness temperature were kindly provided by Drs. John Knaff and Ray Zehr (Cooperative Institute for Research in the Atmosphere, Colorado State University).

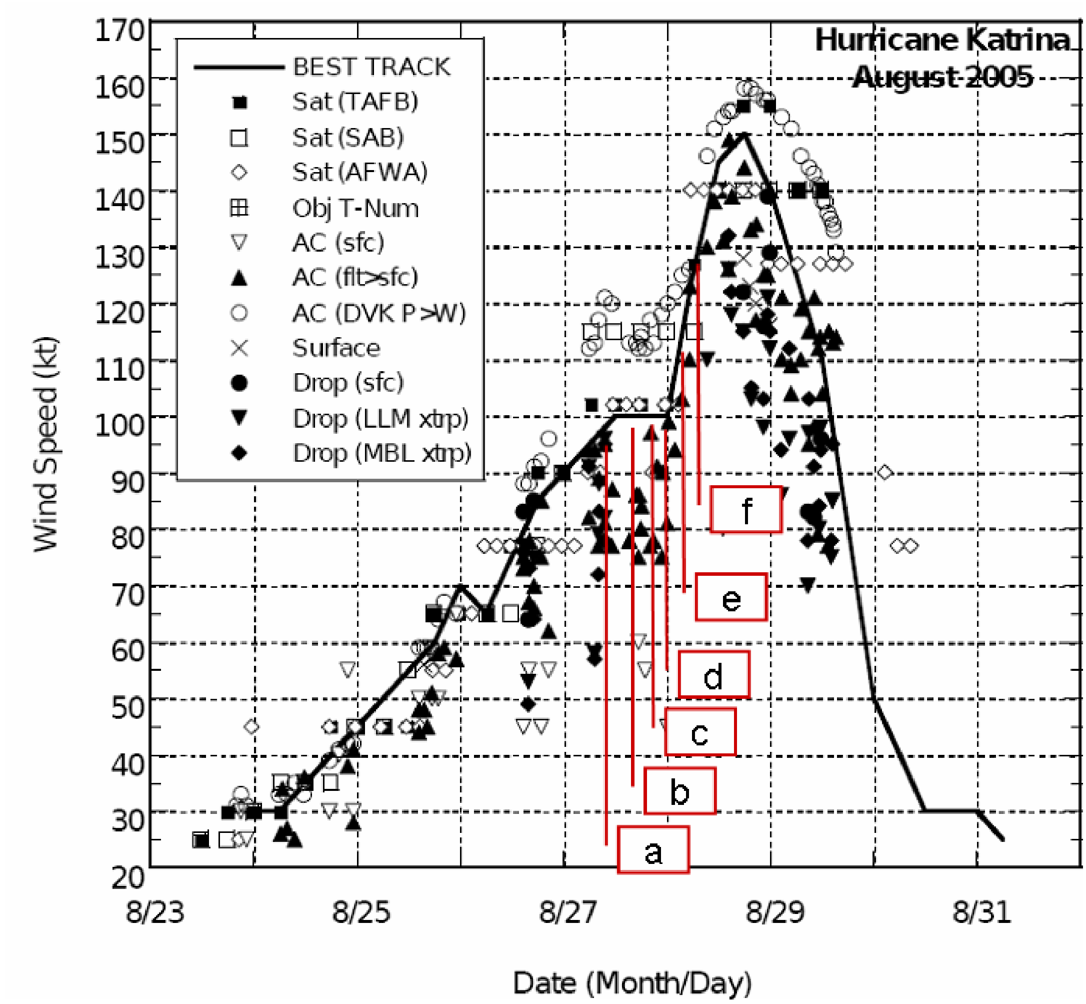

Figure 4.22: Observed maximum wind speed of hurricane *Katrina* from Knabb et al. (2006). Labels a to f mark the times corresponding to images in Figure 4.21

are most likely the remnants from deep convection. At 0730Z on the 28 August (panel f), hurricane *Katrina* becomes symmetric again without the presence of very strong deep convective bursts.

The observed evolution of hurricane *Katrina* is constistent with the symmetric and asymmetric phases described in the previous sections. Specifically, the structure at 1106Z on 27 August (panel a) and 0730Z on 28 August (panel f) resemble the symmetric phase, whereas 1537Z and 2004Z on 27 August (panels b and c, respectively) correspond to the asymmetric phase. To complete the sequence, Figures 4.21d and e can be classified as the transition period from the asymmetric to the symmetric phase. Thus, hurricane *Katrina* has one structure change cycle (symmetric to asymmetric to asymmetric) during a period of 19 h from 1106Z on 27 August (panel a) to 0730Z 28 August (panel e), which is somewhat longer but still of the same order as the vacillation periods of 10 to 11 h found in the model simulation.

The change in the intensity of hurricane *Katrina* during the period mentioned above is consistent with intensity changes associated with the symmetric and asymmetric phases in the simulated vortex. Figure 4.22 shows the observed maxium wind speed and the times of the IR satellite images in Figure 4.21. During the asymmetric phase (panels b and c in Figure 4.21), Hurricane *Katrina* weakens, whereas it reintensifies as the vortex becomes more symmetric (panels d,e and f). Note in Figure 4.22 that during the period from 00Z to 06Z 26 August hurricane *Katrina* briefly weakened . This weakening occurred when Hurricane *Katrina* made landfall on the Florida penisula and, thus, is not considered here as an internal structure change cycle.

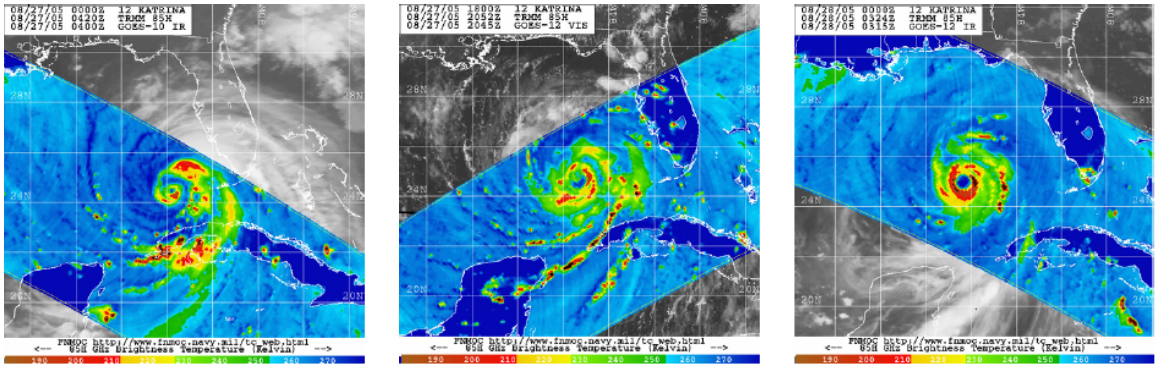

a) 0420Z 27 August b) 2052Z 27 August c) 0324Z 28 August

Figure 4.23: Figure 5 from Knabb et al. (2006). Passive microwave imagery from the NASA TRMM satellite depicting the eyewall replacement cycle in hurricane *Katrina* on 27-28 August 2005. All images are from the 85GHz channel in which ice scattering reveals areas of deep convection displayed in the red shades. Images courtesy of the Naval Research Laboratory (NRL).

During 27 August, the National Hurricane Center (NHC) reported an eyewall replacement cycle (ERC) in Hurricane *Katrina* (Knabb et al., 2006). Figure 4.23 shows the satellite images used by Knabb et al. (2006) as evidence of the ERC. Panels a and c are referred to as the period before and after the ERC, during which hurricane *Katrina* was intensifying, whereas panel b corresponds to the phase when the inner eyewall is broken and the storm experiences some weakening. According to the descriptions of ERCs by Willoughby et al. (1982), the inner eyewall weakens at the emergence of the outer eyewall. However, panel b shows that the outer eyewall to the north-east of the vortex center is weak and covers only a quarter circle, thus, is unlikely to cause the break down and weakening of the inner eyewall. Rather, the structure of the inner eyewall in panel b fits best with the characteristics of the simulated eyewall during the asymmetric phase, wherein the eyewall is broken

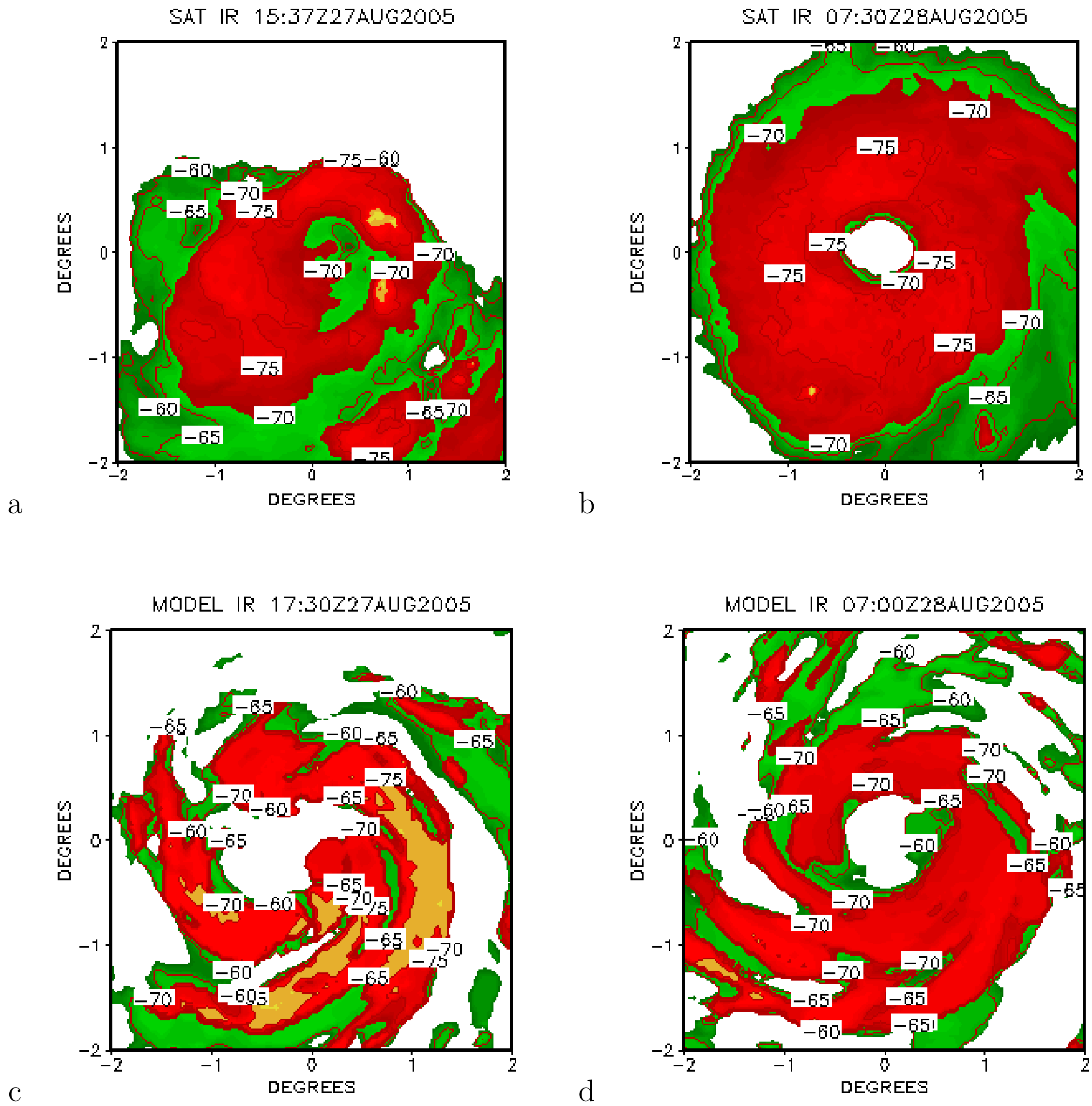

Asymmetric phase **Symmetric phase**

Figure 4.24: Infrared satellite images (top) and simulated brightness temperature (bottom) during the asymmetric (left) and the symmetric (right) phases. Values of the model derived brightness temperature are decreased by 3^0C to appear at similar brightness as that of real satellite images. Note that (a) and (b) are essentially the same images as in Figures 4.21b and f, respectively, but at 5 km resolution.

into strong convective entities. Therefore, we propose that hurricane *Katrina* goes through a symmetric/asymmetric structure change cycle, similar to that in the simulation.

For comparison, the brightness temperature from the satellite and the model output are displayed together in Figure 4.24 with the same horizontal resolution (5 km). Both hurricane *Katrina* and the simulated vortex exhibit two disctinct phases: a) the asymmetric phase with a broken eyewall embedded within regions of isolated strong overshooting convection (brightness temperature colder than -75°C marked with yellow color); and b) the symmetric phase with a ring-like eyewall with relatively evenly distributed moderate convection.

The mean structure of the simulated vortex is validated based on radial profiles of azimuthally-mean and standard deviation of brightness temperatures. Figure 4.25 shows the radial profiles of the azimuthally-mean and standard deviation of brightness temperature from the model output and from the IR satellite image during the 27 August 2005. Unfortunately, during this period, the profiles of the simulated storm do not match well with those observed by IR satellite images. While hurricane *Katrina* exhibits overcast conditions in the central region (in panel b, cold cirrus top extending from the center to about 1 degree), the simulated vortex exhibits a warm core at the center (panel a), resembling an eye. The apparent eye of the simulated vortex is associated also with the maxium of standard deviation of brightness temperature near 0.2-0.3 degrees, which is the region between the eye and the eyewall (panel c). In contrast, Hurricane *Katrina* has low values of standard deviation near the center since its cirrus cloud shield still entirely covers the center.

This difference between the simulated brightness temperatures and those retrieved is due to the method used to represent the synthetic clouds from model output. Currently, only temperature and humidity profiles are used to reproduce brightness temperatures. Other options in the scheme that use microphysical properties have shortcomings, including the assumption that partial ice cover is not allowed in a grid box (Rikus, 2008, personal communication) leading to overestimation of the cirrus cover. This option, however, tends to underestimate clouds near the center, causing the artifical appearance of the eye, even when the real warm eye (which has resulted from strong subsidence at the TC center, followed by drying and warming, and hence, clearing of clouds), has not fully developed in the modelled vortex. Thus, the comparison of cloud structure during the period while the eye is not visible in the IR satellite images may not be ideal using our current method for deriving synthetic clouds from model output.

During 28 August, both hurricane *Katrina* and the simulated storm are in the mature stage, having a well-developed eye and eyewall structure, the simulated vortex produces realistic radial profiles. Figure 4.26a,b shows many similarities between the real and simulated storms, including a warm eye of 290 K, and a cirrus top of 195

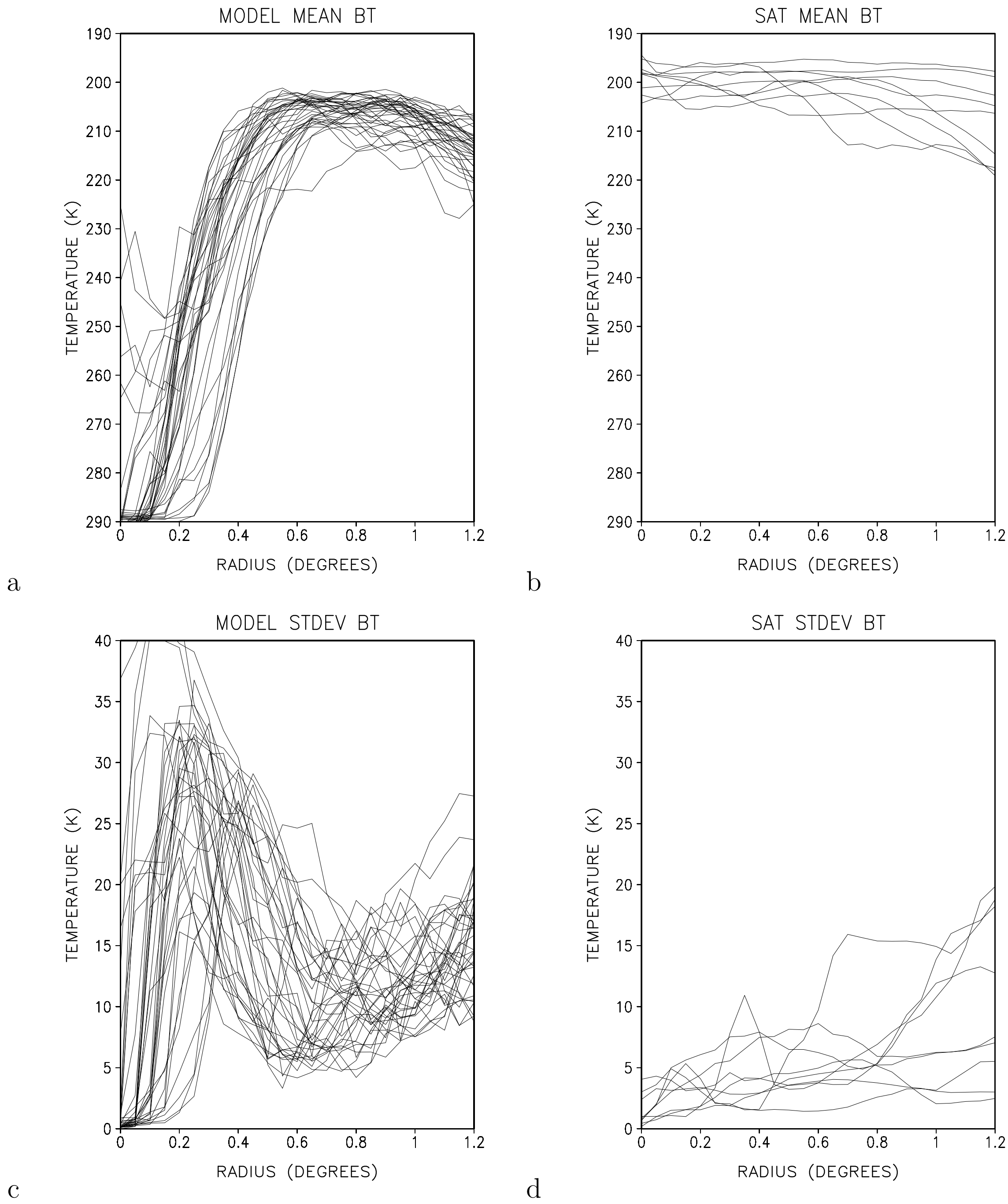

From model output **From satellite images**

Figure 4.25: The azimuthal mean (top panels) and standard deviation (bottom panels) of brightness temperature from the model (left panels) and from the IR satellite images (right panels) during the 27 August 2005.

K to 205 K extending from 40 km radius. Likewise, the maximum standard deviations are found near 30 km radius while the cirrus shield has smallest asymmetries within the radii from about 50 km to 100 km (see Figure 4.26c,d). Although the simulated vortex is different from the real vortex in details such as a warm bias of

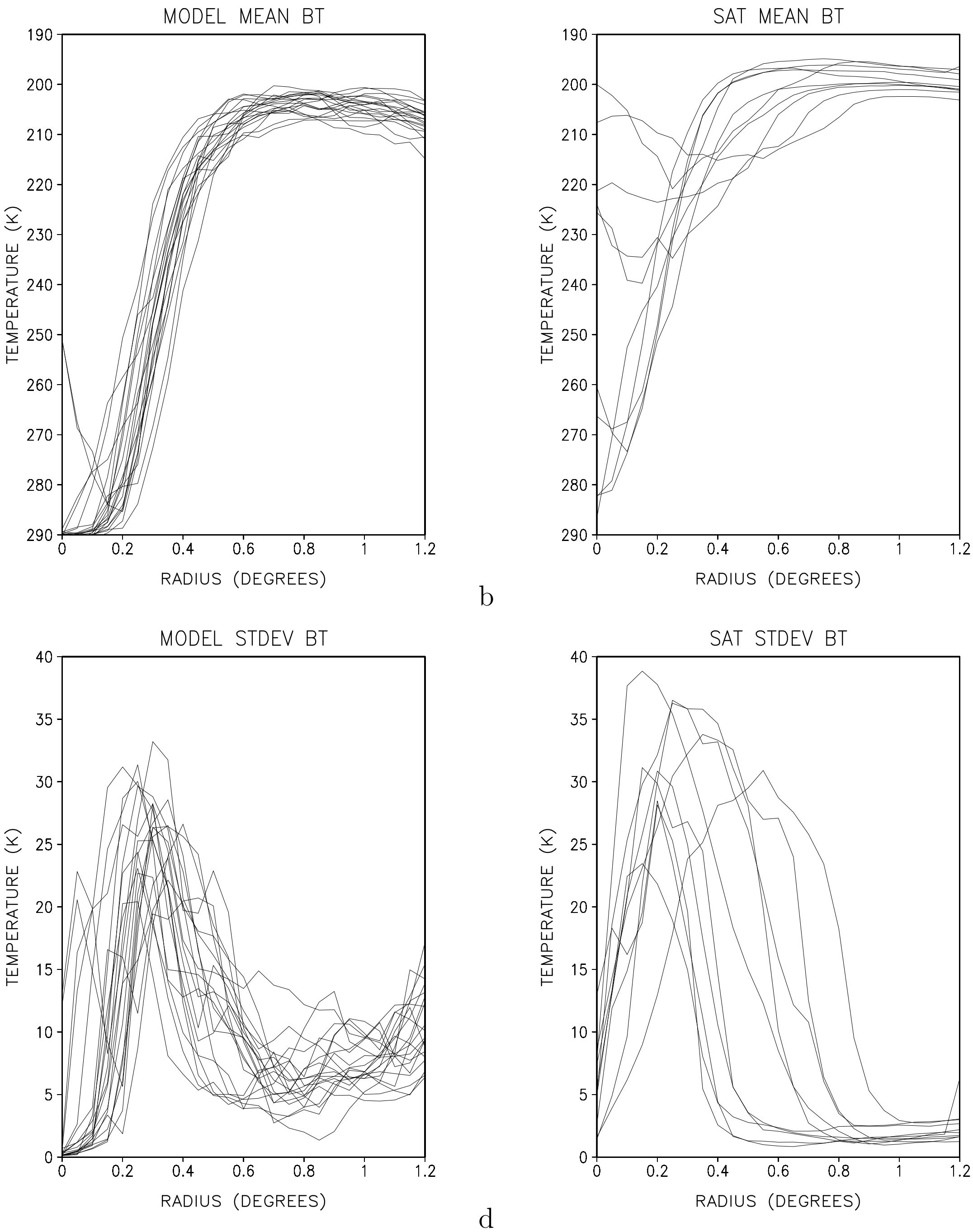

a b

c d

From model output **From satellite images**

Figure 4.26: As for Figure 4.25 but for the 28 August 2005.

brightness temperature of order of 3 K, and a smaller maximum standard deviation near the boundary between the eye and the eyewall (comparing c and d), the overall similarity indicates that the model seems capable of representing the mature vortex structure of hurricane *Katrina* realistically.

4.5 Summary of Chapter 4

In summary, during the rapid intensification phase, the simulated vortex vacillates between symmetric and asymmetric phases, with a period of about 8 to 13 h. In addition, the transition from the symmetric phase to the asymmetric is shorter than the reverse transition from the asymmetric phase to the symmetric phase, corresponding to 2-4 h and 6-9 h, respectively. The structure in the lowest 150 hPa has the following characteristics:

- ***Symmetric phase***. The eyewall is highly symmetric, consisting of relatively uniform elongated convective bands organized in a ring-like form; the low level equivalent potential temperature and vorticity fields exhibits a ring-like structure also; and the largest intensification rates occur near the RMW. This phase is similar to Regime 1 of KE01.

- ***Asymmetric phase***. The eyewall is highly asymmetric, having a polygonal form with VHTs at the vertices; the low-level potential temperature and vorticity fields have the monopole structures with the maximum values near the center; the largest intensification rates of the mean tangential wind occur at the inner radii while the RMW experiences lower intensification rates. This phase is similar to Regime 2 of KE01

During the mature stage at the later times of the integration, these cycles, including the breakdown of the eyewall into asymmetric entities, are not observed. The vortex structure at low levels during this stage is characterised by:

- A nearly symmetric eyewall;
- A ring-like structure of PV, which indicates necessary condition for barotropic instability;
- A monopole structure of equivalent potential temperature with the maximum at the vortex centre;
- CAPE, and thus convective instability, is low in the eyewall region as being consumed by the persistent convection there;
- The flow is strongly strained at the outer periphery of the eyewall; and
- The rapid filamentation zone outside of the RMW is strong implying an unfavourable condition for convection development there.

Chapter 5

THE EVOLUTION OF THE AZIMUTHAL MEAN VORTEX STRUCTURE

The symmetric and asymmetric phases have been identified during rapid intensification; the next step is to study the transition between them. To this end, Chapter 5 analyses the evolution of the radial profiles of azimuthal-mean quantities at low levels and the vertical structure near the vortex core. It is of interest to investigate systematic changes in azimuthal mean fields during the symmetric and asymmetric phases. Budget analyses for absolute vorticity, mean tangential wind component, and equivalent potential temperature, which are included in Appendix E, will be used to interpret the patterns of evolution of the simulated vortex. We choose to include in this chapter only budget analyses to which we refer, whereas the full details are given in a Appendix so as not to distract readers from the main ideas.

5.1 Evolution of radial profiles at low levels

5.1.1 Mean tangential and radial winds

Figure 5.1a shows the evolution of the azimuthal mean tangential wind $\overline{V}$ (contours) and its tendency $\partial\overline{V}/\partial t$ (shaded) at 850 hPa. The patterns of intensification are different during the symmetric and asymmetric phases. Prior to and during the symmetric phase, the maximum acceleration occurs near the RMW (marked with the label S_{RMW}). In contrast, during the asymmetric phase, positive tendencies occur in regions both inside and outside of the RMW (see regions marked by A_{inner} and A_{outer}, respectively), while the tendency at the RMW is small or even negative.

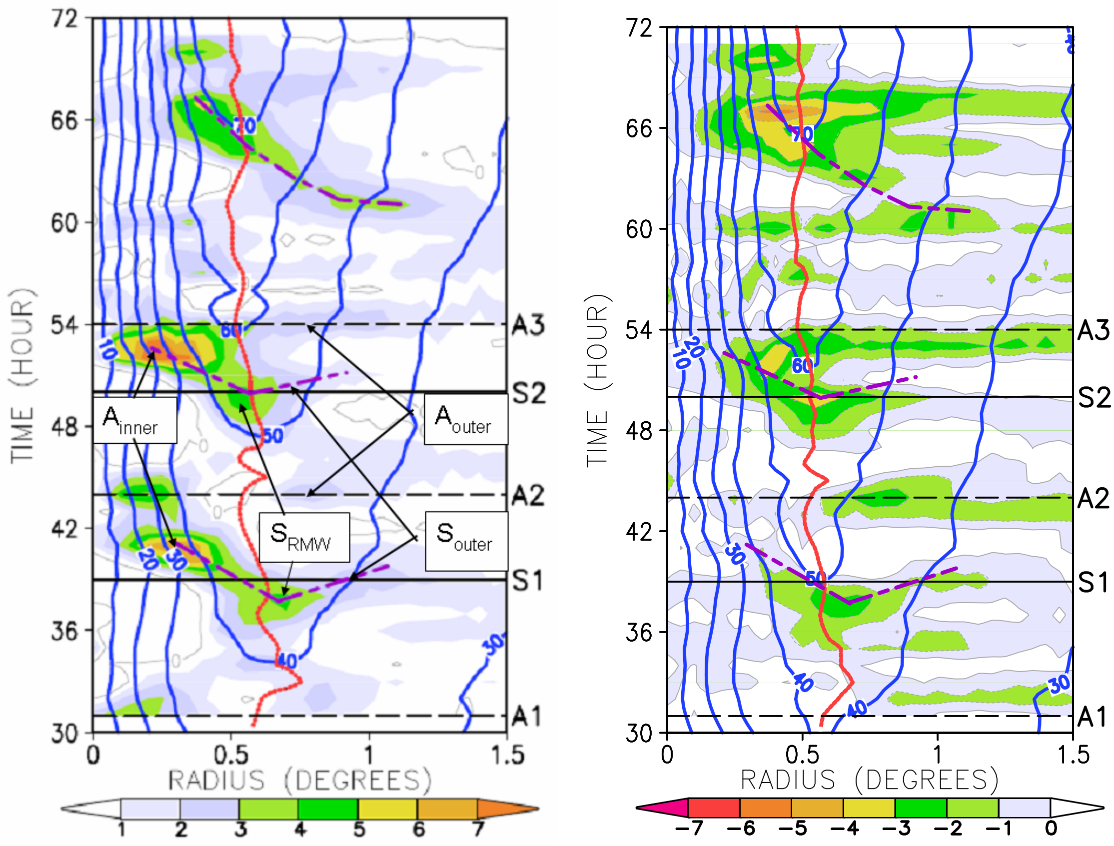

(a) $\partial\overline{V}/\partial t$ at 850 hPa.

(b) $\partial\overline{U}/\partial t$ at 900 hPa

Figure 5.1: Radius-time plots of the tendencies of (a) mean tangential wind $\partial\overline{V}/\partial t$ [m s^{-1} hour^{-1}] (positive tendencies are shaded) at 850 hPa; (b) mean radial wind at 900 hPa $\partial\overline{U}/\partial t$ [m s^{-1} hour^{-1}] (negative tendencies i.e. stronger inflow, are shaded). Blue solid contours are mean tangential wind $\overline{V}$ [m s^{-1}]; solid thick red lines represent RMW at the respective levels. Purple dashed lines indicate the movement of maximum tangential wind acceleration at 850 hPa. Labels S_{RMW}, S_{outer} refer to the regions of positive tendencies of the mean tangential wind during the symmetric phase near the RMW and at outer radii, respectively. Labels A_{inner}, A_{outer} are during the asymmetric phase for the positive tendencies regions at inner and outer radii, respectively.

The tendency pattern has distinct features during transition periods. From the symmetric to the asymmetric phase, the region of maximum acceleration moves from the RMW towards inner radii, i.e. from S_{RMW} to A_{inner}. There is also a region of weak positive tendency moving outwards from the RMW (marked by S_{out}, see purple dashed lines extending outwards from the RMW). From the asymmetric to the symmetric phase, the region of weak maximum positive tendency moves inwards from A_{outer} and reaches the RMW in the next symmetric phase.

In this study, the boundary layer (BL) is defined as the layer adjacent to the surface where frictional drag reduces the absolute angular momentum and leads to strong radial inflow (Smith et al., 2009). The BL is seen in vertical cross-sections as the layer where the absolute angular momentum increases with height (see e.g. Figures 5.2a,c and 5.3a,c). With this definition, the 900 hPa level is just near the top of the BL whereas 850 hPa is just above the BL.

The foregoing tendency patterns of the mean tangential wind ($\partial\overline{V}/\partial t$) in Figure 5.1a are accompanied by changes in the mean radial wind component ($\partial\overline{U}/\partial t$) at 900 hPa shown in Figure 5.1b. A comparison of these two figures shows the following features:

- ***Type A.*** The positive tangential wind tendencies in regions S_{RMW}, S_{outer}, and A_{outer} in panel a are associated with positive tendencies of the inflow near the top of the BL shown in panel b.
- ***Type B.*** The region A_{inner} with positive $\partial\overline{V}/\partial t$ in panel a, which is prior to the asymmetric phase A2, is not associated with the corresponding positive inflow tendencies in panel b.
- ***Type C.*** The region A_{inner}, which is just before the asymmetric phase A3, is accompanied by a region of positive $\partial\overline{U}/\partial t$, which extends outwards to a radius of about 1.5 degrees radius in panel b just prior to A3. This increasing inflow occurs at the same radii as A_{outer} and precedes A_{outer} by about 1 h.

In summary, during the asymmetric phase A2, regions A_{outer} and A_{inner} have different association patterns of types A and B, respectively. However, the associations in type C involve both the A_{outer} and A_{inner} regions during the asymmetric phase A3. We will show later in this section that type C is in fact the combination of types A and B with the regions A_{outer} and A_{inner} close to each other.

We interpret now the foregoing tendency patterns using the tendency equation for the azimuthal mean tangential wind, full details of which are given in Section E.2 of Appendix E. Our analysis follows that used by Persing et al. (2002), who examined the main four terms that contribute to the changes of the azimuthal mean tangential wind as follow.

$$\frac{\partial\overline{V}}{\partial t} = (-\overline{U}\overline{\zeta}) + (-\overline{U'\zeta'}) + (-\overline{\omega}\frac{\partial\overline{V}}{\partial p}) + (-\overline{\omega'\frac{\partial V'}{\partial p}}) + Friction, \qquad (5.1)$$

The terms on the right hand side of Equation 5.1, from left to right, are the vorticity fluxes by the mean flow and by eddies, the vertical advection of the tangential wind by the mean flow and eddies, respectively. Vertical cross-sections of these four terms are shown in Figures 5.2 and 5.3 for the symmetric phase S1 and the asymmetric phase A2, respectively. The resulting tendencies of the mean tangential wind from the model are shown in Figures 5.4 and 5.5.

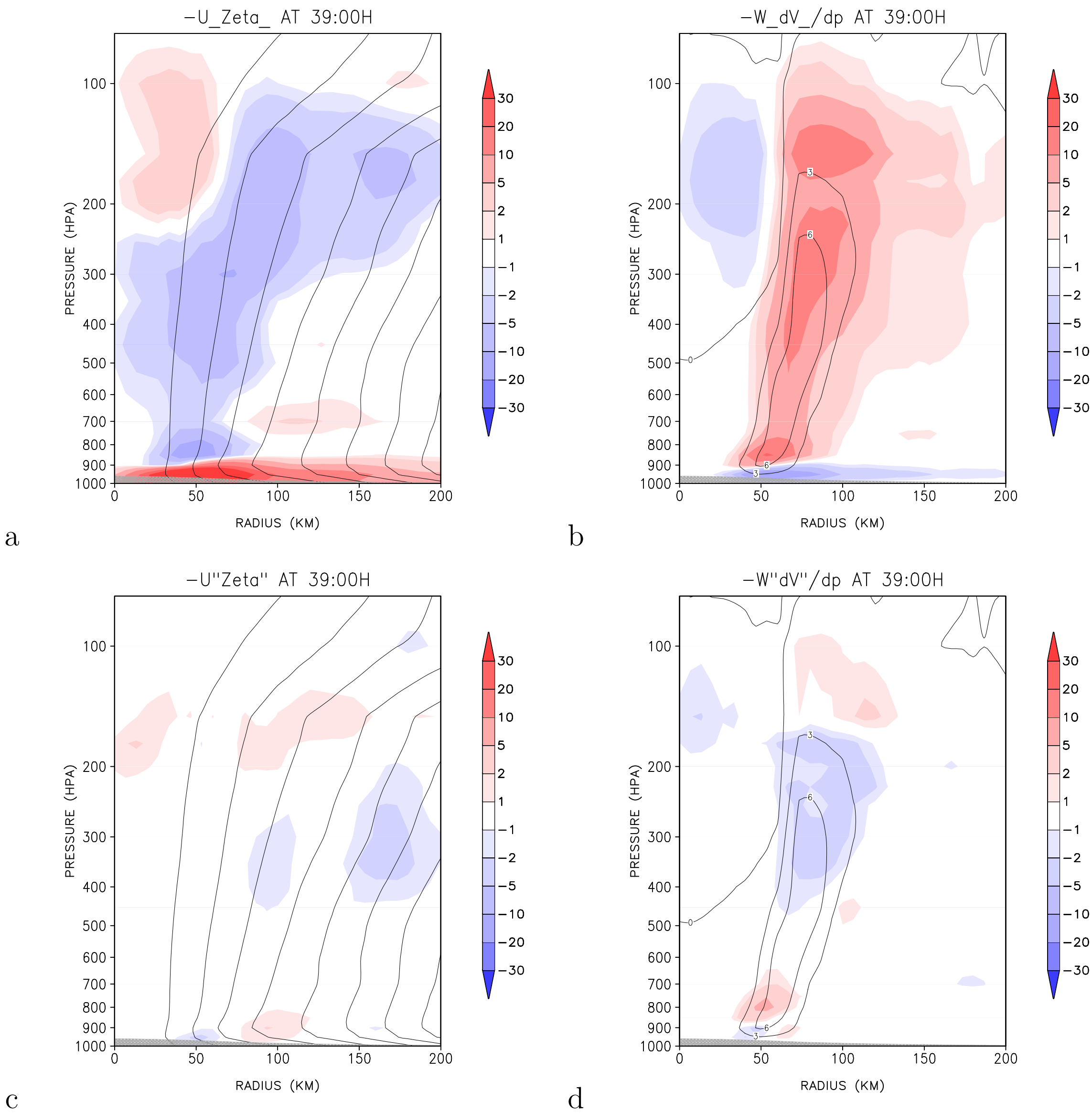

Figure 5.2: Vertical cross-sections of the azimuthal means of the terms in the budget equation for mean tangential wind [5×10^{-3} m s^{-2}], for the symmetric phase S1 at 39 h. a) mean vorticity flux $-\overline{U}\overline{\zeta}$, b) mean vertical advection $-\overline{\omega}\frac{\partial \overline{V}}{\partial p}$, c) eddy vorticity flux $-\overline{U'\zeta'}$, and d) eddy vertical advection $-\overline{\omega'\frac{\partial V'}{\partial p}}$. Contours in panels a,c shows isolines of the absolute angular momentum ($M = rV + r^2 f/2$). Contours in panels b, d shows azimuthally-mean vertical motion $-\omega$ [Pa s^{-1}].

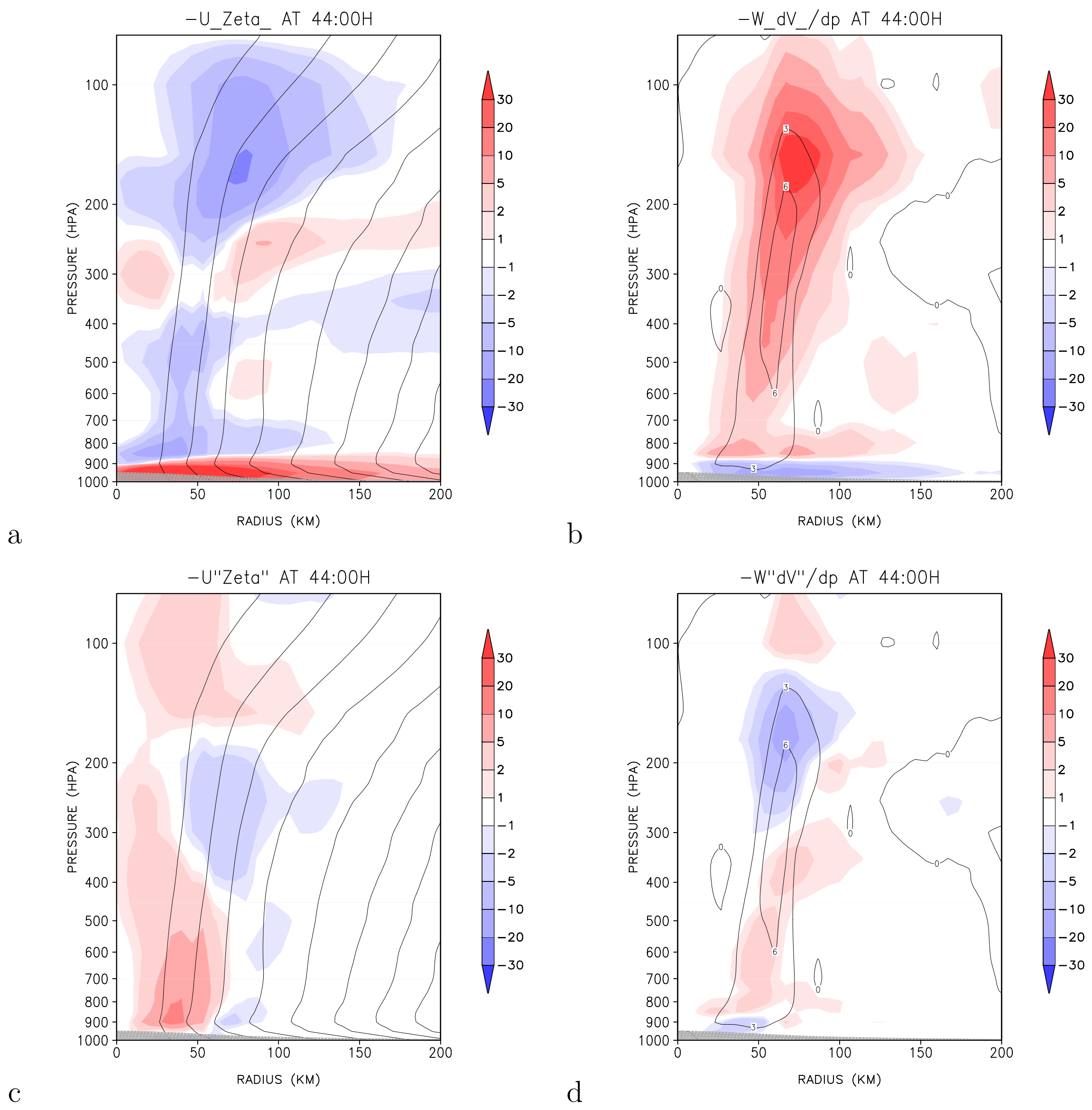

Figure 5.3: As in Figure 5.2 but for the asymmetric phase A2 at 44 h.

During both symmetric and asymmetric phases, the contributions of the mean terms to $\partial\overline{V}/\partial t$ are relatively large and of opposite signs (panels a and b in Figures 5.2 and 5.3). (In a quasi-steady state, this near cancellation would be a reflection of the approximate material conservation of azimuthal mean absolute angular momentum.) Above the BL, the vertical advection increases the mean tangential wind near and just outside of the eyewall, whereas the mean vorticity flux contributes to a negative tendency near and inside of the eyewall. There are subtle differences between the symmetric and the asymmetric phases. During the symmetric phase (Figure 5.2b), the region of positive vertical advection of $\overline{V}$ just above of the BL is confined near the eyewall, whereas it extends to a radius of nearly 150 km during the asymmetric phase (Figure 5.3b) (corresponding to the region A_{outer} described above).

While the eddy vertical advection terms are similar during the two phases (Figures 5.2d and 5.3d), the eddy vorticity flux terms during the asymmetric phase (Figure 5.3c) are of the same order as the mean terms and are significantly larger than that during the symmetric phase (Figure 5.2c). Figure 5.3c shows that eddy vorticity flux contributes to the increase of mean tangential wind at inner radii and a slight decrease in the region between 50 and 100 km, i.e. near the RMW. Thus, during the asymmetric phase A2, the increase of $\overline{V}$ in the region A_{inner} and the slight decrease near the RMW is associated with the eddy vorticity flux term.

The resulting changes in the mean tangential wind (Figures 5.4 and 5.5) during the symmetric and the asymmetric phases occur via different processes as follows.

- ***Mean vertical advection***. During the symmetric phase S1, positive values of $\partial\overline{V}/\partial t$ near and just outside of the RMW (i.e. the S_{RMW} region) are dominated by the mean vertical advection of $\overline{V}$. Note that the maximum tangential wind is located near the top of the boundary layer, which is near 900 hPa. Vertical motion in the well-organized eyewall during the symmetric phase transports absolute angular momentum upward, thereby, increasing the wind at the levels immediately above including 850 hPa (see thick red arrow in Figure 5.4). The positive values of $\partial\overline{V}/\partial t$ in the A_{outer} region are associated also with the mean vertical advection of $\overline{V}$.

- ***Eddy vorticity flux***. During the asymmetric phase A2, positive values of $\partial\overline{V}/\partial t$ in the A_{inner} region and slightly negative values near the RMW are accompanied by an eddy vorticity flux, which is associated with VHTs. The horizontal mixing by the mesoscale circulation of VHTs are symbolised by the couplet of blue arrows on the horizontal plane in Figure 5.4b.

Figure 5.5 shows the same features as those in Figure 5.4, but for the next symmetric phase S2 and the asymmetric phase A3. As the vortex intensifies, the pattern of development is similar to those of earlier times, but with some differences in detail. Specifically, the patterns of $\partial\overline{V}/\partial t$ during the symmetric phases S1 and S2 are similar (compare Figures 5.4a and 5.5a), with positive values near the RMW and negative values inside of this radius. Furthermore, regions with positive values of $\overline{V}$ tendencies A_{inner} and A_{outer} occur during both asymmetric phases A2 and A3 (Figures 5.4b and 5.5b). However, regions A_{inner} and A_{outer} just before A3 are not separated as in the case of A2. During the asymmetric phase A3 (Figure 5.5b), the field of resulting $\overline{V}$ tendencies can be interpreted as having positive eddy vorticity

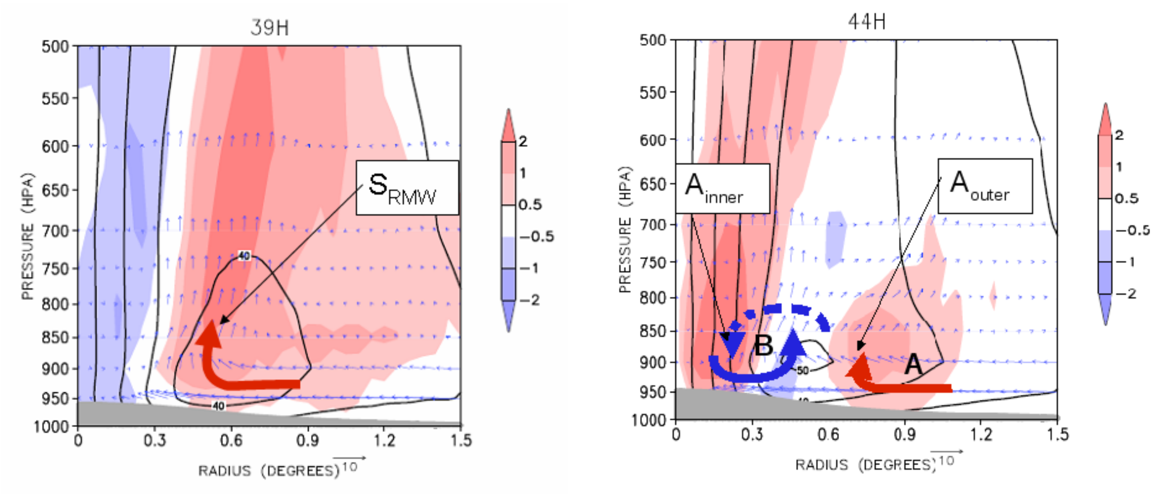

a) Symmetric phase b) Asymmetric phase

Figure 5.4: Vertical cross-sections of mean tangential tendencies (shaded, [m s^{-1} h^{-1}]) at times of minimum (maximum) asymmetry S1 (A2). Black solid contours display isotachs of mean tangential wind [m s^{-1}], the $(V, -\omega)$ vectors are shown in blue. Thick arrows schematically indicate the mean flow. Blue thick arrows near A_{inner} in (b) represent mesovortices rotating on the horizontal plane.

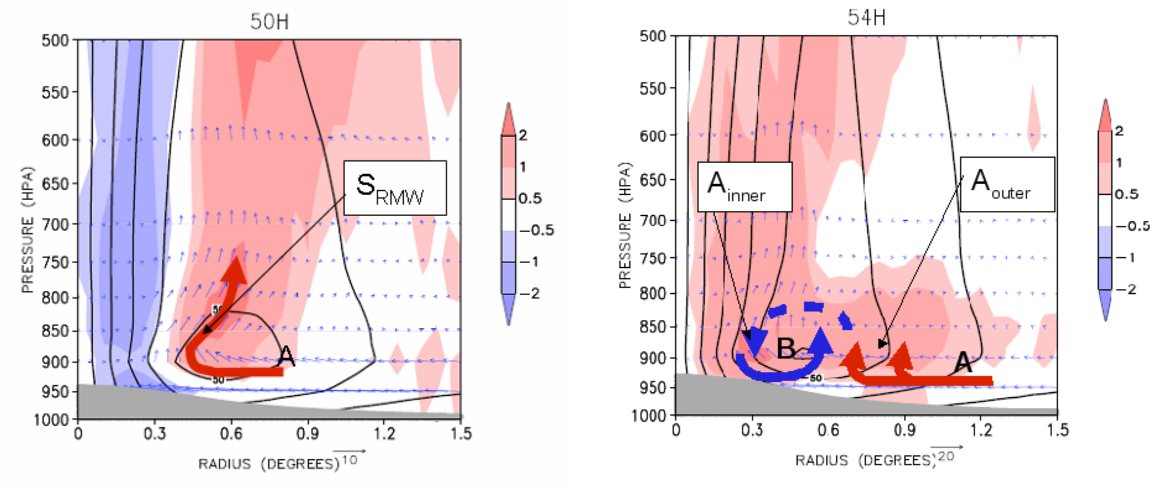

a) Symmetric phase b) Asymmetric phase

Figure 5.5: As in Figure 5.4 but for the symmetric phase S2 and the asymmetric phase A3.

flux at inner radii and mean vertical advection at the outer radii. Note that for the acceleration of the mean tangential wind by positive eddy vorticity flux, the maximum acceleration region occurs at inner radii relative to the maximum of vertical velocity, instead of at the location of the maximum vertical velocity as in the case of mean vertical advection. Thus, the main difference between A2 and A3 is that the A_{outer}, which is located outside of the RMW, occurs at smaller radius as the vortex has contracted.

In addition to an inward and upward transport out of the BL, there is a noticeable outward component just above the inflow layer, towards the RMW (see red arrow in Figures 5.4a and 5.5a). This outward movement can be seen in Figure 5.6a at the inner side of the S_{RMW} regions. This outflow is more pronounced during the later stage when the vortex is more intense (e.g. prior to S2, and during another instance of accelerated tangential wind from 63 to 66 h, marked by a purple dashed line in Figure 5.6a). This relatively strong outflow associated with the increase of mean tangential wind at the top of the BL is a manifestation of the intensification mechanism proposed by Smith et al. (2009), in which the inner core of TCs intensifies by radial convergence within the BL (see discussion in Section 1.2.1). In our simulation, the outflow at the top of the BL is indeed observed near the region of accelerated tangential winds, thus consistent with their proposed mechanism.

5.1.2 Mean vertical motion

The evolution of the azimuthal-mean vertical velocity (Figure 5.6b) vacillations resemble eyewall replacement cycles (ERCs). For example, prior to the symmetric phase S1, the mean eyewall moves inwards (black solid lines in Figure 5.6b mark this inward movement). During the asymmetric phase (e.g. A2 at 44 h), the inner eyewall weakens while the strongest convection develops at some outer radii, similar to the formation of the outer eyewall. Subsequently, this outer eyewall contracts again (see the black line starting from the 0.8 degree radius at 46 h in Figure 5.6b), reminiscent of a typical ERC (Willoughby et al., 1982). In addition, intensity changes during the vacillation cycles are analogous also to that of ERCs, with small (large) intensification rates during the asymmetric (symmetric) phase. Therefore, the two phases of the vortex structure described in the previous chapter have certain similarities with ERCs: the symmetric phase corresponds to the contraction phase of an ERC, and the end of the asymmetric phase to the weakening of the inner eyewall and the formation of the outer eyewall.

It is important to note, however, that the vacillation cycles described here are essentially different processes to ERC. Specifically, the break-down of the eyewall during the asymmetric phase is not due to the formation of the outer eyewall as in ERCs. Rather, the eyewall breaks down as asymmetries develop within the eyewall itself (see e.g. Figure 4.4b,d). Thus, it is suggested that these structure change cycles are an alternative means for the inner core to rapidly intensify.

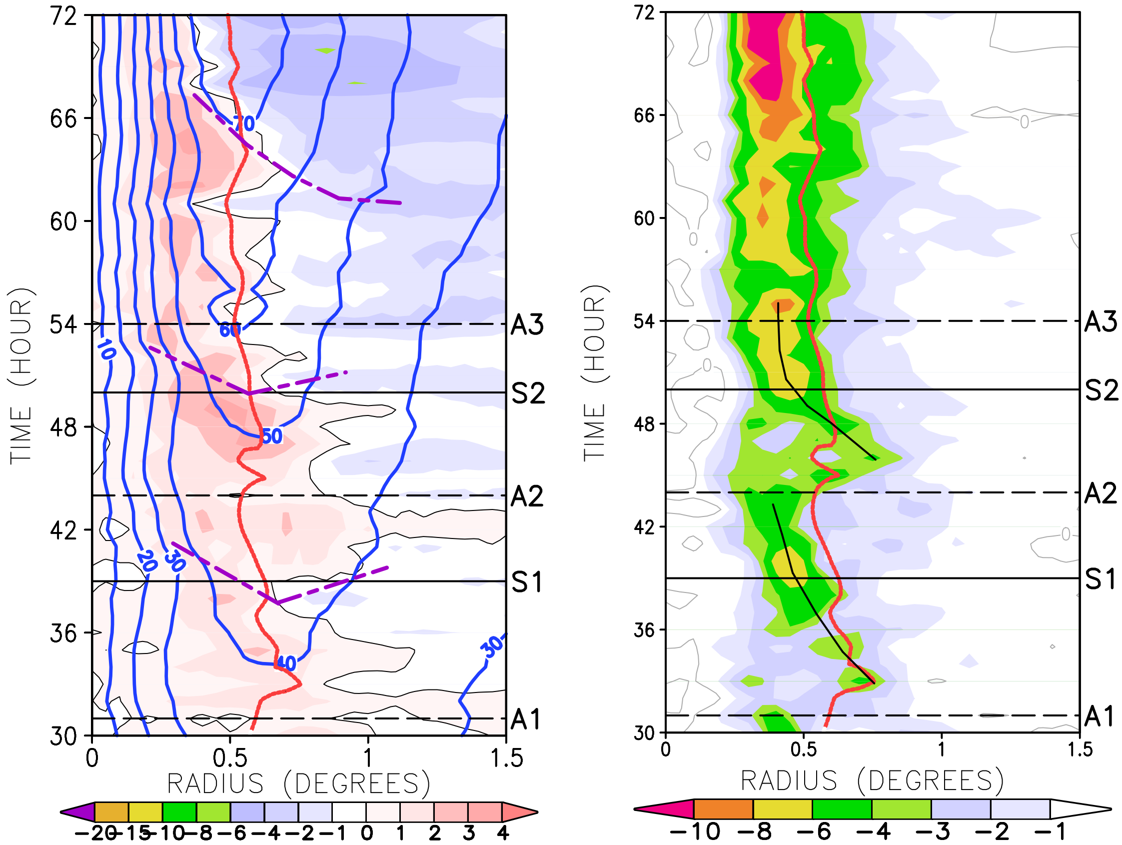

(a) $\overline{U}$ at 850 hPa

(b) $\overline{\omega}$ at 850 hPa

Figure 5.6: Radius-Time plot of the 850 hPa azimuthal-mean: a) radial wind [m s^{-1}] (shaded), and b) vertical velocity [Pa s^{-1}] (areas with upward motion are shaded). Purple dashed lines indicate the movement of maximum tangential wind locations as in Figure 5.1a. Blue solid lines in (a) show the mean tangential wind at 850 hPa. Black solid lines in (b) display locations of maximum upward motion, and thus, show the inward movement of the mean eyewall; red dotted lines in both figures are locations of the RMW.

The diagram in Figure 5.7 summarises the evolution pattern of the azimuthally-mean wind components. The key points of the schematic are as follows:

- ***During the symmetric phase***, while convection is organised into a ring-like eyewall, the largest acceleration occurs near the RMW (S_{RMW}), which is associated with an enhanced local secondary circulation and an accelerated inflow in the BL toward the RMW. At the top of the BL, these regions of large radial acceleration are associated with relatively strong outflow at its inner periphery, which is consistent with Smith et al. (2009)'s intensification mechanism by convergence in the BL.

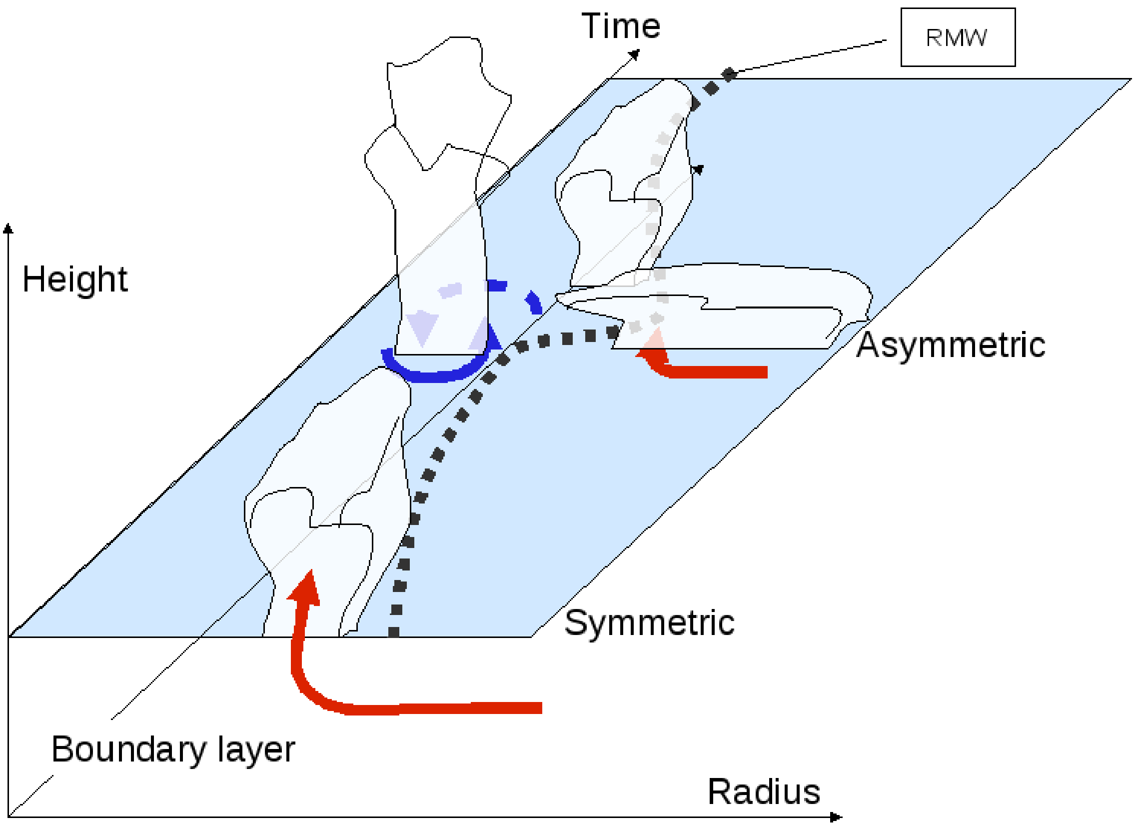

Figure 5.7: Diagram showing the conceptual evolution of the mean structure of the vortex during the transition between the symmetric and asymmetric phases.

- ***During the asymmetric phase***, when the eyewall consists of localised strong convection in the form of VHTs, the strongest tangential wind increases at radii close to the vortex center while at the RMW the acceleration of the tangential wind is reduced. This pattern of acceleration is a result of the horizontal mixing by mesovortices associated with VHTs, which transport high angular momentum from the RMW toward the vortex center.

  Moreover, strong upward velocity within VHTs during the asymmetric phase induces increased inflow in the BL at outer radii, leading to an increase of tangential wind at outer radii (A_{outer}) above the BL (e.g. at 850 hPa). This effect of VHTs is similar to that suggested by Hendricks et al. (2004) and Montgomery et al. (2006), in which rapid increase of upward velocity within VHTs draws air inwards from the surroundings, leading to the strengthening of the mean vortex at some later time.

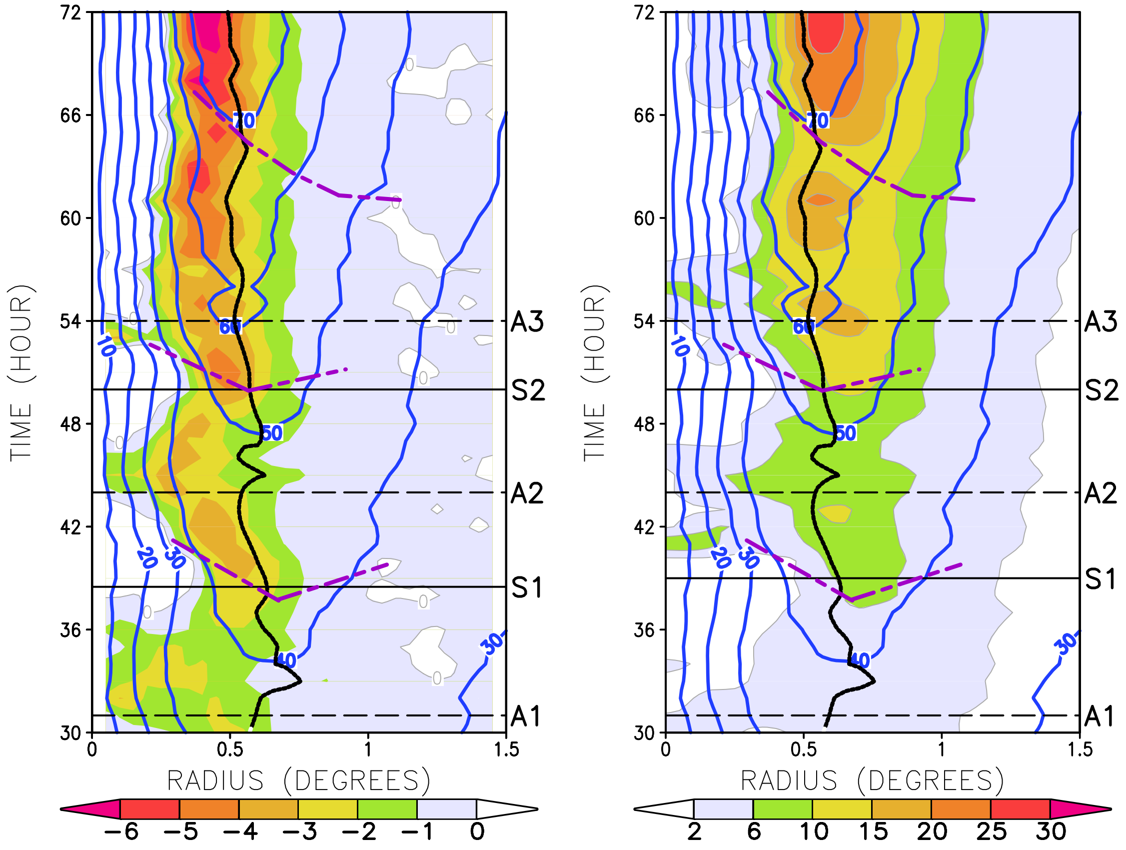

(a) $\frac{\partial \overline{PV}}{\partial r}$ at 850 hPa

(b) $\overline{S^2}$ at 850 hPa

Figure 5.8: Radius-Time plots of (a) radial gradient of mean PV [$10^{-4}\times$ PVU m^{-1}], negative values are shaded, and (b) total strain rate $S^2 = E^2 + F^2$, [$10^{-7}\times$ s^{-2}] at 850 hPa. On both figures, blue solid contours are the isolines of mean tangential wind, solid thick black lines represent the RMW, purple dashed lines indicate regions of maximum acceleration of mean tangential winds at 850 hPa.

5.1.3 Radial gradient of potential vorticity

The evolution of the radial gradient of the mean 850 hPa PV shown in Figure 5.8a illustrates the vacillation between the ring and monopole structure characteristic of the symmetric and asymmetric phases, respectively. The monopole structure has negative radial gradient at all radii from the vortex center, whereas the ring structure has positive radial gradient at inner radii and negative radial gradient at outer radii. Thus, in Figure 5.8a, regions with shaded values from the center indicate the monopole structure, and the regions with blank near the center changing to shaded at some radius constitute the ring structure. The monopole structure occurs during the periods 30-38 h, 44-47 h, and 51-54 h, whereas the ring structure during the intervening periods 38-44 h, 47-51 h, and after 54 h. These structure are not just random realisations of the vortex structure, but the manifestation of systematic changes in the modelled hurricane.

As change in the sign of the mean PV gradient is a necessary condition for barotropic instability (Schubert et al., 1999), it is suggestive that the periods when the vortex is in the symmetric phase are susceptible to break-down due to barotropic instability. Thus, the growth of VHTs which herald the end of the symmetric phase and the transition to the asymmetric phase (which is barotropically stable), may well be initiated and organised by this barotropic instability. The effects of the latter will be examined in Section 6.1.1 of Chapter 6. However, during the later stage (e.g. after 54 h of integration), the simulated vortex establishes a quasi-steady configuration with the mean PV profile having a ring-like structure without switching back to the stable monopole structure. The reasons for this cessation will be addressed in Chapter 6 also.

5.1.4 Total deformation

The evolution of the total deformation, $S^2=E^2+F^2$ as described by Equation 4.1, is shown in Figure 5.8b. Relatively large values of deformation (the shaded area) are found near the centre during the periods from 42 h to 45 h, and from 54 h to 57 h (i.e. during the asymmetric phases A2 and A3), indicating that mixing due to strain is active near the vortex centre. Note that this configuration is different from other periods, including the mature stage, during which the typical structure of horizontal strain has a maximum just outside of the RMW (where angular rotation decreases quickly) and a minimum near the center of the vortex.

During the mature stage after 66 h, rapid filamentation (large positive D) and strain rates are very strong near and just outside of the RMW (see Figure 5.8b). For the analogous configuration of strongly strained flow within the frontal zones, which is a region having concentrated positive vorticity in the form of straight bands, Bishop and Thorpe (1993) show that high strain is unfavourable for the development of barotropic instabilities. Although the hurricane problem is different in the sense that the 'frontal zones' have a ring form, Bishop and Thorpe (1993)'s results may be applicable qualitatively. To the extent that the frontal problem is relevant, high strain may explain the stability of the eyewall during the mature stage despite satisfying the necessary condition for barotropic instability. The relative magnitudes of barotropic growth rates and strain rates will be examined in Chapter 6 to clarify the effects of the latter on inhibiting the former.

5.1.5 Equivalent Potential Temperature

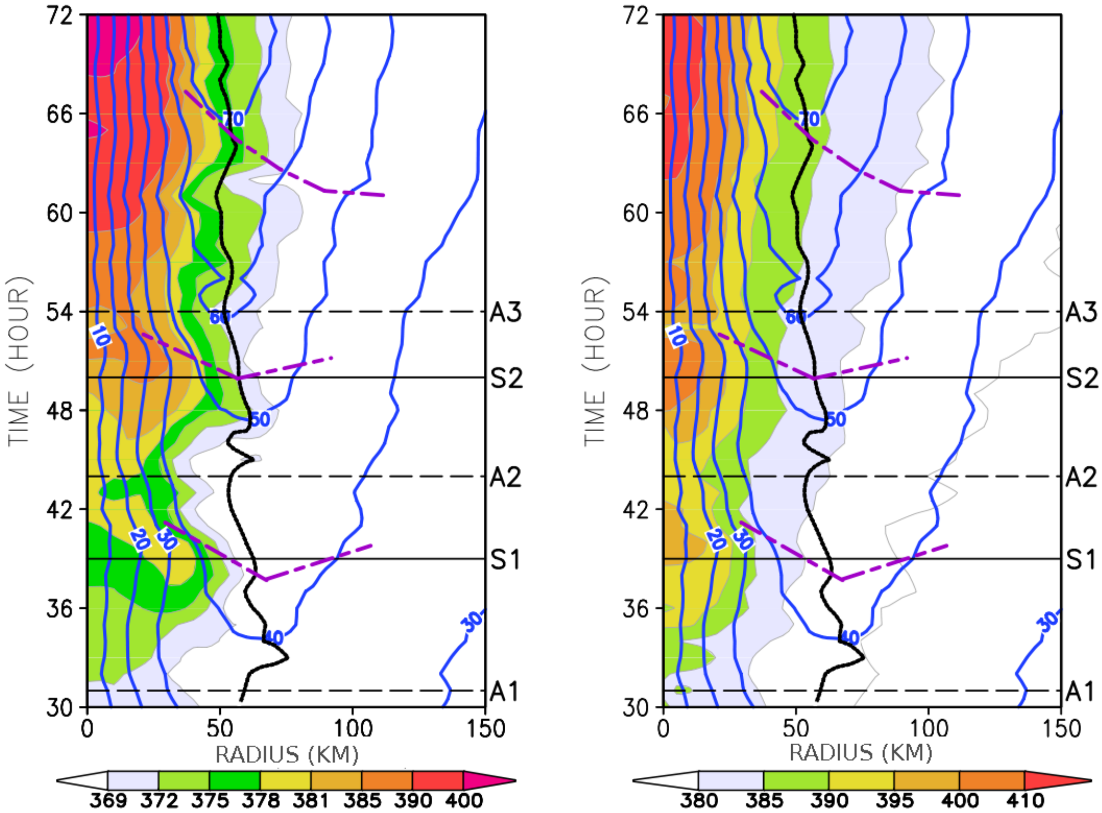

a) At 850 hPa b) At the lowest model level

Figure 5.9: As in Figure 5.8, shaded values are for equivalent potential temperature $\overline{\theta_e}$ [K] at a) 850 hPa, and b) the lowest level of the model.

Since the two phases of structure are most clearly delineated at low levels and they exhibit remarkable differences in the vertical velocity field (i.e. convection), we investigate next the evolution of the low-level equivalent potential temperature which influences the convection.

Figure 5.9a shows radius-time plots of azimuthal mean θ_e at 850 hPa. Here again, the vacillation pattern is evident with the ring structure during the symmetric phase and the monopole structure during the asymmetric phase. During the symmetric phase, a ring of high θ_e occurs at some radius (40 km during S1 and 25 km during S2). During the asymmetric phase, a θ_e maximum occurs at the vortex center and decreases significantly near the RMW. To understand the contributions of different

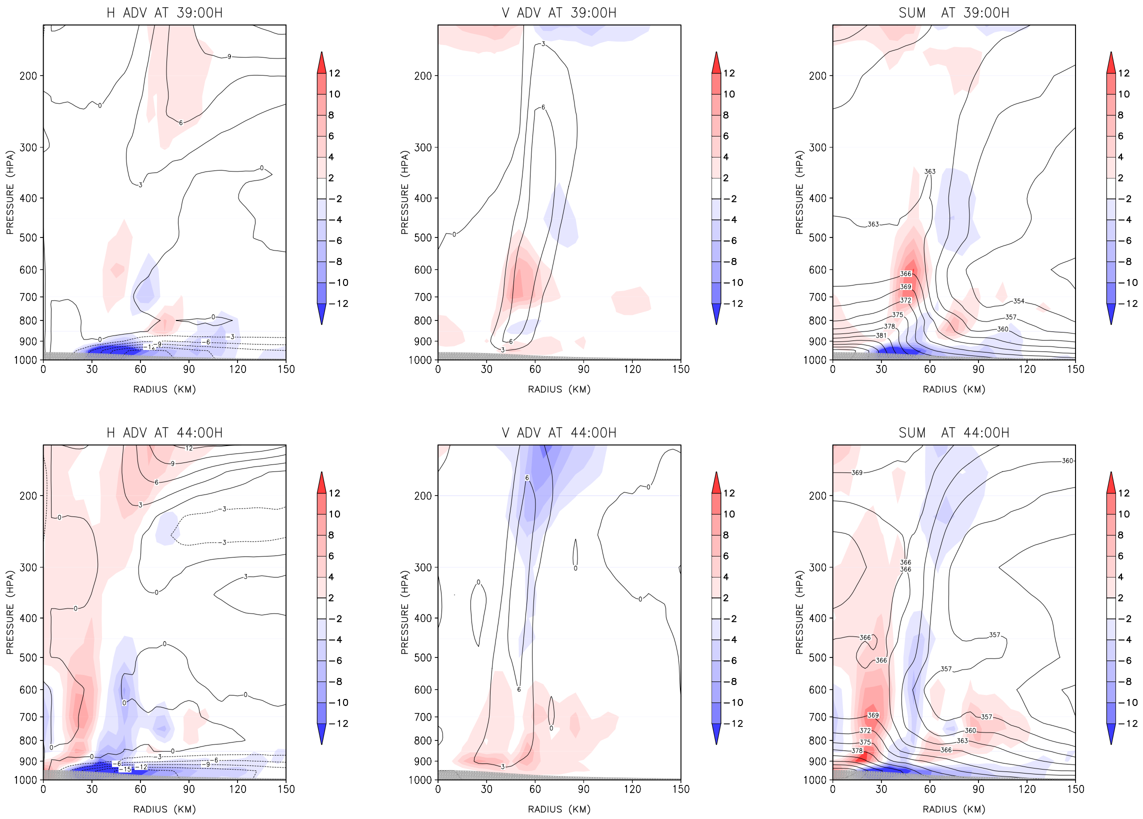

Horizontal advection	Vertical advection	Sum

Symmetric phase S1	a	c	e
Asymmetric phase A2	b	d	f

Figure 5.10: Vertical cross section of azimuthal means of the θ_e tendencies [K h^{-1}] (shaded) due to: (left panels) horizontal advection, (middle panels) vertical advection, and (right panels) the sum of the horizontal and vertical advection terms. Top panels are for the symmetric phase S1 at 39 h, bottom panels are for the asymmetric phase A2 at 44 h. Contours show (a,b) $\overline{U}$, (c,d) $\overline{-\omega}$, and (e,f) $\overline{\theta_e}$.

processes leading to this evolution pattern, we examine a budget equation for θ_e which has the following form:

$$\frac{\partial \theta_e}{\partial t} = -\left(u\frac{\partial \theta_e}{\partial x} + v\frac{\partial \theta_e}{\partial y}\right) - \omega\frac{\partial \theta_e}{\partial p} + S_{\theta_e}, \tag{5.2}$$

where the first term is the horizontal advection and the second term is the vertical advection of θ_e. S_{θ_e} is the source or sink of θ_e due to physical processes such as surface fluxes or vertical diffusion. This term is not calculated here since there is not enough data to calculate them accurately. The terms in Equation 5.2 are then azimuthally averaged to produce vertical cross sections.

Figure 5.10 shows vertical cross sections of the two first terms on the right hand side of Equation 5.2 for the symmetric and asymmetric phases. It can be seen that the high θ_e ring structure during the symmetric phase is due primarily to vertical advection (panels c and e). On the other hand, the decrease of θ_e near the RMW during the asymmetric phase is accompanied by the horizontal advection (panels b and f), which is likely to be associated with VHTs during this phase.

The evolution of the θ_e at the lowest model level shown in Figure 5.9b indicates that the monopole structure is maintained at all times, instead of vacillating as the θ_e at 850 hPa. This difference arises from the fact that θ_e at 850 hPa is subjected to vertical advection from both the high θ_e below and/or low θ_e above, whereas θ_e at the lowest level is determined largely by surface heat fluxes (apart from horizontal advection). During the asymmetric phase, θ_e at the model lowest level decreases near the core. This weakening of the high θ_e core is attributed to the horizontal mixing effects of VHTs that are active near the center during this phase. Indeed, this effect can be seen in Figure 5.11, in which a large area of negative tendencies due to horizontal advection occurs during the asymmetric phase (panel b). During the symmetric phase (panel a), this process is less active.

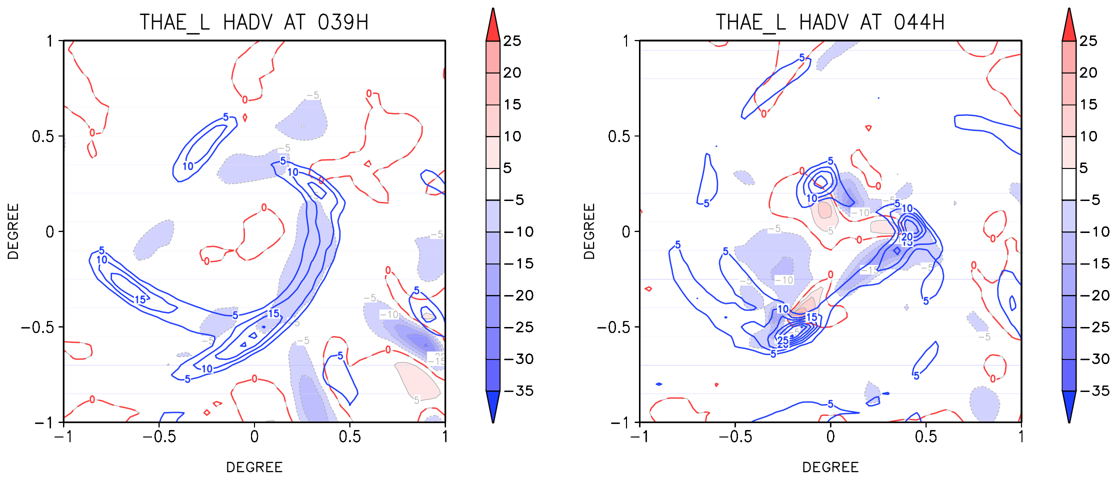

a) Symmetric phase S1

b) Asymmetric phase A2

Figure 5.11: Tendencies of the θ_e at the lowest model level due to horizontal advection $-(u\partial\theta_e/\partial x + v\partial\theta_e/\partial y)$ $[10^{-3}\times$ K s$^{-1}]$.

5.1.6 Convective Available Potential Energy

CAPE and convection are highly interdependent. Increases in CAPE increase the likelihood of convection, which, in turn, works to stabilise the atmosphere, and thus, decrease CAPE. This negative feedback is demonstrated clearly in the evolution of CAPE shown in Figure 5.12a.

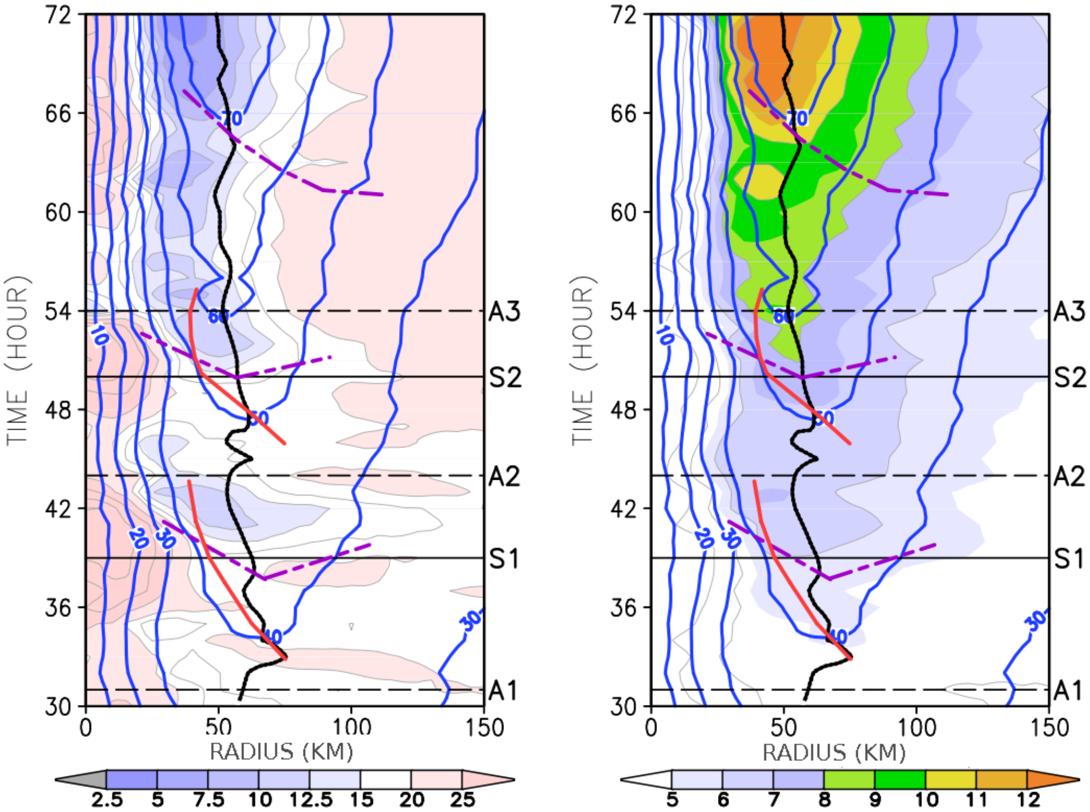

(a) CAPE

(b) Latent heat surface flux

Figure 5.12: Radius time plot of (a) CAPE [$10^2\times$ J kg^{-1}], (b) latent heat surface flux [$10^2\times$ W m^{-2}]. Red solid lines mark the position of maxim vertical motion, black thick lines mark the position of the RMW, dashed purple lines show axes of maximum tangential wind acceleration. All characteristics are at 850 hPa.

- Towards the asymmetric phase, CAPE decreases substantially at the outer side of the axes of maximum tangential acceleration (dashed purple lines), which is where convection is most active. Just prior to the times of maximum asymmetries, regions of minimum CAPE coincide with axes of maximum vertical velocity (red lines in Figure 5.12). Thus, convection indeed consumes CAPE.

- Conversely, during the transition from the asymmetric to the symmetric phase, the CAPE near the RMW is restored to higher values (see regions near the RMW from A1 to S1 and A2 to S2). This increase in CAPE may be explained partly by the reduced activity of VHTs during this period. On the other hand, the increase in CAPE near the RMW is associated with the increase of θ_e in the form of the ring structure at 850 hPa, which is a result of the upward advection of the high θ_e from lower levels (see the formation of the ring structure at 850 hPa presented in the previous section).

Of course, the CAPE is affected by factors other than convection such as latent heat surface fluxes. However, the evolution of the latter, shown in Figure 5.12b, exhibits a steady increase as the mean circulation strengthens. Thus, it appears that the VHTs play a dominant role in consuming CAPE, which in turn, reduces the tendency for further convection.

5.2 Evolution of the vertical structure of the core

The foregoing development pattern of the vortex structure at low levels prompts further interest in understanding the evolution of the vortex's vertical structure. We examine next the evolution of the vertical structure of kinematic and thermodynamic characteristics of the core of the TC.

5.2.1 Vorticity

Time-height plots of the PV and absolute vorticity (ζ_a) at the TC center, shown in Figures 5.13, exhibit a change in structure which is coherent through the depth of troposphere. While there are obvious differences in the vertical structure of the two fields (e.g. PV has maximum near the middle troposphere and absolute vorticity at low levels), they share a similar pattern of development. Both the PV and absolute vorticity evolve toward the mature stage of high intensity in a stepwise manner, with marked weakening just prior to the symmetric phase, reaching minimum at times of minimum asymmetries (i.e. S1 and S2); and strengthening during the asymmetric phase reaching maxima about 1 to 2 h after the times of maximum asymmetries (e.g. A2 and A3).

To understand this development pattern, an analysis of the absolute vorticity budget on pressure surfaces is carried out following Equation 6.1 of Haynes and McIntyre (1987) and can be rewritten in the form:

$$\frac{\partial \zeta_a}{\partial t} = -\nabla \cdot (u\zeta_a, v\zeta_a) - \nabla \cdot \left(\omega\frac{\partial v}{\partial p}, -\omega\frac{\partial u}{\partial p}\right) - \nabla \cdot (-G, F), \tag{5.3}$$

where ζ_a is the absolute vorticity on pressure surfaces, F and G are the horizontal components of the local frictional or other force **F** per unit mass, in the x and y directions respectively. Other symbols are conventional as listed in Table A.1. The first term on the right hand side represents the contribution from the horizontal convergence of the vorticity flux (i.e. changes of vorticity by horizontal advection and convergence); the second term is the generation of vorticity by stretching and

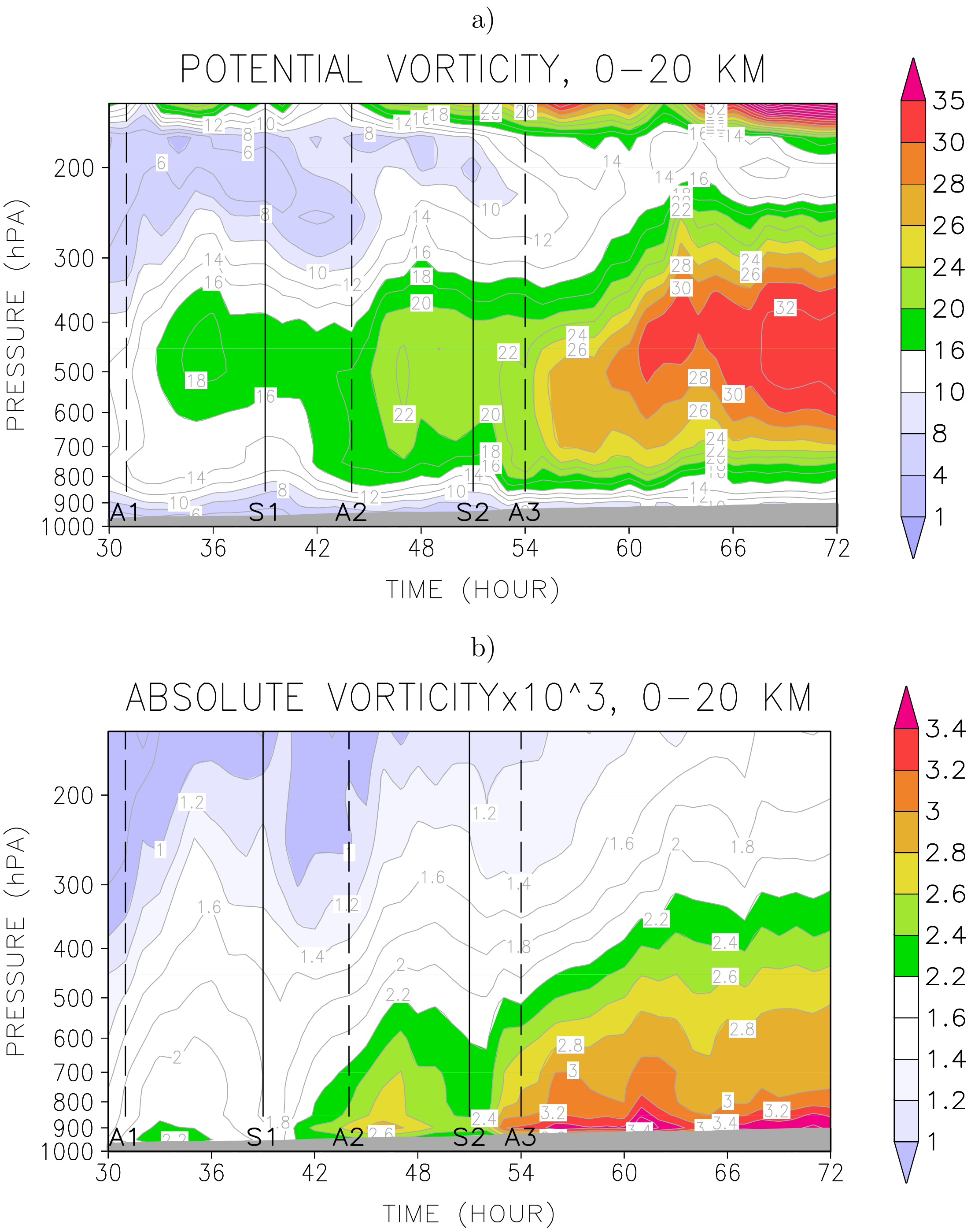

Figure 5.13: Evolution of vertical profiles of a) the potential vorticity [PVU] and b) absolute vorticy [$10^3 \times$ s^{-1}]. Values are averaged within 0 to 20 km radius, thus representing the vortex center. Areas shaded in grey at the bottom lie below the surface.

twisting (including the diabatic effects of convection), and will be referred here as the tilting term; and the last term shows the influence of other forces such as friction.

Here again, detailed descriptions and calculations are included in an Appendix

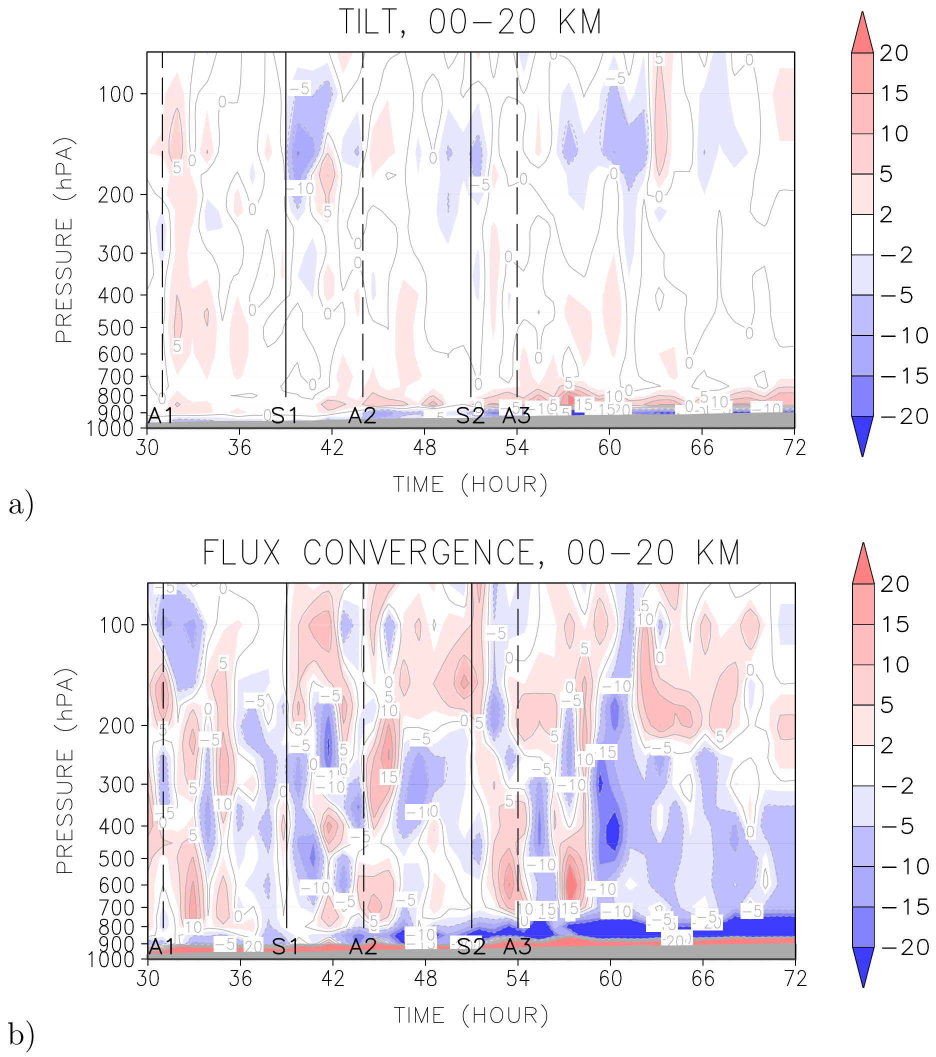

Figure 5.14: Evolution of vertical profiles of tendencies of the absolute vorticity [$10^{-8} \times$ s^{-2}] by a) the tilting term and b) the flux convergence term of the tendency equation for absolute vorticity according to Eq. 6.1 of Haynes and McIntyre (1987) (see Appendix E.1 for more details). Values are averaged for 0 to 20 km radii, representing the core of the TC.

(E.1). We only present in this section material directly related to the process being examined. Figure 5.14 shows the evolution of the azimuthally-averaged values of the two main terms (in Equation 5.3) contributing to changes in absolute vorticity: the tilting term and the flux convergence term, averaged for radii from 0 to 20 km, which represents the vortex center. Figure 5.16 shows the same features but for the 40-60 km annulus.

The comparison of panels a and b in Figure 5.14 shows that the flux convergence term is dominant in this region. During the asymmetric phases A2 and A3, the flux convergence is positive in the lower part of troposphere, which is consistent with the

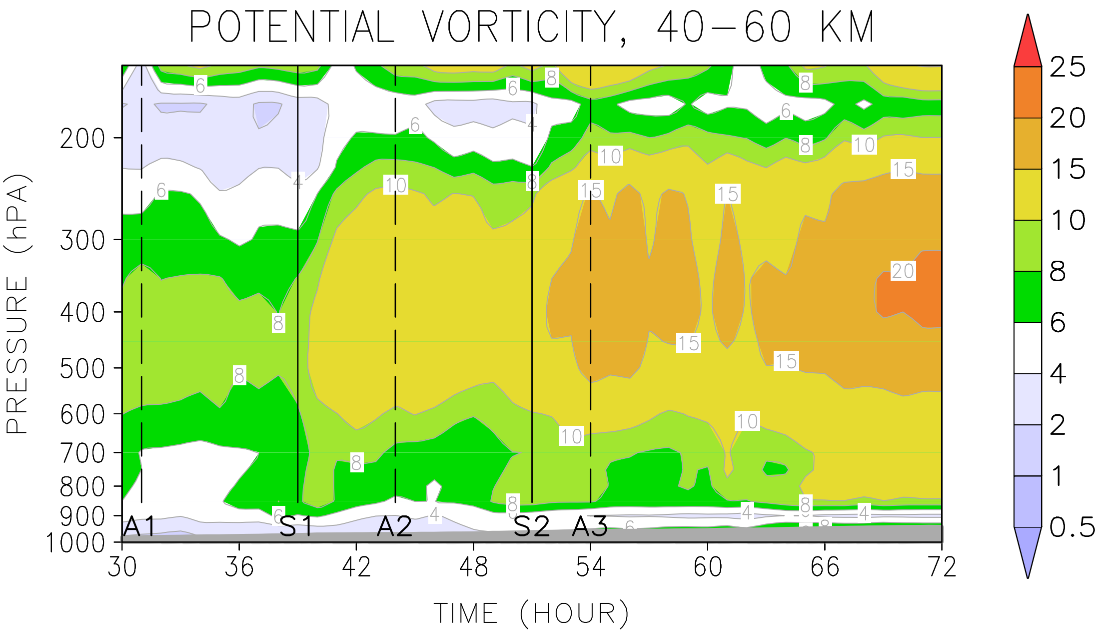

a)

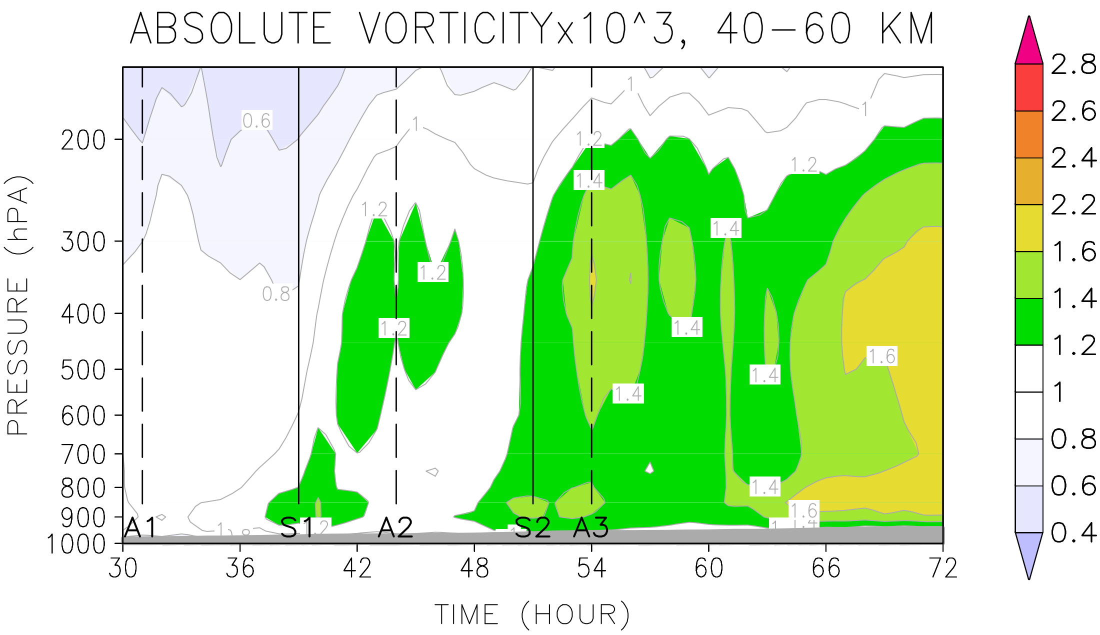

b)

Figure 5.15: As in Figure 5.13 but averaged for the 40-60 km radii, thus, representing the RMW.

increase of absolute vorticity seen in Figure 5.13b. During the same periods, flux convergence contributes to negative vorticity tendencies near the RMW (see Figure 5.16b). Thus, the increase of vorticity at inner radii and decrease near the RMW is the manifestation of horizontal mixing effects of VTHs, which are active during the asymmetric phases.

Figures 5.15 and 5.16 show the same features as in Figures 5.13 and 5.14, respec-

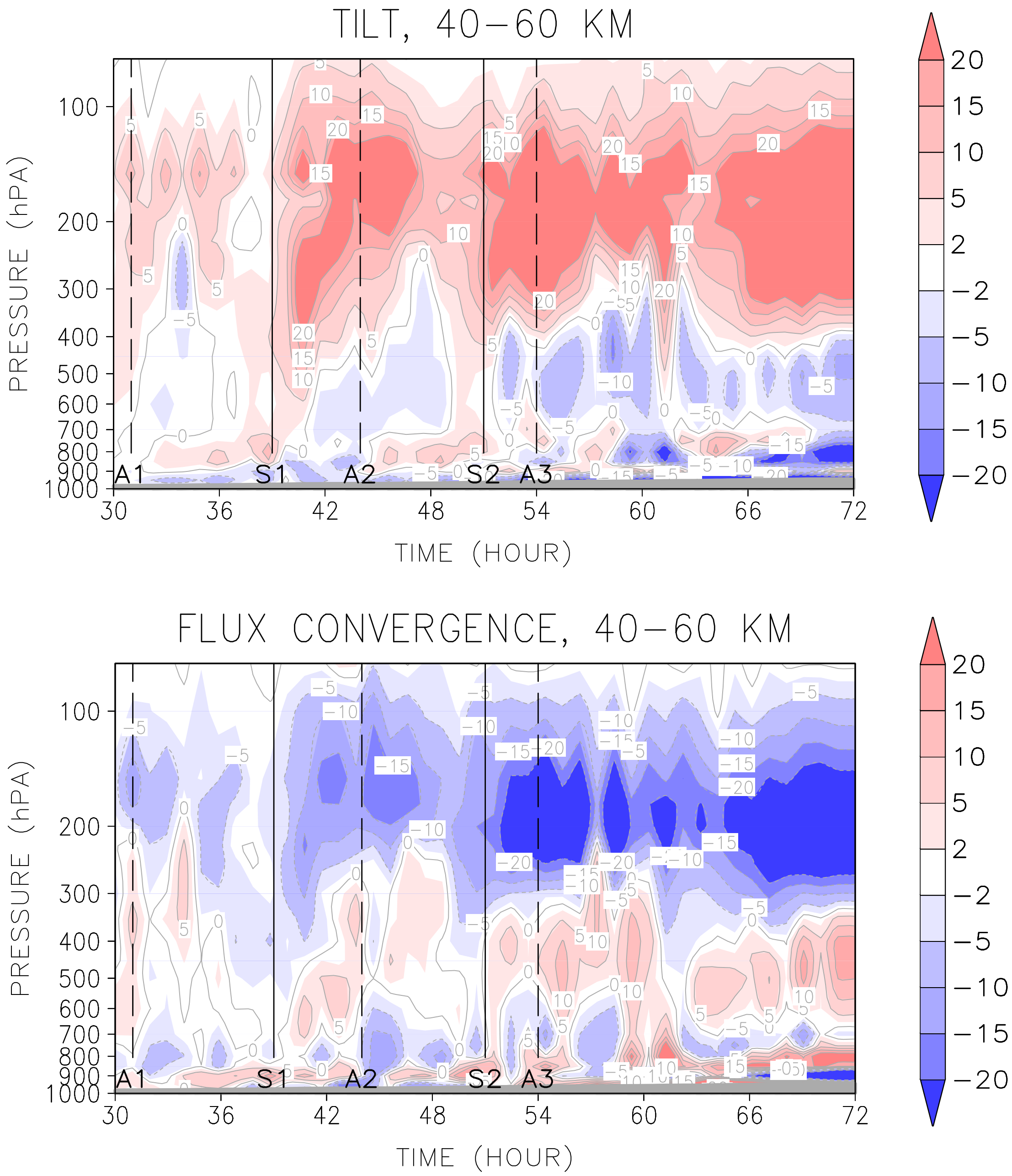

a)

b)

Figure 5.16: Evolution of vertical profiles of the potential vorticity of (a) the center over radii of 0-20 km, and (b) near the RMW, over radii 40-60 km. Areas shaded in grey at the bottom lie below the surface.

tively, but for the region between 40 and 60 km, i.e. near the RMW. At low levels (from surface to 700 hPa), both the PV and absolute vorticity strengthen during the symmetric phase, whereas high levels (say the 600 - 250 hPa layer) see maximum during the asymmetric phase (Figure 5.15b). Budget analysis shown in Figure 5.16a indicates that this spin-up pattern near the RMW is principally due to the tilting term, i.e. by local rate of diabatic heating in the eyewall.

Thus, the evolution of low-level vorticity near the vortex center is out of phase with that near the RMW. Changes of the vorticity in these two regions are consistent with the vorticity theorem of Haynes and McIntyre (1987), which postulates that 'vorticity can neither be created nor destroyed, within a layer bounded by two isobaric surfaces'. In this case, the increase (convergence) of the vorticity near the RMW during the symmetric phase is accompanied by the decrease (dilution) of vorticity in the core region. Therefore, this difference in the timing is not contradictory but can be seen as two parts of the same evolving system.

5.2.2 Equivalent potential temperature

Like the pattern of vorticity described above, the equivalent potential temperature (Figure 5.17a) evolves through cycles, with values near the surface increasing during the symmetric phase but decreasing during the asymmetric phase. However, this pattern is reversed at the levels above (up to about 500 hPa) with an increase during the asymmetric phase and a decrease during the symmetric phase. In fact, during the asymmetric phase, θ_e is nearly constant in the 700-500 hPa layer (seen as the vertical orientation of moist isentropes 365 K and 370 K prior to A2 and A3, respectively).

Figure 5.17b shows the evolution of the vertical structure of the θ_e in the region near the RMW. Below about 500 hPa, θ_e increases during the symmetric phase and decreases during the asymmetric phase, and is thus, in the opposite phase to the θ_e in the vortex center. This vacillation pattern is consistent with the dynamical processes described above, i.e. strong vertical advection near the RMW during the symmetric phase and strong horizontal advection near the vortex center during the asymmetric phase. Indeed, a budget analysis[1] of θ_e, shown in Figure 5.10, indicates that the increase of the θ_e near the RMW during the symmetric phase S1 (panel e) comes mainly from vertical advection (panel c), whereas the increase near the vortex center during the asymmetric phase A2 (panel f) arises mainly from horizontal advection (panel b).

[1]Details of the budget analysis for θ_e are included in Appendix E.3.

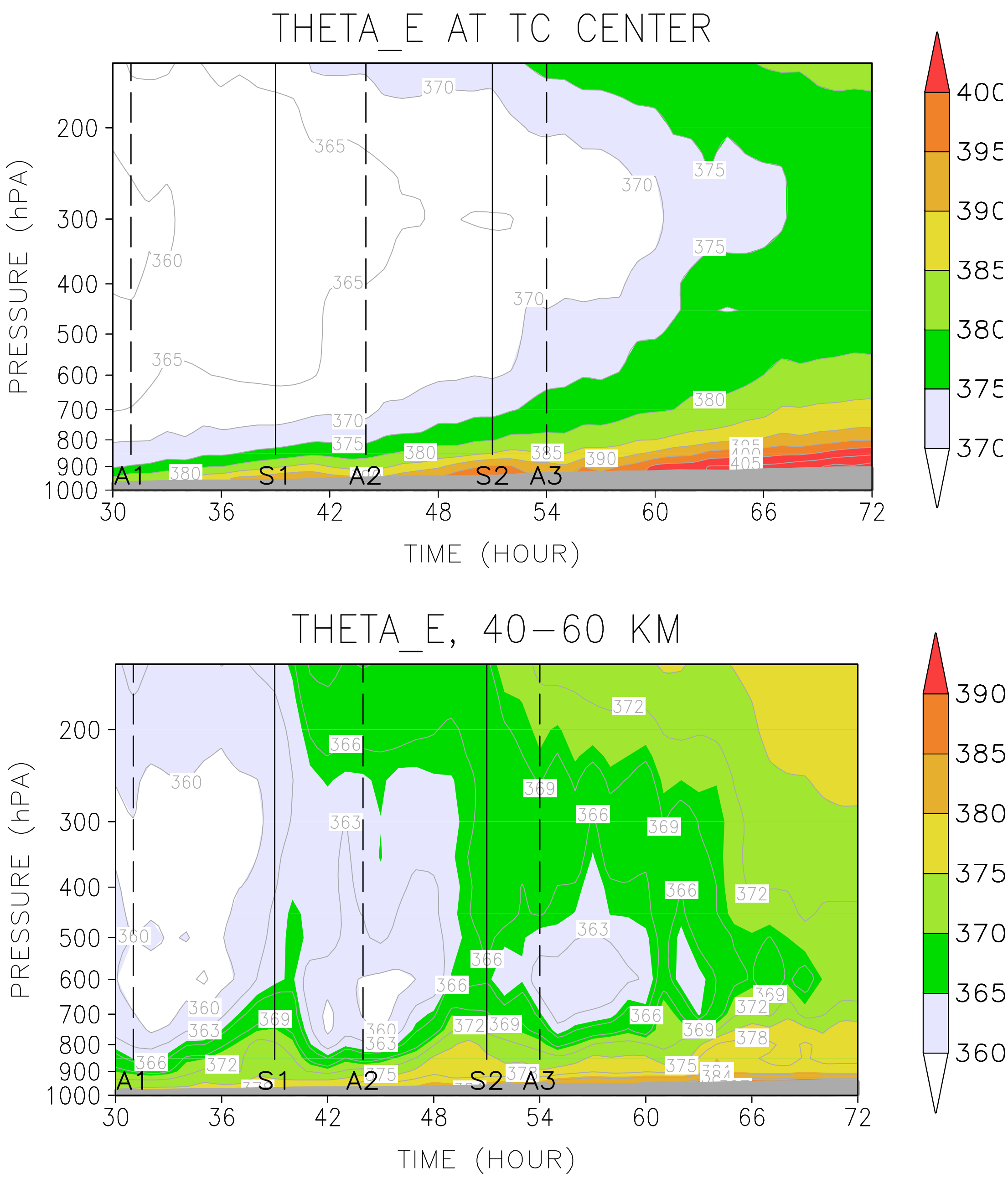

a)

b)

Figure 5.17: Time-height plots of the azimuthally-averaged θ_e [K] averaged for a) the vortex center (0 to 20 km) and b) the RMW (40 to 60 km).

5.3 Summary of Chapter 5

In this chapter, we have investigated the evolution of the structure of the simulated vortex while vacillating between symmetric and asymmetric phases during rapid intensification. The main characteristics of the structure evolution can be summarised as follows:

- ***During the symmetric phase***, the mean vortex has a typical TC structure with the secondary circulation that plays an important role in advecting properties out of the BL. As a result, the mean tangential wind, potential vorticity, and equivalent potential temperature (and thus CAPE) increase in the region near the RMW. By the end of this period, PV and θ_e have ring structures with the maximum located at some distance from the center. This configuration satisfies the necessary conditions for barotropic instability. Thus, the mean vortex intensifies while becoming more barotropically and convectively unstable.

- ***During the asymmetric phase***, the mean tangential wind increases at inner radii while decreasing near the RMW due to the horizontal mixing effects of VHTs that develop during this period. As the rate of intensification near the RMW slows, this phase can be viewed as a disruption of the almost axisymmetric secondary circulation characteristic of the symmetric phase. At outer radii, however, strong updraughts in the VHTs induces enhanced inflow in the BL, leading to slight intensification of mean tangential wind there. At the same time, horizontal vortical circulations associated with the VHTs mix air between the eye and the eyewall producing the monopole structure in the fields of PV and θ_e with their maximum at the center. Hence, the vortex becomes barotropically stable (as the PV gradient does not change sign), and less convectively unstable (as θ_e and hence CAPE decreases) near the RMW. As a result, the VHTs weaken after the asymmetric phase and the vortex evolves to another symmetric phase.

From the evolution of mean fields, it appears that barotropic instability associated with the PV ring structure, and increased convective instability, connected to the high θ_e near the RMW, are the main two factors leading to the rapid growth of the VHTs during the symmetric phase. On the other hand, the weakening of VHTs after the asymmetric phase is related to local decreases in the CAPE, which result from VHTs themselves. Thus, it appears that the VHTs[2] play an important role in the vacillation cycles.

[2]We have examined also the evolution of individual VHTs. However, it is found that the evolution of the mean vortex is influenced by the collective effects of VHTs rather than of individual VHTs. Therefore, the material on life cycles of individual VHTs are included in Appendix F for interested readers.

Chapter 6

TRANSITION MECHANISMS

As the symmetric and asymmetric phases have been analysed in Chapter 4 and the evolution of the vortex structure has been investigated in Chapter 5, the next task is to understand the physical processes leading to these changes. Before proceeding further, we recall the main points identified in the preceding chapters that will prove useful in understanding these underlying physical processes. These points are the following:

- During the symmetric phase, low-level vorticity has a ring structure, which satisfies the necessary condition of barotropic instability.
- The development of VHTs at the start of the asymmetric phase indicates the presence of large convective instability.
- The increase in the mean tangential wind, vorticity and θ_e at inner radii during the asymmetric phase is largey due to horizontal advection by the mesoscale circulations associated with the VHTs.
- The weakening of VHTs after the asymmetric phase is associated with a decrease in CAPE.
- During the mature stage, the vorticity at low levels has a ring structure; the eyewall has low values of CAPE, and hence low convective instability; and the flow is strongly strained outside of the RMW inhibiting convective development. Structure change cycles in which the eyewall breaks into small vortices, or VHTs, do not tend to occur during this period.

6.1 Symmetric to Asymmetric Transition

As discussed in the previous chapter, the transition from the symmetric phase to the asymmetric phase is accompanied by the development of VHTs from weak asymmetries within the eyewall. Given the condition for barotropic instability of the ring structure during the symmetric phase, the immediate explaination for the growth of these VHTs is naturally the barotropic instability. Barotropic instability is also suggested by Kossin and Eastin (2001) (following the work of Schubert et al. (1999)) as the means for the transition from their Regime 1 to Regime 2, which is equivalent to our symmetric to asymmetric transition. The role of barotropic instability in the formation of VHTs and the breakdown of the eyewall will be examined in section 6.1.1.

A difficulty with the barotropic instability argument is that the growth rate of barotropic disturbances is too small. In the calculations presented by Schubert et al. (1999), the whole process including the break-down of the ring-like structure and the formation of a vorticity monopole took about 48 h, which is much longer than observed in Kossin and Eastin (2001) (within 1 to 2 h) and found in our simulation (about 2 to 4 h). Moreover, even though the mature stage satisfies the condition for barotropic instability (i.e. the elevated vorticity ring structure, and thus, the sign change of the radial gradient of PV), the eyewall does not break down as it does during the rapid deepening stage.

In the simulation analysed in Chapters 4 and 5, the VHTs that developed during the asymmetric phases (see e.g Figure. 4.4b,d) grew from weak local maxima of upward motion within the relatively symmetric eyewall (Figures 4.4a and c). The development of the VHTs suggests that convective instability plays a role in this process; this possibility will be examined in Section 6.1.2.

The eyewall mesovortices referred to by Kossin and Eastin (2001) are swirling regions of low-level cloud in the region inside the eyewall (see e.g. Figure 1.7). In contrast, the VHTs in our simulated vortex are regions of strong upward motion, and thus, associated with deep convective clouds. Although both have their own meso-circulations which play roles in mixing air between the eye and the eyewall to form the monopole structure, the mesovortices as reported by Kossin and Eastin (2001) and VHTs in our simulation have very different convective structures; their relationship will be examined in Section 6.1.3.

6.1.1 The Role of Barotropic Instability

We investigate now the barotropic instability of the azimuthally-mean vorticity radial profiles of the simulated vortex and its part in promoting the growth of asymmetric disturbances. For this purpose, we employ the method devised by Weber and Smith (1993), which is based on the non-divergent barotropic vorticity equation to determine the normal modes, and apply for the mean tangential wind profiles from the simulation.

Following Weber and Smith (1993) the barotropic perturbation vorticity equation in cylindrical coordinates (r, θ, z) is:

$$\frac{\partial \zeta'}{\partial t} + \Omega(r)\frac{\partial \zeta'}{\partial \theta} = \frac{1}{r}\frac{d\zeta_a(r)}{dr}\frac{\partial \psi'}{\partial \theta} \tag{6.1}$$

where

$$\zeta' = \frac{1}{r}\frac{\partial}{\partial r}\left[r\frac{\partial \psi'}{\partial r}\right] + \frac{1}{r^2}\frac{\partial^2 \psi'}{\partial \theta^2} \tag{6.2}$$

ζ' is the relative vorticity perturbation; ψ' is the perturbation streamfunction satisfying $u' = (\partial\psi'/\partial\theta)/r$ and $v' = (\partial\psi'/\partial r)$; $\Omega(r) = V(r)/r$ is the angular velocity of the vortex flow; and $\zeta_a(r) = [dV(r)/dr] + \Omega(r) + f$ is the absolute vorticity.

Normal mode solutions of the form

$$\psi'(s, \theta, t) = \Re\{\widehat{\psi}(s) exp[i(k\theta - \omega t)]\} \tag{6.3}$$

are sought, where $s = r/r_m$ is the non-dimensional radius, r_m is the RMW, k is the azimuthal wavenumber and ω the frequency of the mode in question. Equation 6.1 is integrated numerically and stability is investigated based on the imaginary part of the solution 6.3. Equation 6.1 is rewritten as a set of four first-order equations for the variables ψ_r, ψ_i, $(d\psi_r/ds)$, $(d\psi_i/ds)$, where indices of r and i denote the real and imaginary parts. Then, for the prescribed values of k, ω_r, and ω_i, these first-order differential equations are integrated inwards into a finite point s_c within the domain using boundary conditions at s_0 and s_∞. An eigensolution is the one having the two parts of the solution (integrated from s_0 outwards and s_∞ inwards) joining smoothly at s_c. This condition is satisfied if a function $F(\omega_r, \omega_i, k)$, calculated using the solutions at two sides of s_c, is zero. Then, for a given wavenumber k, eigenvalues are searched by finding the points on the surface $(\omega_r, \omega_i, F(\omega_r, \omega_i, k))$ touches the plane $(\omega_r, \omega_i, 0)$. Such eigenvalues are determined accurately by the downhill method proposed by Bach (1969). For the full description of the numerical method, refer to Weber and Smith (1993).

Figure 6.1 shows the evolution of the amplitudes of azimuthal wavenumbers 2, 3

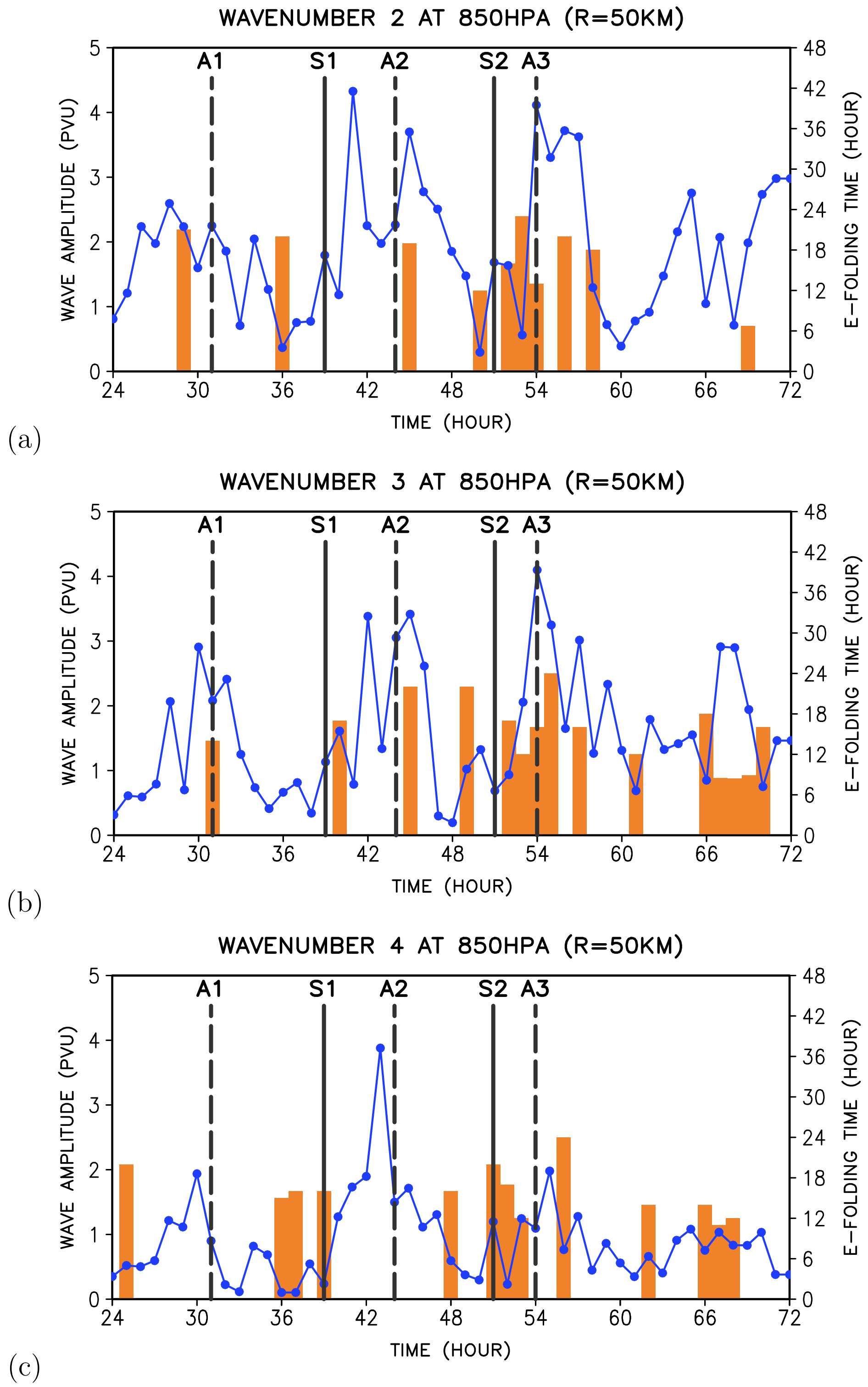

Figure 6.1: Evolution of azimuthal wave amplitudes of PV (lines) at 850 hPa along the 50 km radius and e-folding time [h] (columns) of perturbations imposed on the symmetric vorticity profiles of the simulated vortex. Panels a, b, and c are for wavenumbers 2, 3, and 4 respectively. The slow growth rates having inverse greater than 24 h are not plotted.

and 4 and e-folding time calculated as the inverse of the imaginary frequency ω_i^{-1}[1] of the corresponding wavenumbers calculated by the Weber and Smith's method. Slow growth rates with the e-folding times greater than 24 h are not plotted. The results presented in Figure 6.1 are for the ring at 50 km radius (which is near the eyewall) on the 850 hPa surface. Similar results for other radii and at the 250 hPa level are included in Appendix D.

As can be seen from these figures, episodes of fast growth rates (i.e. small e-folding time), which are indicated by the shaded columns, occur just prior to the subsequent asymmetric phase where wave amplitudes peak. This can be seen clearly in Fig. 6.1c for wavenumber 4 with periods of small e-folding time near 18 to 24 h (before the first asymmetric phase A2); 39 h (before the asymmetric phase A2); and shortly before asymmetric phase A3 at 54 h. However, toward the later times (for example between 66 and 68 h), although the mean profile are unstable for wavenumber 4 (small inverse growth rate), subsequent increase in amplitudes of this wavenumber is not observed. This non-development, despite the favourable barotropic instability, is consistent with the findings of Wang (2008a) that wavenumbers 4 and higher are damped effectively by rapid filamentation, which is typically strong during the mature stage. For wavenumbers 2 and 3 (Fig. 6.1a,b), relatively small invere-folding time occurs also from the symmetric phase S2 to the asymmetric phase A3, thus, consistent also with the increased wave amplitudes during the asymmetric phase A3.

The e-folding time calculated above are slower than the transition times in the simulation. This is probably to be expected since they are strictly valid for the linear instabilities of the unforced barotropic vortex, whereas our simulation is essentially baroclinic with a full presentation of the physical processes. Nonetheless, the agreement between the timing of the calculated fast growth rates and the observed subsequent peaks in amplitudes of the corresponding wavenumbers suggest that barotropic instability plays a part promoting the asymmetries during the transition toward the asymmetric phase.

Note that the 850 hPa level is chosen for the barotropic instability calculation due to the occurence of the PV ring structure at this level (see e.g. Figures 4.17a and c in Chapter 4). Although it is a shallow layer, the agreement between the calculated

[1]If the solution of perturbations has the form $\psi' = \hat{\psi}\exp(-i\omega t)$, similar to Equation 6.3, then the inverse of the growth rate $\omega_i^{-1} = \frac{t}{ln(\psi'/\hat{\psi})} = \frac{t}{1}$ if the perturbation has increased e times, i.e. $(\psi'/\hat{\psi} = e)$. Thus, the inverse growth rate represents the time taken for the perturbation to amplify e times, i.e. the e-folding time.

growth rates of barotropic instability and the development of asymmetries just discussed above indicates that this layer is important. As the 850 hPa level is near the top of the BL, from which convective entities (VHTs) develop, barotropic instability may play a role in the initial organisation of the VHTs. It is then not surprising that the VHTs are seen located relatively evenly around the eyewall (see e.g. Figure 4.4).

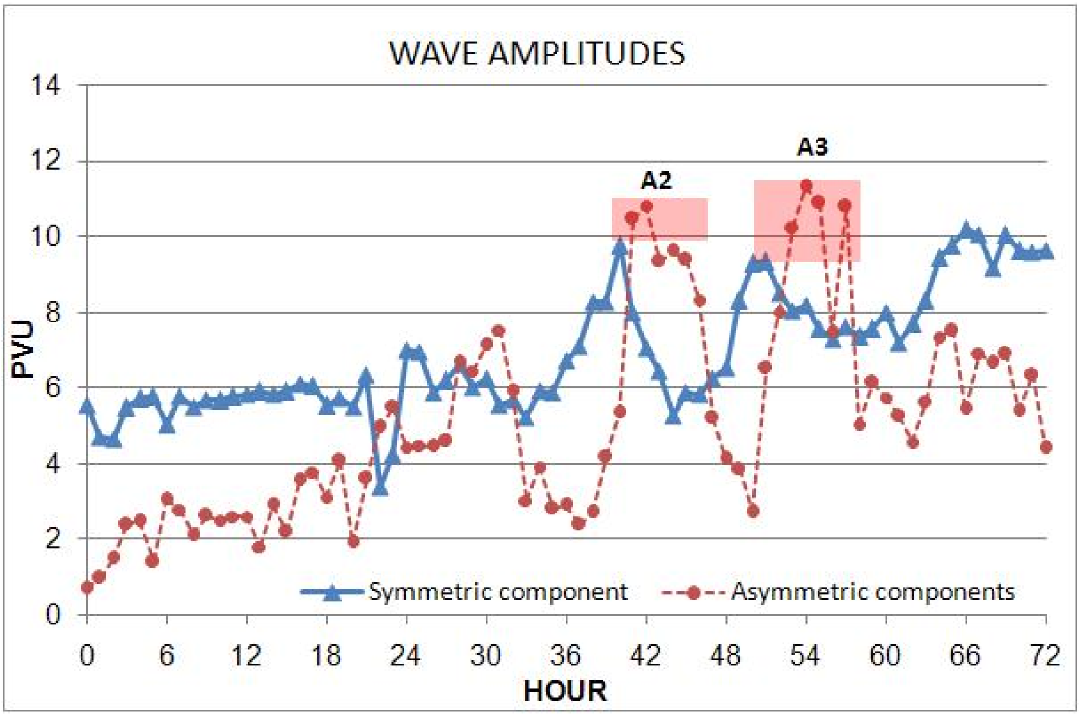

Figure 6.2: Evolution of PV wave amplitudes of symmetric component (blue line with triangles) and asymmetric component (dashed red line with circles) calculated as the sum of amplitudes of wavenumbers from 1 to 4.

Furthermore, recall that Figure 4.1b in Chapter 4 shows a shift of the maximum amplitude from symmetric to asymmetric components during the transition from the symmetric to asymmetric phase. This transition can be seen more clearly in Figure 6.2 which shows the evolution of wave amplitudes[2] of the PV symmetric and asymmetric components along the 50 km radius circle at 850 hPa. The asymmetric component is calculated as the sum of the amplitudes of wavenumbers from 1 to 4. During the symmetric phases, the amplitude of the symmetric component reaches a local maximum which is greater than that of the asymmetric component. The asymmetric phase emerges soon after that with a rapid increase of the asymmetric component (to a value larger than the symmetric amplitude during the preceding symmetric phase), while the symmetric component decreases. This shift of the max-

[2]Recall that PV is decomposed by Fourier series into different azimuthal wavenumbers as presented in Figure 4.1b.

imum apmplitude from the symmetric to asymmetric components is consistent with barotropical conversion, in which the growth of asymmetries comes from the unstable symmetric component.

While the evolution of PV asymmetries at 850 hPa indicates possible roles of barotropic instability during the symmetric to asymmetric transition, similar evidence is unclear at 250 hPa, despite a high level of asymmetry there. For instance, the evolution of amplitudes of PV azimuthal wavenumbers at 250 hPa for the 50 km radius shown in Figure 6.3, which is similar to Figure 4.1b, does not show the shift of maximum amplitude from the symmetric to asymmetric component. Instead, maxima of both symmetric and asymmetric components occur at the same times, during the identified asymmetric phases. Furthermore, growth rates due to barotropic instability calculated for the mean profiles at this level (shown in Figures D.7 to D.10 in Appendix D) do not show a clear association pattern with the PV asymmetries as the low-level counterpart. Thus, this indicates that asymmetries at upper levels are the manifestation of the overshooting convection from lower levels, rather than being generated in-situ by barotropic instability of the symmetric component.

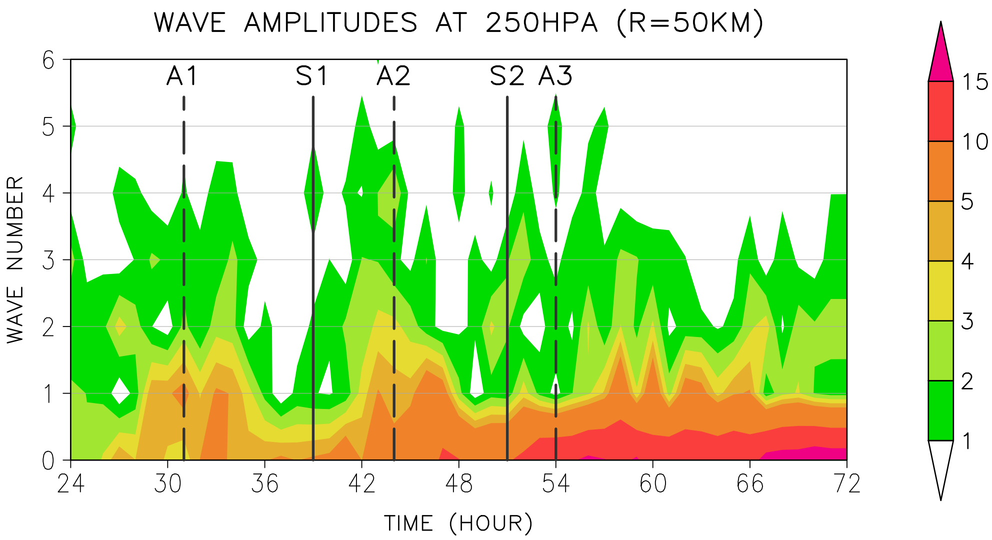

Figure 6.3: Evolution of PV wave amplitudes [PVU] at the 50 km radius on the 250 hPa level.

.

6.1.2 The Role of Convective Instability

In the simulations using the full-physics TCLAPS model, deep convection is present as in nature, and its occurrence may offer an explanation for the rapid development of asymmetries during the symmetric-to-asymmetric transition. We will examine the role of convective instability during this transition.

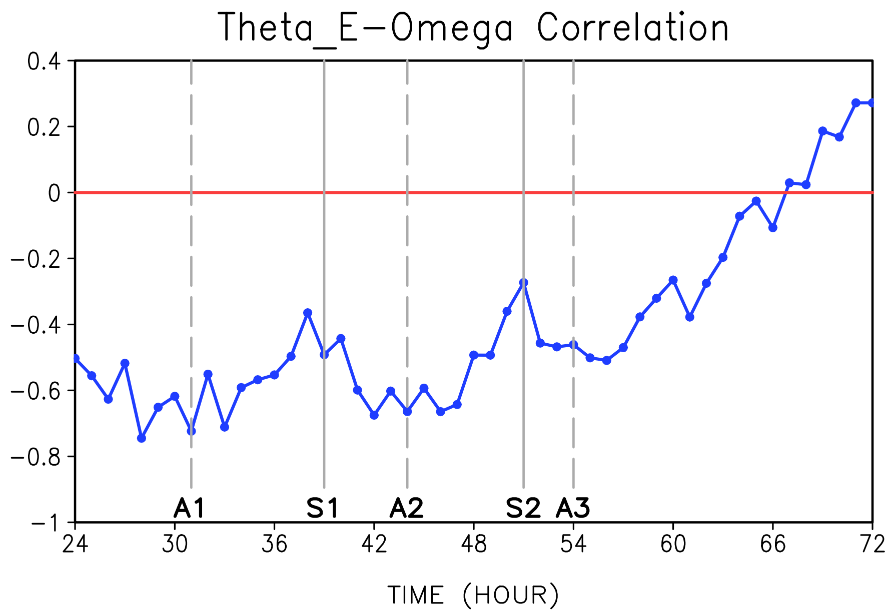

Figure 6.4: Evolutions of spatial correlation coefficients between ω and θ_e of the inner core region inside of the 50 km radius at 850 hPa.

The transition from the symmetric to the asymmetric phase is accompanied by VHTs growing from initially-weak asymmetric disturbances on the eyewall. These VHTs are found in regions with local maxima in the CAPE (Fig. 4.14b,d) and low-level θ_e (Fig. 4.11b,d), and are clearly associated with convective instability. This association is further confirmed by the examination of spatial correlation coefficients between vertical velocity (representing VHTs) and low-level θ_e shown in Figure 6.4. Relatively large values of negative correlation coefficient are indeed found during the asymmetric phases (marked as A1, A2, and A3), confirming the close ties of VHTs to the convectively unstable locations.

As both barotropic and convective instability appear to play parts in promoting convection in VHTs, it is necessary to explain how they work cooperatively. We explain this process as follows. First, weak vorticity anomalies within the eyewall grow through barotropic instability. These cyclonic vorticity anomalies at low levels are associated with upward motion, which strenghthen as vorticity anomalies strengthen. Second, as mass is transported upwards in the strengthening updraughts, low-level air in the vicinity is drawn inwards inducing stronger convergence. In turn, this increasing converging wind causes larger surface fluxes, leading to the increase of the atmospheric θ_e at low levels. Finally, the increasing low level θ_e means a more unstable condition for convection, thus, induces stronger upward motion. This positive feedback loop is shown and discussed early in Section 4.2.1.

It appears that the transition from the symmetric to the asymmetric phase is not simply due to barotropic instability as proposed by Kossin and Eastin (2001), but rather a result of deep convection initiated along the eyewall by barotropic instabilities. Furthermore, an interaction of surface flux and convective circulations appear to be important in the coupling between barotropic instability and convective instability.

6.1.3 The formation of the monopole structure

The subsequent mixing of vorticity as described by Kossin and Eastin (2001) can be viewed in a different light when the presence of VHTs in the eyewall region is considered. While eyewall mesovortices are observed as meso-circulations inside of the eyewall with low-level spiralling cloud systems (see for example Figure 1.7), the VHTs are certainly associated with deep convection within the eyewall. Thus, although VHTs have their own meso-circulations, they are different from eyewall mesovortices. We will investigate next the relationship between them.

Figure 6.5 shows the evolution of a PV local maximum represented by the Laplacian[3] of PV ($-\nabla^2 PV$) that is initially associated with a VHT, but subsequently becomes detached from the area of convection. During a 40 minute period, the cyclonic anomaly (marked by a filled circle inside of a triangle) is initially associated with a deep convective area (panel a), then gradually detaches from the convective area (panels b,c,d), and moves towards the vortex center (panels e and f). The vorticity monopole structure with the maximum at the vortex centre develops through a sequence of similar episodes.

The movement of the cyclonic PV local maxima towards the vortex center can be explained by the process similar to the non-linear β effect leading to north-west (south-west) drifting of TCs in the Northern (Southern) Hemispheres (see e.g. Chap-

[3]It is shown in Appendix B that Laplacian can be regarded as a proxy for anomaly.

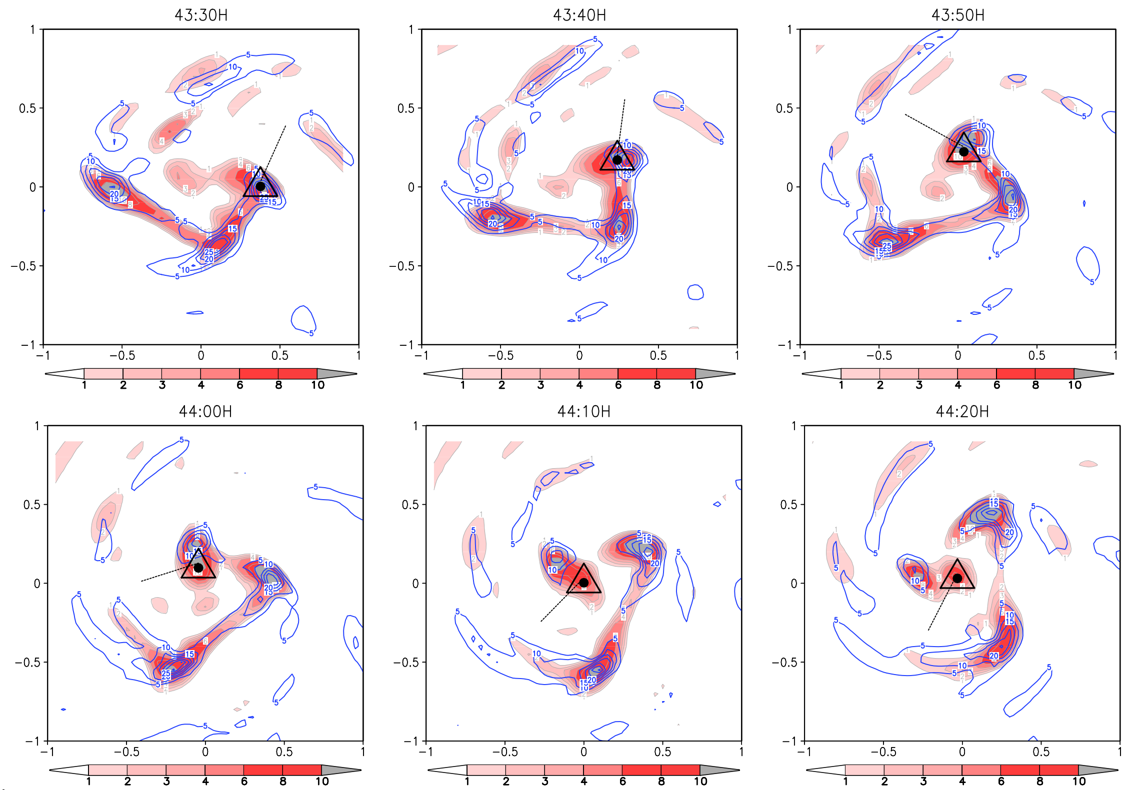

,

a	b	c
d	e	f

Figure 6.5: Local PV maxima calculated by $-\nabla^2(\mathrm{PV})$, $[10^{-8}\times$ PVU $\mathrm{m}^{-2}]$ (red shades represent positive anomalies). Contours are vertical velocity [-1$\times$ Pa s^{-1}]. Dotted lines ending with filled circles inside triangles mark the positions of local PV maxima. The figures show the fields at 10 minutes intervals after 43:30 h of integration, during the transition from the symmetric to the asymmetric phase.

ter 4 in Elsberry et al., 1987). In this process, non-linear advection of the planetary vorticity by the TC circulation induces a positive cyclonic tendencity in the poleward side of TC, causing the TC to shift poleward. During the symmetric-to-asymmetric transition, a similar process is suggested to occur with the VHTs, which are located in the negative mean PV radial gradient (as shown in Figure F.13 in Appendix F). Then, analogous to a TC vortex on the β plane, the VHTs move toward the vortex centre where the PV has higher values. During this inward movement, the VHTs-vortices mix high PV near the eyewall and low PV near the eye, thus increase the vorticy near the vortex center[4]. The detachment of the local maximum PV from the local maximum of convection (as depicted in Figure F) can be explained by different processes that control the vorticity and convection: the voricity circulation

[4]Although the physical size of VHTs appear to be small, of the order of 10-20 km, the advection by their circulations affect a much larger surrounding areas (in the order of 50 km as can be seen in Figures E.2a in Appendix E).

is driven toward the vortex centre by the β gyre-like process, whereas the convection maximum centre does not move inward due to the unfavourable stable environment near the TC eye by the warm core aloft.

6.2 Asymmetric to Symmetric Transition

6.2.1 The weakening of the Vortical Hot Towers

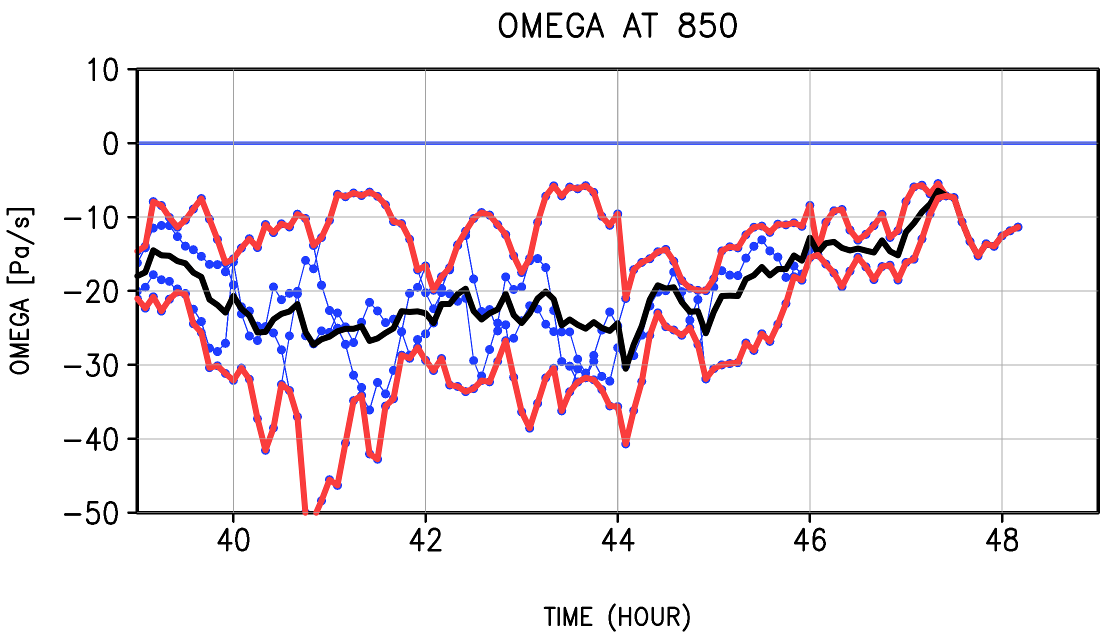

Figure 6.6: Evolution of the vertical velocity ω $[Pa/s]$ for all VHTs. Red thick lines indicate maximum and minimum values among all VHTs, which serve as the envelope of all VHTs. Thick black line shows the average values for all active VHTs.

Figure 6.6 shows the evolution of vertical velocity of all four VHTs during the period from 39 h (i.e. the symmetric phase S1) to 48 h (just before the symmetric phase S2). Although the times at which each individual VHT[5] reaches its maximum updraft are different, there is a noticeable weakening trend of all four VHTs after the asymmetric phase A2 at 44 h.

On one hand, the collective weakening of the VHTs after the asymmetric phase can be explained by the reduction of CAPE, which is consumed by the VHTs themselves, as described in Section 5.1.6. On the other hand, the evolution of the local vertical wind shear in the eyewall region may offer another explanation and will be

[5]The evolution of each VHT and the thermo-dynamical conditions along their tracks are included in Appendix F.

described now.

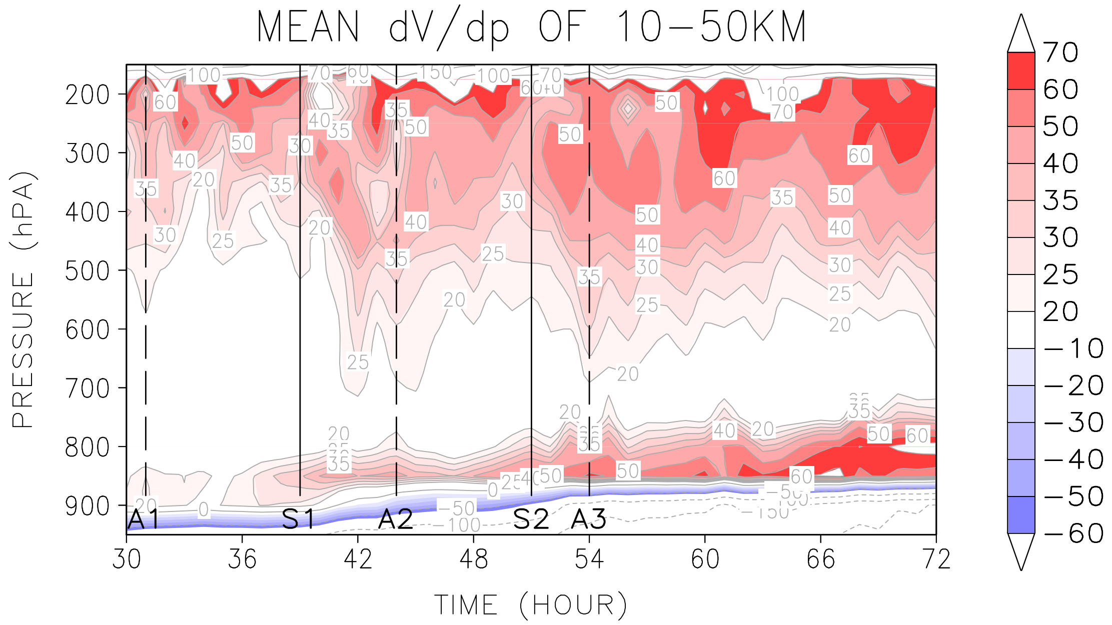

(a)

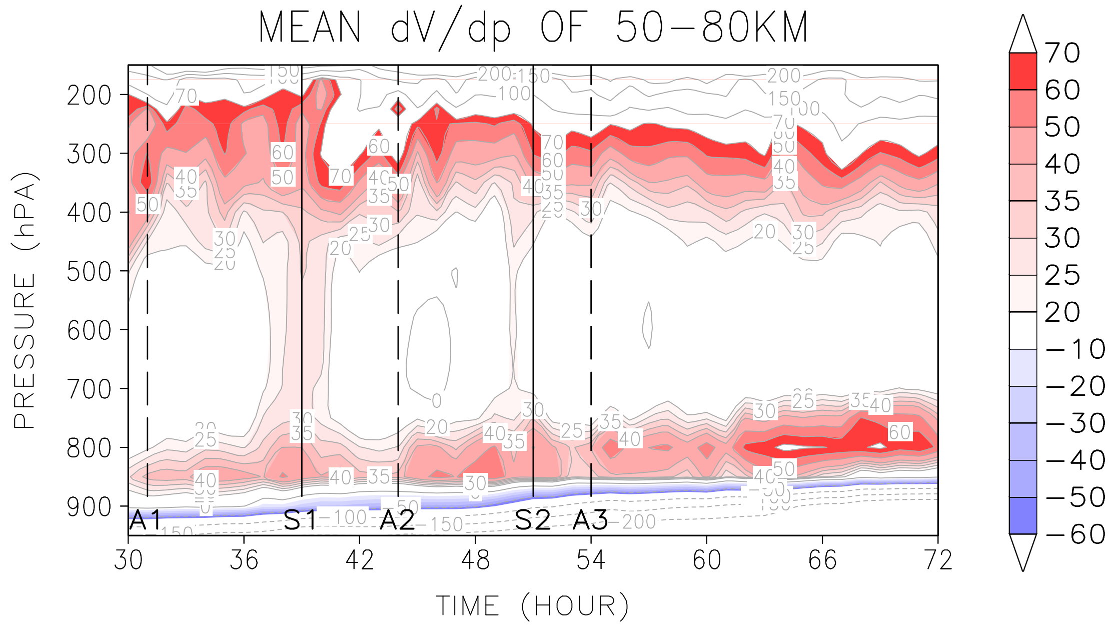

(b)

Figure 6.7: Evolution of the vertical gradient of the mean tangential wind [$\partial\bar{V}/\partial p$, unit $10^{-5} \times ms^{-1}Pa^{-1}$] averaged for radii of a) 10 to 50 km, and b) 50 to 80 km.

The decrease of the cyclonic tangential wind with height (which is the signature of warm-cored systems) may create an environment unfavourable for the development of deep convection; while the lower part of a VHT is embedded in the rapidly rotating flow in the lower troposphere, its upper part may encounter much slower cyclonic rotation. As a result, VHTs in such an environment may be tilted backward (i.e. upstream) with height, ventilating and weakening the convection. To study this effect, the evolution of the vertical gradient of mean tangential wind[6] is examined.

Figure 6.7a shows the evolution of the vertical gradient of the mean tangential wind near the eyewall (averaged over 10-50 km radii), which is the region in which the VHTs are located. The vertical shear of mean tangential wind in the upper part of the troposphere (see the red shades above the 700 hPa level) increases noticeably towards the asymmetric phase, as the vortex spins up at low levels. This spin up is a result of both the horizontal mixing by the VHTs and vertical advection by the mean circulation of the vortex (as described in the previous Section on the evolution of mean radial and tangential wind at low levels). Thus, the resultant large shear that develops after the asymmetric phase is less favourable for convection.

The vertical gradient of the mean tangential wind just outside of the RMW (i.e. averaged for radii between 50 and 80 km), shown in Figure 6.7b, exhibits the vacillation pattern with the opposite phase of its counter part at inner radii. Specifically, the mean tangential wind decreases with height faster during the symmetric phase. This pattern implies that the local vertical wind shear at outer radii is smaller during the asymmetric phase compared with the symmetric phase, and consequently less prohibiting for the development of convection at these radii. This configuration is consistent with the development of convection outside of the RMW (see in Figure 5.6b the region outside of the RMW and after phase A2) and acceleration of mean tangential wind in region A_{outer} (Figure 5.1).

Thus, the weakening of VHTs after the asymmetric phase can be explained by the collective effects of the reduced CAPE and a high-shear local environment. In other words, these interdependent relationships of convection with CAPE and local vertical shear behave, respectively, as the thermodynamic and dynamic negative feedbacks.

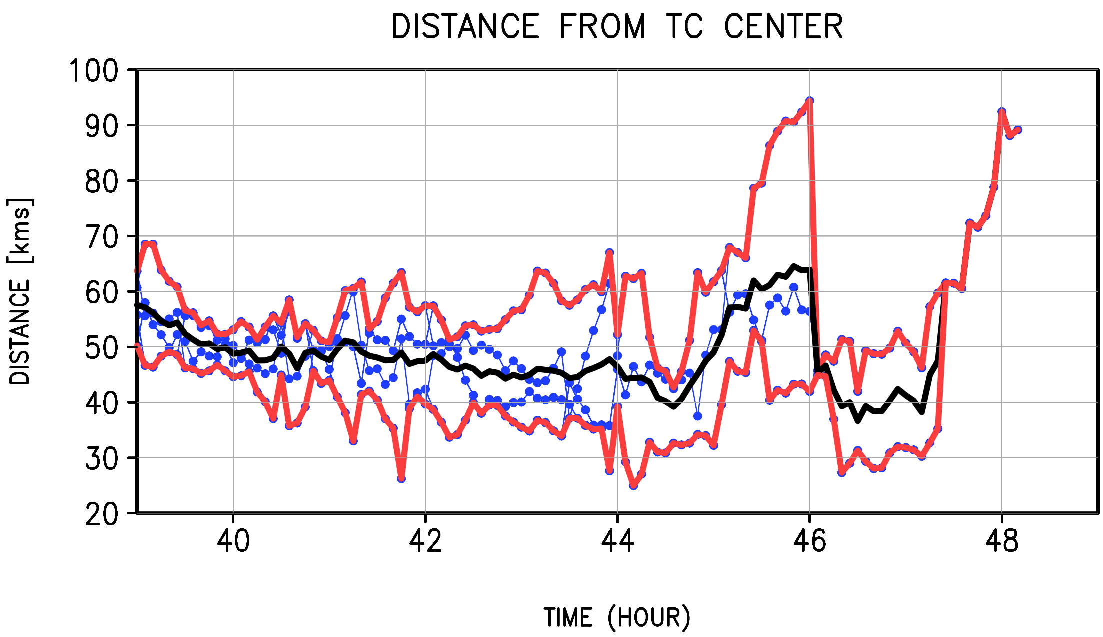

Figure 6.8: Evolution of the distance from all VHTs to the vortex center [km]. Red thick lines indicate maximum and minimum values among all VHTs, which serves as the envelope of the VHT plume. Thick black line shows the average values for all active VHTs.

6.2.2 Vortex Rossby Waves

Azimuthal propagation

Figure 6.8[7] shows the evolution of the distance from all VHTs to the vortex center. After the asymmetric phase A2 at 44 h, the mean movement of the VHTs is outward as indicated by the thick black line in Figure 6.8. In the horizontal plane, this outward movement of the weakened VHTs has the form of elongated convective bands moving outwards and more slowly than the mean tangential wind component. This behaviour is similar to that of VRWs and is to be expected from the negative radial gradient of azimuthal mean PV, which is consistent with the monopole structure of the vortex during the asymmetric phase. For this reason, the presence of VRWs in the simulated vortex will be examined now.

The theoretical properties of VRWs such as their phase and group propagation speeds are computed using the formulae derived by Möller and Montgomery (2000)

[6]The evolution of local wind shear along the trajectories of individual VHTs is presented in Appendix F. It is shown that while the association between local vertical wind shear magnitudes and VHT's vertical velocity (ω in pressure coordinates) is present at times, it does not necessarily correspond to the azimuthal tilt of the VHT in question.

[7]This figure shows also the inward movement of the VHTs during the transition from symmetric phase S1 at 39 h to the asymmetric phase A2 at 44 h.

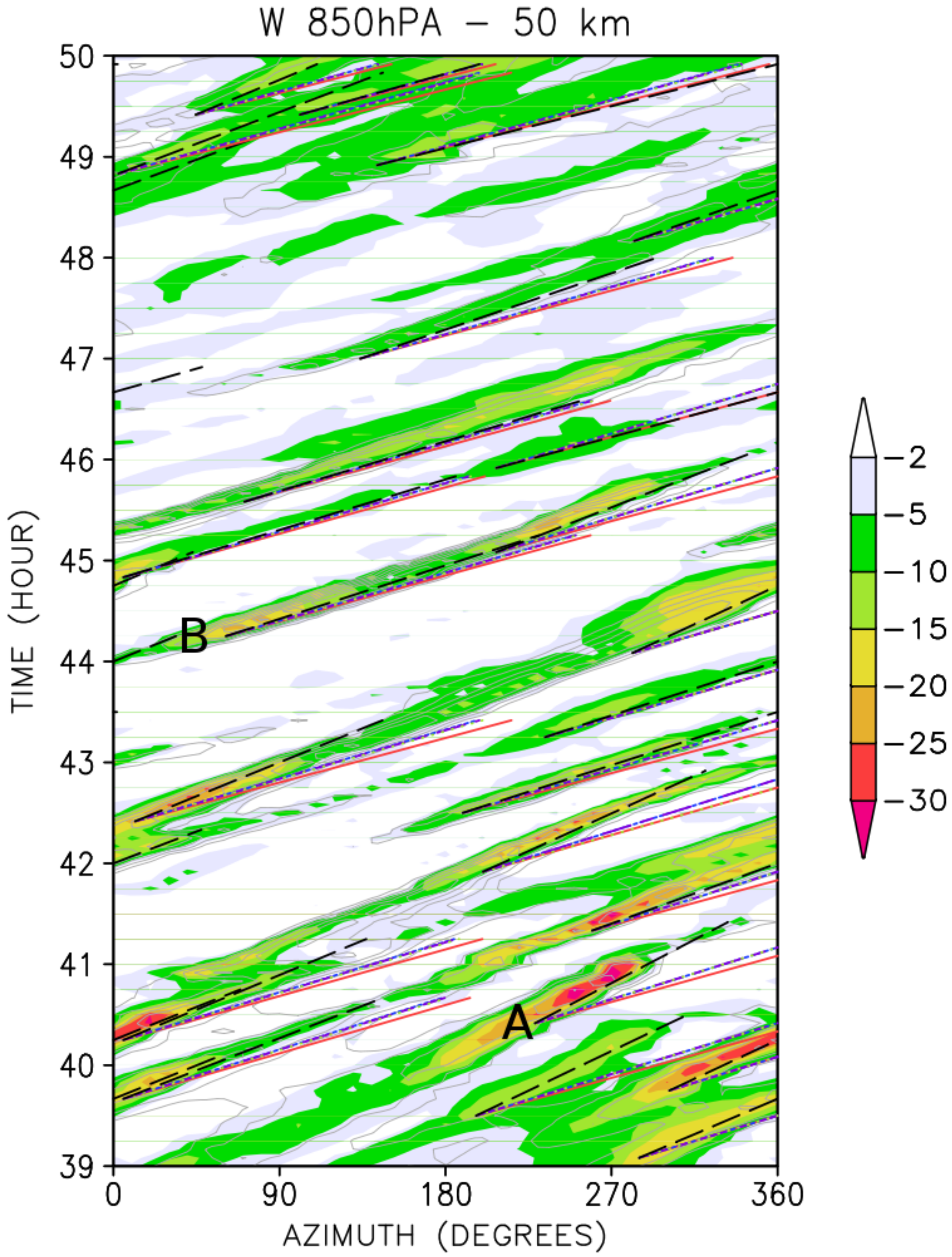

Figure 6.9: Hovmöller diagram of vertical velocity ω [Pa/s] (areas with upward motion are shaded) and PV (grey contours) at 850 hpa along the 50 km radius circle. On the horizontal axis, the direction from left to right is the cyclonic displacement. Red lines are the direction of movement with the mean tangential flow. Black long dashed lines indicate the movement directions of the traced VHTs/PV anomalies. Purple dashed-dotted lines show the movement with the VRW phase speeds calculated according to Möller and Montgomery (2000) for wave numbers 2 and 3. Radial and vertical wavenumbers are chosen arbitrarily corresponding to the length scales of 50 km, and 10 km in the respective directions.

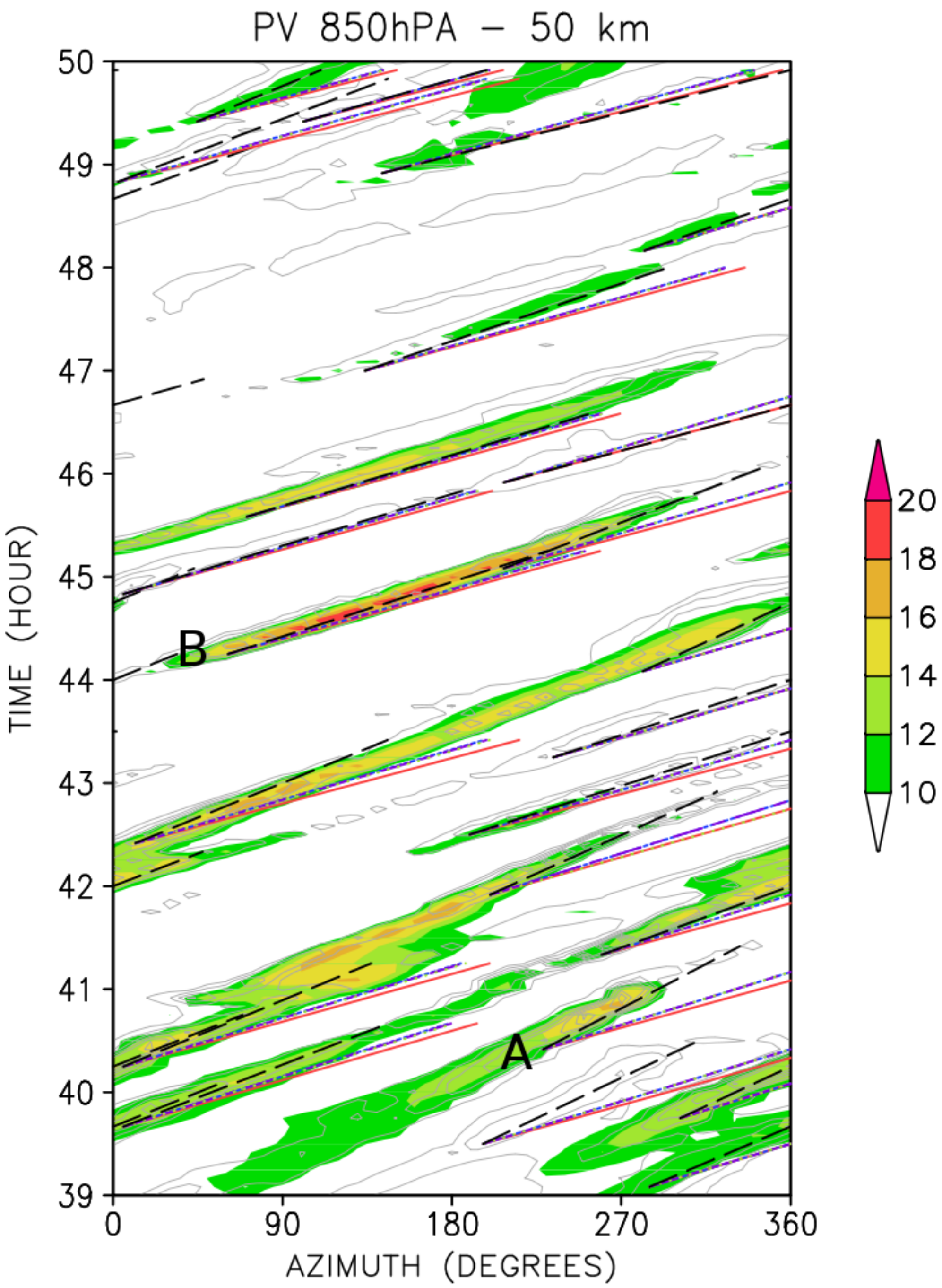

Figure 6.10: Similar to Figure 6.9 except for the PV is shaded instead of ω.

and are included in Section 1.2.3 of Chapter 1. These calculations use azimuthal mean profiles at 850 hPa of the simulated vortex for disturbances having azimuthal wavenumbers of 2, 3 or 4. The radial and vertical wavenumbers are chosen arbitrary corresponding to the length scales of 50 km and 10 km in the respective directions.

Figure 6.9 shows a azimuthal Hovmöller diagram of vertical velocity (shaded) overlayed by the PV along the 50 km radius circle. The VHTs, as marked by strong upward motion and positive vorticity anomalies, are tracked and their azimuthal speeds are compared with the theoretical phase speeds of VRWs calculated by Equation 1.3. In this figure, the larger the angle between the trajectory with the red line (representing the movement with the mean tangential wind), the slower the movement of the VHT compared with the mean flow. It can be seen that the tracked VHTs (marked by black dashed lines) move noticeably slower than both the mean flow (red lines) and the calculated phase speeds of VRWs. This retrogression of VHTs is pronounced during the symmetric-to-asymmetric transition (e.g. from S1 at 39 h to A2 at 44 h) while the VHTs are strengthening. In contrast, after the asymmetric phase A2, the weakening VHTs move nearly with the theoretical VRW speeds which predicts small retrogression relative to the mean flow.

Figure 6.10 shows the same features as in Figure 6.9 except for the shaded characteristics being PV instead of ω. Although the tracked entities are associated with both cyclonic vorticity and upward motion that constitute their VHT status, there is a remarkable difference between these two characteristics. A comparison of Figures 6.9 and Figure 6.10 shows that the VHTs have strong upward motion during the transition from symmetric to asymmetric phase, whereas they exhibit strong vorticity characteristics after the asymmetric phase. For example, the VHT marked with letter A appears to be stronger than the VHT marked with letter B in the upward motion field (Figure 6.9). However, A appears to be weaker than B in the PV field (Figure 6.10). The difference of the two characteristics within the VHTs is not surprising. While cyclonic vorticity anomalies are produced by the vertical gradient of diabatic heating by convection, the produced vorticity anomalies is not destroyed by the same processes that control the convection. For example, while VHT B has diminished upward motion due to unfavourable conditions for convection as discussed in the previous section, its associated cyclonic vorticity is not affected and still attains high values. Thus, the dominant cyclonic vorticity characteristics of this VHT explains its close resemblance to VRWs propagation, which is governed by the dry dynamical configuration of the vortex. On the other hand, large retrogression, and hence, large deviation from theoretical VRW phase speeds for VHT A can be attributed to its strong convective characteristics, which is not controlled exclusively by dry dynamical processes.

The retrogression of the VHTs can be seen more clearly in Figure 6.11. Near symmetric phases, e.g. S1 at 39 h and S2 at 50 h, the average retrogression of the tracked VHTs is of the order of 30%, whereas it drops to around 10%, which is close to the theoretical estimates just after the asymmetric phase A2 near 44-45 h.

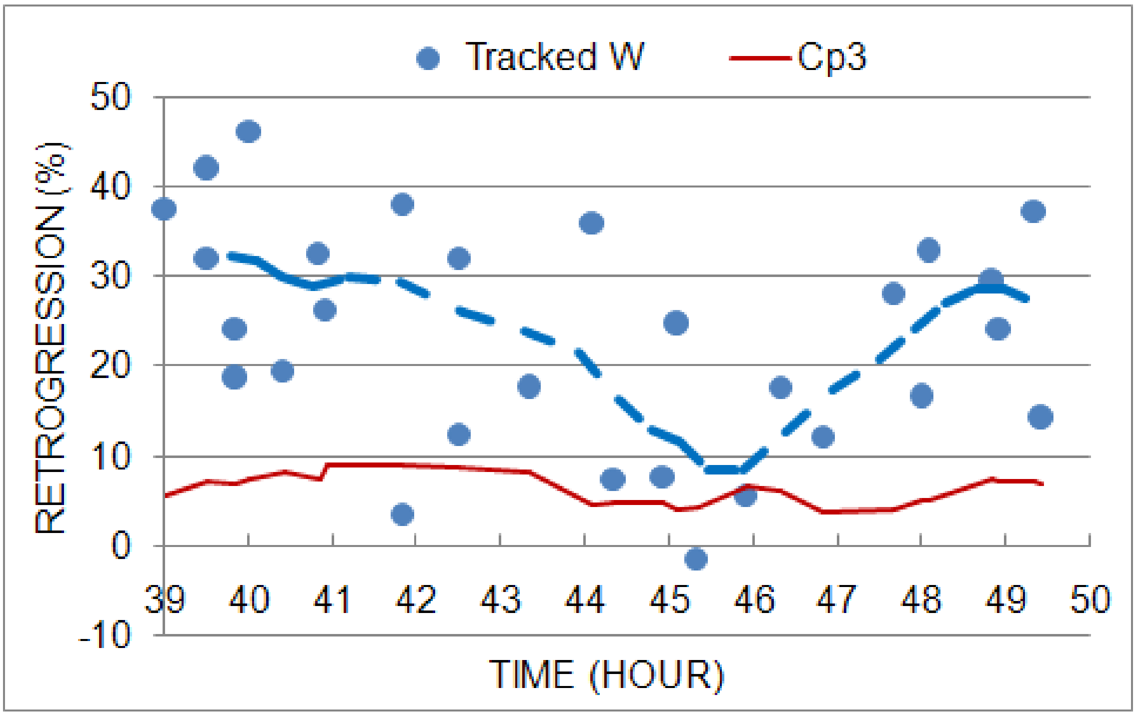

Figure 6.11: Retrogression calculated by $(\bar{V} - C)/\bar{V} \times 100\%$ (circles) of tracked convective entities (i.e. VHTs) and the calculated VRW phase speed for wave number 3 (solid thin line). The thick dashed line represents the smoothed average retrogression of the tracked convective entities. $\bar{V}$ is the mean tangential wind speed, C is the tangential speed of the VHTs.

Thus, if one considers the retrogression as a qualitative indication of the presence of VRWs, then the transition from the asymmetric to symmetric phase shows an increasing resemblance of VRWs. In other words, the tracked convective entities behave more like VRWs during the asymmetric-to-symmetric transition than during the symmetric-to-asymmetric transition.

The retrogression of the calculated phase speed of VRWs (red line in Figure 6.11) is small, fluctuating between 5 to 10%, thus, smaller than the observed azimuthal phase speeds of the VHTs. Here again, as in the case of the theoretical barotropic instability, one should not expect these calculated quantities to be identical to the observed features, since important assumptions used in the derivation of the formulae being used (i.e. linear barotropic dynamics) are not met in the real simulation. Nevertheless, the retrogression characteristics seen in the simulations do suggest the presence of VRWs.

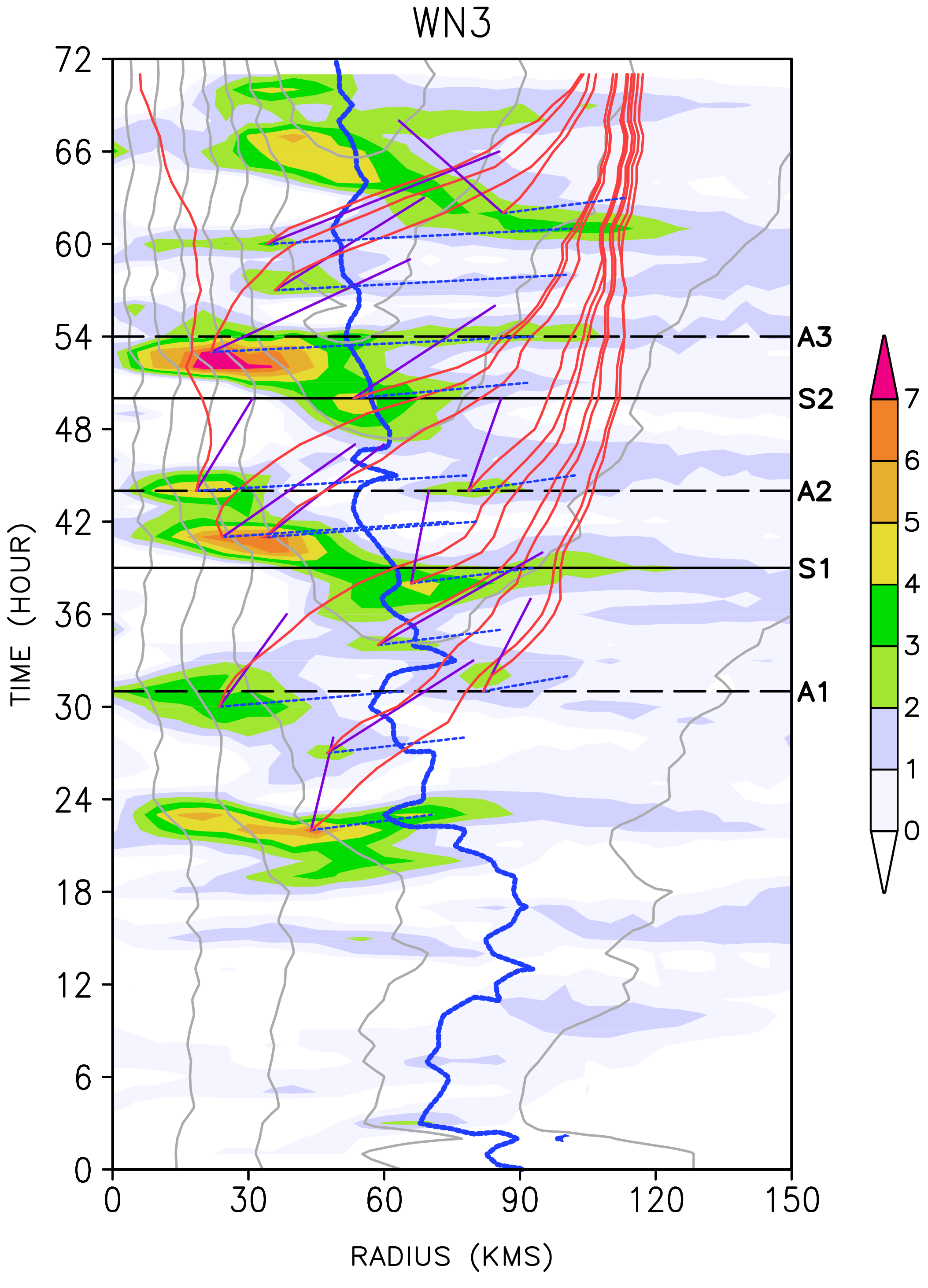

Figure 6.12: Radial phase (Cp_r) and group (Cg_r) speeds the theoretical VRWs calculated by Equations 1.5 and 1.6 for the azimuthal wavenumber 3. The shaded areas show positive tendencies of mean tangential wind at 850 hPa. Gray contours show the azimuthally-mean tangential wind speed. The RMW is shown by the dotted blue line. Red solid lines show the radial propagation with the radial group speed Cgr, blue dashed lines are for radial phase speed Cpr, and purple solid lines illustrate mean radial wind at each point of interest.

Radial propagation

Figure 6.12 shows the theoretical radial phase and group speeds of the VRWs calculated from Equations 1.5 and 1.6. The propagation of these waves are superimposed on the tendencies of the mean tangential wind (as in Figure 5.1a) with the intention to identify a possible association of VRWs with changes in the mean tangential flow. One interesting feature of this diagram is the coincidence of the outward phase speed of the calculated VRWs (blue dashed lines) with the regions S_{outer} having positive tangential tendencies as shown in Figure 5.1a. The association of the S_{outer} regions with the phase speeds of the VRWs can be explained as follows. From the symmetric phase, when the maximum acceleration occurs near the RMW, asymmetric features on the outer side of the eyewall move outwards as they are embedded in a negative vorticity gradient environment. These features resemble the spiral bands which move outwards with the radial phase speed of VRWs. As these bands are convective, they convection may continue to produce cyclonic vorticity, hence, contributing to the increase of the tangential wind in regions S_{outer}.

The wave-mean flow interaction effects of VRWs are suggested to occur at some critical radius where the group propagation of the VRWs is zero (Montgomery and Kallenbach, 1997, Montgomery and Enagonio, 1998). In this simulation, this critical radius is evident near 120 km, at which traces of radial group propagation (red lines in Figure 6.12) converge. However, this radius does not seem to show any significant increase in the mean tangential wind as would be expected from the above wave-mean flow interaction argument.

6.2.3 The reduced strain at outer radii

It was shown in Chapter 4 that the strain-dominated region just outside of the RMW is stronger during the asymmetric phase than during the symmetric phase (see Figures 4.9b,d). Rozoff et al. (2006) suggest that the strain-dominated regions, with the filamentation time scale τ_{fil} is less than the convective time scale, are unfavourable for convection. On the other hand, recall from Section 5.1.1 that during the asymmetric-to-symmetric transition convection develops at outer radii and appears to move inwards towards the RMW (the A_{outer} region). We investigate next the evolution of the filamentation time scale at some outer radii and its relationship with convection in this region.

Figure 6.13 shows the evolution of the filamentation time scale τ_{fil} and the mean

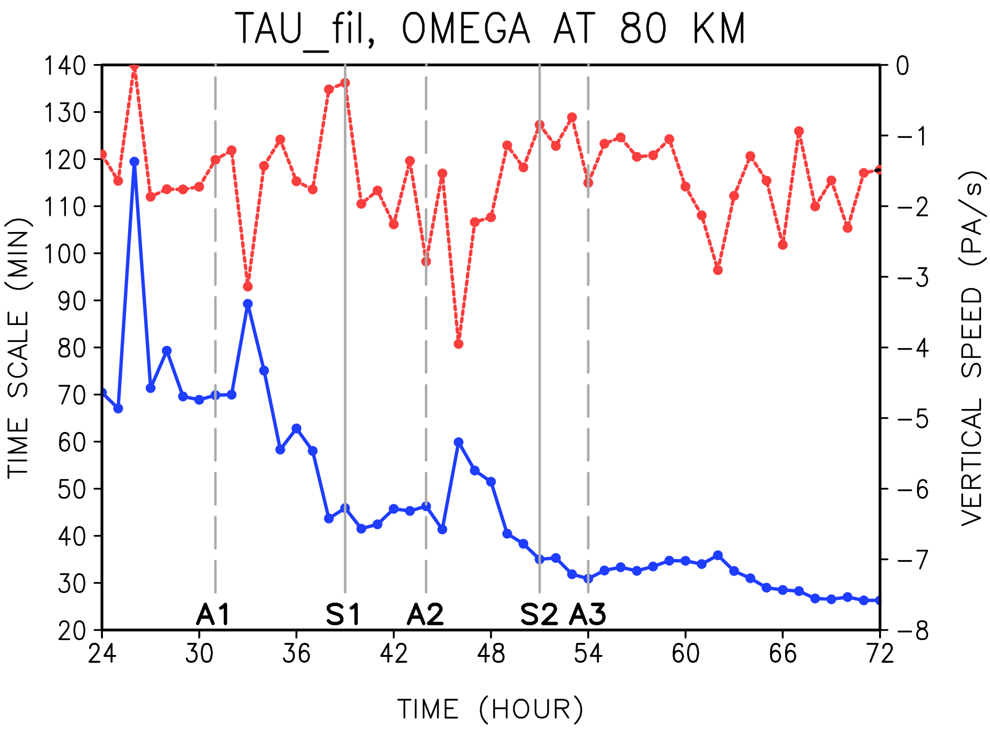

a)

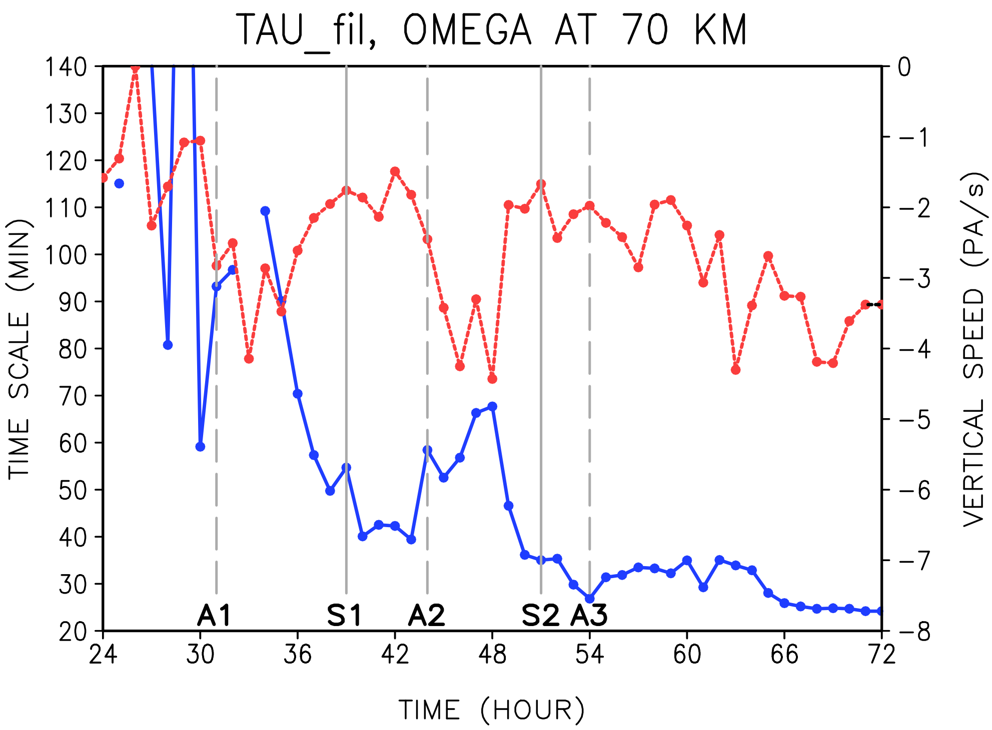

b)

Figure 6.13: The evolution of the vertical speed ω [Pa s^{-1}] (red dashed line) and the filamentation time scale $\tau_{fil} = 2D^{-1/2}$ [minutes] (blue solid line) at the 80 km (a) and 70 km (b) radii on the 850 hPa level.

vertical speeds ω at the 80 km and 70 km radii (which are outside of the RMW at all times) on the 850 hPa level. As the vortex strengthens, the filamentation time scale in this region broadly decreases, which is consistent with a stronger strained vortex with the faster spinning inner core. Nevertheless, during the vacillation cycles, a noticeable increase in τ_{fil} (implying condition more favourable for convection) occurs shortly after the times of maximum asymmetries (e.g. at 32 h after the asymmetric phase A1, and 46 h after the asymmetric phase A2 inf Figure 6.13a). Accordingly, the mean upward motion ω, representing convection, increases during these times, thus, justifying relationship suggested by Rozoff et al. (2006). In addition, examination of the 70 km radius (panel b) shows that large values of τ_{fil} occur at 1 to 2 hours after that at the 80 km. Thus, this region of reduced strain, which is more favourable to convection, moves inwards towards the RMW, consistent with the inward movement of strenghthening convection areas accompanied by acceleration of the mean tangential wind in the A_{outer} areas (shown earlier in Figure 5.1a).

The more favourable conditions for convection associated with the decreased strain, and hence increased τ_{fil} outside of the RMW after the asymmetric phase can be explained by the weakening of the VHTs. It is because the VHTs produce strain (and convergence) especially at their outer peripheries (see regions of strong D just outside of the VHTs during the asymmetric phase in Figures 4.9b,d). Thus, as the VHTs weaken after the times of maximum asymmetries, their associated strongly-strained zones weaken as well, leaving favourable conditions for convection at outer radii.

The development of convection in A_{outer} regions and their subsequent inward movement resembles the development of the secondary eyewall in ERCs (see Figure 5.6b and discussion thereof). Furthermore, the A_{outer} region, for example the one near the asymmetric phase A2, appears to satisfy all conditions for the formation of a secondary eyewall hypothesised by Terwey and Montgomery (2008), including: (i) reduced strain as shown above, (ii) a moderate negative PV gradient (see Figure 5.8a), and (iii) a substantial amount of CAPE of the order of 2000 J kg^{-1} K^{-1} (Figure 5.12a). It is hypothesised in the idealised simulations of Terwey and Montgomery (2008) that sporadic convection at outer radii can develop into regular deep convection given the favourable conditions mentioned above. On the other hand, in this simulation, the increased convection at outer radii is seen associated with convective inward spiral bands[8] at outer raddi (Figure 4.4b,d). Thus, although the vacillation cycles are different from the ERCs, the processes for the formation of the convective development at outer radii in the former may be similar to the formation

[8]The inward movement of these bands are explained by Wang (2008b) as being advected by the mean inflow in the BL.

of the secondary eyewall in the latter.

6.3 The mature stage

As shown in the previous chapters, the vacillation cycles tend not to occur during the mature stage even though the conditions necessary for barotropic instability are present. We present here evidence that the reduced CAPE and increased strain near the eyewall may serve as possible factors preventing the eyewall from breaking down.

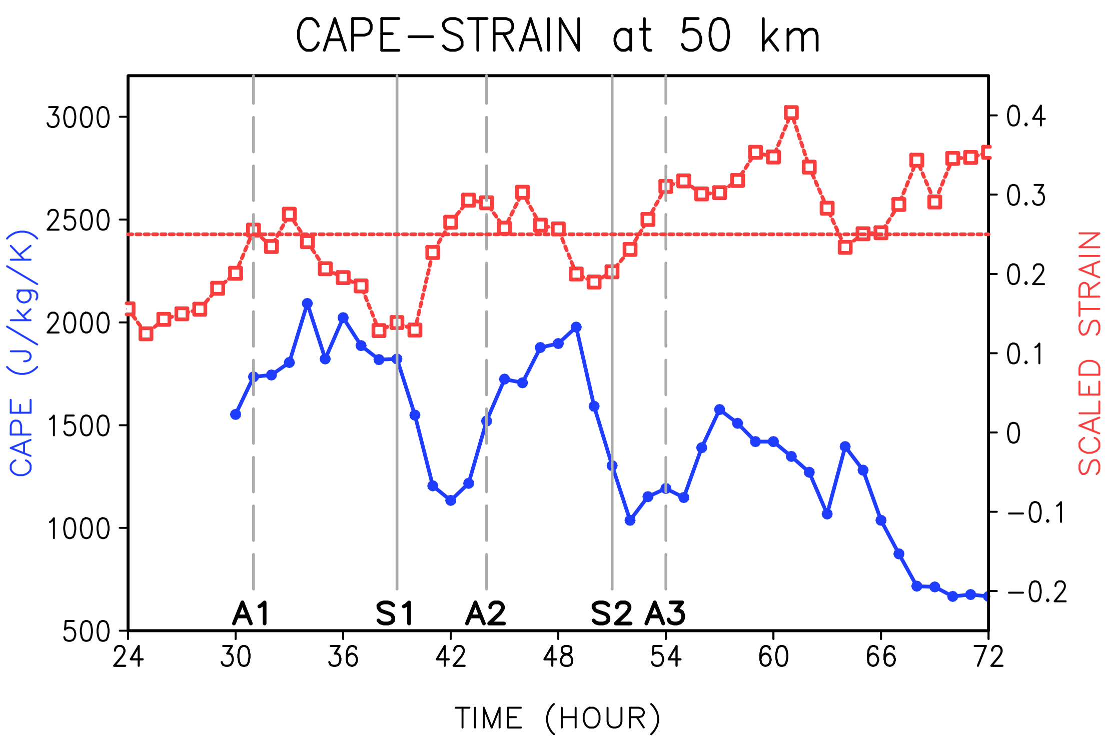

Figure 6.14: Evolution of the azimuthally-mean CAPE (blue solid line) [J kg^{-1} K^{-1}] and strain rate scaled with the relative vorticity $\gamma = S/\zeta$ (red dashed line) for the 50 km radius.

Figure 6.14 shows the evolution of the azimuthally-mean CAPE (blue line) at the 50 km radius, which is near the eyewall. Despite large fluctuations during the vacillation cycles (which is the manifestation of the inter-dependent relationship between convection and CAPE as discussed earlier in Section 6.2.1), CAPE has the mean tendency to decrease, reaching values of the order of 500 J kg^{-1} K^{-1} after 66 h. Consequently, the eyewall region during the mature stage is not favourable for very strong convection such as that in VHTs. Accordingly, this stage is characterised by a scarcity of very strong updraughts or VHTs, both in the modelled storm (Figure

4.20a) and in hurricane *Katrina* (Figure 4.21f). Thus, as convective instability is shown to play a part in growing asymmetries during the symmetric-to-asymmetric transition of the vacillation cycles (Section 6.1.2), its reduction during the mature stage may explain the lack of the vacillation cycles.

On the other hand, enhanced strain may also explain the lack of vacillation cycles during the mature stage. The dashed red line in Figure 6.14 show the evolution of the scaled strain $\gamma = S/\zeta$, where S and ζ are the strain rate and relative vorticity, respectively, averaged for the 50 km radius. Although the strain fluctuates strongly during the integration (which is likely due to vacillations of convection in this area), it has the mean increasing tendency. As barotropic instability appears to play a role in growing asymmetries during the symmetric-to-asymmetric transition (Section 6.1.1), the increased strain during the mature stage may impose a limiting effect on the growth of asymmetries.

It is shown by Dritschel et al. (1991) that a scaled strain γ as small as 0.25 may be enough to suppress conventional Rayleigh shear instability (i.e. the barotropic instability), and thus, prevent a strip of enhanced vorticity from breaking down into vortices. Although the configuration of the PV ring in TCs is different from the straight vorticity strip used by Dritschel et al., their finding may well apply, at least qualitatively, to TC vortices. In this simulation, the scaled strain maintains high values mostly above the threshold of 0.25 (marked by the horizontal dashed red line in Figure 6.14) after the last identified asymmetric phase A3. Thus, scaled strain in excess of 0.25 may explain the lack of vacillation cycles thereafter.

6.4 Summary of Chapter 6

In summary, the processes occuring during transitions between the symmetric and asymmtric phases within vacillation cycles are hypothesised as follow:

Symmetric to Asymmetric transition

- ***Barotropic instability*** associated with the ring structure during the symmetric phase allows asymmetries to grow of initially small amplitudes within the eyewall into regions of enhanced local rotation.
- ***Convective instability*** further develops these perturbations with enhanced rotation into VHTs. In addition, a local WISHE mechanism is effective in cou-

pling the barotropic and convective instabilities at locations of VHTs within the eyewall.

- ***The VHTs*** move inwards toward the vortex centre by a process similar to the non-linear β effect that induces a polewards movement for TCs in the planetary vorticity gradient environment. While moving inwards, the meso-circulation of the VHTs effectively mix properties between the eye and the eyewall, and eventually bring about the monopole structure.

- ***Eyewall mesovortices*** in the form of mesoscale vortices without deep convection, similar to those described by Kossin and Schubert (2004), are seen in our simulations. They originated from VHTs, but become detached while moving inwards by a similar process to that governing the inward movement of the VHTs mentioned above. Meanwhile, deep convective entities that are associated originally with the VHTs do not move much further inwards, probably due to the convectively unfavourable conditions near the eye.

- ***The monopole structure*** during the asymmetric phase is achieved by the collective lateral mixing of the mesoscale circulations associated with the VHTs and mesovortices.

Aymmetric to Symmetric transition

- ***The weakening of the VHTs.*** The VHTs weaken after the times of maximum asymmetry as they exhaust the convective available energy and increase local vertical windshear.

- **Vortex Rossby Waves.** The weakened VHTs, while attaining their cyclonic vorticity properties, behave like VRWs in the negative PV gradient environment, which is characteristic of the monopole structure. The VHTs move radially outwards and retrogress in the azimuthal direction while becoming axisymmetrised in the strained environment.
  VRWs appear to be present also in the region near the RMW during the symmetric phase and move outwards. The radial phase speeds of the VRWs predicted by Möller and Montgomery (2000) match with the acceleration of the mean tangential wind there (S_{outer} areas). The strengthening of the wind there is suggested to be the result of the VRWs coupled with convection in the forms of outward spiral bands. The effect of this type of VRW is, thus, to increase the wind at outer radii rather than the RMW.

- ***The reduction of strain at outer radii.*** The weakening of the VHTs leads to a reduction of the strain outside of the RMW, which creates more favourable condition for convection at outer radii. Consequently, convection develops at outer radii and subsequently moves inwards, similar to the behaviour of the secondary eyewall in the ERCs.

- Consequently, the following symmetric phase emerges as a result of the combination of two processes: a) the outward propogating axisymmetrising VRWs that originate from the weakened VHTs after the asymmetric phase; and b) the inward movement of the convection that developes at outer radii after the asymmetric phase.

It is important and interesting to note that the convective entities investigated in this chapter have a dual nature of both vortex and wave. During the symmetric-to-asymmetric transition, they exhibit characteristics of vortices, i.e. VHTs. In contrast, during the reverse transition from the asymmetric to symmetric phase, they resemble VRWs.

The mature stage. The lack of vacillation cycles during the mature stage is suggested to be the result of reduced CAPE and increased strain in the eyewall region.

Chapter 7

SUMMARY AND CONCLUSION

Vacillation cycles in the ensemble simulations.

High-resolution ensemble simulations of hurricane *Katrina* (2005) using TCLAPS show that the majority of the simulated vortices vacillate between phases of low and high asymmetries. These phases correlate with the intensification rate of the mean tangential wind. The highly symmetric phase tends to be associated with a faster intensification rate and the highly asymmetric phase with a slower intensification rate.

It is found from the ensemble runs that, during a 48 hour integration period, simulated vortices on average go through 2 vacillation cycles. The mean duration of a vacillation cycle, during which a simulated vortex transforms from a symmetric phase to an asymmetric phase and then back to a symmetric phase, is between 9 to 11 hours, and the mean amplitude of the PV maximum asymmetry during vacillation cycles is of the order of 2.7 PVU. In addition, the simulated vortices with stronger cycles (based on the correlation between asymmetries and intensification rates) tend to encounter a cooler but more variable mean SST along their trajectories. It is also noted that, larger vortices tend to have stronger vacillation cycles than smaller vortices.

Symmetric and Asymmetric phases.

Detailed analysis of an ensemble run reveals that the low-level structures during these phases are similar to the two regimes reported by Kossin and Eastin (2001) based on aircraft data.

- During the ***symmetric phase***, which is similar to Regime 1 of Kossin and Eastin, the vortex structure has the form of a ring-like eyewall consisting of elongated bands of moderate convection; the low level PV and θ_e has a ring-like structure with a maximum located at some distance (roughly 30 km) from the vortex centre; and the maximum acceleration of the mean tangential wind occurs near the RMW. Thus, the intensification rate ($\partial V_{max}/\partial t$) is high during this time.

- During the ***asymmetric phase***, the eyewall is deformed into polygonal shapes with deep convective entities resembling VHTs located at the vertices. The low-level structure of PV and θ_e has a monopole structure with the maximum located at the vortex centre. This phase is similar to the Regime 2 described by Kossin and Eastin (2001). The intensification rate during this phase is relatively low as the maximum acceleration of the mean tangential wind occurs at inner radii inside of the RMW. Thus, this phase may be seen as a temporary break of the inner-core intensification.

Observational evidence of a vacillation circle in hurricane *Katrina*

High resolution IR images of hurricane *Katrina* indicate that a similar process occurred during 27 August 2005. Although this period is referred to by National Hurricane Center as an ERC, the eyewall appears to break down with embedded VHTs suggesting the occurrence of a vacillation cycle instead.

Transition mechanisms.

While Kossin and Eastin (2001) suggest barotropic instability as an explanation for the transition from their Regime 1 to Regime 2, which is equivalent to the symmetric-to-asymmetric transition in vacillation cycles, we hypothesise that convective instability plays a part as well. We suggest that vacillation cycles involve several inner-core processes.

- During the ***Symmetric-to-Asymmetric*** transition, release of barotropic and convective instabilities, coupled by a local WISHE mechanism, develops asymmetries within the eyewall in the form of VTHs. These VHTs move inward while effectively mixing properties between the eye and the eyewall, bringing the vortex to an asymmetric phase with a monopole structure.

- The ***Asymmetric-to-Symmetric*** transition occurs as the VHTs weaken (due to exhausted or consumed convective instability and increased local vertical windshear). The weakened VHTs become stretched bands of moderate convection, and move outward as axisymmetrising VRWs in a strongly sheared mean flow. During this time, convection develops at outer radii in a favourable region of reduced strain (due to the weakened VHTs) and high convective instability. This region of outer convection appears to move inwards towards the RMW, resembling the contraction of the secondary eyewall in ERCs.

During the mature stage (i.e. at the later times of the integration), these cycles, including the breakdown of the eyewall into asymmetric entities, are not observed despite large barotropic instability being present near the eyewall region. This cessation is suggested to be the result of a) reduced convective instability within the eyewall, and b) the strong damping effect of large strain and rapid filamentation near the RMW.

Vacillation cycles versus ERCs

While vacillation cycles resemble ERCs in a number of ways, including the intensity change pattern (i.e. slow intensification rate while the eyewall weakens or breaks), and an apparent inward movement of a convective region from outer radii in the mean vertical velocity field, they are essentially different from ERCs. During an ERC, the inner eyewall weakens nearly uniformly upon the appearance of the outer eyewall. In contrast, the eyewall breaks down into vortices (VHTs) during a vacillation cycle, followed by an increase of convection at outer radii.

We hypothesise that vacillation cycles tend to occur during rapid intensification stage when the vortex structure is not fully developed into a strongly strained circulation. In a mature hurricane, large strain in the region near the eyewall will prevent the eyewall from breaking down into smaller vortices. In other words, we propose vacillation cycles as an internal intensification mechanism that tend to occur in 'young' TCs with structures which are not fully developed. They are different from ERCs, which tend to occur in strong and mature hurricanes.

Implications of vacillation cycles and future work

Intensity changes associated with vacillation cycles imply that knowledge of the evolution of asymmetries may be important in predicting the intensity of TCs. With high resolution models, which can resolve small scale features such as VHTs in detail, it becomes even more important to be able to represent asymmetric characteristics accurately. Thus, the capability of such models to assimilate convective structures such as VHTs would be of great benefit.

To confirm the validity of vacillation cycles, more work is needed to be done with different numerical models and different TCs. Also, as suggested from the ensemble simulations, sensitivity tests are also desirable to investigate the occurrence of these cycles with respect to vortex size and SST.

Furthermore, it is of great interest to understand the interaction of vacillation cycles with the large-scale environment. For instance, the development of favourable conditions for convection during the asymmetric-to-symmetric transition suggests a favourable condition for the outer environment to interact with the TC in question.

Lastly, along the logic of the reduced strain at outer radii, we speculate that the process leading to ERCs in strongly-strained vortices (in a quiescent environment) may occur as a result of: (i) the weakening of the eyewall due to reduced convective instability, and (ii) a subsequent reduced strain outside of the eyewall. This conditions would be favourable for convection to develop at outer radii, and hence lead the formation of the outer eyewall as suggested by Terwey and Montgomery (2008). Therefore, it would be of great interest to test this idea, for example, by running longer integrations and examining when the switch from vacillation mode to the ERC mode occurs.

References

Anthes, R., 1972: Development of asymmetries in a three-dimensional numerical model of the tropical cyclone. *Mon. Wea. Rev.*, **100**, 461–476.

Bach, H., 1969: On the Downhill Method. *Communications of the ACM*, **12**, 675–687.

Beljaars, A. and A. Betts, 1992: Validation of the boundary layer representation in the ECMWF model. *ECMWF Seminar Proceedings, Validation of Models over Europe, Vol II, 7-11 September 1992, European Centre for Medium-Range Weather Forecasts, Shinfield Park, U.K.*, **II**, 159–195.

Bender, M. and I. Ginis, 2000: Real-case simulations of hurricaneocean interaction using a high-resolution coupled model: Effects on hurricane intensity. *Mon. Wea. Rev.*, **128**, 917–946.

Bender, M., I. Ginis, and Y. Kurihara, 1993: Numerical simulations of tropical cyclone-ocean interaction with a high-resolution coupled model. *J. Geophys. Res.*, **98**, 23245–23263.

Bender, M., I. Ginis, R. Tuleya, B. Thomas, and T. Marchok, 2007: The Operational GFDL Coupled HurricaneOcean Prediction System and a Summary of Its Performance. *Mon. Wea. Rev.*, **135**, 3965–3989.

Beven, J., L. Avila, E. Blake, D. Brown, R. Franklin, R. Knabb, R. Pasch, J. Rhome, and S. Stewart, 2008: Atlantic Hurricane Season of 2005. *Mon. Wea. Rev.*, **136**, 1109–1173.

Bishop, C. H. and A. J. Thorpe, 1993: Frontal Wave Stability during Moist Deformation Frontogenesis. Part II: he Suppression of Nonlinear Wave Development. *J. Atmos. Sci.*, **51**, 874–888.

Bister, M. and K. Emanuel, 1998: Dissipative heating and hurricane intensity. *Meteor. Atm. Phys.*, **52**, 233–240.

Black, M. L., R. W. Burpee, F. D. Marks, C. e. Samsury, and H. E. Willoughby, 2002: Eastern Pacific Hurricanes Jimena of 1991 and Olivia of 1994: The effect of vertical shear on structure and intensity. *Mon. Wea. Rev.*, **130**, 2291–2312.

Bosart, L., C. Veldon, W. Bracken, J. Molinari, and P. Black, 2000: Environmental influences on the rapid intensification of Hurricane Opal (1995) over the Gulf of Mexico. *Mon. Wea. Rev.*, **128**, 322–352.

Braun, S., M. T. Montgomery, and Z. Pu, 2006: High-Resolution Simulation of Hurricane Bonnie (1998). Part I: The Organization of Eyewall Vertical Motion. *J. Atmos. Sci.*, **63**, 19–42.

Challa, M. and R. Pfeffer, 1980: Effects of Eddy Fluxes of Angular Momentum on Model Hurricane Development. *J. Atmos. Sci.*, **37**, 1603–1618.

Chen, Y., G. Brunet, and M. Yau, 2003: Spiral Bands in a Simulated Hurricane. Part II: Wave Activity Diagnostics. *J. Atmos. Sci.*, **60**, 1239–1256.

Chen, Y. and M. Yau, 2001: Spiral Bands in a Simulated Hurricane. Part I: Vortex Rossby Wave Verification. *J. Atmos. Sci.*, **58**, 2128–2145.

Chen, Y. and M. Yau, 2003: Asymmetric Structures in a Simulated Landfalling Hurricane. *J. Atmos. Sci.*, **60**, 2294–2311.

Corbosiero, K., J. Molinari, A. Aiyyer, and M. Black, 2006: The Structure and Evolution of Hurricane Elena (1985). Part II: Convective Asymmetries and Evidence for Vortex Rossby Waves. *Mon. Wea. Rev.*, **134**, 3073–3091.

Dare, R., 2004: The BMRC Bulk Explicit Microphysics (BEM) scheme. Technical report, BMRC Research Report, Bureau of Meteorology, Australia.

Davidson, N. and K. Puri, 1992: Tropical Prediction Using Dynamical Nudging, Satellite-defined Convective Heat Sources, and a Cyclone Bogus. *Mon. Wea. Rev.*, **120**, 2501– 2522.

Davidson, N., J. Wadsley, K. Puri, K. Kurihara, and M. Ueno, 1993: Implementation of the JMA typhoon bogus in the BMRC tropical prediction system. *J. Met. Soc. Japan*, **71**, 437–467.

Davidson, N. and H. Weber, 2000: The BMRC High-Resolution Tropical Cyclone Prediction System: TC-LAPS. *Mon. Wea. Rev.*, **128**, 1245–1265.

Davis, C., S. Jones, and M. Riemer, 2008: Hurricane vortex dynamics during Atlantic extratropical transition. *J. Atmos. Sci.*, **65**, 714–736.

DeMaria, M. and J. Kaplan, 1994: A Statistical Hurricane Intensity Prediction Scheme (SHIPS) for the Atlantic Basin. *Wea. Forecasting*, **9**, 209–220.

Dritschel, D., P. Haynes, M. Juckes, and T.G.Shepherd, 1991: The Stability of a Two-dimensional Vorticity Filament under Uniform Strain. *J. Fluid. Mech.*, **230**, 647–665.

Dvorak, V., 1975: Tropical Cyclone Intensity Analysis and Forecasting from satellite imagery. *Mon. Wea. Rev.*, **103**, 420–430.

Eliassen, A., 1951: Slow thermally or frictionally controlled meridional circulation in a circular vortex. *Astrophys. Norv.*, **5**, 19–60.

Elsberry, R., W. Frank, G. Holland, J. Jarrel, and R. Southern, 1987: *A global view of tropical cyclones*. Univ. of Chicago Press, Chicago, IL.

Emanuel, K., 1986: An Air-Sea Interaction Theory for Tropical Cyclones. Part I: Steady-State Maintenance. *J. Atmos. Sci.*, **43**, 585605.

Emanuel, K., 2003: Tropical cyclones. *Annu. Rev. Earth Planet. Sci.*, **31**, 75–104.

Emanuel, K., 2005: *Divine Wind : The Hurricane in History, Art, and Science*. Oxford University Press.

Fels, S. and M. Schwarzkopf, 1975: The simplified exchange approximation: a new method for radiative transfer calculation. *J. Atmos. Sci.*, **32**, 1475–1488.

Fortner, L., 1958: Typhoon sarah, 1956. *Bull. Amer. Meteor. Soc.*, **39**, 633–639.

Frank, W., 1977a: The structure and energetics of the tropical cyclone i. storm structure. *Mon. Wea. Rev.*, **105**, 1119–1135.

Frank, W., 1977b: The structure and energetics of the tropical cyclone ii. dynamics and energetics. *Mon. Wea. Rev.*, **105**, 1136–1150.

Frank, W. and E. Ritchie, 2001: Effects of vertical wind shear on the intensity and structure of numerically simulated hurricanes. *Mon. Wea. Rev.*, **129**, 2249–2269.

Gray, W., 1968: Global view of the origin of tropical disturbances ens storms. *Mon. Wea. Rev.*, **96**, 669–700.

Gray, W. and D. Shea, 1973: The Hurricane's Inner Core Region. II. Thermal Stability and Dynamic Characteristics. *J. Atmos. Sci.*, **30**, 1565–1576.

Guin, T. and W. Schubert, 1993: Hurricane spiral rainbands. *J. Atmos. Sci.*, **50**, 3380–3403.

Hausman, S., K. Ooyama, and W.H.Schubert, 2006: Potential Vorticity structure of simulated hurricanes. *J. Atmos. Sci.*, **54**, 1014–1026.

Hawkins, H., 1983: Hurricane Allen and island obstacles. *J. Atmos. Sci.*, **40**, 1360–1361.

Haynes, P., 1999: Transport, stirring and mixing in the atmosphere. Dordrecht, Kluwer Academic Publishers, Cargese, Corse, France, 229-272.

Haynes, P. and M. McIntyre, 1987: On the Evolution of Vorticity and Potential Vorticity in the Presence of Diabatic Heating and Frictional or Other Forces. *J. Atmos. Sci.*, **44**, 828–841.

Hendricks, E., M. Montgomery, and C. Davis, 2004: On the role of "vortical" hot towers in formation of tropical cyclone Diana (1984). *J. Atmos. Sci.*, **61**, 1209–1232.

Hendricks, E., W. Schubert, R. Taft, H. Wang, and J. Kossin, 2009: Life Cycles of Hurricane-Like Vorticity Rings. *J. Atmos. Sci.*, **66**, 705–722.

Hill, K. and G. Lackmann, 2009: Influence of Environmental Humidity on Tropical Cyclone Size. *Mon. Wea. Rev.*, **137**, 3294–3315.

Holland, G., 1983: Tropical Cyclone Motion: Environmental Interaction Plus a Beta Effect. *J. Atmos. Sci.*, **40**, 328–342.

Holliday, C., 1977: Double intensification of Typhoon Gloria, 1974. *Mon. Wea. Rev.*, **105**, 523–528.

Holton, J., 2004: *An introduction to dynamic meteorology.* Academic Press, London.

Hoose, H. and J. Colon, 1970: Some aspects of the radar structure of Hurricane Beulah on September 9, 1967. *Mon. Wea. Rev.*, **98**, 529–533.

Hoskins, B., M. McIntyre, and A. Robertson, 1985: On the use and significance of isentropic potential vorticity maps. *Quart. J. Roy. Meteor. Soc.*, **111**, 877–946.

Jones, S., 1995: The evolution of vortices in vertical shear. I: Initially barotropic vortices. *Quart. J. Roy. Meteor. Soc.*, **121**, 821–851.

Jorndan, C., 1966: Surface pressure variations at coastal stations during the period of irregular motion of Hurricane Carla of 1961. *Mon. Wea. Rev.*, **94**, 454–458.

Knabb, R., J. Rhome, and D. Brown, 2006: Tropical Cyclone Report. Hurricane Katrina. Technical report, National Hurricane Center.

Kodama, Y. and T. Yamada, 2005: Detectability and Configuration of Tropical Cyclone Eyes over the Western North Pacific in TRMM PR and IR Observations. *Mon. Wea. Rev.*, **133**, 2213–2226.

Kossin, J. and M. Eastin, 2001: Two disctinct regimes in the kinematic and thermodynamic structure of the hurricane eye and eyewall. *J. Atmos. Sci.*, **58**, 1079–1090.

Kossin, J. and W. Schubert, 2004: Mesovortices in hurricane Isabel. *Bull. Amer. Meteor. Soc.*, **85**, 151–153.

Kossin, J., W. Schubert, and M. Montgomery, 2000: Unstable interactions between a hurricanes primary eyewall and a secondary region of enhanced vorticity. *J. Atmos. Sci.*, **57**, 3893–3917.

Kossin, J. and M. Sitkowski, 2009: An Objective Model of Identifying Secondary Eyewall Formation in Hurricanes. *Mon. Wea. Rev.*, **137**, 876–892.

Kuo, H., L. Lin, C. Chang, and R. Williams, 2004: The Formation of Concentric Vorticity Structures in Typhoons. *J. Atmos. Sci.*, **61**, 2722–2734.

Lacis, A. and J. Hansen, 1974: A parameterization for the absorption of solar radiation in the earth's atmosphere. *J. Atmos. Sci.*, **31**, 118–133.

Lighthill, J., 1998: Fluid mechanics of tropical cyclones. *Theoret. Comput. Fluid. Dyn.*, **10**, 321.

Lin, I., C. Wu, K. Emanuel, and I. Pun, 2008: Upper-Ocean Thermal Structure and the Western North Pacific Category 5 Typhoons. Part I: Ocean Features and the Category 5 Typhoons Intensification. *Mon. Wea. Rev.*, **136**, 3288–3306.

Lin, I., C. Wu, K. Emanuel, and I. Pun, 2009: Upper-Ocean Thermal Structure and the Western North Pacific Category 5 Typhoons. Part II: Dependence on Translation Speed. *Mon. Wea. Rev.*, **137**, 3744–3757.

Lin, Y., R. Farley, and H. Orville, 1983: Bulk parameterization of the snow field in a cloud model. *J. Climate and Appl. Met.*, **22**, 1065–1092.

Louis, J., 1979: A parametric model of vertical eddy forces in the atmosphere. *Bound.-Layer Meteor.*, **17**, 187–202.

Mainelli, M., M. DeMaria, L. Shay, and G. Goni, 2008: Application of Oceanic Heat Content Estimation to Operational Forecasting of Recent Atlantic Category 5 Hurricanes. *Wea. Forecasting*, **23**, 3–16.

Mallen, K., M. Montgomery, and B. Wang, 2005: Reexamining the near-core radial structure of the tropical cyclone primary circulation: Implications for vortex resiliency. *J. Atmos. Sci.*, **62**, 408–425.

McBride, J. and R. Zehr, 1981: Observational analysis of tropical cyclone formation. Part II: Comparison of non-developing versus developing systems. *J. Atmos. Sci.*, **38**, 1132–1151.

McDonald, A., 1986: A Semi-Lagrangian and Semi-Implicit Two Time-Level Integration Scheme. *Mon. Wea. Rev.*, **114**, 824–830.

McDonald, N., 1968: The evidence for the existence of Rossby-type in the hurricane vortex. *Tellus*, **20**, 138–150.

McTaggart-Cowan, R., L. Bosart, J. Gyakum, and E. Atallah, 2007: Hurricane Katrina (2005). Part I: Complex Life Cycle of an Intense Tropical Cyclone. *Mon. Wea. Rev.*, **135**, 3905–3926.

Merrill, R., 1988: Environmental influences on hurricane intensification. *J. Atmos. Sci.*, **45**, 1678–1687.

Molinari, J., S. Skubis, and D. Vollaro, 1995: External influences on hurricane intensity. Part III: Potential Vorticity Structure. *J. Atmos. Sci.*, **52**, 3593–3606.

Molinari, J., S. Skubis, D. Vollaro, and F. Alsheimer, 1998: Potential Vorticity Analysis of Tropical Cyclone Intensification. *J. Atmos. Sci.*, **55**, 2632–2644.

Molinari, J. and D. Vollaro, 1989: External influences on hurricane intensity. Part I: Outflow Layer Eddy Angular Momentum Fluxes. *J. Atmos. Sci.*, **46**, 1093–1115.

Molinari, J. and D. Vollaro, 1990: External influences on hurricane intensity. Part II: Vertical Structure and Response of the Hurricane Vortex. *J. Atmos. Sci.*, **47**, 1902–1918.

Möller, J. and M. Montgomery, 1999: Vortex Rossby waves and hurricane intensification in a barotropic model. *J. Atmos. Sci.*, **56**, 1674–1687.

Möller, J. and M. Montgomery, 2000: Tropical cyclone evolution via potential vorticity anomalies in a three-dimensional balance model. *J. Atmos. Sci.*, **57**, 3366–3387.

Montgomery, M. and J. Enagonio, 1998: Tropical cyclogenesis via convectively forced vortex Rossby waves in a three-dimensional quasigeostrophic model. *J. Atmos. Sci.*, **55**, 3176–3207.

Montgomery, M. and R. Kallenbach, 1997: A theory for vortex Rossby waves and its application to spiral bands and intensity changes in hurricanes. *Quart. J. Roy. Meteor. Soc.*, **123**, 435–465.

Montgomery, M., J. Möller, and L. Shapiro, 2009: Do tropical cyclones intensify by WISHE? *Quart. J. Roy. Meteor. Soc.*, **134**, 1697–1714.

Montgomery, M., M. Nicholls, T. Cram, and A. Saunders, 2006: A vortical hot tower route to tropical cyclogenesis. *J. Atmos. Sci.*, **63**, 355–386.

Moon, I., I. Ginis, T. Hara, and B. Thomas, 2007: A Physics-Based Parameterization of AirSea Momentum Flux at High Wind Speeds and Its Impact on Hurricane Intensity Predictions. *Mon. Wea. Rev.*, **135**, 2869–2878.

Nguyen, C., R. Smith, H. Zhu, and W. Ulrich, 2002: A minimal axisymmetric hurricane model. *Quart. J. Roy. Meteor. Soc.*, **128**, 2641–2661.

Nguyen, S., R. Smith, and M. Montgomery, 2008: Tropical-cyclone intensification and predictability in three dimensions. *Quart. J. Roy. Meteor. Soc.*, **134**, 563–582.

NHC, 2008: National hurricane center forecast verification, updated 21 may 2008. Technical report, National Hurricane Center, NOAA.

Nong, S. and K. Emanuel, 2003: A numerical study of the genesis of concentric eyewalls in hurricanes. *Quart. J. Roy. Meteor. Soc.*, **129**, 3323–3338.

Ooyama, K., 1969: Numerical simulation of the life cycle of tropical cyclones. *J. Atmos. Sci.*, **26**, 3–40.

Ooyama, K., 1982: Conceptual Evolution of the Theory and Modeling of the Tropical Cyclone. *J. Meteor. Soc. Japan*, **60**, 369–379.

Persing, J., M. Montgomery, and R. Tuleya, 2002: Environmental interactions in the GFDL hurricane model for Hurricane Opal. *Mon. Wea. Rev.*, **130**, 298–317.

Puri, K., G. Dietachmayer, G. Mills, N. Davidson, R. Bowen, and L. Logan, 1998: The new BMRC Limited Area Prediction System, LAPS. *Aust. Meteor. Mag.*, **47**, 203–233.

Rayleigh, L., 1880: On the stability, or instability, of certain fluid motion. *Proc. London Math. Soc.*, **11**, 57–70.

Raymond, D., S. Sessions, and Z. Fuchs, 1998: Case-studies of developing east pacific easterly waves. *Quart. J. Roy. Meteor. Soc.*, **124**, 2005–2034.

Reasor, P., M. Montgomery, and L. Grasso, 2004: A new look at the problem of tropical cyclones in vertical shear flow: Vortex resiliency. *J. Atmos. Sci.*, **61**, 3–22.

Riehl, H. and J. Malkus, 1958: On the heat balance in the equatorial trough zone. *Geophysica*, **6**, 503–538.

Rikus, L., 1997: Application of a scheme for validating cloud in an operational global NWP model. *Mon. Wea. Rev.*, **125**, 1615–1637.

Rogers, R., S. Chen, J. Tenerelli, and H. Willoughby, 2003: A numerical study of the impact of vertical shear on the distribution of rainfall in Hurricane Bonnie (1998). *Mon. Wea. Rev.*, **131**, 1577–1599.

Rosenkrantz, W. A., 1997: *Introduction to probability and statistics for scientists and engineers*. McGraw-Hill in Probability and Statistics.

Rotunno, R. and K. Emanuel, 1987: An Air-Sea Interaction Theory for Tropical Cyclones. Part II: Evolutionary Study Using a Nonhydrostatic Axisymmetric Numerical Model. *J. Atmos. Sci.*, **44**, 542–561.

Rozoff, C., J. P. Kossin, W. Schubert, and P. J. Mulero, 2009: Internal Control of Hurricane Intensity Variability: The Dual Nature of Potential Vorticity Mixing. *J. Atmos. Sci.*, **66**, 133–147.

Rozoff, C., W. Schubert, D. Brian, and J. Kossin, 2006: Rapid Filamentation Zones in Intense Tropical Cyclones. *J. Atmos. Sci.*, **63**, 325–340.

Rozoff, C., W. Schubert, and J. Kossin, 2008: Some dynamical aspects of tropical cyclone concentric eyewalls. *Quart. J. Roy. Meteor. Soc.*, **134**, 583–593.

Sadler, J., 1978: Mid-Season Typhoon Development and Intensity Changes and the Tropical Upper Tropospheric Trough . *Mon. Wea. Rev.*, **106**, 1137–1152.

Schubert, W., M. Montgomery, R. Taft, T. Guinn, S. Fulton, J. Kossin, and J. Edwards, 1999: Polygonal eyewalls, asymmetric eye contraction, and potential vorticity mixing in hurricanes. *J. Atmos. Sci.*, **56**, 1197–1223.

Seaman, R., W. Bourke, P. Steinle, T. Hart, G. Embery, M. Naughton, and L. Rikus, 1995: Evolution of the Bureau of Meteorology's Grobal Assimilation and Prediction System. Part I: Analysis and initialisation. *Australian Meteorological Magazine*, **44**, 1–18.

Shapiro, L. and H. Willoughby, 1982: The Response of Balanced Hurricanes to Local Sources of Heat and Momentum. *J. Atmos. Sci.*, **39**, 378–394.

Shay, L., G. Goni, and P. Black, 2000: Effects of a Warm Oceanic Feature on Hurricane Opal. *Mon. Wea. Rev.*, **128**, 1366–1383.

Shea, D. and W. Gray, 1973: The Hurricanes Inner Core Region. I. Symmetric and Asymmetric Structure. *J. Atmos. Sci.*, **30**, 1544–1564.

Shin, S. and R. Smith, 2008: Tropical-cyclone intensification and predictability in a minimal three-dimensional model. *Quart. J. Roy. Meteor. Soc.*, **134**, 1661–1671.

Smith, R., 2000: The role of cumulus convection in hurricanes and its representation in hurricane models. *Rev. Geophys.*, **38**, 465–489.

Smith, R., M. Montgomery, and V. Nguyen, 2009: Tropical Cyclone Spin-up Revisited. *Quart. J. Roy. Meteor. Soc.*, **135**, 1321–1335.

Sun, Z. and L. Rikus, 2004: Validating model clouds and their optical properties using Geostationary satellite imagery. *Mon. Wea. Rev.*, **132**, 2006–2020.

Terwey, W. and M. Montgomery, 2008: Secondary eyewall formation in two idealized, full-physics modeled hurricanes. *Journal of Geophysical Research*, **113**, D12112.

Thunis, P. and R. Bornstein, 1996: Hierachy of mesoscale flow assumptions and equations. *J. Atmos. Sci.*, **53**, 380–1397.

Tiedtke, M., 1989: A comprehensive mass flux scheme for cumulus parameterisation in a large-scale models. *Mon. Wea. Rev.*, **117**, 1779–1800.

Wang, Y., 2002a: Vortex Rossby waves in a numerically simulated tropical cyclone. Part I: Overall structure, potential vorticity, and kinetic energy budgets. *J. Atmos. Sci.*, **59**, 1213–1238.

Wang, Y., 2002b: Vortex Rossby waves in a numerically simulated tropical cyclone. Part II: The role in tropical cyclone structure and intensity changes. *J. Atmos. Sci.*, **59**, 1239–1262.

Wang, Y., 2008a: Rapid Filamentation Zone in a Numerically Simulated Tropical Cyclone. *J. Atmos. Sci.*, **65**, 1158–1181.

Wang, Y., 2008b: Structure and Formation of an Annular Hurricane Simulated in a Fully Compressible, Nonhydrostatic ModelTCM4. *J. Atmos. Sci.*, **65**, 1505–1527.

Weber, H. and R. Smith, 1993: The stability of Barotropic Vortices: Implications for Tropical Cyclone motion. *Geophys. Astrophys. Fluid Dyn.*, **70**, 1–30.

Willoughby, H., 1988: The dynamics of the tropical cyclone core. *Aust. Meteorol. Mag.*, **36**, 183–191.

Willoughby, H., 1990: Temporal changes of the primary circulation in tropical cyclones. *J. Atmos. Sci.*, **47**, 242–264.

Willoughby, H., 1995: Mature structure and evolution. In *Global perspective on tropical cyclones*, Elsberry, R., editor, volume No.693. WMO/TD, pp. 21–62.

Willoughby, H., J. Clos, and M. Shorebah, 1982: Concentric Eye Walls, Secondary Wind Maxima, and The Evolution of the Hurricane vortex. *J. Atmos. Sci.*, **39**, 395–411.

Willoughby, H., H. Jin, S. Lord, and J. Piotrowicz, 1984: Hurricane Structure and Evolution as Simulated by an Axisymmetric, Nonhydrostatic Numerical Model. *J. Atmos. Sci.*, **41**, 1169–1186.

Yablonsky, R. and I. Ginis, 2009: Limitation of one-dimensional ocean models for coupled hurricane-ocean model forecasts. *Mon. Wea. Rev.*, **137**, 4410–4419.

Yamasaki, M., 1968a: A tropical-cyclone model with parameterized vertical partition of released latent heat. *J. Meteor. Soc. Japan*, **46**, 202–214.

Yamasaki, M., 1968b: Detailed analysis of a tropical-cyclone simulated with a 12-layer model. *Papers in Meteorology and Geophysics*, **20**, 559–585.

Yamasaki, M., 1968c: Numerical simulation of tropical-cyclone development with the use of primitive equations. *J. Meteor. Soc. Japan*, **46**, 178–201.

Yau, M. K., Y. Liu, D.-L. Zhang, and Y. Chen, 2004: A multiscale Numerical Study of Hurricane Andrew (1992). Part VI: Small-Scale Inner-Core Structures Stuctures and Wind Streaks. *Mon. Wea. Rev.*, **132**, 1410–1433.

Zehr, R., 1992: Tropical cyclonegenesis in western north pacific. Technical report, NOAA Tech. Rep. NESDIS, 181 pp.

Zhu, H., R. Smith, and W. Ulrich, 2001: A minimal three-dimensional tropical cyclone model. *J. Atmos. Sci.*, **58**, 1924–1944.

Zhu, T., D.-L. Zhang, and F. Weng, 2004: Numerical simulation of Hurricane Bonnie (1998). Part I: Eyewall evolution and intensity changes. *Mon. Wea. Rev.*, **132**, 225–241.

Appendix A

List of Symbols and Constants

Variable - Constants	**Description**
a	radius of the earth (6.371 $\times 10^6$ m)
c_p	specific heat (1004.6 J kg^{-1})
Ω	angular speed of the earth (7.292 $\times 10^{-5}$ s^{-1})
R	gas constant (287.04 J kg^{-1} K^{-1})
D	divergence [s^{-1}]
$f = 2\Omega sin\theta$	Coriolis parameter [s^{-1}]
Φ	geopotential [m^2 s^{-2}]
Φ_s	surface geopotential [m^2 s^{-2}]
$\sigma = p/p_s$	vertical coordinate
$\dot{\sigma} = d\sigma/dt$	σ -vertical velocity [Pa s^{-1}]
p	pressure [Pa]
p_s	surface pressure [Pa]
PV	potential vorticity [PVU]
PVU	potential vorticity unit [$10^6\times$ m^{-2} K kg^{-1}]
t	time [s]
T	temperature [K]
Td	dew point temperature [K]
Tv	virtual temperature [K]
θ	potential temperature [K]
u	zonal wind speed [m s^{-1}]
v	meridional wind speed [m s^{-1}]
ω	vertical wind speed in pressure coordinates [Pa s^{-1}]
U	radial wind speed in cylindrical coordinates [m s^{-1}]
V	tangential wind speed in cylindrical coordinates [m s^{-1}]
$\overrightarrow{V}$	horizontal velocity vector
ζ	vertical component of relative vorticity s[$^{-1}$]
ζ_a	vertical component of absolute vorticity s[$^{-1}$]
ϕ	latitude [degrees]
λ	longitude [degrees]

Table A.1: List of variables and constants

Appendix B

On the use of the Laplacian.

Laplacians of variables are used to enhance their local small-scale structures. It is well-known that regions with positive (negative) values of Laplacian represent concave (convex) surfaces, hence, local minima (maxima). For analyses in the inner core region, the use of the Laplacian is preferred over the use of anomaly calculated by conventional linearisation about the mean state. This is because in the inner core region of TCs, where radius circles are small, there is no clear scale separation between the mean state and disturbances. For example, an increase in the amplitude of an asymmetric disturbance with a size of 10 km, which is the typical dimension for convective towers, will project strongly on the mean at radius circles smaller than 20 km. Furthermore, the conventional assumption of zero average perturbations ($\overline{\psi'} = 0$, where ψ' represents anomalies of the variable ψ) is not likely to be satisfied. Here, we demonstrate that the Laplacian of a scalar variable is proportional to its anomaly and thus can be regarded as a proxy for the anomaly.

A two-dimensional variable $\psi(x, y)$ can be linearised as follows:

$$\psi(x, y) = \overline{\psi} + \psi'(x, y) \tag{B.1}$$

where $\overline{\psi}$ is a reference value of the basic state, and $\psi'(x, y)$ is the deviation from the basic state $\overline{\psi}$.

If, in an idealised case, a field $\psi(x, y)$ consists of only one wave having an amplitude $\hat{\psi}_{mn}$, and horizontal wavenumbers m and n in the x and y directions, respectively, the anomaly $\psi'(x, y) = \psi'(x, y)_{mn}$ can be expressed as

$$\psi'(x, y) = \psi'(x, y)_{mn} = \hat{\psi}_{mn} \exp\left[i(mx + ny)\right] \tag{B.2}$$

Then, the Laplacian of $\psi'(x,y)$ has the form

$$\nabla^2\psi'(x,y) = -(m^2+n^2)\psi'(x,y) \tag{B.3}$$

Since $\nabla^2\overline{\psi} = 0$, the Laplacian becomes

$$\nabla^2\psi(x,y) = \nabla^2\psi'(x,y) = -(m^2+n^2)\psi'(x,y) \tag{B.4}$$

Equation B.4 shows that the Laplacian is proportional to the anomaly with a factor of $-(m^2+n^2)$ which has units of $[m^{-2}]$. Therefore, the Laplacian can be regarded as a proxy for the anomaly.

In reality, the anomaly of a variable can be represented as a combination of multiple waves in the form

$$\psi'(x,y) = \Sigma_{m=1}^{\infty}\Sigma_{n=1}^{\infty}\psi'(x,y)_{mn} \tag{B.5}$$

Then, the Laplacian can be expressed as follows

$$\begin{aligned}
\nabla^2\psi(x,y) &= \nabla^2\Sigma_{m=1}^{\infty}\Sigma_{n=1}^{\infty}\psi'(x,y)_{mn} && \text{(B.6)}\\
&= \Sigma_{m=1}^{\infty}\Sigma_{n=1}^{\infty}\nabla^2\psi'(x,y)_{mn} && \text{(B.7)}\\
&= -\Sigma_{m=1}^{\infty}\Sigma_{n=1}^{\infty}(m^2+n^2)\psi'(x,y)_{mn} && \text{(B.8)}
\end{aligned}$$

Equation B.8 indicates that high wavenumbers, i.e. small structures, project with larger amplitudes using the Laplacian. Thus, it explains why the Laplacian enhances the representation of small-scale structures.

Appendix C

The ensemble experiments

C.1 The relationship of SST and TC intensity.

Table C.1 shows the statistical characteristics of the SSTs along the tracks of the modelled vortices. Pmin and Vmax are the minimum surface pressure and the maximum wind speed achieved during the 48 h integration periods. Values of the SSTs are averaged over the regions inside of 100 km from the vortex center. For each simulation, the mean (μ) and standard deviation (σ) of SST is calculated using hourly value of the averaged SSTs along the track of the simulated vortex. The ensemble simulations are grouped into two groups, W1 and W0, which use the SST analyses of the previous week and of the same week, respectively. Subgroup W1* within group W1, which includes runs C0, C1 to C4, E4 and E5, has similar configurations of the initial vortex, the model and the large scale environment. Thus, the differences between W1* and W0 are likely to be influenced predominantly by differences in the SSTs.

One-sided t-tests[1] are carried out to determine if there are significant differences in the SSTs encountered by the simulated vortices in these different groups. For the mean SSTs, the t-test uses hourly values of SSTs following the tracks of the vortices in each groups (i.e. 49×10, 49×16, and 49×3 data for groups W1*, W1 and W0, respectively). The t-tests for other characteristics such as Pmin, Vmax and σ use the averaged value for each run, thus, having 10, 16 and 3 data points for groups W1*, W1 and W0, respectively. Since group W0 has only 3 data values, test results for Pmin, Vmax and σ (marked with *Italic* font) should be used with caution.

The above mentioned t-tests indicate that vortices in groups W1 and W1* achieve

[1]Descriptions of the t-test method can be found in most textbooks on basic statistics such as Rosenkrantz (1997).

significantly higher intensities than those in group W0. The mean SSTs encountered by the vortices in group W1* is on average higher than those in group W0 (with p-value of 0.03). Thus, the higher intensities in group W1*, since the vortex structure and large scale environment are the same, are most likely due to the higher SSTs along the tracks of these simulated vortices. This possible cause is further confirmed by the high correlations between SSTs and Pmin/Vmax for these experiments (see Figure 3.7 in Chapter 3). On the other hand, although the intensities of the vortices in group W1 are significantly higher than those in W0, there is not enough evidence to reject the claim that the mean SSTs along the tracks in W1 are similar to those in W0 (with p-value of 0.099). In this case, the overall higher intensities of the vortices in group W1 (over those of group W0) may be explained by other factors such as vortex configurations (AS1, AS2), environmental influences (E1-E3) and model configuration (CB).

Table C.1 shows also that the simulated vortices in W0, on average, tend to encounter larger variations of the SSTs along their tracks than those in W1 and W1* with p-values of 0.0011 and 0.0023, respectively. Similar results (not shown here for brevity) are also found using the SSTs averaged over the regions of 50 and 200 km from the vortex center.

C.2 Vacillation cycles

Tables C.2 and C.3 show details of the vacillation cycles in the ensemble simulations. The criteria for determining these cycles are defined in Chapter 3 and are reproduced below for convenient referencing:

1. Change in SDPVmax is not less than 2 PVU,
2. The phase of higher asymmetry has SDPVmax not less than 4 PVU
3. The Symmetric to Asymmetric (S-A) transition period is calculated as hours elapsed from the time of lowest asymmetry until the SDPVmax becomes greater than 4 PVU
4. The Asymmetric to Symmetric (A-S) transition period is calculated as hours elapsed from the time the SDPVmax becomes greater or equal 4 PVU until the SDPVmax reaches the next local minimum.

Each row of Tables C.2 and C.3 shows characteristics of one vacillation cycle. The content of the columns in these tables has the following meaning:

1. **[Run ID]** Identification of the current simulation.
2. **[Figure]** Index of the Figure containing the evolution of asymmetries.
3. **[No]** The order of the current vacillation cycle during the 48 h forecast period.
4. **[h1]** The hour at which the current vacillation cycle starts.
5. **[S-A]** The duration [h] of the symmetric to asymmetric transition.
6. **[A-S]** The duration [h] of the asymmetric to symmetric transition.
7. **[h2]** The hour at which the current vacillation cycle ends.
8. **[S-A]** The duration [h] of the whole cycle.
9. **[Amp.]** The amplitude [PVU] of the current vacillation cycle.
10. **[A-I$_{\mathbf{corr}}$]** The correlation between Asymmetries (SDPVmax) and the Intensification rates ($\partial\overline{V}_{max}/\partial t$) during the current cycle.
    Cycles with A-I$_{\mathbf{corr}}$ less than -0.5 are shown with **bold** face.

Table C.1: Characteristics of the SSTs along the tracks of the modelled vortices. Values of SST are averaged over the region inside of the 100 km radius from the TC center. Statistical characteristics are calculated using hourly data during 48 h forecast period from 00Z 27 August 2005.

Source	Run ID	Pmin	Vmax	SST (radius $\leq$ 100 km)	
				μ	σ
W1	C0	887.4	163.7	302.815	0.506
	C1	883.8	162.4	302.894	0.412
	C2	883.8	170.7	302.870	0.397
	C3	883.6	160.4	302.890	0.428
	C4	883.9	163.6	302.874	0.440
	A0	884	167.6	302.874	0.439
	B0	887.3	164.3	302.856	0.460
	D0	886.9	160.8	302.825	0.521
	E4	879.6	171.3	303.281	0.370
	E5	888.9	159.9	303.300	0.365
	All W1*	**884.92**	**164.47**	**302.948**	**0.434**
	E1	905.5	147.7	303.016	0.163
	E2	907.6	141.5	302.947	0.093
	E3	907.3	144.2	302.820	0.233
	AS1	907.9	161	302.688	0.505
	AS2	886.3	171.8	302.835	0.538
	CB	902.6	151.2	302.913	0.467
	All W1	**891.65**	**160.13**	**302.92**	**0.396**
W0	STC	902.8	150.7	302.797	0.513
	E5C	903.8	147.7	302.898	0.509
	E5CS	900.4	153.2	302.889	0.491
	All W0	**902.33**	**150.53**	**302.861**	**0.504**

t-test

W1*-W0	Δ	-17.41	13.94	0.087	-0.07
	p-value	***1.48e-5***	***5.03e-4***	**0.0321**	***0.0011***
W1-W0	Δ	-10.68	9.6	0.058	-0.108
	p-value	***6.71e-4***	***2.57e-3***	0.099	***0.0023***

Table C.2: Characteristics of vacillation cycles in the ensemble runs

1 **ID**	2 **Figure**	3 **No**	4 **h1**	5 **S-A**	6 **A-S**	7 **h2**	8 **S-A-S**	9 **Amp.**	10 **A-I$_{corr}$**
Group I: Observation perturbations									
C0	3.13	1	10	3	4	17	7	2.3	-0.154
		2	35	3	5	43	8	3.2	**-0.728**
C1	3.10	1	2	2	5	9	7	2	0.735
C2	3.10	1	5	4	10	19	14	3.2	-0.180
		2	20	5	6	31	11	2	0.301
		3	31	5	11	47	16	3.2	**-0.598**
C3	3.10	1	6	1	6	13	7	2.5	0.342
C4	3.10	1	32	11	4	47	15	2	-0.277
Group II: Nudging methods									
A0	3.10	1	4	2.2	7.8	14	10	3	-0.218
		2	14	3	2	19	5	2	**-0.626**
		3	21	1	3	25	4	2	0.258
		4	35	1.2	8.8	45	10	3	-0.456
B0	3.10	1	4	4	2	10	6	2	-0.120
D0	3.10	1	27	2.5	9.5	39	12	3.8	**-0.501**
Group III: Boundary conditions									
E1	3.11	1	13	5	10	28	15	2	0.181
		2	32	4	8	44	12	2	-0.431
E2	3.11	1	7	3	9	19	12	2	-0.031
		2	29	3	10	42	13	2	0.313
E3	3.11	1	7	3	3	13	6	3.5	-0.440
		2	13	4	7	24	11	3.0	-0.330
		3	24	2	1	27	3	2	-0.259
		4	30	2	2	34	4	1.5	-0.240
		5	34	3	6	43	9	3	0.187
E4	3.11	1	7	4	3	14	7	2.5	0.609
		2	17	4	7	28	11	2	0.487
		3	35	3	7	45	10	2	-0.141
E5	3.11	1	7	2.5	2.5	12	5	3	-0.276
		2	26	4	10	40	14	2	-0.136

Table C.3: Characteristics of vacillation cycles in the ensemble runs (continued)

1 **ID**	2 **Figure**	3 **No**	4 **h1**	5 **S-A**	6 **A-S**	7 **h2**	8 **S-A-S**	9 **Amp.**	10 **A-I$_{\mathbf{corr}}$**
Group IV: Model and vortex configuration									
STC	3.13	1	17	4	3	24	7	2.5	0.283
		2	33	5	6	44	11	4	**-0.862**
CB	3.13	1	24	3	8	35	11	3	-0.338
		2	35	3	8	46	11	3	**-0.741**
AS1	3.13	1	38	7		47	7		**-0.525**
AS2	3.13	1	7	5	2	14	7	2.5	0.625
		2	14	5	7	26	12	2	0.433
		3	26	11	9	47	20	4	**-0.731**
E5C	3.13	1	15	3	9	27	12	3.8	**-0.944**
		2	27	3	5	35	8	4	**-0.695**
E5CS	3.13	1	22	5	6	33	11	2.2	0.106
		2	33	3	11	47	14	4	-0.441
Group V: Constant SST									
STF	3.12	0	–	–	–	–	–	–	–
EF1	3.12	1	17	4	9	30	13	3.5	0.044
		2	30	3	12	45	15	3.2	-0.452
EF2	3.12	1	21	5	5	31	10	2	-0.226
EF3	3.12	0	–	–	–	–	–	–	–
EF4	3.12	0	–	–	–	–	–	–	–
EF5	3.12	0	–	–	–	–	–	–	–
ASF1	3.13	0	–	–	–	–	–	–	–
ASF2	3.13	1	15	4	5	24	9	3	-0.347
		2	24	5	6	35	11	2	-0.089

Appendix D

Barotropic Instability of the Mean Flow

In this section, we present our investigations on the roles of barotropic instability in promoting the observed vacillations of asymmetries in the simulation E5C. Asymmetries of potential vorticity (PV) along various radius circles at 850 and 250 hPa are analysed by Fast Fourier Transform decompositions. Next, barotropic instability analyses, which are described in section 6.1.1, are performed using the azimuthally-average tangential wind profiles from the simulated vortex. The development of asymmetries and the calculated barotropic e-folding times for the corresponding wavenumbers are then plotted together so that their relationship can be determined.

D.1 Evolution of asymmetries

Figure D.1 shows the development of wave amplitudes of PV along 25, 50 and 75 km radius circles on the 850 hPa levels. The times of maximum and minimum asymmetries (A1,A2,A3, S1 and S2), which are identified in section 4.1 based on the asymmetric characteristics of the 50 km radius circle on 850 hPa, are marked on all plots for reference. It can be seen from this figure that the vacillation is strongest at 50 km radius. While radius 25 km exhibits high asymmetries during the identified asymmetric phases A1, A2 and A3, the 75 km radius shows high level of asymmetries only during the asymmetric phase A2. Thus, this fact suggests that at low levels the vacillation occurs mainly in the inner core inside of 75 km radius.

The development of asymmetries on the 250 hPa level, shown in Figure D.1, differs from the asymmetric characteristics at 850 hPa in a number of ways, which can be described below:

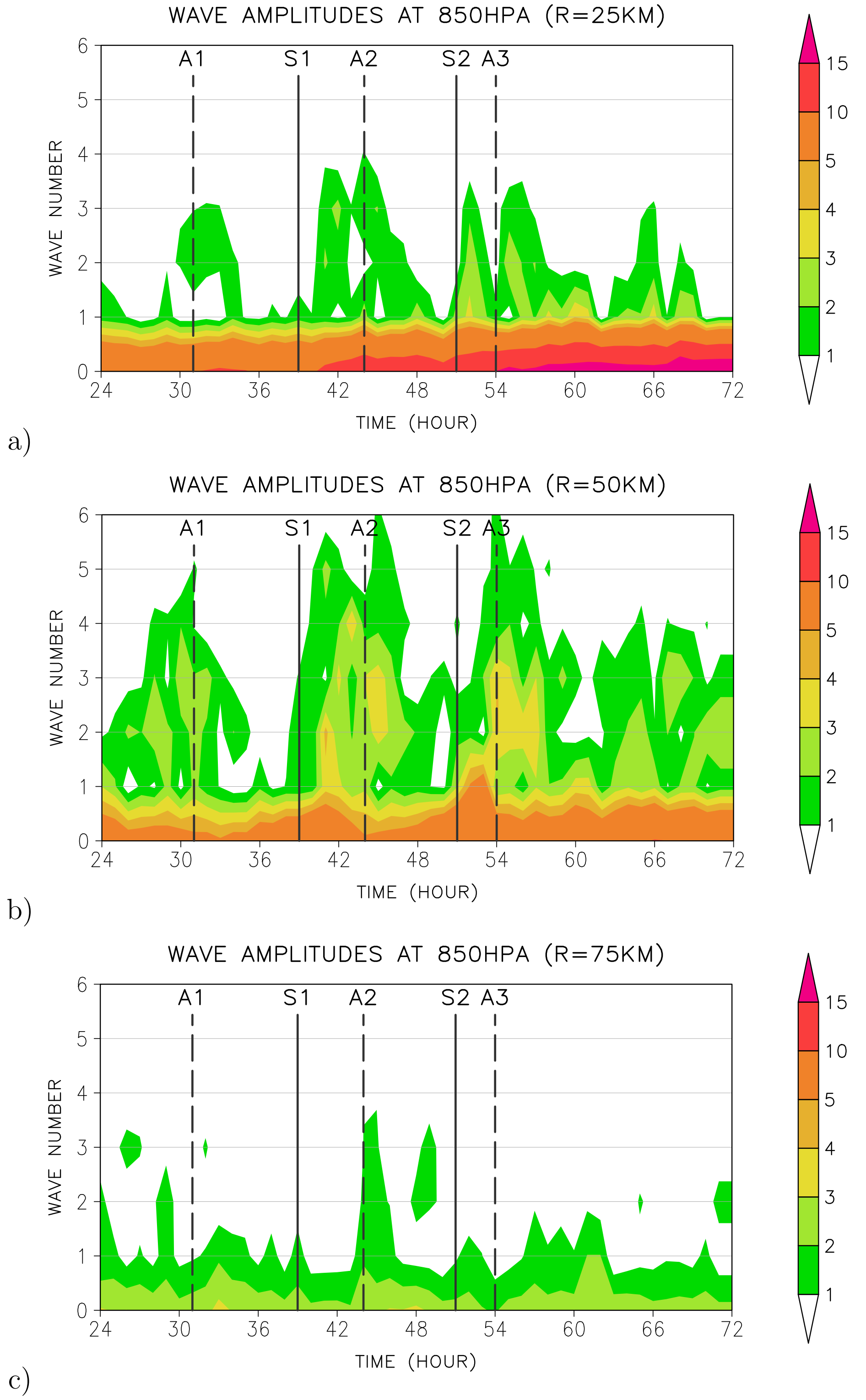

Figure D.1: Evolution of PV azimuthal wave amplitutes of wavenumbers from 0 to 6 at 850 hPa. Panels a,b, and c are for the 25, 50 and 75 km radius circles, respectively.

- The vacillation pattern of asymmetries occurs at all radii from 25 to 75 km with similar amplitudes, instead of being confined inside of the 75 km with the

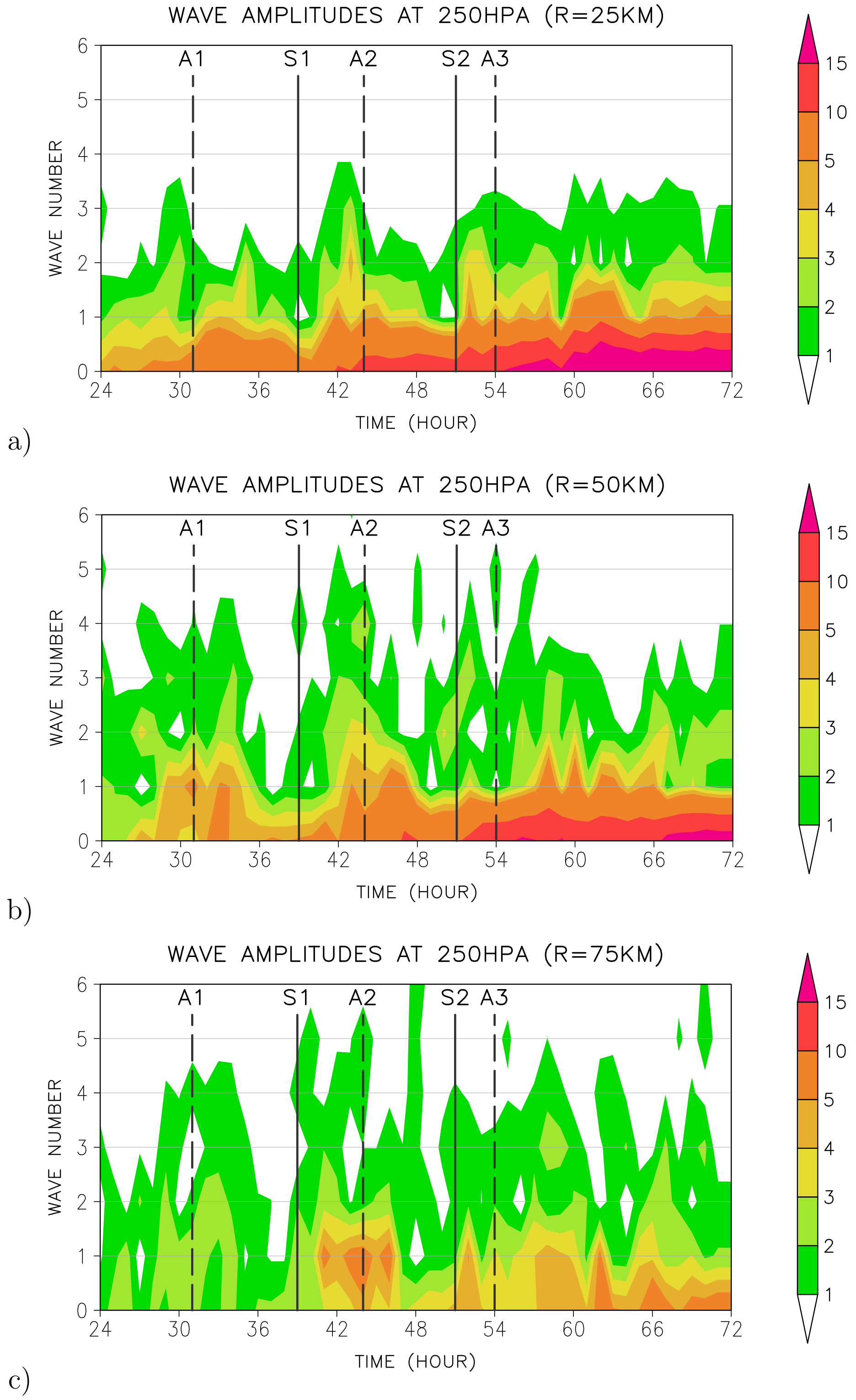

Figure D.2: The same as Figure D.1 but for the 250 hPa level

.

strongest amplitudes near the 50 km radius as at 850 hPa. This large spread of asymmetries to larger radii at upper levels is consistent with low inertial stability at upper levels of TCs (see Equation 1.1 and discussions thereof) .

- Radii 50 and 75 km exhibit simular phases of high asymmetries (A1 and A2). This similarity in the vacillation phases of radii 50 and 75 km, instead of the association between the 25 and 50 km radii as that at 850 hPa, is consistent with the outward-tilt configuration, which is typical of the eyewall cloud system.

- At 250 hPa, the symmetric (wavenumber 0) and asymmetric (wavenumbers greater than 0) amplitudes vary in phase with each other. For example, during the identified asymmetric phases A1 and A2, amplitudes of all wavenumbers including the symmetric wavenumber 0 increase. In contrast, during the symmetric phases S1 and S2, the symmetric amplitudes are not large as that at lower levels. Thus, it is suggestive that the transfer of energy between the mean flow (i.e. the symmetric component) and the eddies or asymmetric features (i.e. wavenumbers greater than 0) does not likely to occur. In addition, it is plausible also that the mechanism responsible for the increase of the mean flow (i.e. the symmetric component) is not present at upper levels as in the case of lower level.

The above characteristics of asymmetries at upper levels indicate that the observed asymmetries at upper levels are associated with the development of VHTs during the identified asymmetric phases.

D.2 Barotropic instability associated with the mean vortex profiles

Figures D.3 to D.10 show the evolution of PV wave amplitudes and the e-folding time for the perturbations of the corresponding wavenumbers due to barotropic instability of the mean flow. Note that e-folding times τ_e for the periods of stable flow with $\tau_e > 24$ h are not plotted.

Table D.1 lists the characteristics of figures in this Appendix.

Table D.1: Characteristics of figures showing the results of the asymmetry analysis and the barotropic instability calculations.

Characteristics	Level	Radius	Wavenumber	Figure
Asymmetry analysis	850 hPa	25-50-75 km	0-5	D.1
	250 hPa			D.2
E-folding time	850 hPa	25 km	2,3,4	D.3
		50 km	1,2,3	D.4
		50 km	4,5,6	D.5
		75 km	2,3,4	D.6
	250 hPa	25 km	2,3,4	D.7
		50 km	1,2,3	D.8
		50 km	4,5,6	D.9
		75 km	2,3,4	D.10

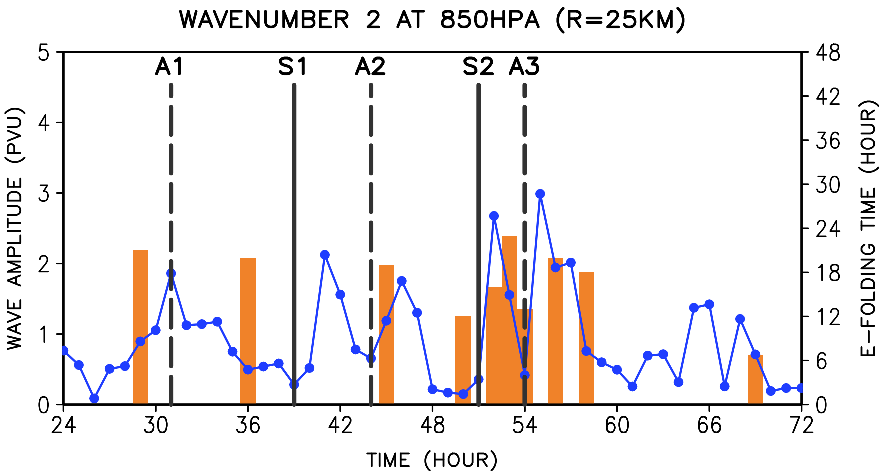

a)

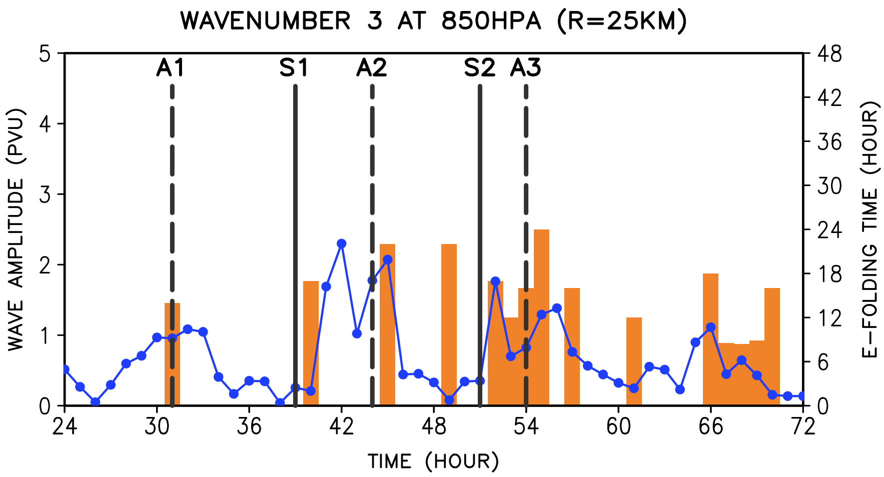

b)

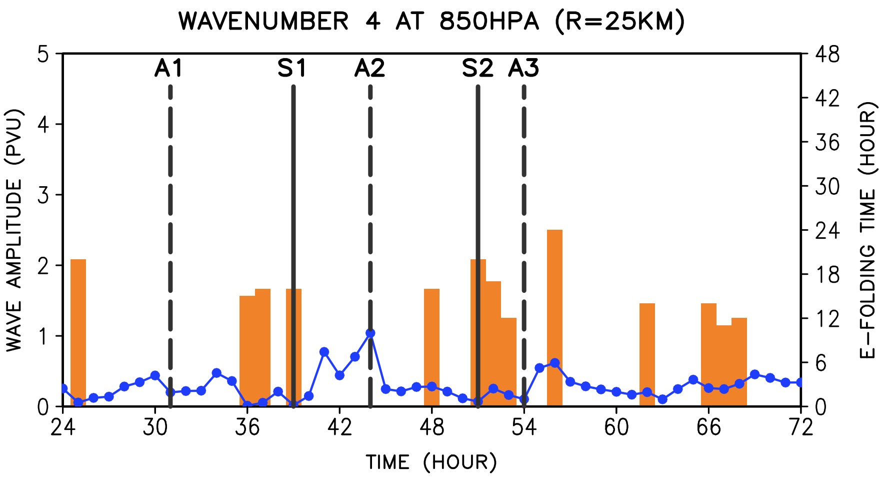

c)

Figure D.3: Wave amplitudes [PVU] (blue lines) at the 25 km radius and e-folding time [hour] (shaded collumns) of the corresponding wavenumbers at 850 hPa. Panels a,b and c are for wavenumbers 2, 3 and 4, respectively. E-folding times greater than 24 h are not plotted. Thus, periods without plotted collumns are barotropically stable with e-folding times greater than 24 h.

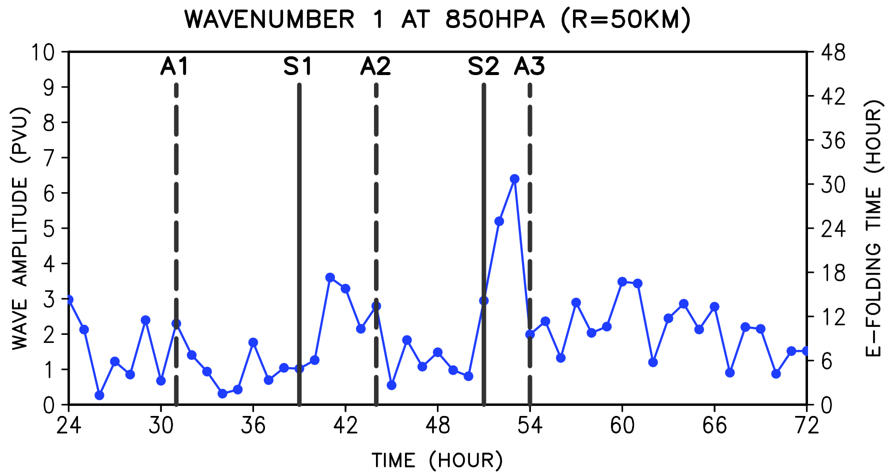

a)

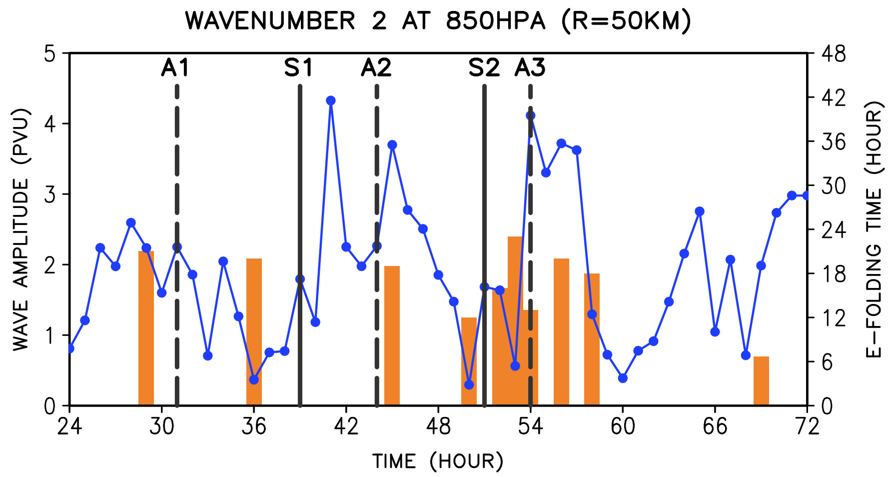

b)

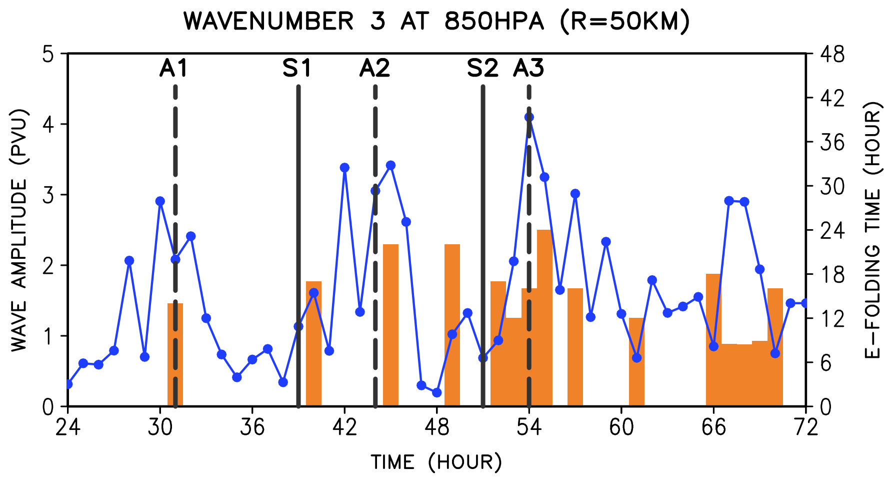

c)

Figure D.4: As in Figure D.3 but for the 50 km radius and wavenumbers 1 to 3.

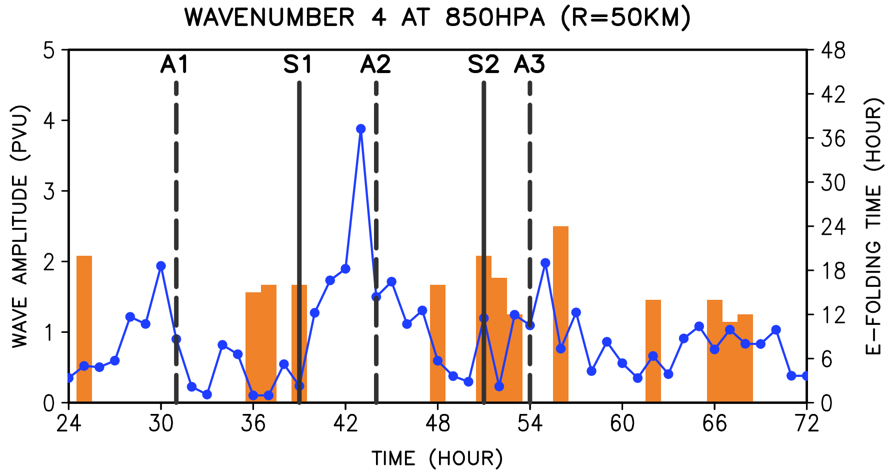

a)

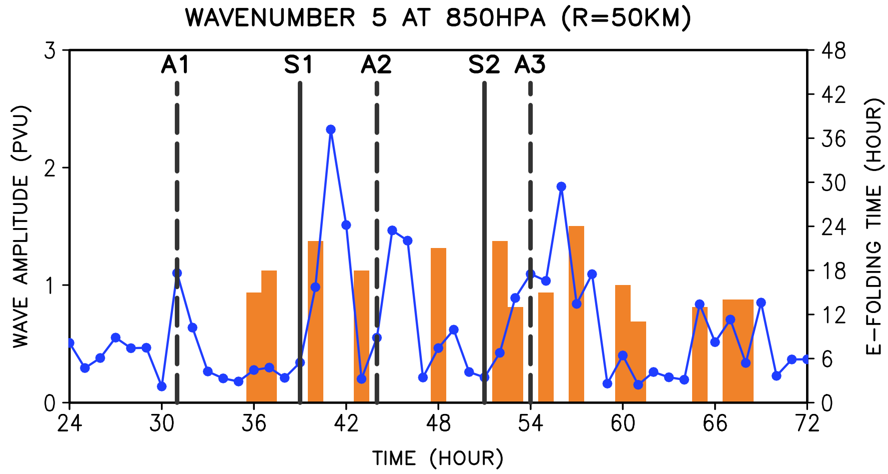

b)

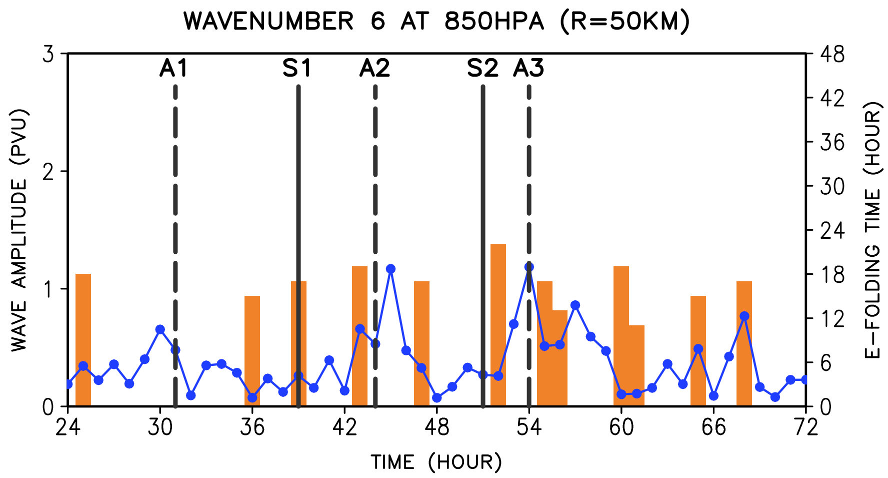

c)

Figure D.5: As in Figure D.4 except for wavenumbers 4 to 6.

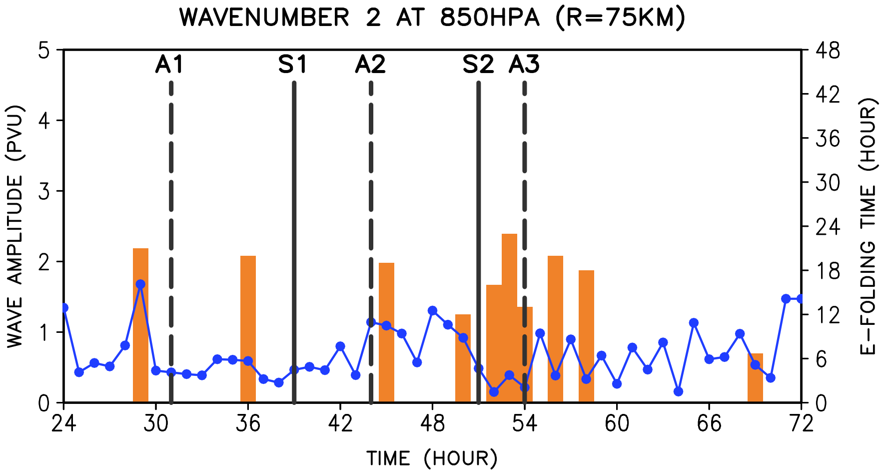

a)

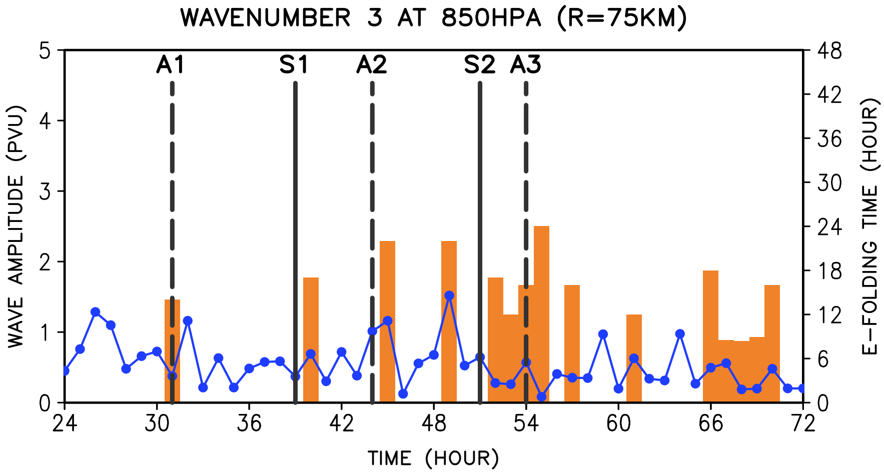

b)

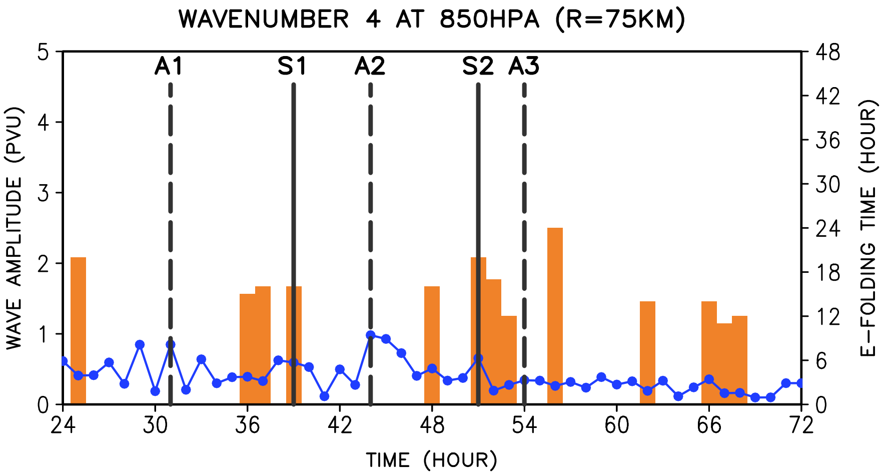

c)

Figure D.6: As for Figure D.3 except for the 75 km radius.

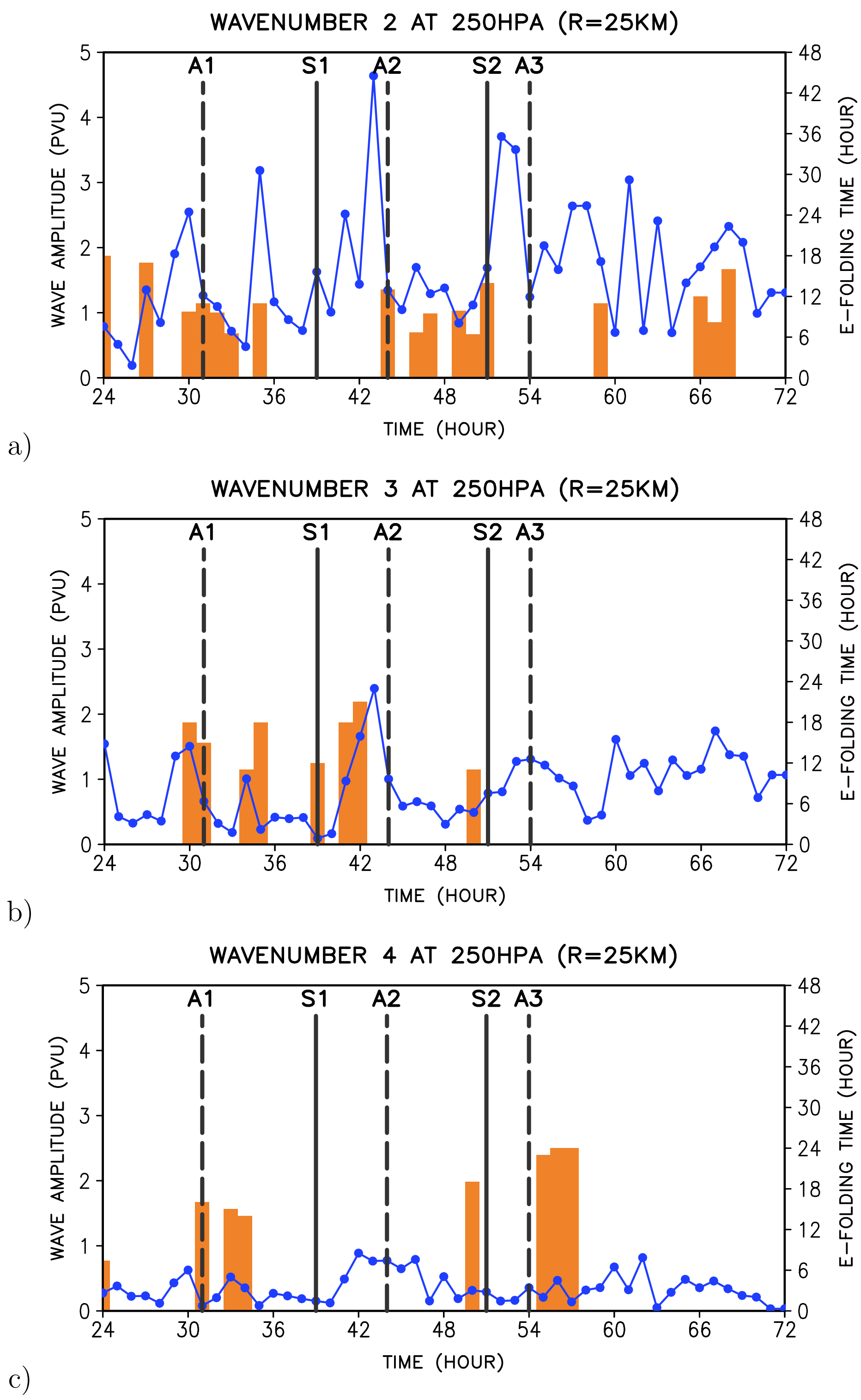

Figure D.7: As in Figure D.3 except for 250 hPa.

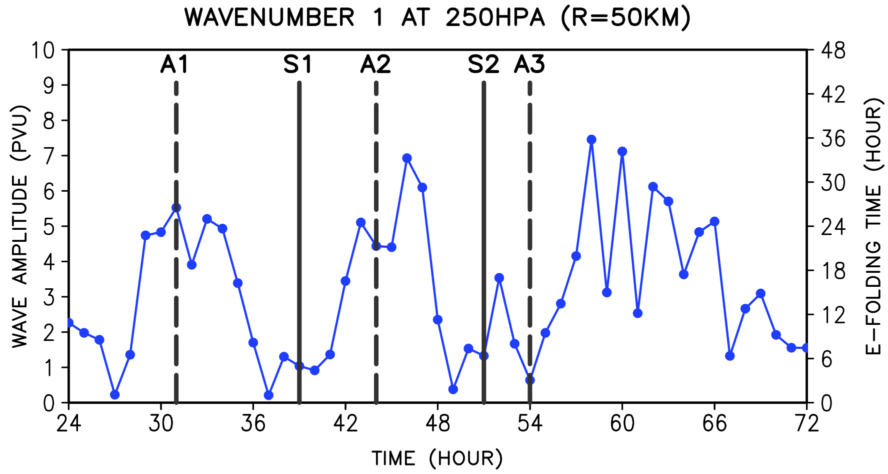

a)

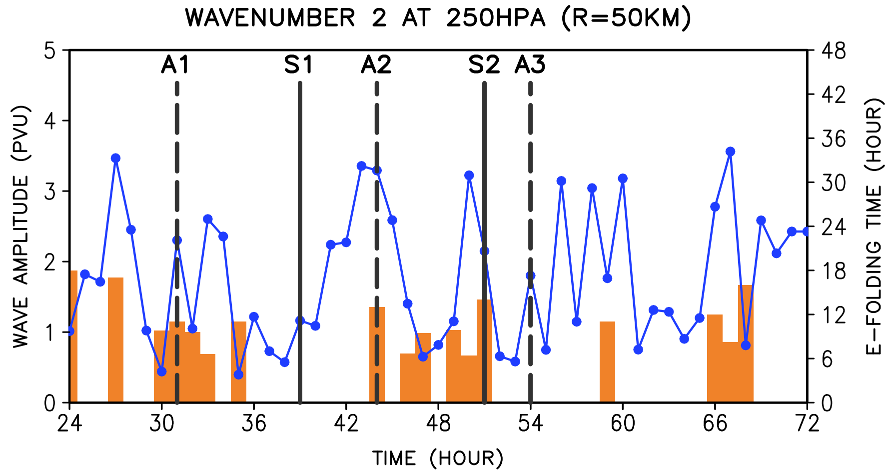

b)

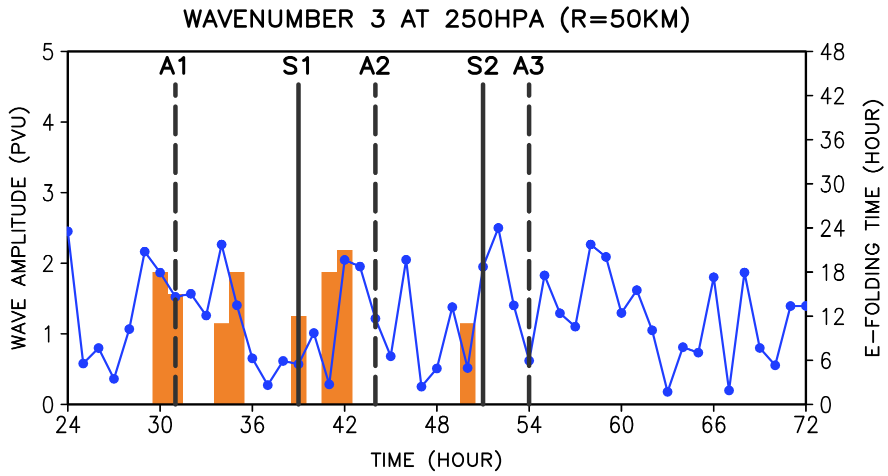

c)

Figure D.8: As in Figure D.4 except for 250 hPa.

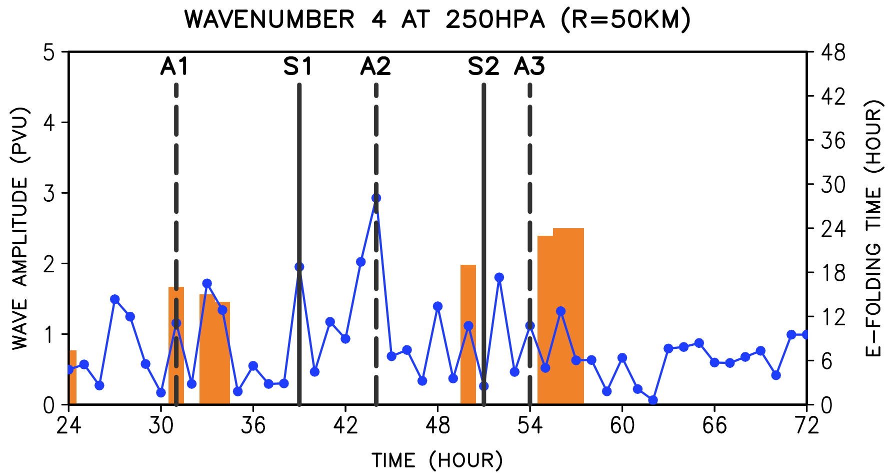

a)

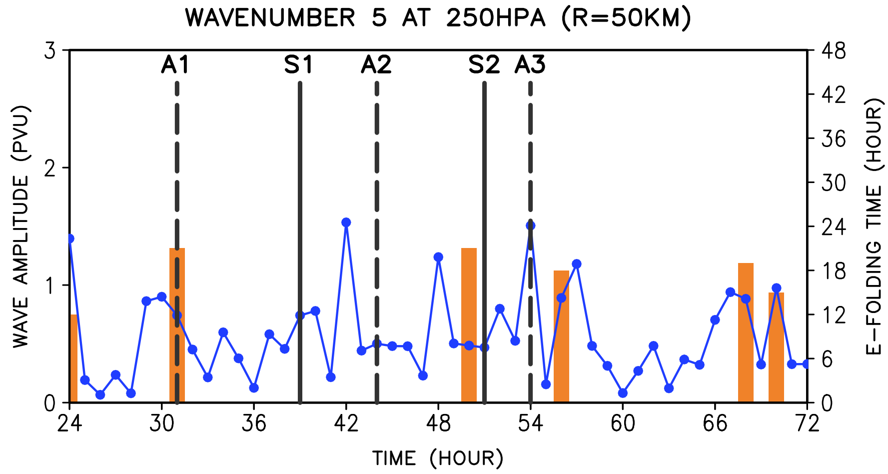

b)

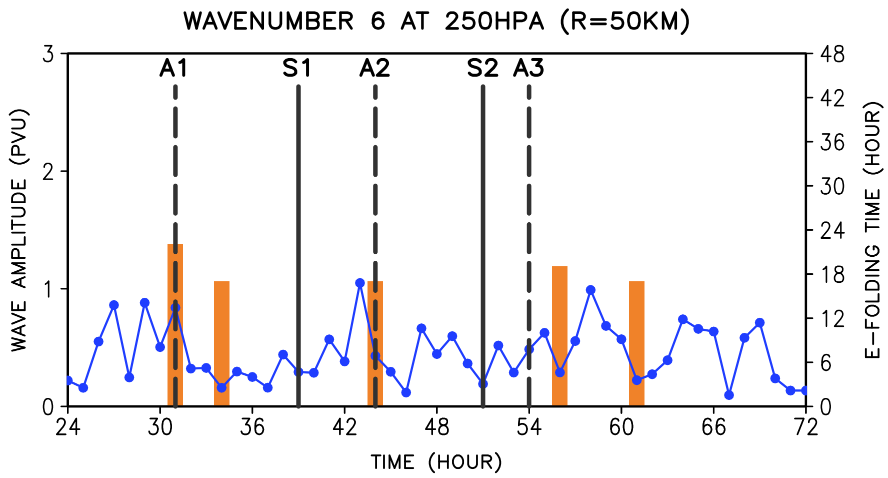

c)

Figure D.9: As in Figure D.5 except for 250 hPa.

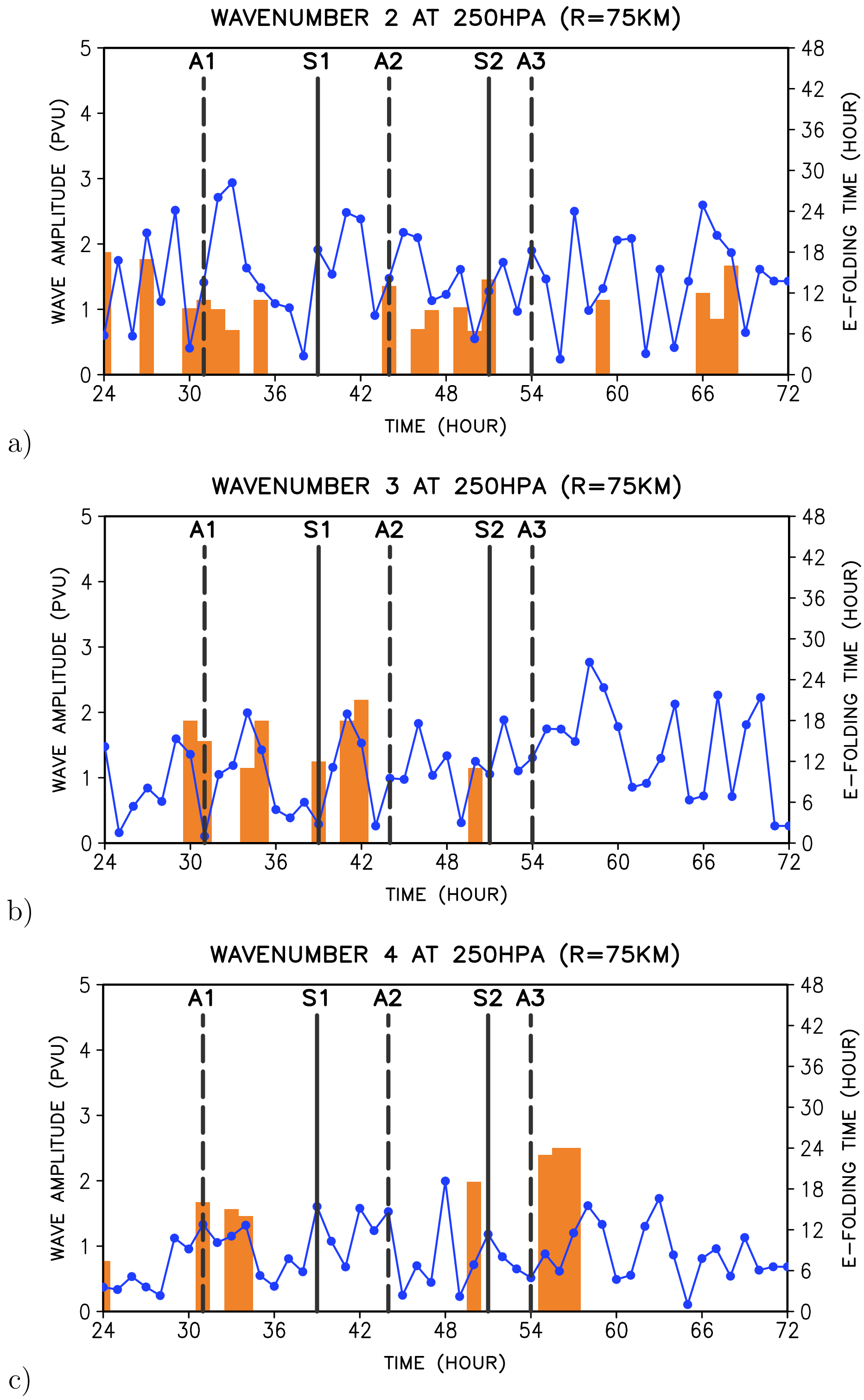

Figure D.10: As in Figure D.10 except for 250 hPa.

Appendix E

Budget analysis

E.1 Budget analysis of vorticity

Changes of the vorticity structure during the two different phases are studied by calculating vorticity budget using equation 6.1 of Haynes and McIntyre (1987). This equation has the following form:

$$\frac{\partial \zeta_{ap}}{\partial t} + \frac{\partial}{\partial x}\left(u\zeta_{ap} + \omega\frac{\partial v}{\partial p} - G\right) + \frac{\partial}{\partial y}\left(v\zeta_{ap} - \omega\frac{\partial u}{\partial p} + F\right) = 0, \qquad \text{(E.1)}$$

where ζ_{ap} is the absolute vorticity on the pressure vertical coordinate, F and G are the horizontal components of the local frictional or other force **F** per unit mass, in the x and y directions respectively.

Equation 6.1 of Haynes and McIntyre (1987) and can be rewritten in the form:

$$\frac{\partial \zeta_{ap}}{\partial t} = -\nabla\cdot(u\zeta_{ap}, v\zeta_{ap}) - \nabla\cdot\left(\omega\frac{\partial v}{\partial p}, -\omega\frac{\partial u}{\partial p}\right) - \nabla\cdot(-G, F), \qquad \text{(E.2)}$$

where the first term represents the contribution from the horizontal convergence of the vorticity flux (i.e. changes of vorticity by horizontal advection and convergence); the second term is the generation of vorticity by stretching and twisting (including the diabatic effects of convection), and will be referred here as the tilting term; and the last term shows the influence of other forces such as friction.

Horizontal and vertical differential operators are computed by centered differencing. Transient tendencies are calculated using a five-point time derivative differencing scheme, which has the errors of the fourth order, and are expressed as follow:

$$\frac{\partial \zeta_{ap}}{\partial t} = \frac{-\zeta_{ap,x+2h} + 8\zeta_{ap,x+h} - 8\zeta_{ap,x-h} + \zeta_{ap,x-2h}}{12h} - 0(h^4), \tag{E.3}$$

where h is the time step (5 minutes) of the model outputs used for this calculation. Note that the best way to calculate tendencies are to get tendencies after each integration time step. However, the tendency calculations using model output, even though after short time interval, may be affected by different numerical procedures such as numerical filtering, which is common in numerical models, as well as the nonlinearity of physical processes. Thus, while the diagnostic terms on the right hand side of budget equations can be determined accurately, local tendencies calculated buy model outputs at different times do not have the same level of accuracy. Thus, differences between the sum of the diagnostic terms and the resultant tendencies are common. Nevertheless, they do resemble each other in general. Equation E.3 is also used for transient tendencies of the budget calculations for tangential wind and equivalent potential temperatures.

E.2 Budget analysis for tangential wind

Budget for mean tangential wind is analysed using the formulation similar to that used by Persing et al. (2002), and has the following form:

$$\frac{\partial \overline{V}}{\partial t} = (-\overline{U\zeta}) + (-\overline{U'\zeta'}) + (-\overline{\omega}\frac{\partial \overline{V}}{\partial p}) + (-\overline{\omega'\frac{\partial V'}{\partial p}}) + Friction, \tag{E.4}$$

E.3 Budget analysis for equivalent potential temperature

The budget equation for θ_e has the following form:

$$\frac{\partial \theta_e}{\partial t} = -\left(u\frac{\partial \theta_e}{\partial x} + v\frac{\partial \theta_e}{\partial y}\right) - \omega\frac{\partial \theta_e}{\partial p} + S_{\theta_e}, \tag{E.5}$$

where the first term is the horizontal advection and the second term is the vertical advection of θ_e. S_{θ_e} is the source or sink of θ_e due to physical processes such as surface fluxes or vertical diffusion. This term is not calculated here since there is not enough data to calculate them accurately.

Table E.1 lists the characteristics of figures in this Appendix. Note that cross-sections are produced by taking azimuthal averages of the terms in budget equations.

Table E.1: Characteristics of figures showing the results of the budget calculations.

Equation	Variable	Plane	Level	Time	Figure
E.2	ζ_{ap}	Horizontal (lon-lat)	850 hPa	S1 - 39 h	E.1
				A2 - 44 h	E.2
				S2 - 50 h	E.3
			200 hPa	S1 - 39 h	E.4
				A2 - 44 h	E.5
				S2 - 50 h	E.6
		Cross section (r-p)	1000-100 hPa	S1 - 39 h	E.7
				A2 - 44 h	E.8
E.4	V	Cross section (r-p)	1000-100 hPa	S1 - 39 h	E.9
				A2 - 44 h	E.10
E.5	θ_e	Cross section (r-p)	1000-100 hPa	S1 - 39 h	E.11
				A2 - 44 h	E.12

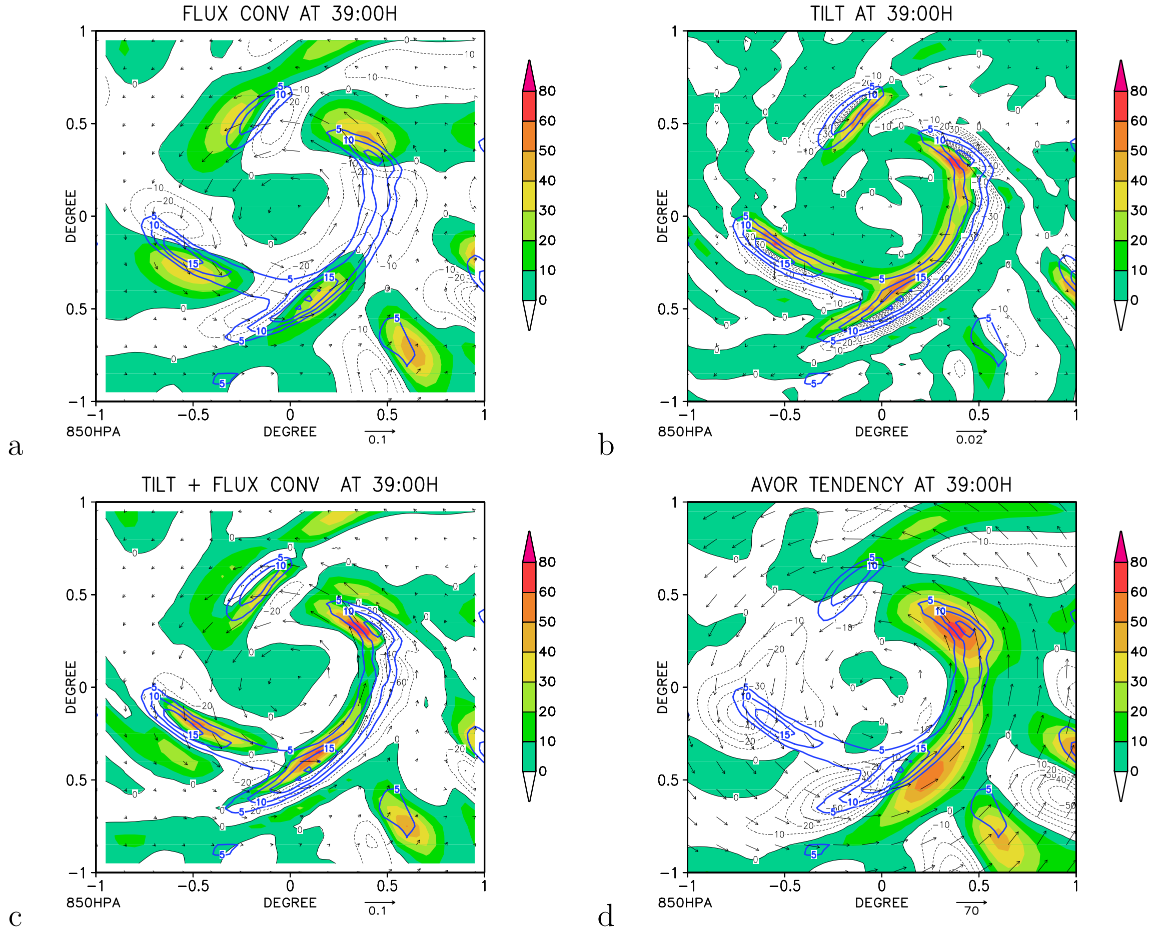

Figure E.1: Contribution of different terms in Equation E.2 from Haynes and McIntyre (1987) to the vorticity generation (positive tendencies are shaded, negative tendencies are contoured with dashed lines, unit [4×10^{-7} s^{-2}]) during the the symmetric phase S1 (at 39 h). a) The tilting term $[-\nabla \cdot \left(\omega \frac{\partial v}{\partial p}, -\omega \frac{\partial u}{\partial p}\right)]$; b) horizontal flux convergence $[-\nabla \cdot (u\zeta_{ap}, v\zeta_{ap})]$; c) sum of the above two terms; and d) actual vorticity tendencies $[\frac{\partial \zeta_{ap}}{\partial t}]$. Thick blue solid lines are vertical upward motion ω, [Pa s^{-1}].

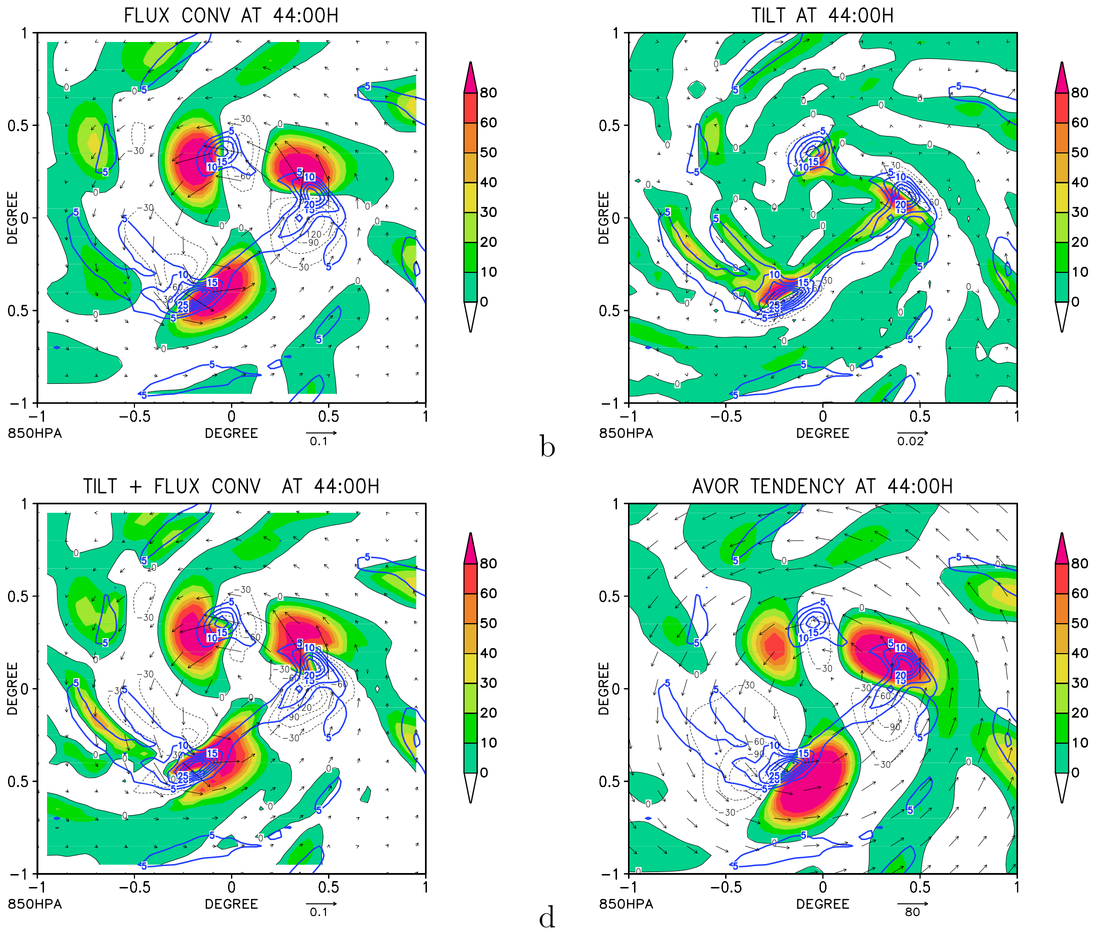

a b c d

Figure E.2: As in Figure E.1 but for the asymmetric phase A2 at 44 h.

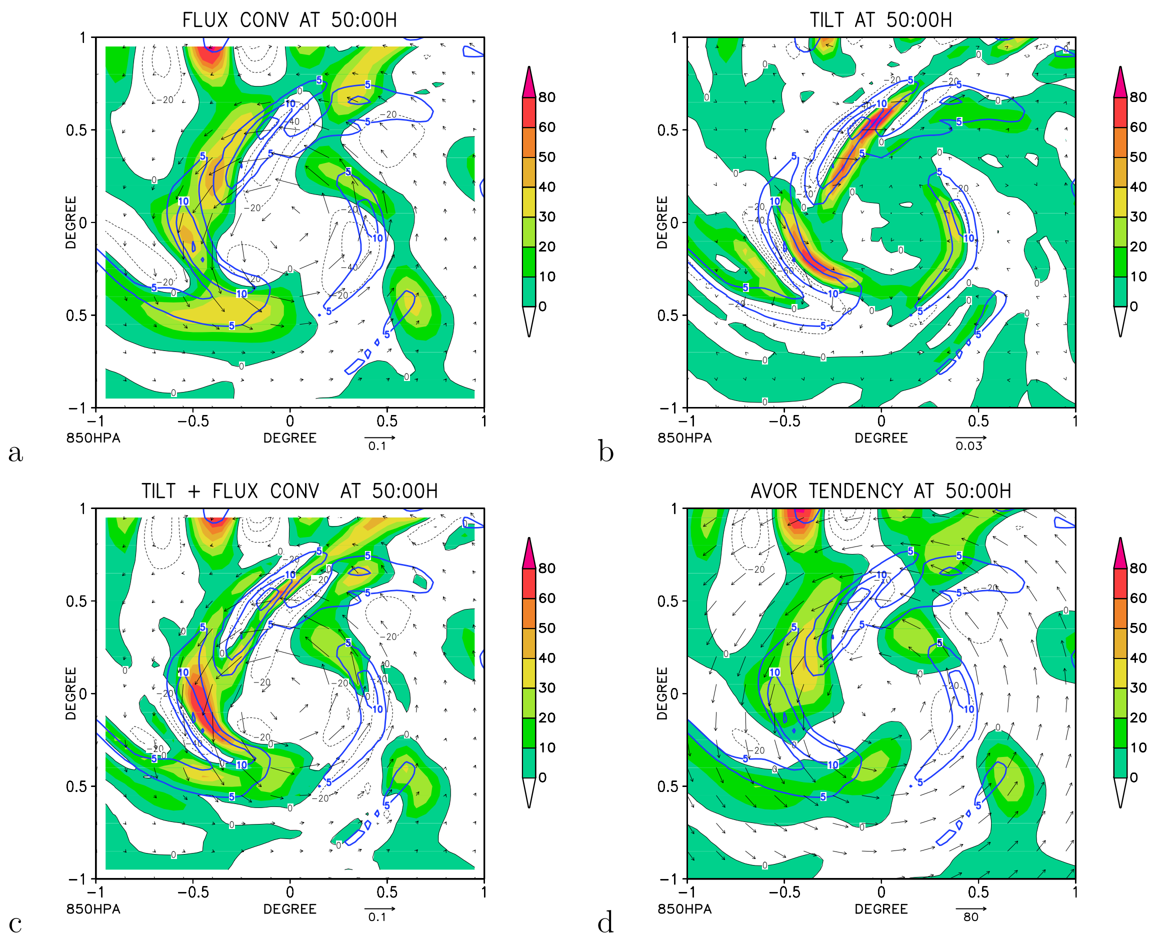

Figure E.3: As in Figure E.1 but for the symmetric phase S2 at 50 h.

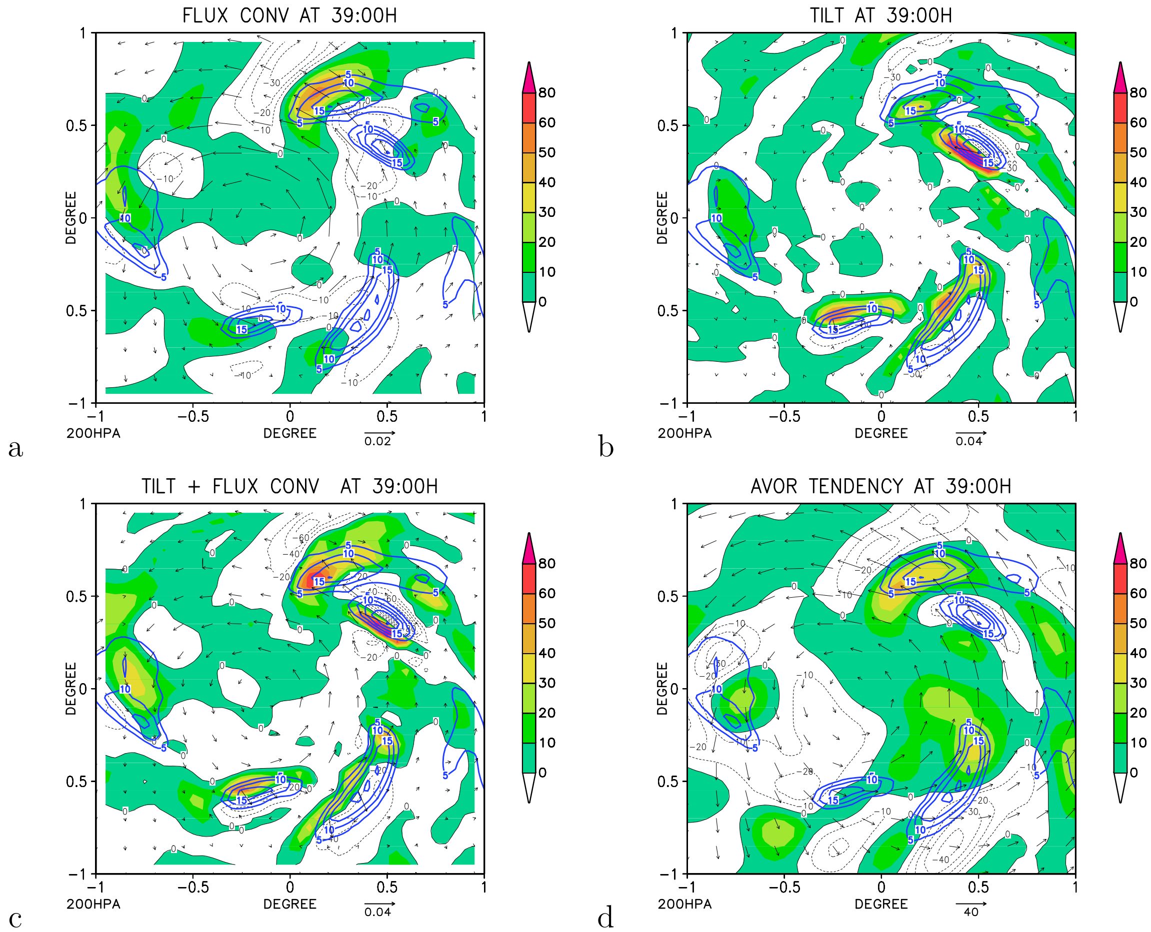

Figure E.4: As in Figure E.1 except for 200 hPa.

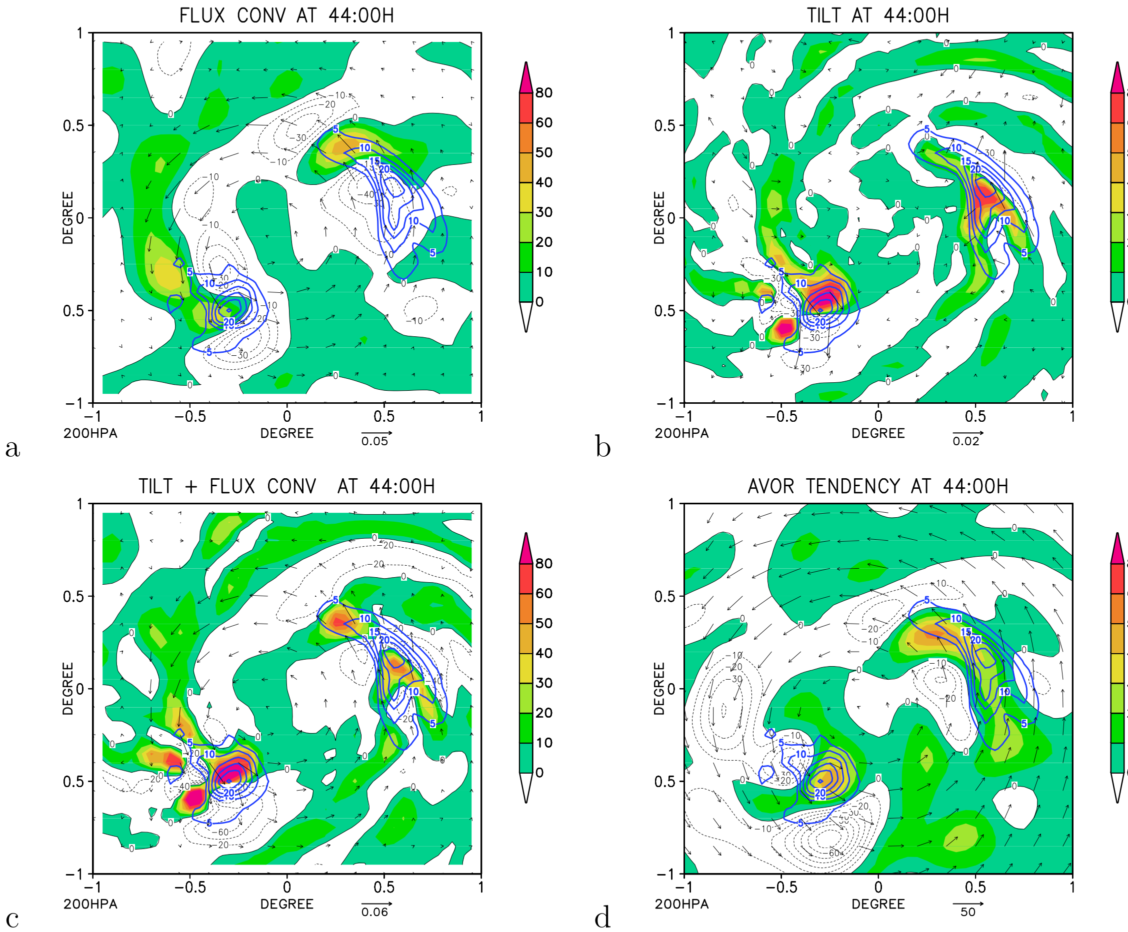

Figure E.5: As in Figure E.4 but for the asymmetric phase A2 at 44 h.

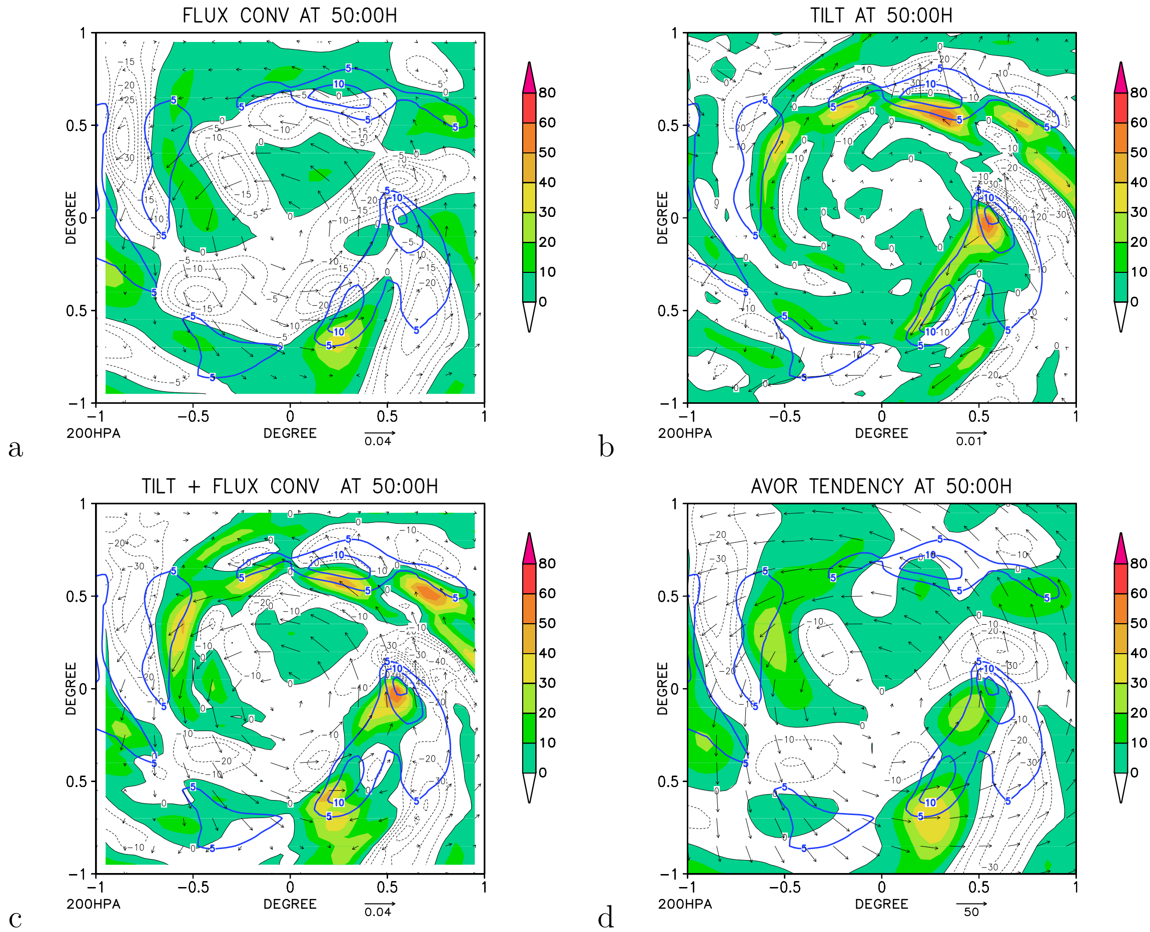

Figure E.6: As in Figure E.4 but for the symmetric phase S2 at 50 h.

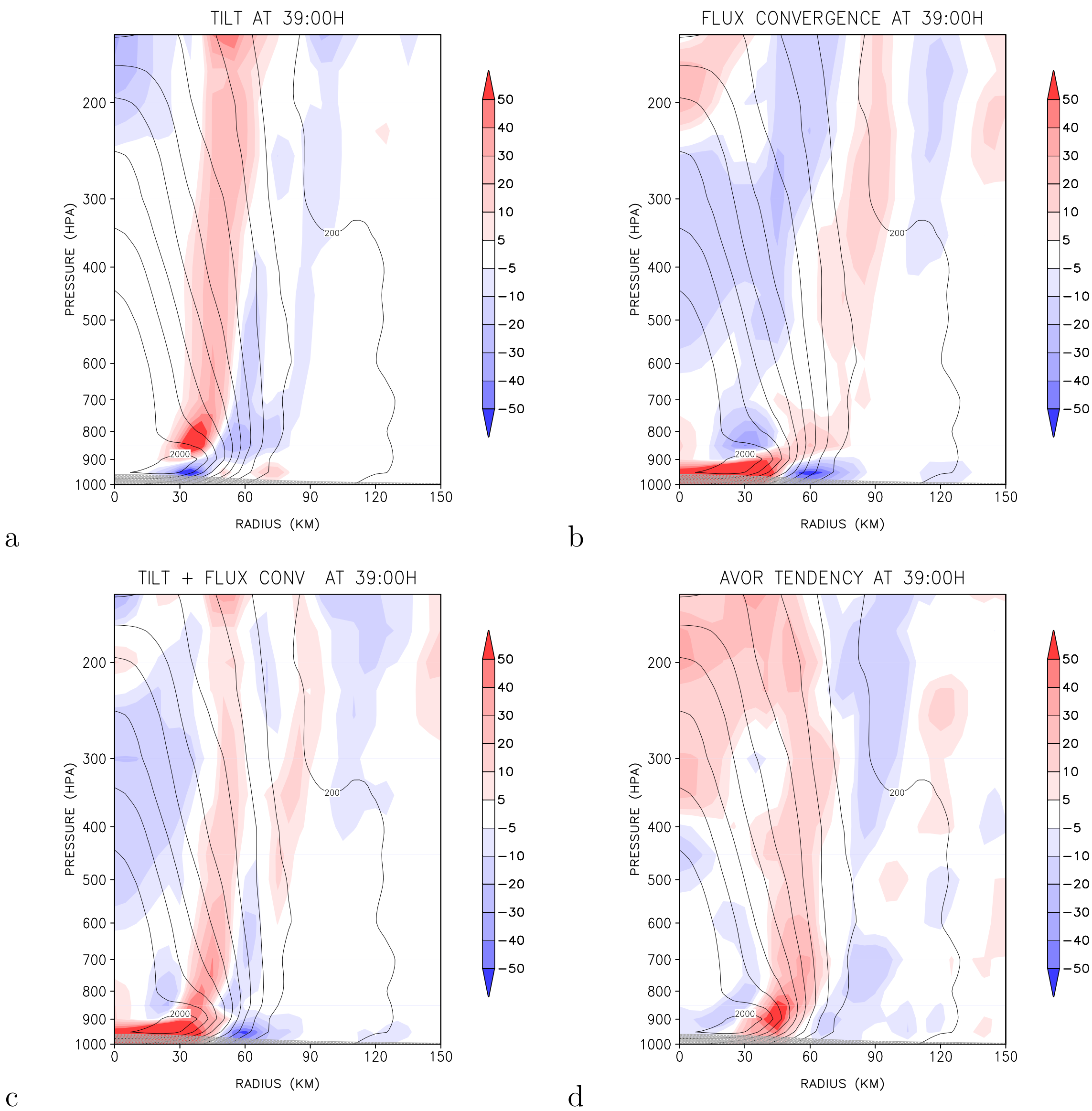

Figure E.7: Vertical-radius plots of different terms [$10^6 \times$ s^{-2}] (shaded) in the vorticity budget equation. a) Tilting term, b) Horizontal vorticity flux term, c) Sum of the tilting and Horizontal vorticity flux terms, and d) Observed tendencies of absolute vorticity at the symmetric phase S1 (at 39h). Blue contours show azimuthal means of absolute vorticity [$10^6 \times$ s^{-2}] .

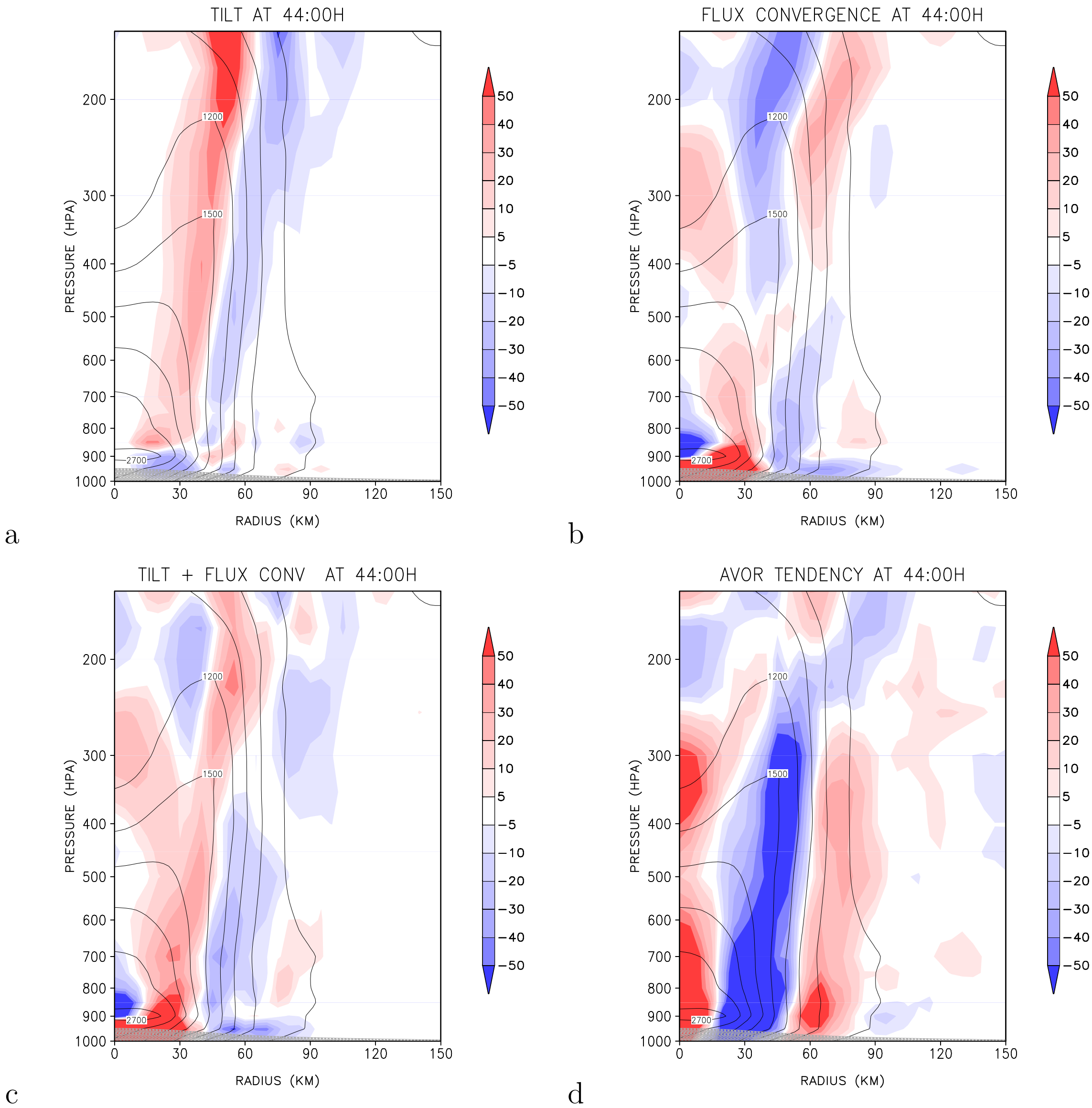

Figure E.8: Similar to Figure E.7 but for the asymmetric phase A2 at 44 h.

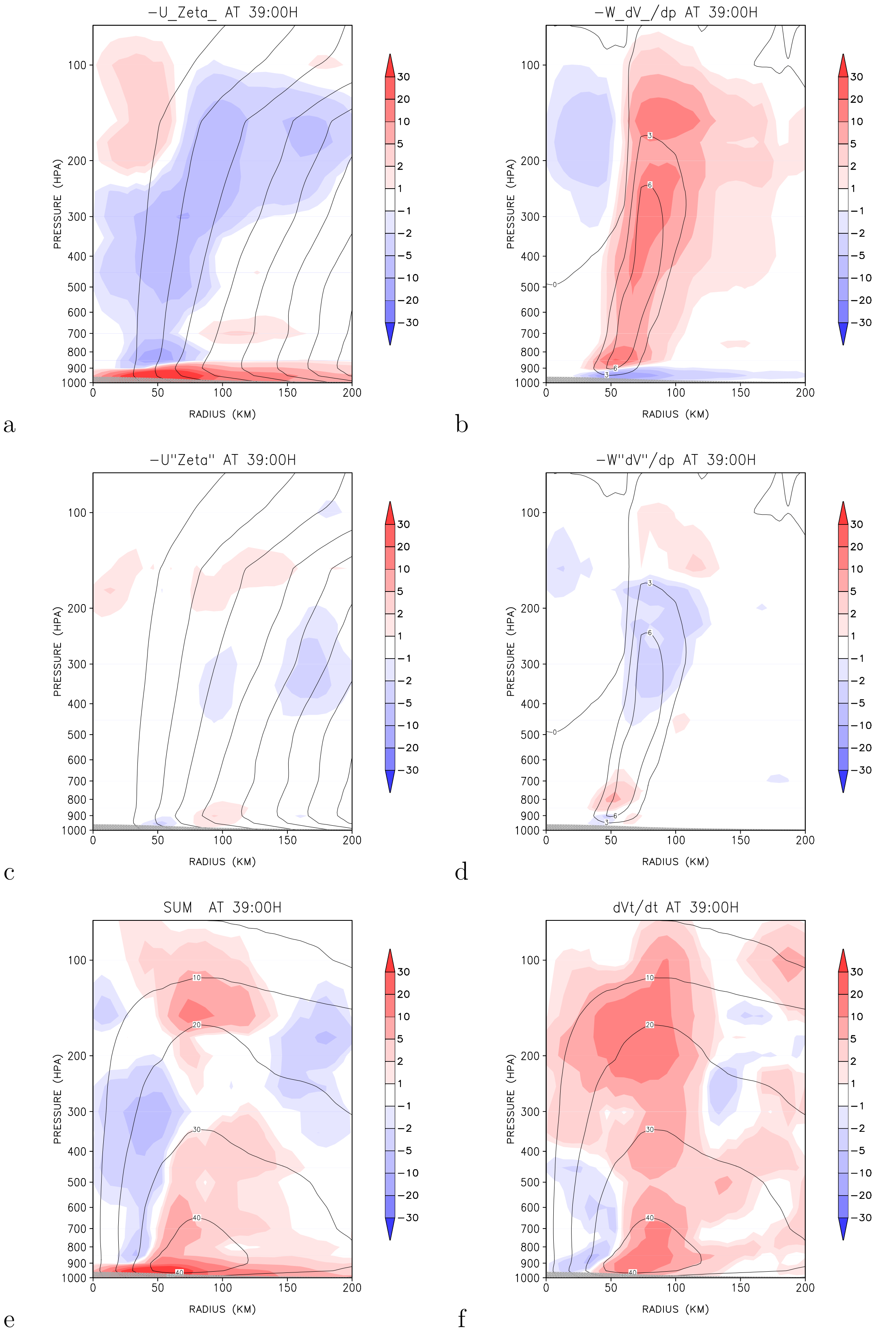

Figure E.9: Vertical cross section of azimuthal means of the term in the budget equation for mean tangential wind, for the symmetric phase S1 at 39 h.

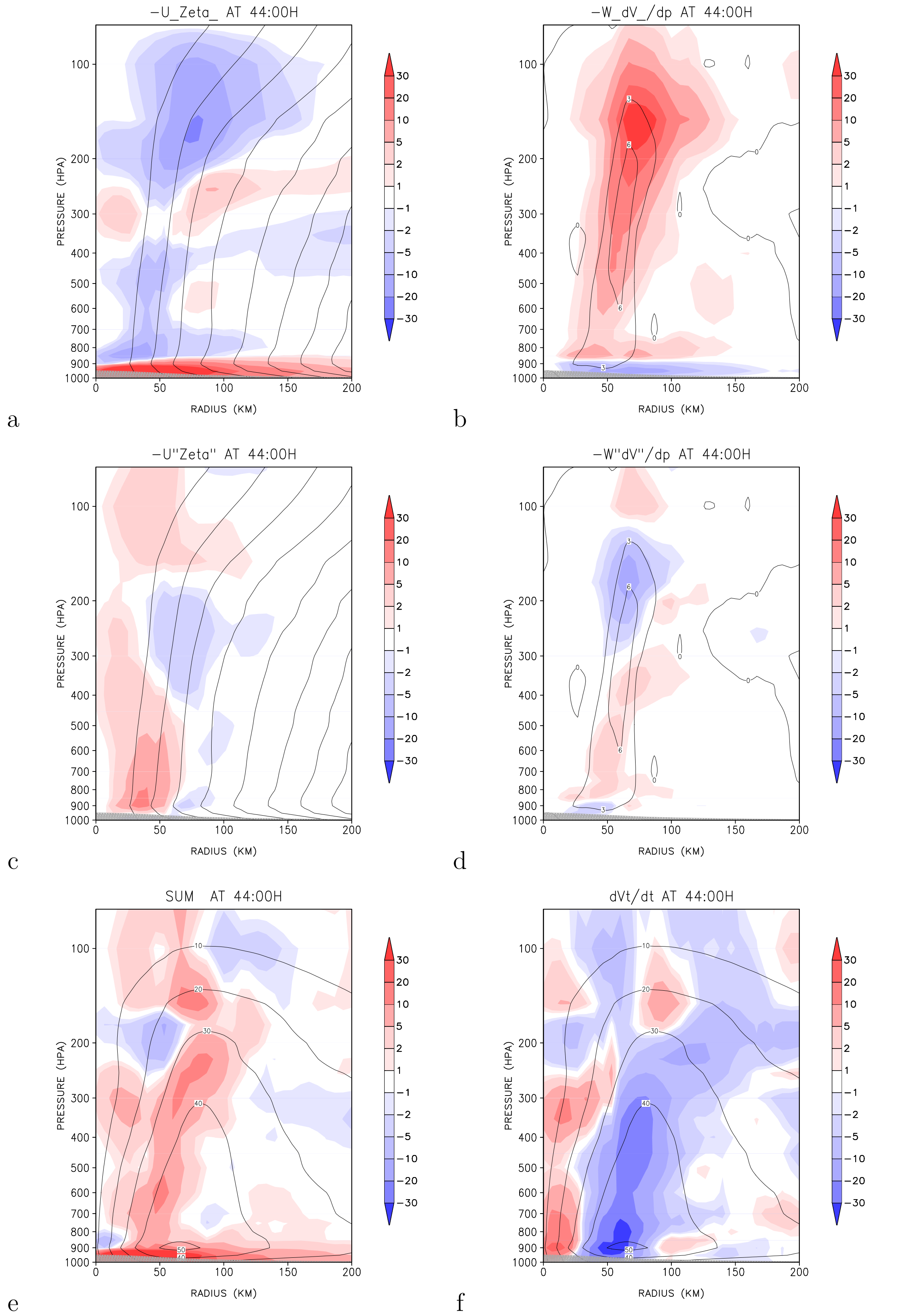

Figure E.10: Vertical cross section of azimuthal means of the term in the budget equation for mean tangential wind, for the asymmetric phase S2 at 44 h.

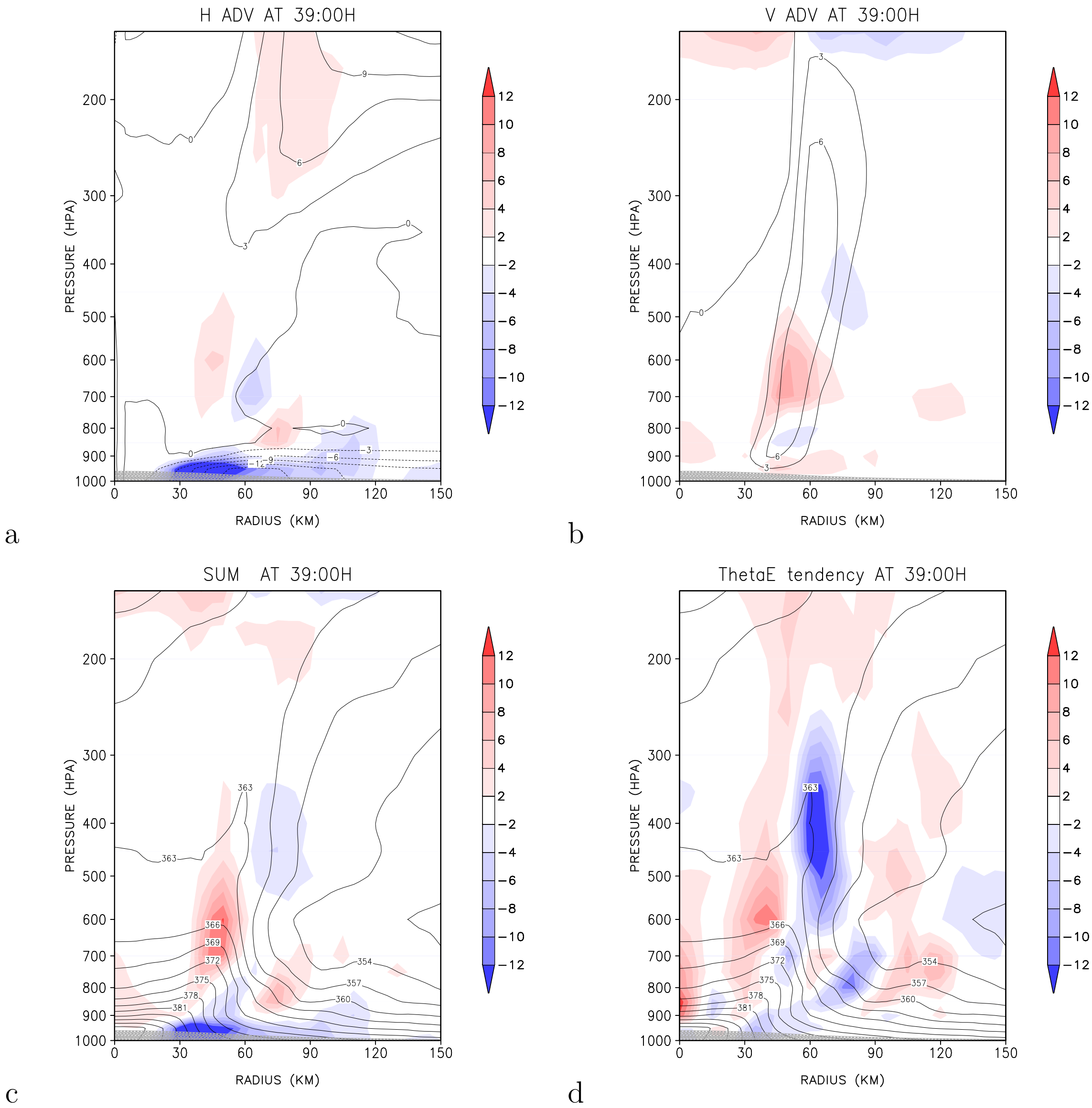

Figure E.11: Vertical cross section of azimuthal means of the term in the budget equation for θ_e, for the symmetric phase S1 at 39h.

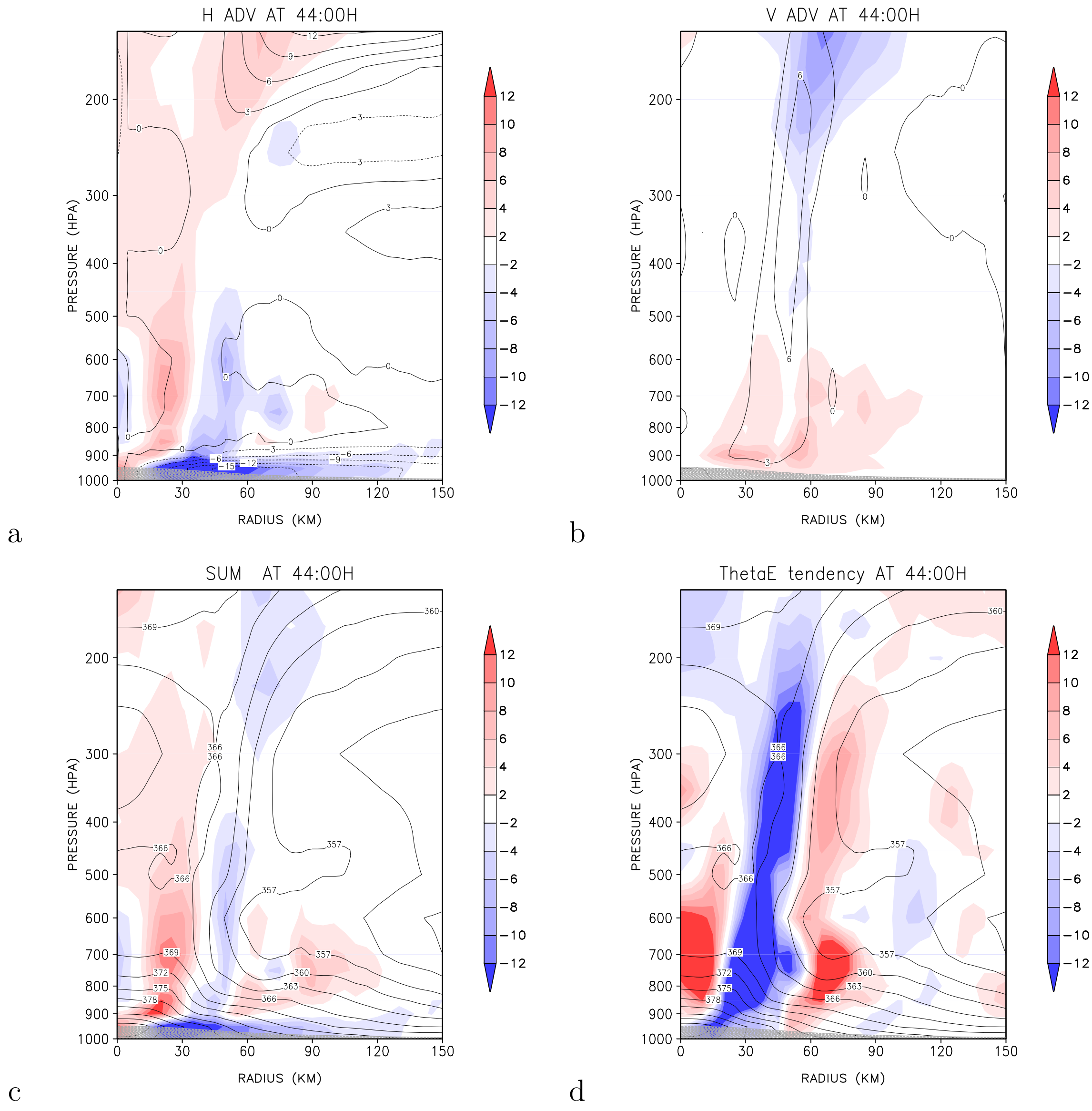

Figure E.12: Vertical cross section of azimuthal means of the term in the budget equation for θ_e, for the asymmetric phase A2 at 44h.

Appendix F

Evolution of Vortical Hot Towers

Local maxima in vertical velocity in the eyewall, which are called VHTs, are tracked using model output with 5 minute intervals. Different characteristics along the trajectories of these VHTs are recorded and plotted in Figures F.1-F.16, whose characteristics are listed in Table F.1.

Table F.1: Characteristics of figures showing the results for the tracked VHTs.

Characteristics of the VHTs	Level (hPa)	Variable	VHT number	Figure
Initial locations	850-500 hPa	ω	1- 4	F.1
Trajectories	850, 500	tracks	1 2 3 4	F.2 F.3 F.4 F.5
Along-track values	850, 500	distance R ω	1-4	F.6 F.7
	Surface	CAPE	1-4	F.8
	850, 200 850, 200 850, 500 Surface	$\overrightarrow{V}_{200} - \overrightarrow{V}_{850}$ $\bar{V}_{200} - \bar{V}_{850}$ $\lambda_{500} - \lambda_{850}$ $\nabla^2 p_s$	1-4	F.9 F.10 F.11 F.12
VHTs on the mean PV gradient	850	$\partial\overline{PV}/\partial r$, R	1-4	F.13
Vertical cross-sections along trajectories	1000-100	ω,$\nabla^2 PV$	1	F.14
		θ_e,$\nabla^2 Tv$	1	F.15
Vertical soundings of VHT1	1000-100	T, Td	1	F.16

In Table F.1 λ denotes the azimuthal angle of the VHTs relative to the vortex centre, other variables are conventional as described in Table A.1

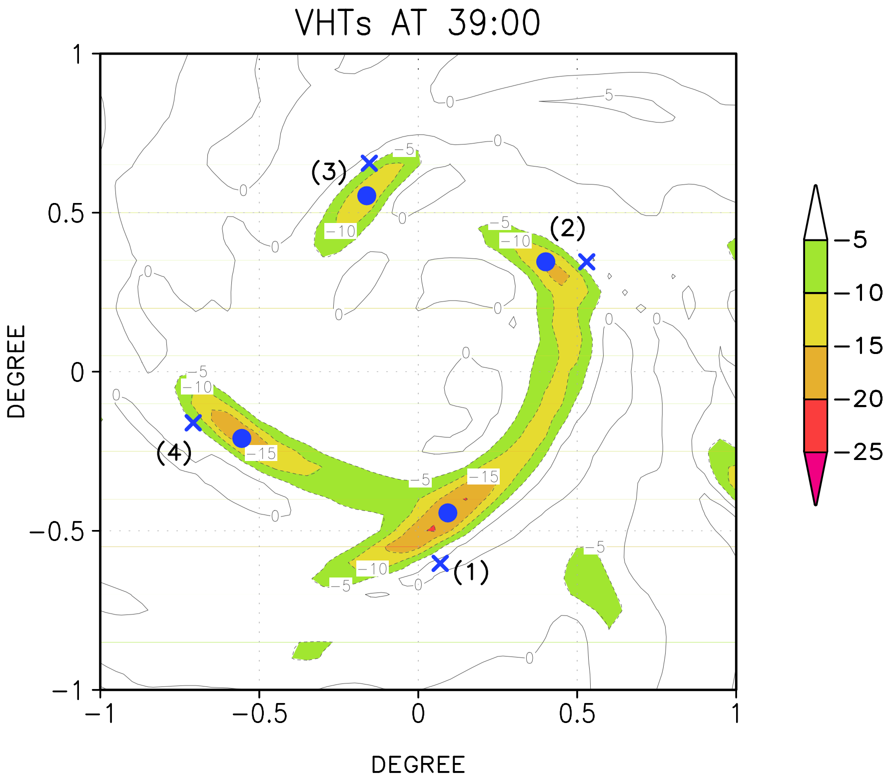

Figure F.1: Locations of VHTs at the initial time of tracking, at S1 (39 h). Vertical velocity at the 850hPa is shaded. Cirles(crosses) represent the locations of VHTs at the 850 (500) hPa.

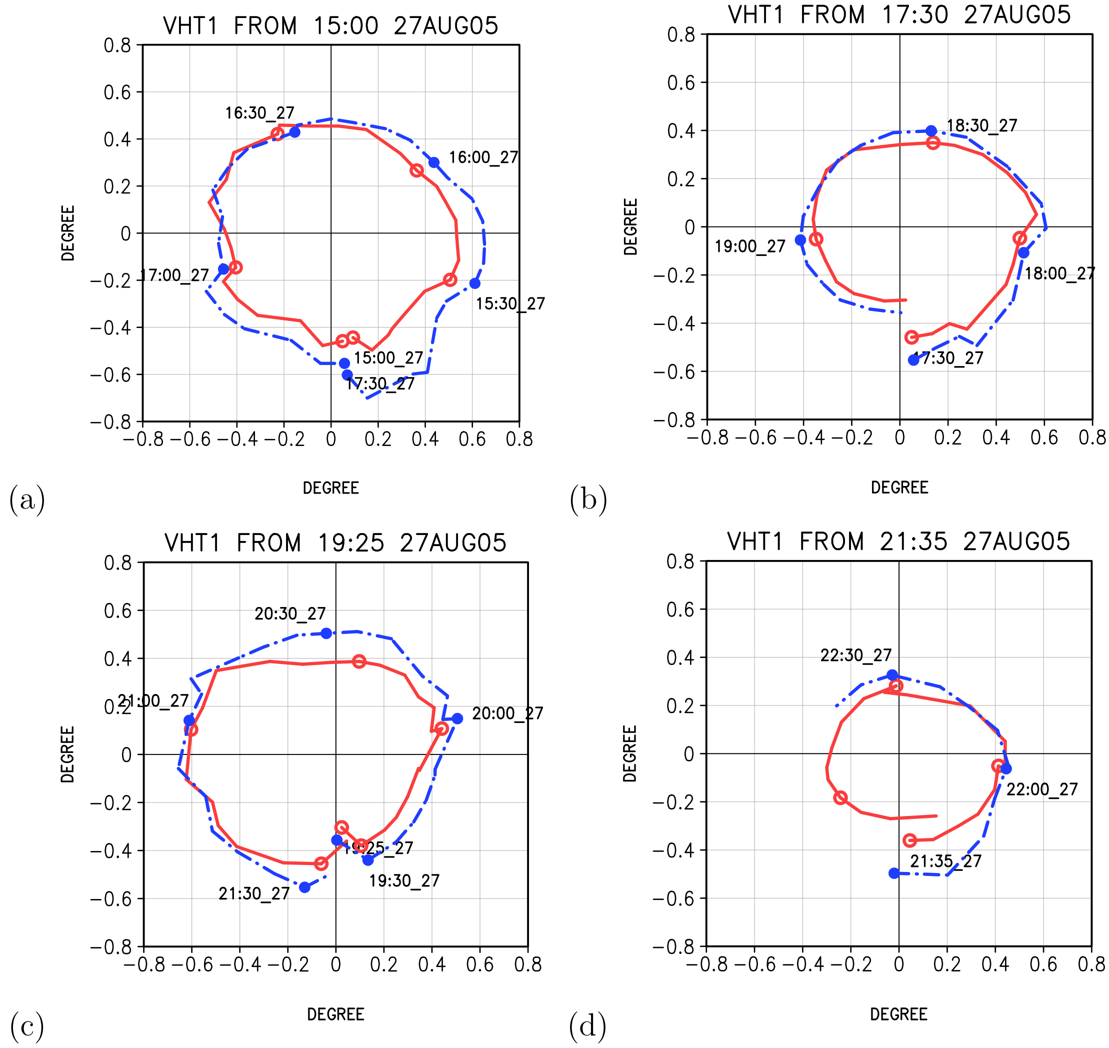

Figure F.2: Trajectories of VHT1 relative to vortex center at 850hPa (blue solid lines) and 500hPa (red dashed lines). Figures are ordered with the increased time

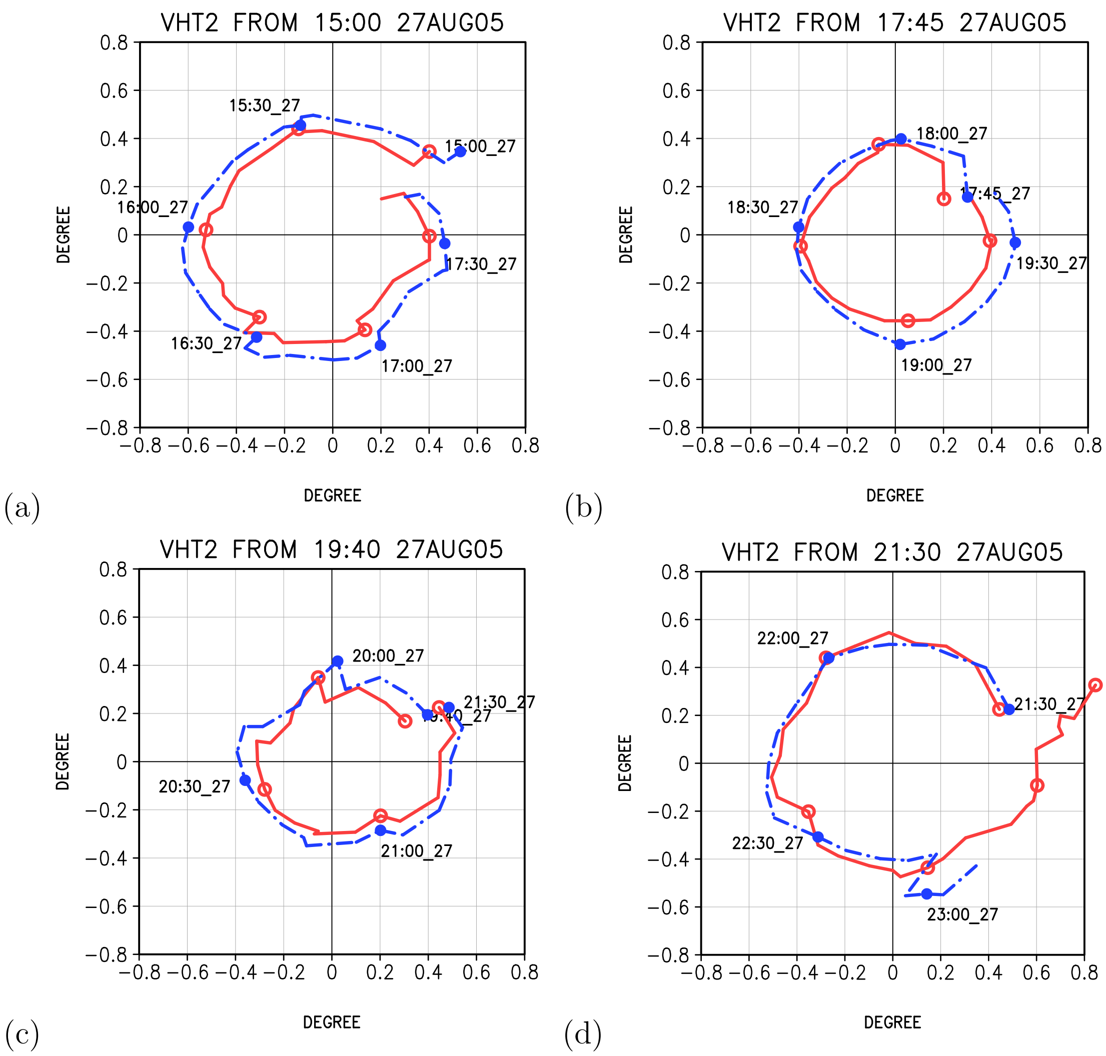

Figure F.3: Same as Figure F.2 but for VHT2

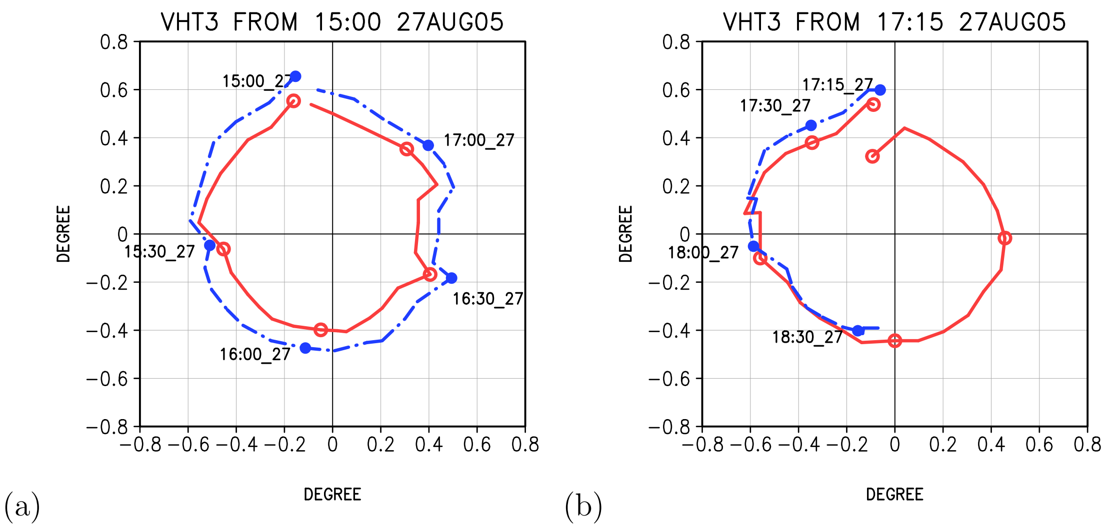

Figure F.4: Same as Figure F.2 but for VHT3

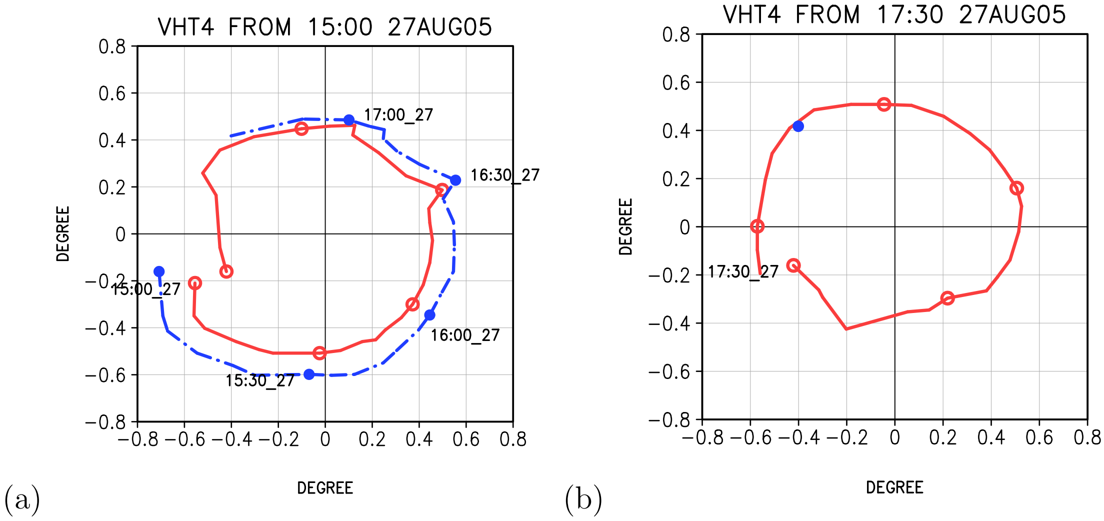

Figure F.5: Same as Figure F.2 but for VHT4

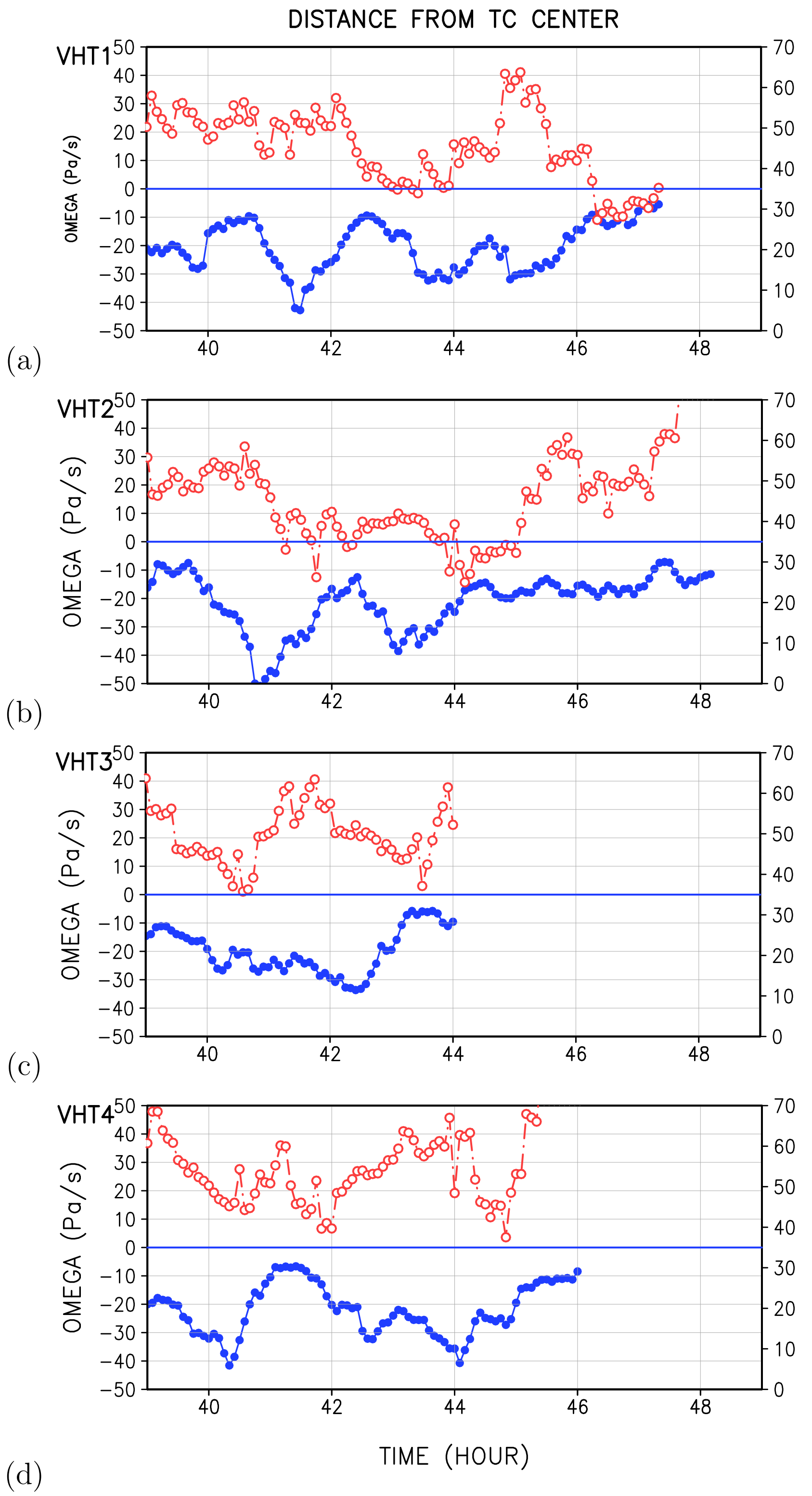

Figure F.6: Evolution of distance from the VHTs to the vortex center (red dotted-dashed lines with open circles). Blue lines with filled circles mark the intensity of vertical velolities at the VHT's location at the 850hPa level.)

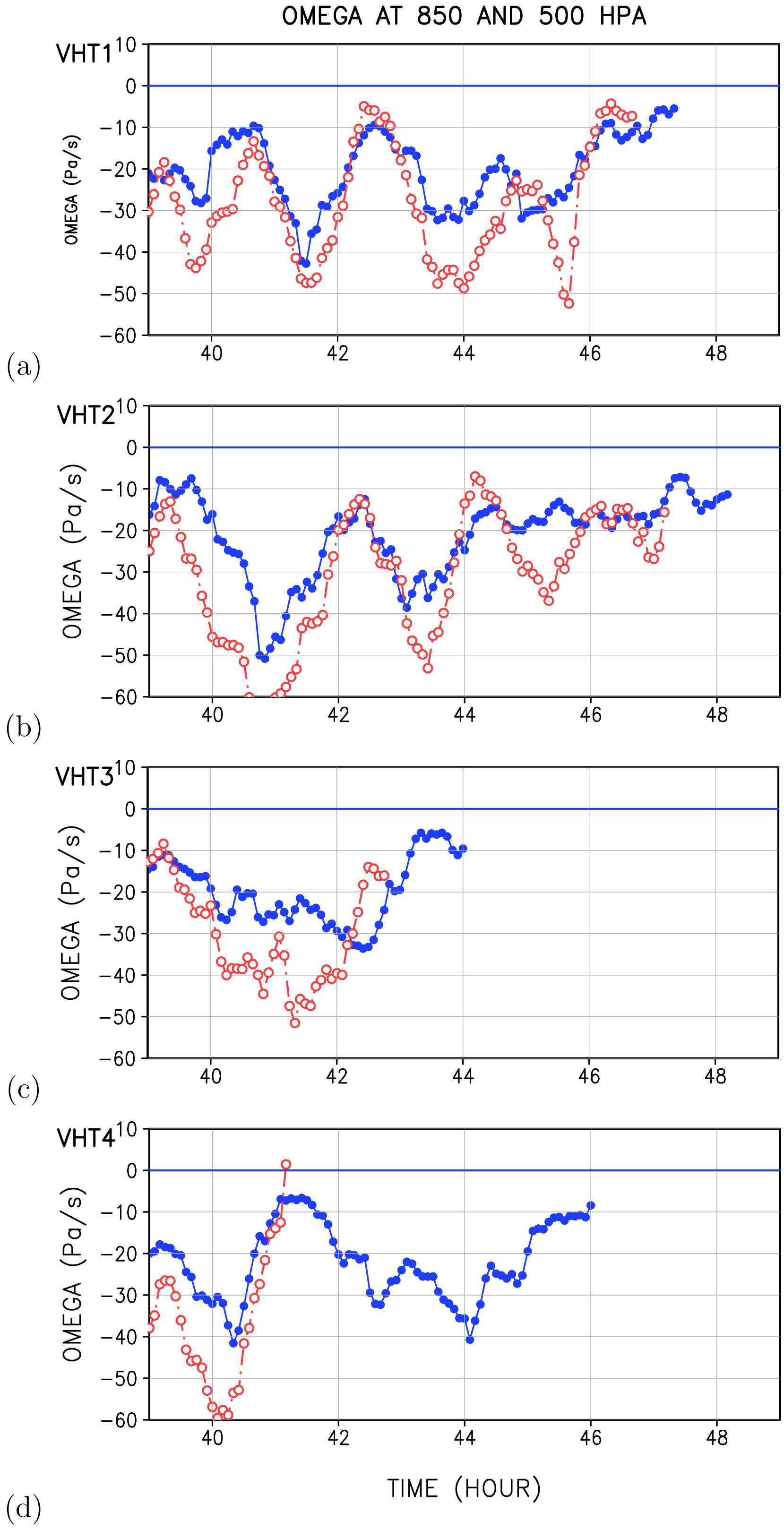

Figure F.7: Evolution of vertical velocity at 500 hPa (red dotted-dashed lines with open circles, unit [Pa s^{-1}]) along the trajectories of the VHTs. Blue lines are the same as those in Figure F.6

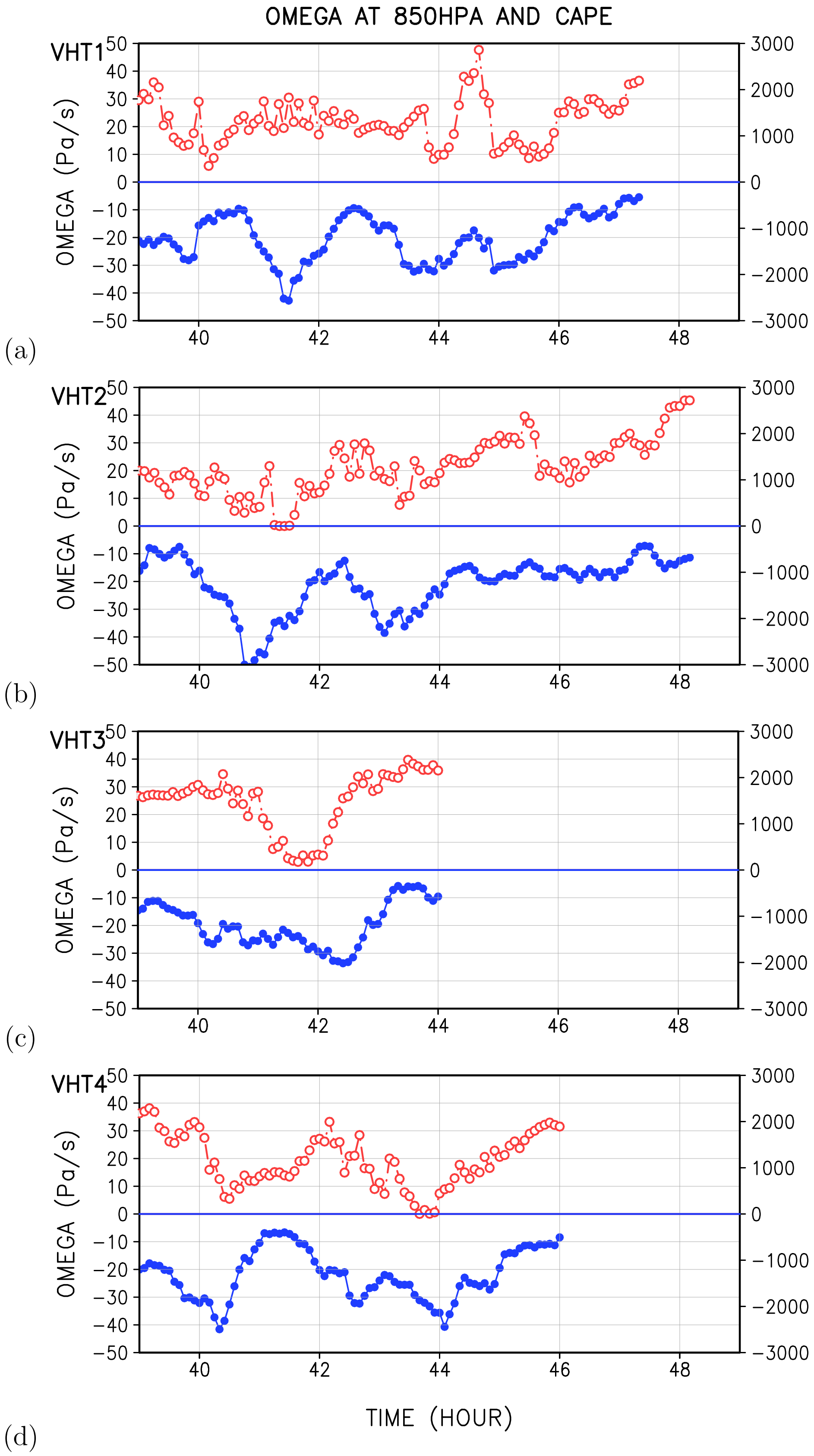

Figure F.8: Evolution of CAPE (red dotted-dashed lines with open circles, unit [J Kg K^{-1}]) along the trajectories of the VHTs. Blue lines are the same as those in Figure F.6

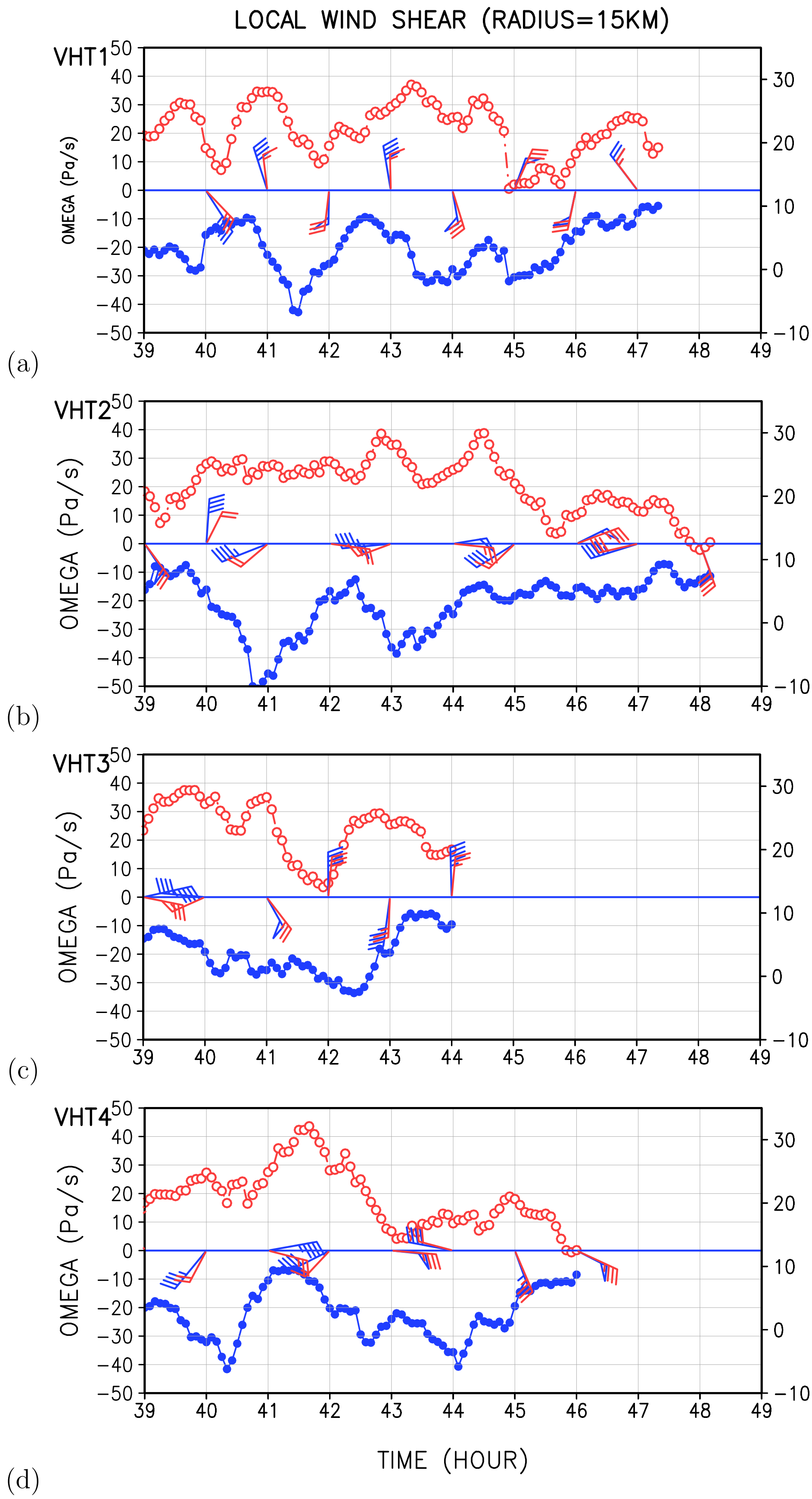

Figure F.9: Evolution of local vertical wind shear (red dotted-dashed lines with open circles) along the trajectories of the VHTs. Blue lines are the same as those in Figure F.6. Blue(red) wind barbs show the winds at the 850(200)hPa level. Wind shear is calculated as the difference between the winds at 200 and 850 hPa, averaged over the area of 15 km radius centered at the locations of the VHTs

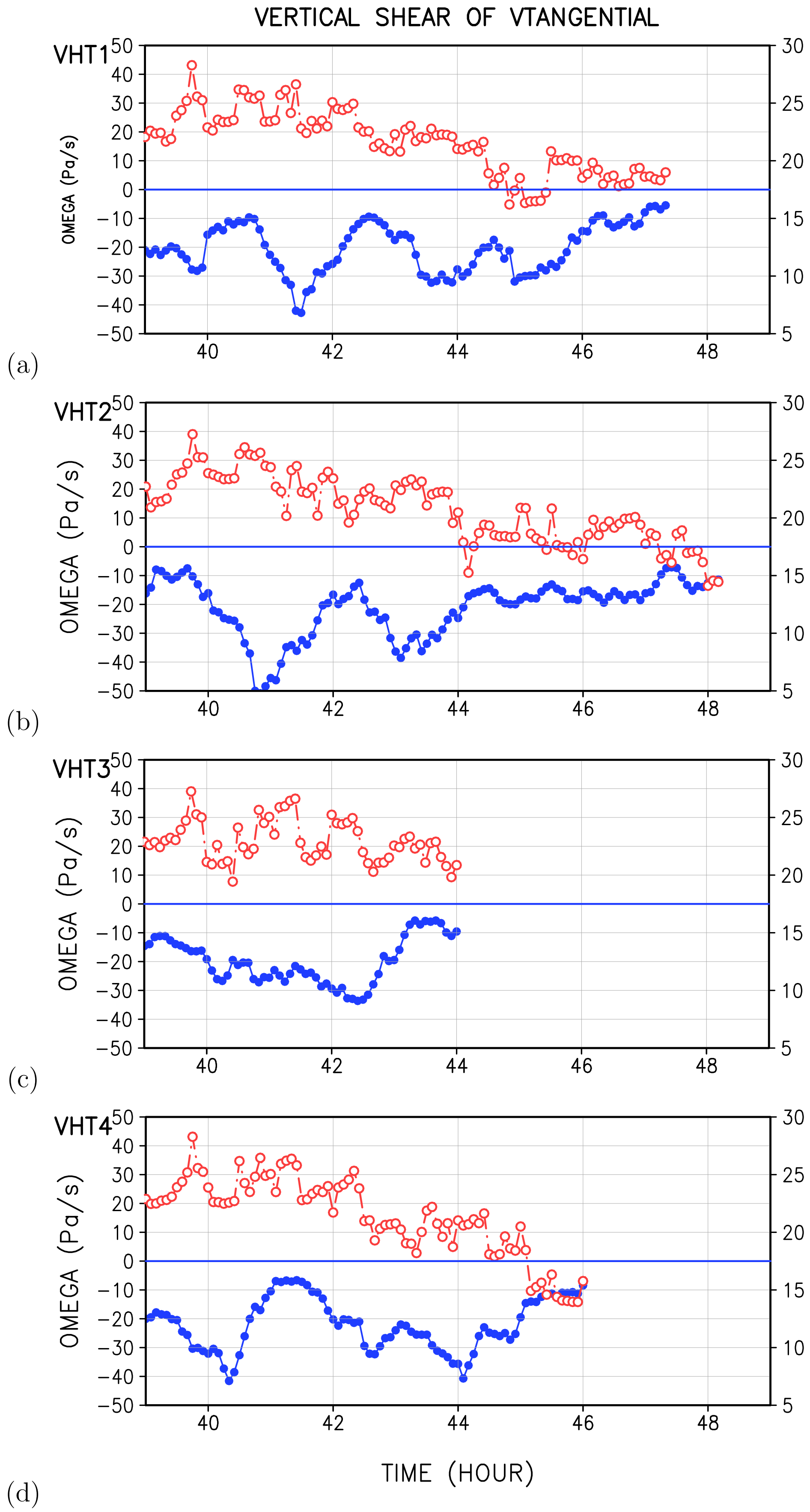

Figure F.10: Similar to Figure F.9 but for the vertical shear of mean tangential wind

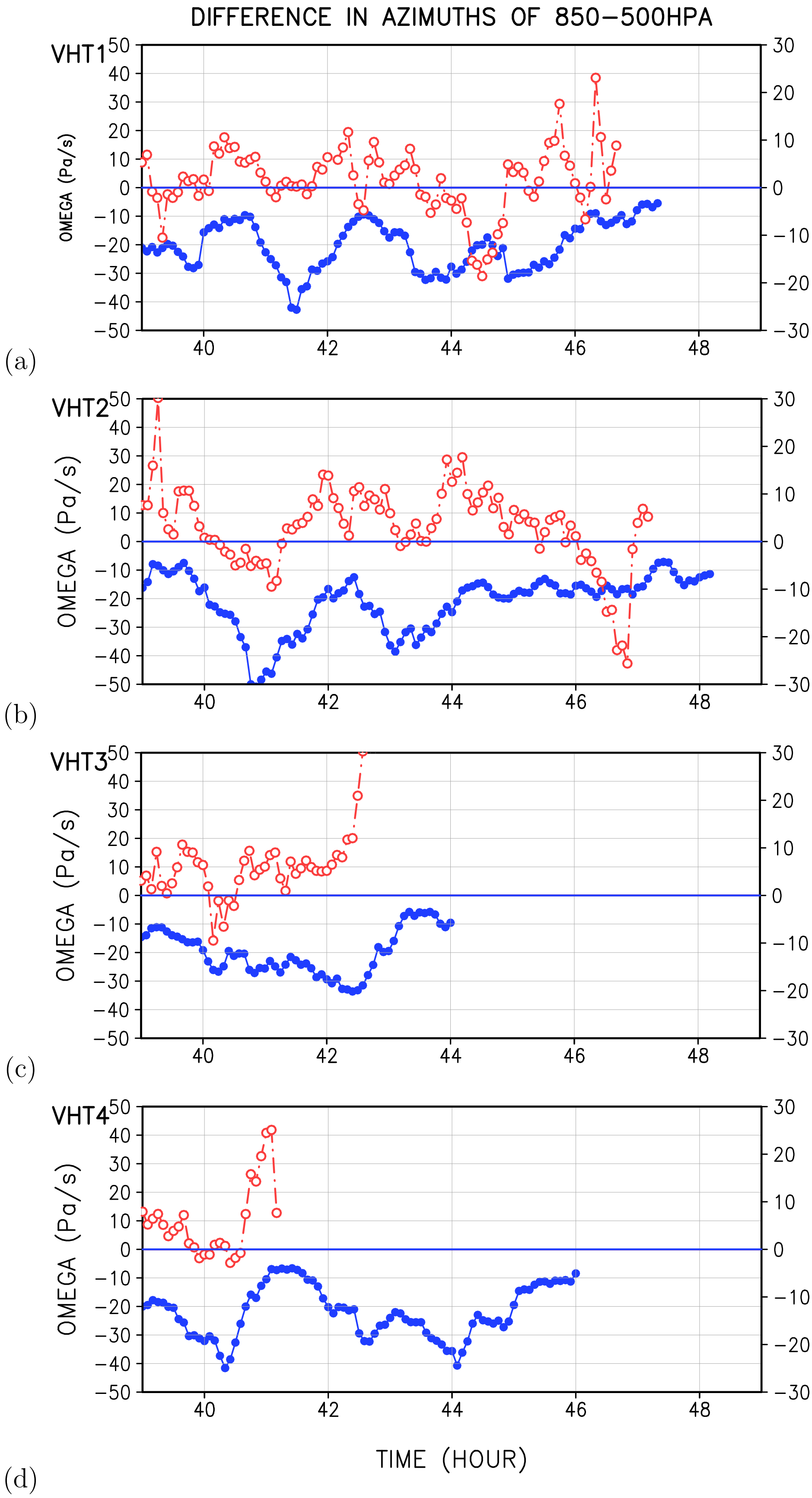

Figure F.11: Evolution of the differences between azimuthal angles of the VHTs at 850 and 500 hPa along trajectory of the VHTs)

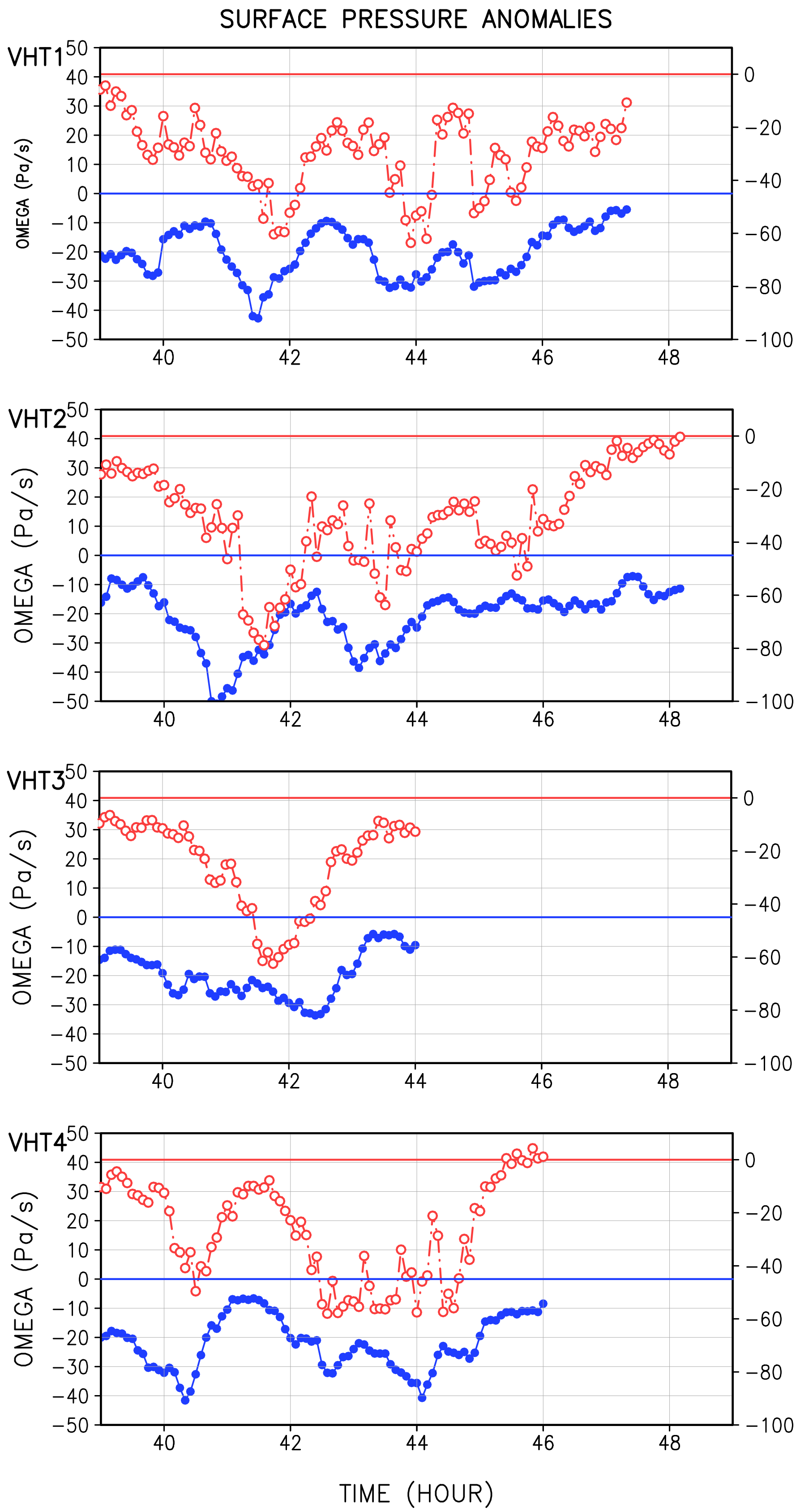

(a)

(b)

(c)

(d)

Figure F.12: Evolution of the differences between azimuthal angles of the VHTs at 850 and 500 hPa along trajectory of the VHTs)

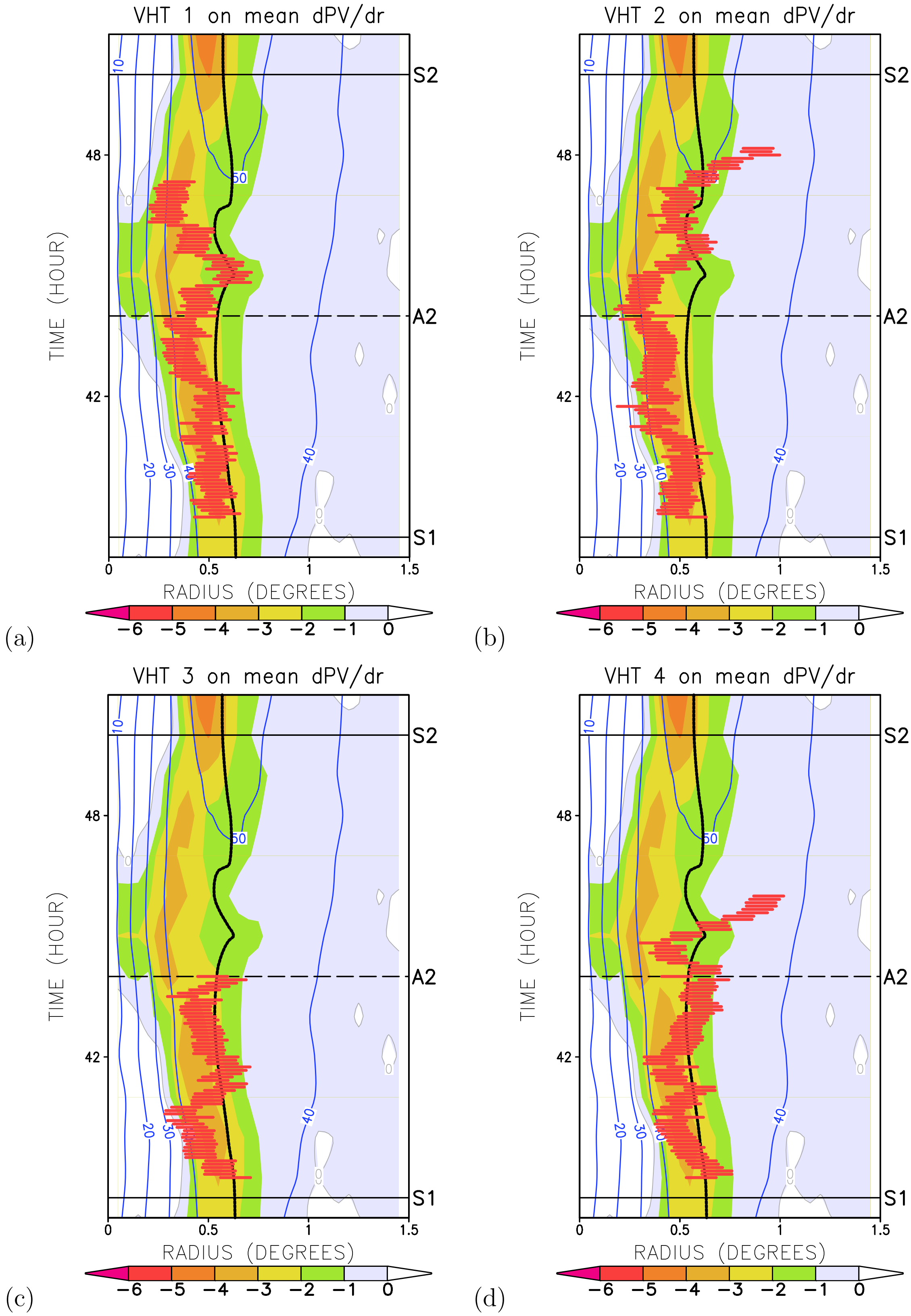

Figure F.13: Localtions of the VHTs (marked with red horizontal lines representing the VHTs with a diameter of 15 km centered) on the mean PV radial gradients (shaded).

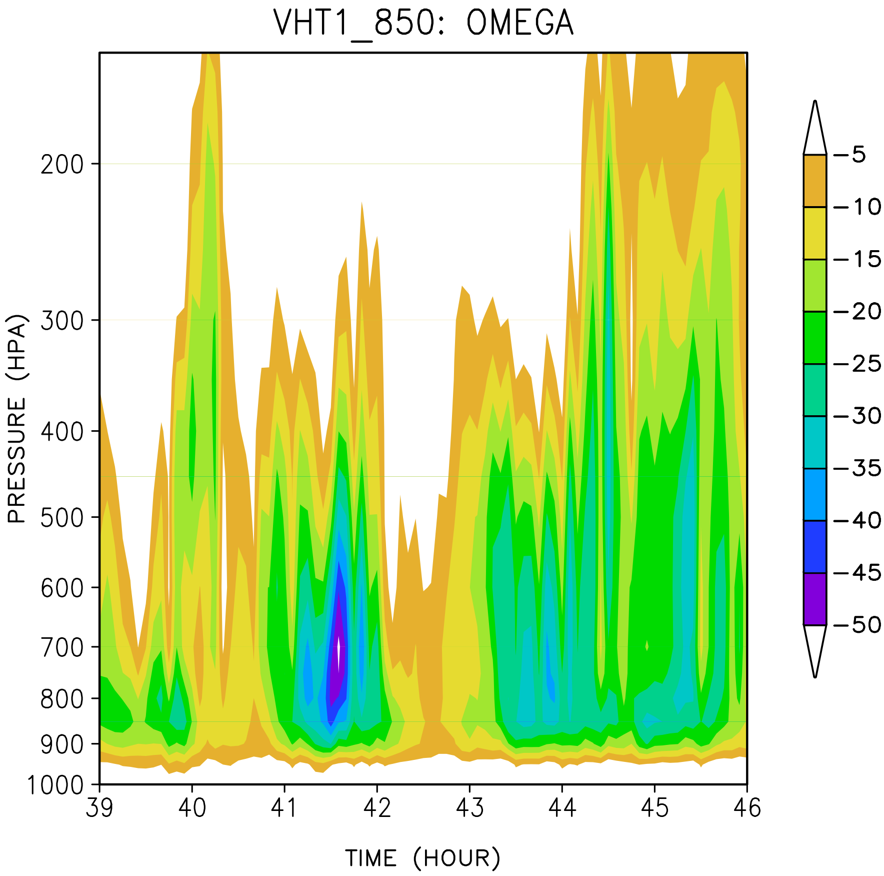

(a)

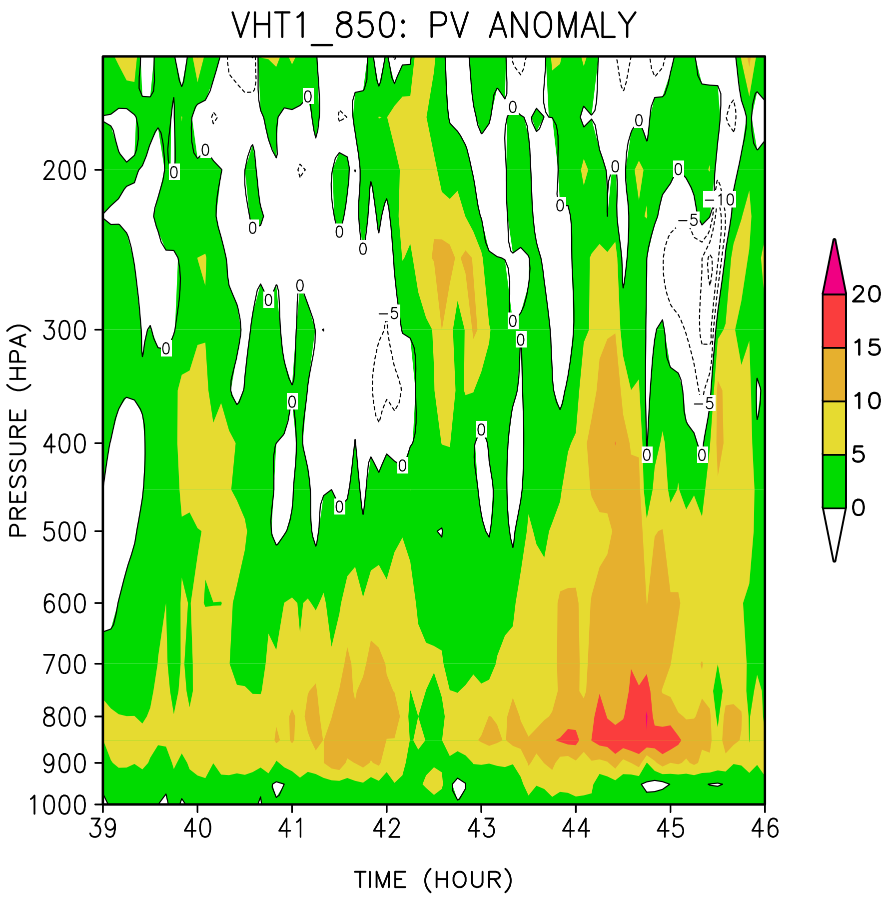

(b)

Figure F.14: Evolution of vertical cross-section along trajectories of VHT1 for ω and $\nabla^2 PV$

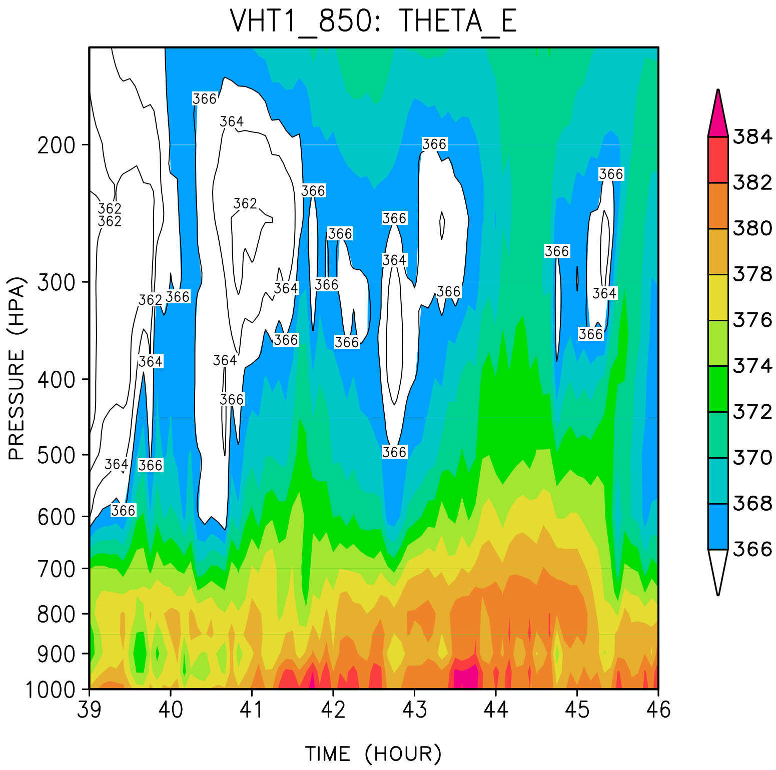

(a)

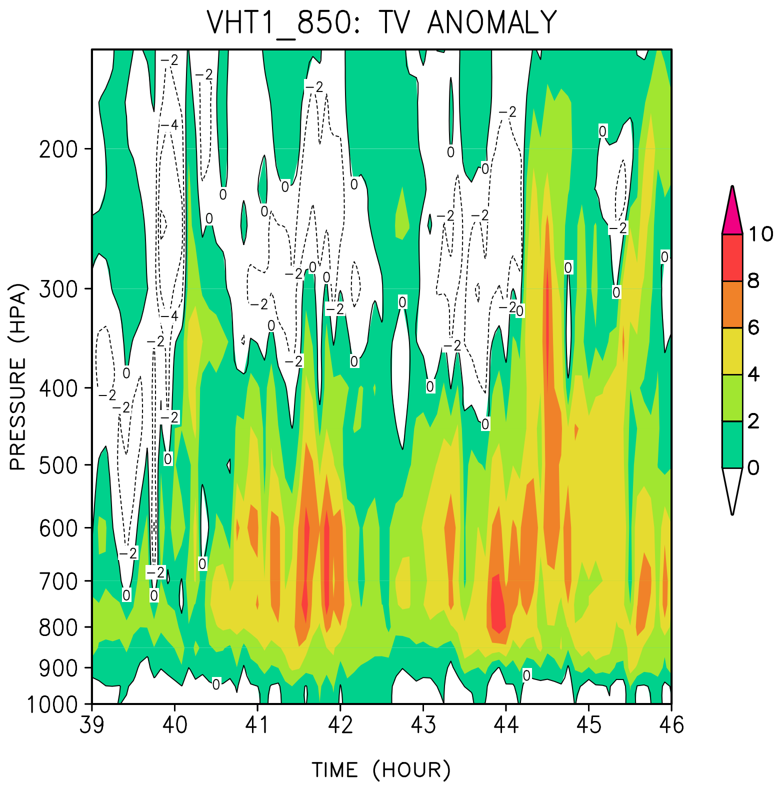

(b)

Figure F.15: Evolution of vertical cross-section along trajectories of VHT1 for θ_e and $\nabla^2 Tv$

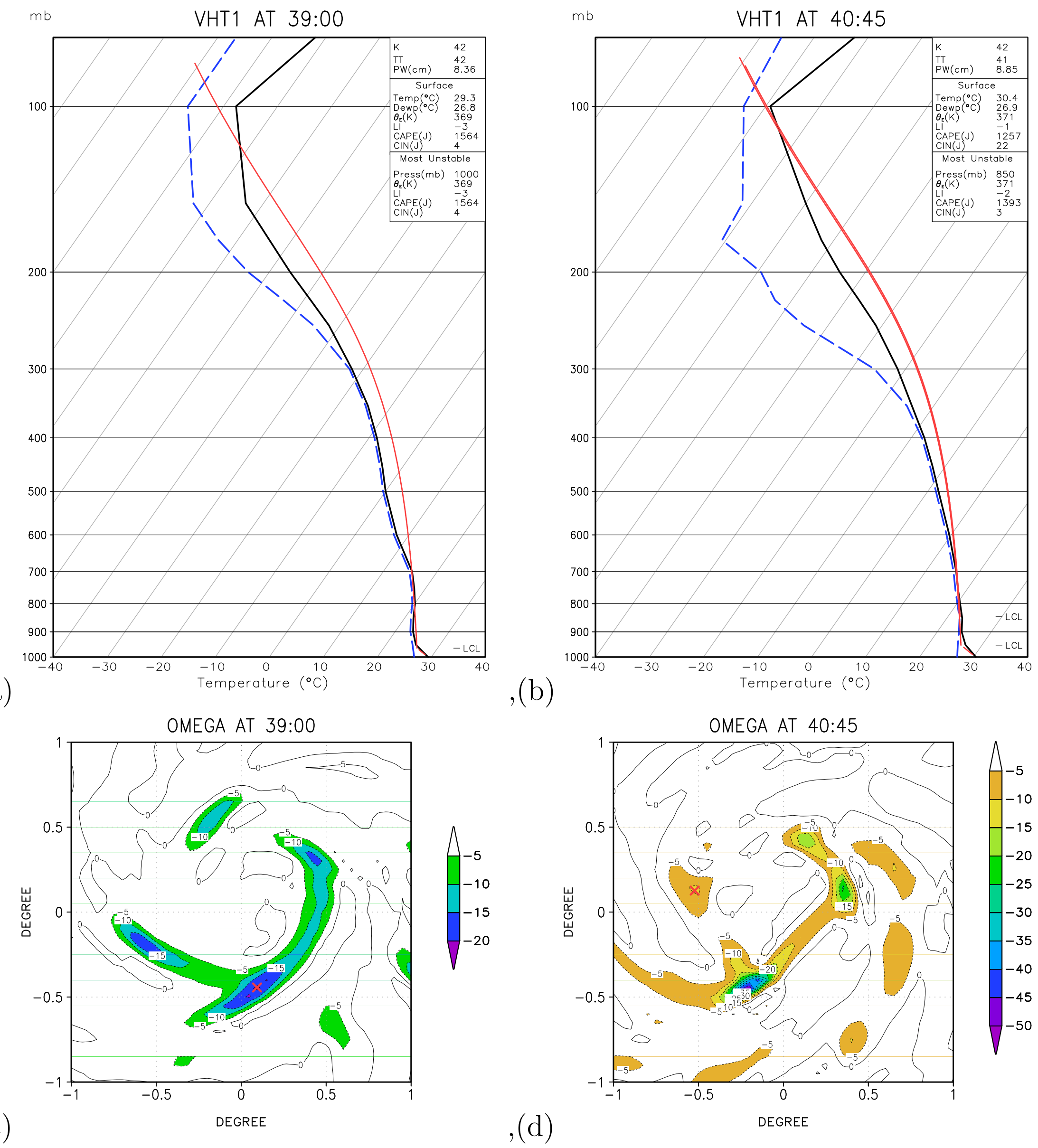

Figure F.16: Vertical temperature and dew-point tempterature profiles of VHT1 at the times of high and low intensity (a and b, respectively); and their positions marked in the vertical velocity fields at 850 hPa at the respective times (c and d).